A New, Clean Catalogue of Extragalactic Non-nuclear X-ray Sources

Hannah Penn Earnshaw

A thesis presented in accordance with the regulations for admittance to the degree of Doctor of Philosophy

Centre for Extragalactic Astronomy
Department of Physics
University of Durham
United Kingdom

April 2017

A New, Clean Catalogue of Extragalactic Non-nuclear X-ray Sources

Hannah P. Earnshaw

Abstract

We use the *XMM-Newton* Serendipitous Source Catalogue to create a catalogue of non-nuclear extragalactic X-ray sources that is both large, containing 1,464 sources, and clean, with steps taken to minimise contamination. This catalogue contains 372 ultraluminous X-ray sources (ULXs), objects with extreme luminosities ($L_{\rm X} > 10^{39}\,{\rm erg\,s^{-1}}$) higher than expected for a stellar-mass black hole (BH) accreting at its Eddington limit, and thought to mainly be super-Eddington accreting compact objects. We find the colour properties of ULXs to be similar to lower-luminosity sources, distinct from active galactic nuclei, and similar between populations in spiral and elliptical galaxies. Our catalogue contains eight new candidate intermediate-mass BHs (IMBHs) amongst the most luminous sources, 33 transient ULXs, and five ULXs with high short-term variability. Of these highly variable ULXs, we closely examine M51 ULX-7, which exhibits a persistently hard spectrum and evidence of band-limited noise, arguments in favour of it being an IMBH. However, a possible high-energy spectral turnover and its high dynamic range of flux bear similarities to properties observed in neutron star ULXs discovered to date. A useful subpopulation of our catalogue are sources at the Eddington Threshold ($10^{38} < L_{\rm X} < 3 \times 10^{39}\,{\rm erg\,s^{-1}}$), the luminosity regime in which stellar-mass BHs may be accreting at or just below the Eddington limit. Our catalogue contains 666 such objects, four of which we studied in detail and found to demonstrate the heterogeneous nature of this luminosity regime, including high-luminosity sub-Eddington accretion states, the ultraluminous supersoft accretion regime, and sources in intermediate accretion modes. Finally, we searched for evidence of the most highly obscured and down-scattered super-Eddington accreting sources by looking for ultraluminous ultraviolet (ULUV) sources in UV source catalogues. We discovered six ULUV candidates in the *Swift* UVOT catalogue that are ideal for follow-up observations using *HST*.

Declaration

The work described in this thesis was undertaken between 2013 and 2017 while the author was a research student under the supervision of Dr Timothy P. Roberts in the Department of Physics at the University of Durham. No part of this thesis has been submitted for any other degree at the University of Durham or any other university.

Portions of this work have appeared in the following papers:

- Chapter 2: *A new, clean catalogue of extragalactic X-ray binaries in nearby galaxies*, Earnshaw, H.P., Roberts, T.P., Middleton, M.J., Mateos, S., in preparation
- Chapter 3: *A variable ULX and possible IMBH candidate in M51a*, Earnshaw, H.M., Roberts, T.P., Heil, L.M., Mezcua, M., Walton, D.J., Done, C., Harrison, F.A., Lansbury, G.B., Middleton, M.J., Sutton, A.D., MNRAS, 456, 3840, (2016)
- Chapter 4: *Soft extragalactic X-ray binaries at the Eddington Threshold*, Earnshaw, H.M., Roberts, T.P., MNRAS, 467, 2690, (2017)

Please note that while the author's current middle initial is P., it was M. at the time of publication for the papers mentioned above.

Acknowledgements

First of all, I would like to thank my supervisors Dr Timothy Roberts and Prof Chris Done. My work has only been made possible through your steadfast support, both academic and emotional. Thank you both for your high expectations of me and your guidance to help me meet them. I am also grateful to Dr Andrew Sutton and Dr Matthew Middleton, who have been particularly helpful in showing me the ropes when it comes to X-ray analysis. Thanks also to my officemates, next-door-officemates and honorary next-door-officemates Andrew, James, Ben, Flora, Emma, Daniel, Greg, Ra'ad and Raj – your excellent company and illuminating discussions over coffee have helped to make my time in the department especially enjoyable.

Thank you to my friends outside of work who have been interested in hearing me talk about black holes over falafel and other foods that are not falafel. Thank you to the Dexters, and later my sister Ruth, for being great housemates and especially tolerant and understanding during the more stressful periods of my degree. And thank you to my family, who have supported me in each and every one of my space-related ambitions, including but not limited to a PhD in astronomy – your encouragement has always been a real blessing to me.

Contents

List of Tables

List of Figures

CHAPTER 1

Introduction

This work is concerned with investigating bright extragalactic non-nuclear X-ray sources – those located outside of the centre of their host galaxy – including ultraluminous X-ray sources (ULXs) and sources with luminosities just below the ULX regime. This population is largely made up of compact objects – black holes (BHs) or neutron stars (NSs) – accreting matter at rates close to or above their so-called Eddington limit, a hypothetical upper limit to accretion based on simple assumptions, the breaking of which indicates extreme behaviours and gives the sources their characteristic high luminosities. Study of these sources allows us to probe the extremes of accretion physics that occur close to and above the Eddington limit. Therefore we begin by introducing how X-ray sources are observed and the instrumentation involved (Section 1.1), the analysis techniques used to investigate X-ray sources (Section 1.2), the physical processes relevant to accreting objects (Section 1.3), and an overview of what is known about both sub-Eddington (Section 1.4) and super-Eddington accretion (Section 1.5).

1.1 X-ray observatories: past, present and future

Like many of the most fascinating discoveries in science, the field of X-ray astronomy began with serendipity.

Since X-rays are absorbed by Earth's atmosphere, X-rays from beyond Earth could only be observed with the advent of rocket flight, but a solar X-ray corona had been predicted as far back as the 1930s as an explanation for the highly ionised optical coronal lines observed in the solar spectrum (Grotrian, 1939; Edlén & Swings, 1942). Thus the first space missions to observe X-rays examined the Sun as a source of this high-energy emission (e.g. Friedman et al. 1951), as it was expected that X-ray emission from other

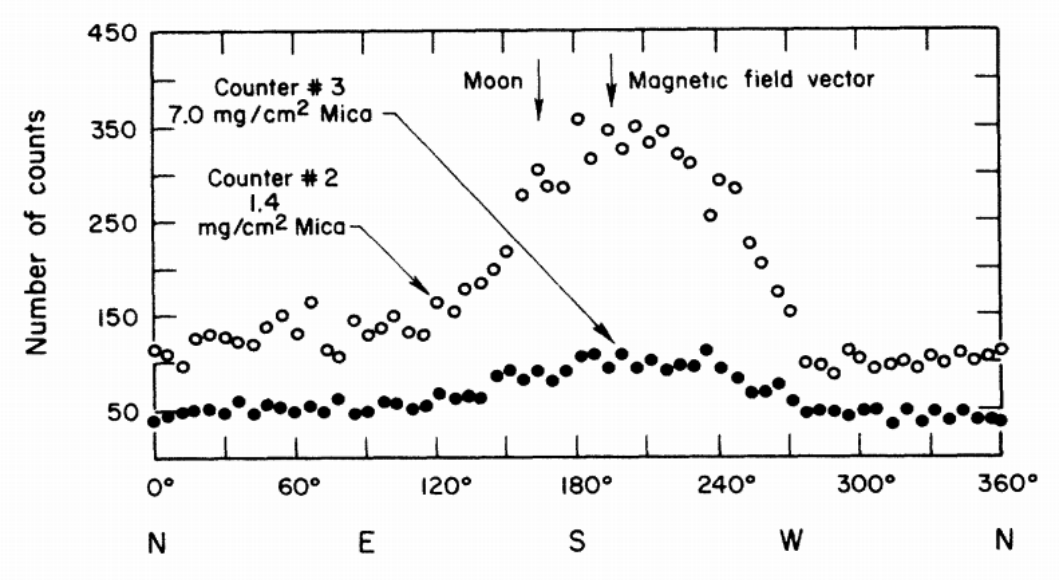

Figure 1.1: The counts recorded by the two operational counters versus the azimuthal angle in the discovery of Scorpius X-1, from Giacconi et al. (1962), showing the counts in bins of 350 s at 6 degree intervals. The location of the Moon and of the unexpected source (labelled 'Magnetic field vector') are indicated with arrows. The peak of Scorpius X-1 dominates the X-ray emission, and lies on a diffuse X-ray background that extends over the entire observed sky.

stars would be far too faint to detect. However, when a rocket flight in 1962 pointed a detector to look at the Moon for evidence of fluorescence X-rays caused by the incidence of solar X-rays, the Galactic X-ray source Scorpius X-1 was discovered (Giacconi et al. 1962; see Fig. 1.1). This remains the brightest persistent source of X-rays in the sky apart from the Sun, with an intrinsic X-ray luminosity many orders of magnitude greater than that of the Sun.

The hitherto unknown window upon the Universe afforded by X-ray astronomy led to the development of dedicated X-ray astronomy satellites, placed in Earth orbit, to allow for long exposure times and scanning of the entire sky. These early missions, such as *Uhuru* (Giacconi et al., 1971b), *Ariel V* (Smith & Courtier, 1976) and *Einstein* (Giacconi et al., 1979), led to the discovery of further X-ray binaries – both NSs and BHs – in our Galaxy and in other galaxies, the presence of active galactic nuclei (AGNs) in the centres of other galaxies, hot gas in galaxy clusters, and the X-ray background (e.g. Bradt et al. 1992; Giacconi 2003). *Einstein* in particular paved the way towards this thesis with the discovery of exceptionally bright extragalactic non-nuclear X-ray sources with

Table 1.1: Properties of the main instruments used in this investigation, on the X-ray space telescopes *XMM-Newton* (*XMM*), *Chandra* and *NuSTAR*.

Instrument	FoV[a]	Energy[b]	PSF[c]	Eff. Area[d]	Pix.[e]	Time Res.[f]
XMM EPIC-pn	30′ radius	0.3–10 keV	6″	1227 cm^{-2} @ 1 keV	4.1″	73.3 ms
XMM EPIC-MOS				922 cm^{-2} @ 1 keV	1.1″	2.6 s
Chandra ACIS-I	$16.9 \times 16.9'$	0.3–10 keV	0.5″	340 cm^{-2} @ 1 keV	0.5″	3.2 s
Chandra ACIS-S	$8.3 \times 50.3'$					
NuSTAR FPMA/B	$12.5 \times 12.5'$	3–79 keV	18″	420 cm^{-2} @ 10 keV	12.3″	0.1 ms

[a]Full field of view of the instrument.
[b]The most effective energy range of the instrument and that used for analysis in this thesis.
[c]The FWHM of the on-axis PSF.
[d]The on-axis effective area at the given energy (except for *NuSTAR*, for which is given the effective area at 1 arcminute off-axis).
[e]The pixel size of the camera.
[f]The time resolution of the instrument, after timing calibrations.

luminosities greater than the Eddington limit for NSs or even stellar-mass BHs (Fabbiano, 1988, 1989) – these sources eventually became known as ultraluminous X-ray sources (ULXs), and later missions such as *ROSAT* and *ASCA* allowed for the creation of the first catalogues of these objects (e.g. Roberts & Warwick 2000; Colbert & Ptak 2002).

The current generation of X-ray space telescopes broke new ground in sensitivity and resolution that allows for the discovery and in-depth study of more ULXs and lower-luminosity non-nuclear sources than ever before. This work uses three in particular: *XMM-Newton*, *Chandra* and *NuSTAR*. Various properties of the main instruments used in this investigation are given in Table 1.1.

1.1.1 XMM-Newton

The X-ray Multi-Mirror Mission, known as *XMM-Newton*, is a European Space Agency mission that was launched in 1999. It is made up of three X-ray telescopes and an optical telescope, and three instruments: the European Photon Imaging Camera (EPIC), the reflection grating spectrometer (RGS) and the optical monitor (OM), all of which are operated simultaneously (Lumb et al., 2012). An illustration of the telescope is shown in Fig. 1.2.

The EPIC instrument is made up of three charge-coupled device (CCD) cameras, one for each X-ray telescope, which are capable of recording the position, time and energy

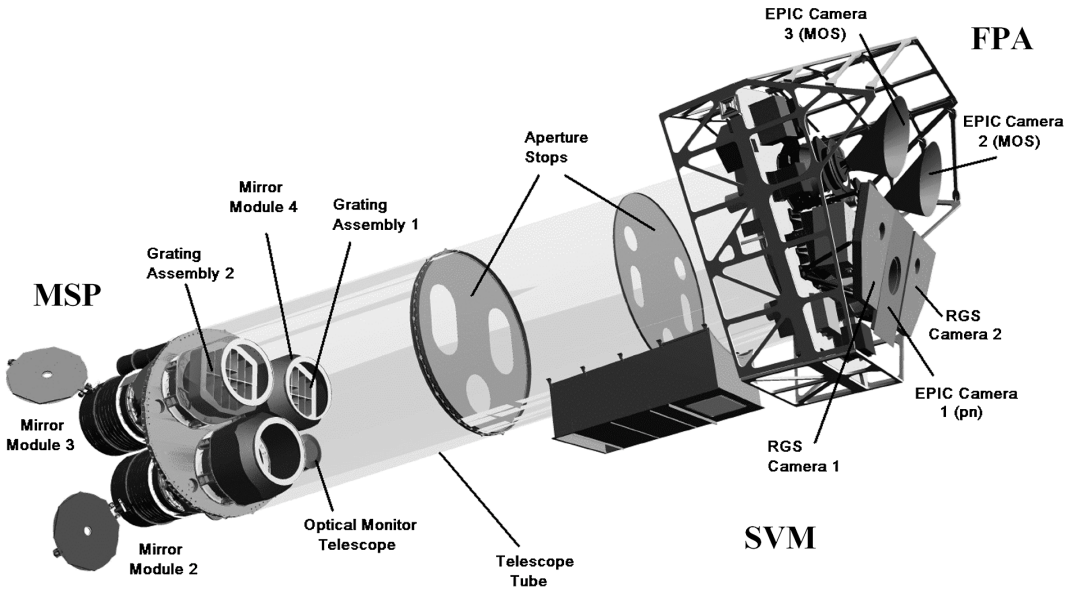

Figure 1.2: Annotated illustration of the *XMM-Newton* space telescope from Lumb et al. (2012), with the EPIC-pn, EPIC-MOS, RGS and OM instruments marked.

of each photon arrival event – data which can later be converted into images, spectra and light curves (see Section 1.2). Two of these cameras are seven-chip arrays of Metal Oxide Semi-conductor CCDs, referred to as MOS1 and MOS2, which both share their telescope with one of the RGS gratings and therefore receive about 44% of the incident flux of their telescope (Turner et al., 2001). The third camera is a twelve-chip array of pn CCDs, referred to as the pn, which receives the entirety of the flux from its telescope (Strüder et al., 2001). These cameras are sensitive over the energy range 0.15–15 keV, although due to quantum efficiency and the instrumental background, their most effective energy range and that used for the analysis in this work is 0.3–10 keV. They have a moderately good point spread function (PSF) with a full width at half-maximum (FWHM) of $\sim$6 arcseconds, sufficient to resolve most point sources from each other in nearby galaxies, and a spectral resolution of $E/\Delta E \sim$ 20–50. The RGS is able to produce a high-resolution spectrum of on-axis sources, with a spectral resolution of $E/\Delta E \sim$ 100–800, allowing the resolution of individual emission lines and discrete absorption features (den Herder et al., 2001). The OM is able to take optical or ultraviolet (UV) observations simultaneous to X-ray observations in one of six different bands (V, B, U, UVW1, UVM2 and UVW2), over the full sensitivity of the detector ('white' band), or through two grisms optimised to the optical and UV bands respectively (Mason et al., 2001).

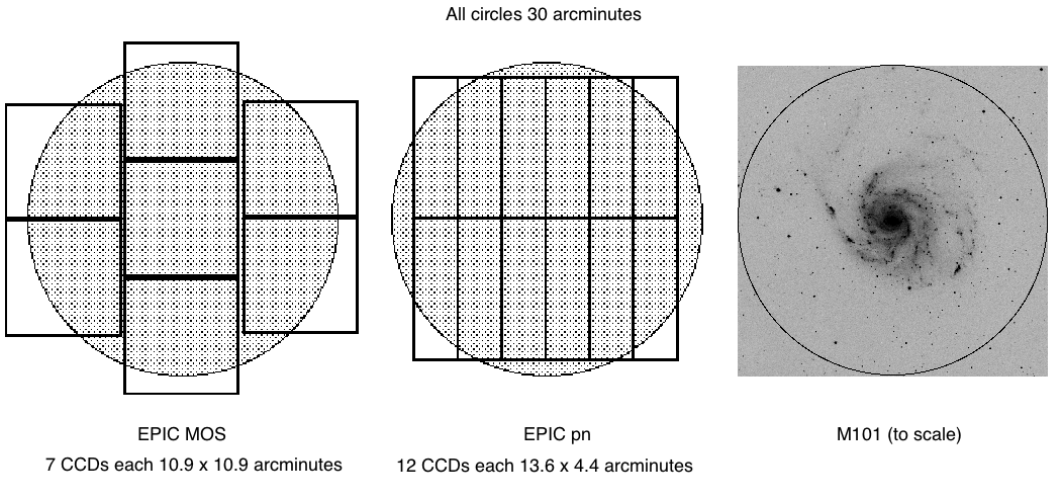

Figure 1.3: The 30 arcminute *XMM-Newton* field of view for the EPIC-pn and EPIC-MOS cameras (adapted from the *XMM-Newton* User's Handbook[1]) alongside spiral galaxy M101 for scale.

One of the most useful aspects of *XMM-Newton* for this work is EPIC's large field of view, which is 30 arcminutes in diameter each for the pn and MOS cameras (Fig. 1.3), and over which the PSF stays reasonably consistent albeit becoming slightly wider and more elliptical (e.g. Read et al. 2011). This not only allows the vast majority of nearby galaxies to be imaged completely in a single pointing by *XMM-Newton*, but also increases the chances of making serendipitous discoveries as many objects other than the specified target of an observation will also be observed. Indeed, the primary data source for this work is the *XMM-Newton* Serendipitous Source Catalogue (Watson et al., 2001), a database of all X-ray sources that happen to have been detected with *XMM-Newton*, including their positions and a number of source properties such as the count rate and flux in various energy bands, and the resulting X-ray colours. The high effective area of *XMM-Newton* makes it an ideal telescope for collecting large amounts of data from these sources, even at relatively low fluxes.

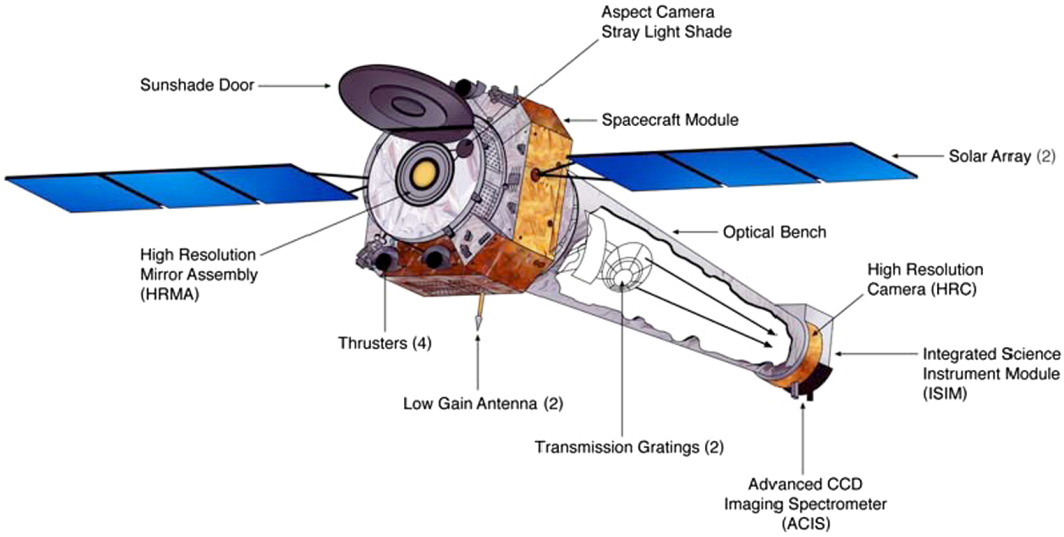

Figure 1.4: Annotated illustration of the *Chandra* space telescope from Weisskopf (2012), with the HRC, ACIS and transmission gratings marked.

1.1.2 Chandra

The *Chandra X-ray Observatory*[2] is a NASA mission, also launched in 1999 (Weisskopf et al., 2002). It contains four instruments: the High Resolution Camera (HRC), the Advanced CCD Imaging Spectrometer (ACIS), and two high resolution spectrometers. Unlike *XMM-Newton*, these instruments cannot be used all at once. An illustration of the telescope is shown in Fig. 1.4.

This work primarily uses the ACIS instrument (Garmire et al., 2003), made up of two arrays of CCDs, sensitive over the energy range 0.2–10 keV – as with *XMM-Newton*, we use the most effective energy range, 0.3–10 keV, in our analysis. The ACIS-I array contains four CCDs and is used for imaging, and the ACIS-S array contains six CCDs that can either be used for imaging or as a read-out array for the high resolution spectrometers (Fig. 1.5). While its lower effective area and smaller field of view make it less efficient than *XMM-Newton* for collecting data, *Chandra* has a superior angular resolution with a PSF FWHM of 0.5 arcseconds for the ACIS instrument (Jerius et al., 2000). This makes it a powerful complement to *XMM-Newton*, with the ability to determine source positions with very high precision and to resolve sources close to one another that are blended in

[1] https://xmm-tools.cosmos.esa.int/external/xmm_user_support/documentation/uhb/XMM_UHB.html
[2] http://asc.harvard.edu/proposer/POG/html/index.html

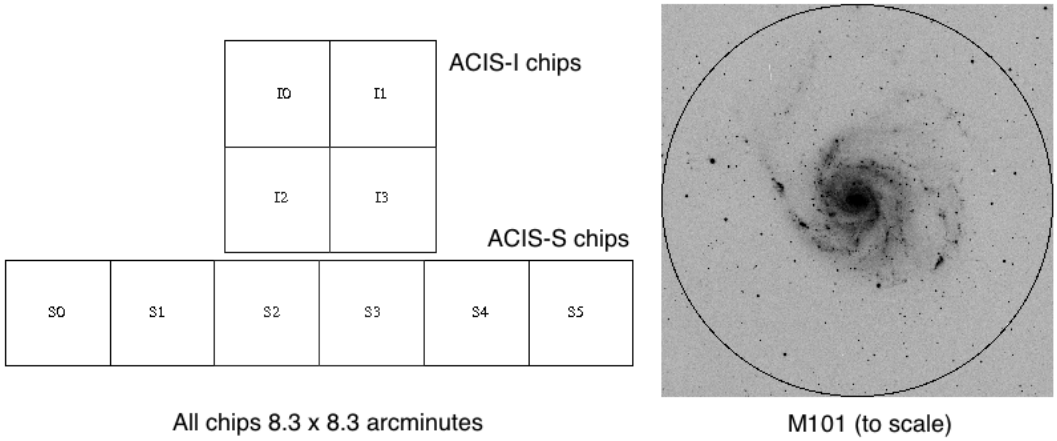

Figure 1.5: The *Chandra* field of view for ACIS (adapted from the *Chandra* ACIS information page[3]) alongside spiral galaxy M101 for scale.

XMM-Newton observations. It also allows for better isolation of emission from a point source with less contamination from its environment.

The *Chandra* instruments are particularly vulnerable to pile-up. This occurs when two or more photons arrive at a detection cell before the chip is read out, causing them to be registered as a single event with the combined energy of the photons, and leads to both a distorted spectrum containing spurious high-energy events, and a distorted light curve with fewer events recorded than actually occurred (Davis, 2001). This can be a problem for very luminous sources in nearby galaxies, which have correspondingly high count rates. These require a sub-array to be used when observing, which allows the *Chandra* CCDs to be read out faster at the expense of field of view, or for the source to be observed off-axis, which effectively defocuses the PSF. For lower-flux sources, if the piled-up fraction is a few per cent or lower, it can be safely disregarded in most cases.

1.1.3 NuSTAR

The *Nuclear Spectroscopic Telescope Array* (*NuSTAR*) is a NASA mission launched in 2012 (Harrison et al., 2013), and is particularly ground-breaking because it is the first telescope to be able to focus high-energy X-rays, allowing for imaging and spectral analysis in a new electromagnetic energy range (Fig. 1.6). *NuSTAR* is made up of two X-ray

[3]http://cxc.harvard.edu/cal/Acis/

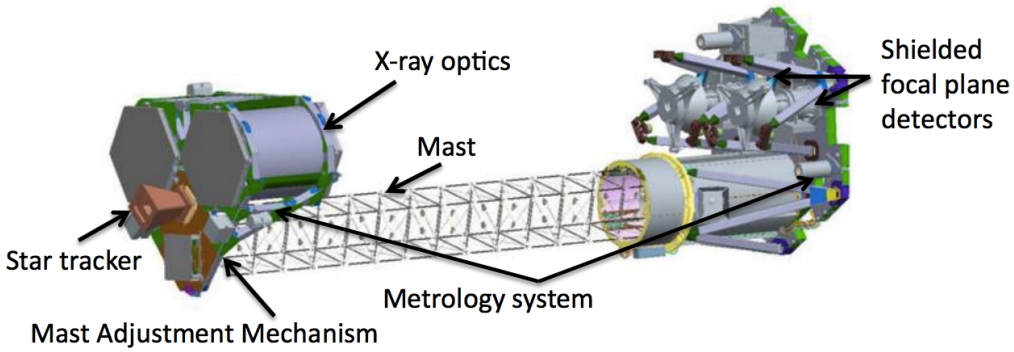

Figure 1.6: Annotated illustration of the *NuSTAR* space telescope, from Harrison et al. (2010), marking the positions of the optics and detectors. The 10 m mast is not to scale.

telescopes, with one detector module for each, which observe simultaneously (Madsen et al., 2014). Both detector modules are identical 2x2 arrays of Cadmium-Zinc-Telluride detectors called Focal Plane Module A and B (FPMA/B; Kitaguchi et al. 2014; shown in Fig. 1.7). Its angular resolution is coarser than *XMM-Newton* and *Chandra*, with a PSF FWHM of 18 arcseconds, however its energy sensitivity extends well beyond them into the range 3–79 keV (Forster et al., 2014). Access to this energy range is vital to distinguish between different models of accretion, especially for ULXs.

1.1.4 Future missions: Hitomi and Athena

Although the following missions are not yet operational, it is a good idea to bear their predicted functionality in mind when planning current investigations. Projects that rely on the very best data that *XMM-Newton* has to offer (such as the study on soft Eddington threshold sources in Chapter 4) will be able to be extended to much larger sample sizes, and sources that are insufficiently bright to be easily studied with the current generation of X-ray telescopes will be suitable targets for more sensitive instruments in the future.

Hitomi was a JAXA mission launched in 2016 (Takahashi et al., 2016) that was lost just over a month after its launch due to problems with its attitude control system, however the possibility of a near-copy replacement mission in the early 2020s is currently being considered by the Japanese government. *Hitomi* (known before launch as *ASTRO-H*) was

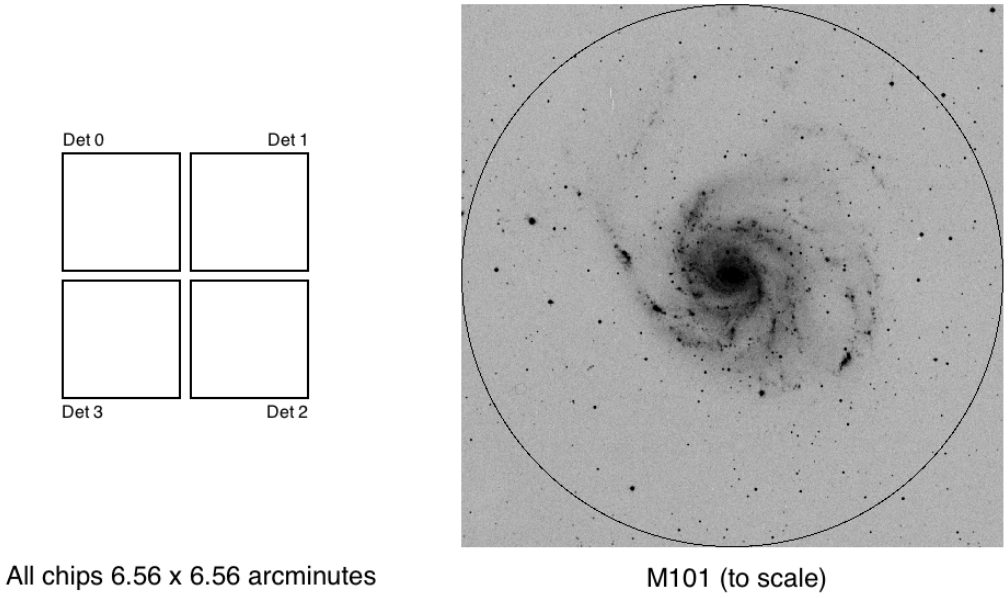

Figure 1.7: The *NuSTAR* field of view for each FPM detector unit, alongside spiral galaxy M101 for scale.

made up of four X-ray telescopes and two gamma-ray detectors. The X-ray telescopes were divided into two soft X-ray telescopes and two hard X-ray telescopes, between them capable of imaging between 0.3–80 keV. The soft X-ray band (over a similar energy range to *XMM-Newton* and *Chandra*) could be imaged with a wide field of view of 38 arcminutes across four CCDs with one telescope using the Soft X-ray Imager instrument (Hayashi et al., 2016; Tsunemi et al., 2016), and high-resolution ($\Delta E < 5$ eV) spectra produced with the other telescope using the Soft X-ray Spectrometer, which used a microcalorimeter rather than a dispersion grating, allowing a very high energy resolution to be reached (Leutenegger et al., 2016). The hard X-ray telescopes were capable of imaging over a similar energy range to *NuSTAR* and with a similar angular resolution, using the Hard X-ray Imager instrument (Awaki et al., 2016). A replacement mission for *Hitomi*, if carrying the same instruments, would be capable of obtaining simultaneous soft and hard data on sources (although *XMM-Newton* retains the highest effective area in the soft X-rays), and good quality, high resolution soft spectra especially useful for characterising soft outflowing winds (for why these are important, see Section 1.5.3).

Athena is a proposed ESA mission currently in the Phase A stage of development and projected to launch in 2028 (Nandra et al., 2013). It is planned to contain two instruments:

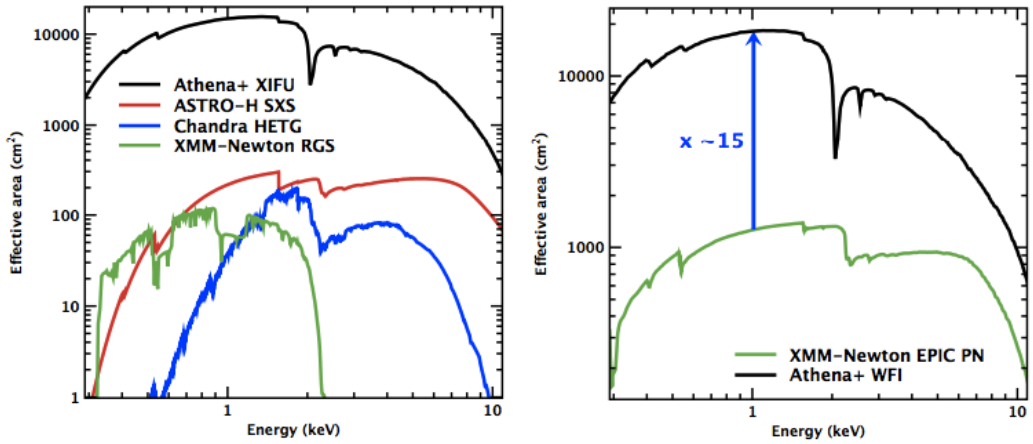

Figure 1.8: The expected effective area of *Athena* instruments compared with the best current instrumentation from *XMM-Newton*, *Chandra* and *Hitomi* (labelled as *ASTRO-H*), from Barret et al. (2013). High-resolution spectrometer instruments are compared on the right plot, and wide-field imagers on the left.

an X-ray integrated field unit (X-IFU) and a wide field imager (WFI). The X-IFU will be made up of 5 arcsecond pixels over a field 5 arcminutes across, with each pixel producing a spectrum of 2.5 eV resolution using microcalorimeter technology (Barret et al., 2016). The WFI will have a 40 arcminute field of view, with an angular resolution of 5 arcseconds and excellent time resolution of 5 ms (Meidinger et al., 2016). This is possible due to using active pixels – instead of being read out in rows like a CCD, each pixel is read out individually, eliminating losses due to charge transfer and out-of-time events (Rau et al., 2013). It will be sensitive to fluxes orders of magnitude below *XMM-Newton's* capabilities, making it ideal for survey science of non-nuclear X-ray sources at luminosities below the ULX regime. Comparisons of the effective area of *Athena's* instruments to current instrumentation is shown in Fig. 1.8.

1.2 Data analysis techniques for X-ray astronomy

The data recorded by X-ray telescopes is first reduced into the form of an event list that records, among other things, the position, energy and time of each recorded event (usually the arrival of a single photon, although in the case of pile-up, multiple photons can be recorded as single events). The position data allows the selection of only those photons from the source of interest by using a circular source region centred on the source location,

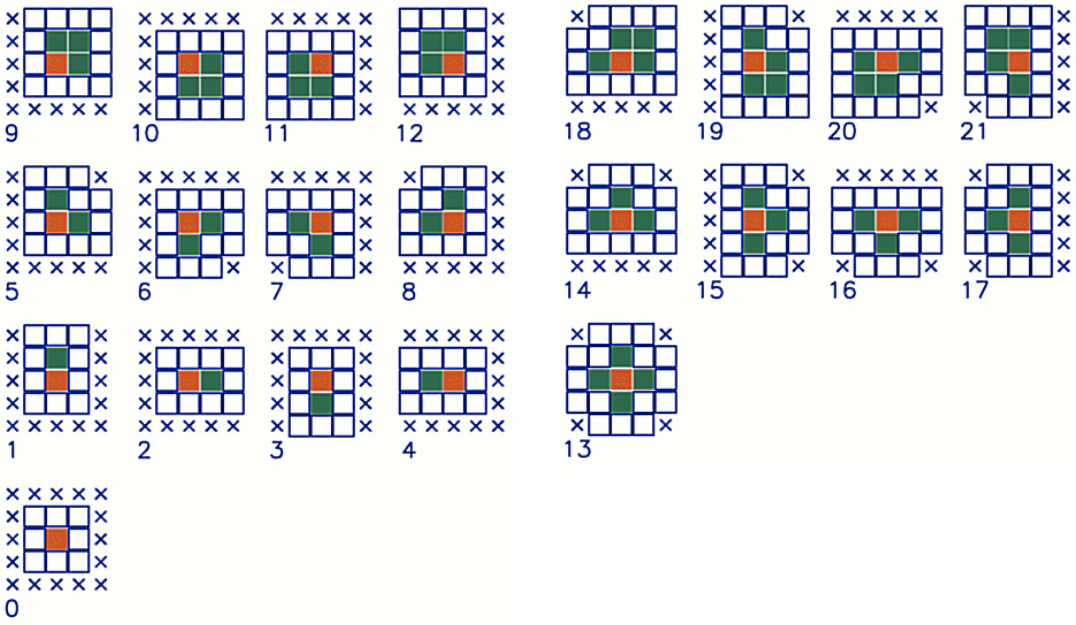

Figure 1.9: Example pixel patterns for the *XMM-Newton* cameras (adapted from the *XMM-Newton* User's Handbook[4]), with the pixel with the highest charge shown in red, and other pixels above a threshold value shown in green. White pixels are below the threshold value and pixels with crosses are not considered when identifying the pattern. Patterns 0–12 are those generally filtered for in analysis for this investigation.

with a large enough radius to encompass the majority of the source emission – typical source region radii used in this investigation are 20 arcseconds for *XMM-Newton* and 3 arcseconds for *Chandra*. Events are also selected from a representative background region in order to subtract the effects of the X-ray background and instrumental noise. For *XMM-Newton*, the background region is selected to be a region free from point sources on the same chip and at a similar distance from the readout node as the source. For *Chandra*, sources are typically sufficiently resolved from each other to enable background selection from a circular annulus around the source location.

The arrival of a photon to the CCD chip may trigger more than one pixel, creating a distribution of pixels for the event called a pattern. Genuine incoming X-rays are expected to form compact patterns centred on the brightest pixel. The source events are filtered to select only those events with an acceptable pattern, in order to filter out events caused by non-X-ray sources such as cosmic rays. This is achieved, for example, by filtering

[4]https://xmm-tools.cosmos.esa.int/external/xmm_user_support/documentation/uhb/XMM_UHB.html

for patterns with values ≤ 12 for EPIC-MOS and ≤ 4 for EPIC-pn when selecting events from *XMM-Newton* (see Fig.1.9). Additionally, data from EPIC-pn is further filtered by excluding events on pixels flagged as bad (for example, due to the pixels being 'hot' or 'dead').

The event lists are further filtered to remove the effect of soft proton flaring, which particularly affects *XMM-Newton* observations, caused by the population of protons in the Earth's magnetosphere that can be focussed through the telescope like X-rays and result in a background count rate subject to bright flaring events as the telescope passes through high concentrations of particles (e.g. Briel et al. 2000). This filtering is done by defining good time intervals – periods of time in which the count rate across the CCD at energies above 10 keV, an energy range in which source flux is negligible compared to background flux, is low (generally $\lesssim 0.4\,\mathrm{ct\,s^{-1}}$ for the *XMM-Newton* cameras) – and only selecting events which occur within these intervals.

A clean, source-specific event list is then the starting point for the analysis of an X-ray source in both the energy and time domains. What follows is a brief description of the X-ray spectral and timing analysis toolbox used for the investigation.

1.2.1 Spectral analysis

At its most basic, an energy spectrum is produced by plotting an intensity against photon energy E, usually grouped into bins of ~ 20 photons so that the distribution is approximately Gaussian and χ^2 statistics can be used in analysis (in cases where there are insufficient photons to do this effectively, the C-statistic can be used with smaller bins, which will have a Poissonian distribution). In order to interpret energy spectra, they are compared with models of the predicted emission from the source (such as the emission from an accretion disc, see Section 1.3) convolved with the detector response to imitate what would be detected by the telescope were the source emitting in the predicted fashion. In this investigation, this process is done using the XSPEC software (Arnaud, 1996). This software can adjust the parameters of the model to minimise the χ^2 statistic when comparing the source and model spectra in order to find the best-fitting model parameters, from which we can infer the physical properties of the source. However, the best fit with a certain model is only valid if that model is a good fit to the data in the first

place, so a goodness-of-fit test is also calculated using χ^2, from which we can calculate the probability that the observed spectrum came from an intrinsic spectrum described by the model.

Both source and background spectra can be loaded into XSPEC, allowing the software to subtract the background spectrum from the source spectrum to give something closer to the intrinsic spectrum. At this stage, we instruct the software to ignore energy channels outside of the energy range we are interested in, which depends upon the most effective energy range of the telescope (see Section 1.1) and on the energies at which the background becomes dominant (which tends only to apply for *NuSTAR* data). The spectrum will then consist of source emission within the selected energy range which can be approximated by a model (for example, a power-law, for which we would use the `powerlaw` model in XSPEC). The source emission may be more complex and originate in different regions of the source via different processes, requiring the use of multiple models which are added together. Source emission is also affected by photoelectric absorption by intervening matter between the source and the observer (see Section 1.3.5), which is accounted for using a multiplication model (in this investigation we use `tbabs`; Wilms et al. 2000). XSPEC varies the free parameters of all components of the resultant model to find a best fit, but hand-setting parameters to reasonable starting values and making manual adjustments during the fitting process is sometimes required to avoid the software settling in local χ^2 minima and to find the genuine best fit.

The spectrum can be plotted as the counts per second per keV against E, which can show where the data agrees or disagrees with a given model, but does not in itself give much physical insight since it is tied up in the detector response and only shows the counts detected, rather than those emitted by the source. For a more physical perspective on the spectrum, it can be unfolded from the detector response using a model, and plotted as $EF(E)$ against E, where $F(E)$ is the flux at energy E – using $EF(E)$ on the intensity axis means that, when plotted logarithmically, the area under the curve gives the flux and the spectrum peaks at the energy with the most power in the spectrum (e.g. Zdziarski & Gierliński 2004; Done 2010). On such a plot, a power-law with a photon index $\Gamma = 2$ is flat. A power-law with $\Gamma > 2$ rises to low energies and is described as 'soft', being dominated by low-energy emission, and a power-law with $\Gamma < 2$ rises to high energies

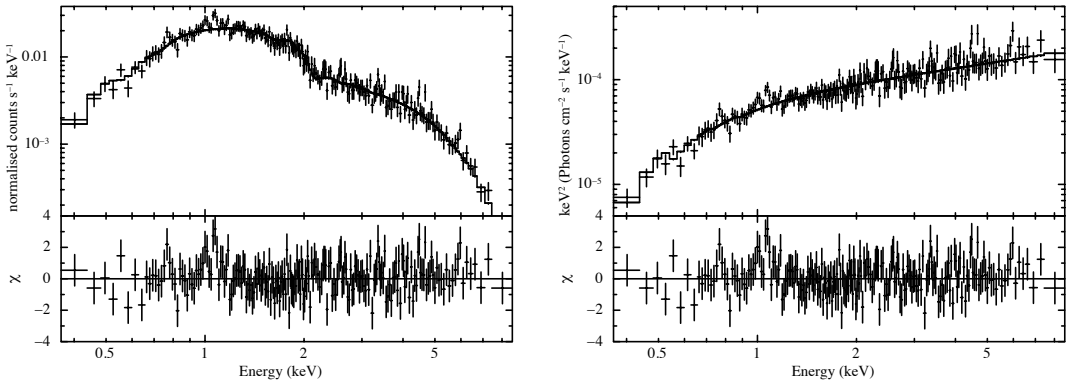

Figure 1.10: The *Chandra* energy spectrum for source M51 ULX-7 from observation 13814, fitted with an absorbed power-law model with $N_{\rm H} = 1.59 \times 10^{21}\,{\rm cm}^{-2}$ and $\Gamma = 1.54$ (i.e. a hard power-law). *Left*, the spectrum in normalised counts per second per keV. *Right*, the spectrum unfolded from the detector response, plotted in $EF(E)$. Both plots also show the residuals between the model and the data in $\Delta\chi^2$ – the residuals are identical between these two methods of plotting the spectrum.

and is described as 'hard', dominated by hard-energy emission. These types of plot are compared in Fig. 1.10. For the most part, this investigation shows spectra plotted with $EF(E)$ on the intensity axis.

1.2.2 Timing analysis

The behaviour of a source over time is shown by its light curve, a plot of the count rate against time, with counts binned at regular intervals (for example, in bins of 100 s), and with the background light curve subtracted. We can represent this count rate as a time series $x_k(t_k)$ where time $t_k = kdt$, dt is the bin size and $0 \leq k \leq N-1$. N is the total number of bins in the light curve, giving a total duration $T = Ndt$. An example light curve is plotted in Fig. 1.11 (left) and can be produced using the FTOOLS software task LCURVE. However, it is common to probe the physics behind variability by examining the power spectrum, which is calculated by first taking the discrete Fourier transform of the light curve, given by,

$$X_n(f_n) = \sum_{k=0}^{N-1} x_t e^{2\pi ikn/N}, \tag{1.2.1}$$

where frequency $f_n = n/(Ndt)$ for $1 \leq n \leq N/2$. From this, the periodogram can be defined as:

$$P(f_n) = \frac{2dt}{\mu^2 N_f}|X_n(f_n)|^2, \tag{1.2.2}$$

where μ is the mean count rate of the light curve and the number of frequency bins is $N_f = T/(2dt)$. This normalisation puts the periodogram in units of the squared fractional rms, so that the integral of $P(f_n)$ gives the squared fractional rms over the frequency range examined.

The discrete periodogram is only an estimate of the underlying continuous power spectrum, and has fractional error $\sim 100\%$ on each bin. There are two main methods for improving this (van der Klis, 1989). One is obtaining a better estimate by dividing up the original light curve into a number of equal-length intervals and taking the mean of the resulting periodograms (Bartlett, 1948). This gives us a well-behaved average power spectrum ranging from a low frequency of $1/T_{\rm int}$, where $T_{\rm int}$ in the interval length, and a high frequency of $1/(2dt)$ (the Nyquist frequency), with a frequency resolution of $df = 1/(N_{\rm int}dt)$, where $N_{\rm int}$ is the number of bins in each interval.

The errors in the power spectrum can be further improved by geometric rebinning, done by combining bins and averaging the power within them, such that the number of data points combined to make the J^{th} new bin is given by $N(J) \leq c_0^J$, where c_0 is a constant greater than 1. This effectively results in $\sim$logarithmic binning for high values of J (at high frequencies) while leaving wider bins at lower frequencies intact to ensure that every new bin contains at least one of the original data points.

All power spectra presented in this investigation are both averaged over ~ 20 light curve intervals (to ensure approximately Gaussian statistics so that χ^2 can be used in model-fitting) and geometrically rebinned. An example power spectrum is plotted in Fig. 1.11 (right). The pay-off for this treatment is that low-frequency information is lost, and the frequency resolution is decreased at high frequencies.

Power spectra will still be subject to Poissonian counting error, which manifests as a white noise (i.e. flat) contribution to the power spectrum with a mean value of $2/\mu$ (in the fractional rms normalisation; e.g. Vaughan et al. 2003), and signals need to be detected significantly above this level to be considered genuine. In many cases, the white noise level is subtracted from the power spectrum; in this investigation the average white noise level is plotted with a grey dashed line.

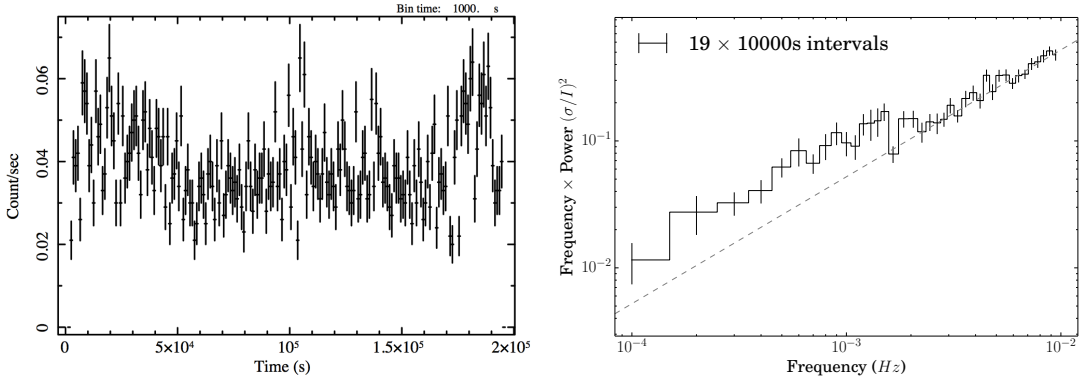

Figure 1.11: The *Chandra* light curve (*left*) and power spectrum (*right*) for source M51 ULX-7 from observation 13814. The light curve is plotted in bins of 1000 s. The power spectrum is an average of 19 consecutive intervals, each 10,000 s long, and is also geometrically rebinned with a rebinning constant of 1.05. The white noise level is plotted as a grey dashed line.

A periodic signal in a light curve is represented by a delta function in frequency space, so will manifest as a sharp peak in a power spectrum. Broader peaks are also observed in X-ray power spectra, the result of quasi-periodic oscillations (QPOs), and can be found in the power spectra of all kinds of accreting systems. There are a number of different methods by which the various types of observed QPOs could be generated, including instabilities within the accretion flow, relativistic precession, a warped accretion disc, or resonances in the orbital motion of the system (e.g. Motta 2016). The study of QPOs is a broad and complex field in its own right, however they do not feature in this particular investigation. Intrinsic stochastic variability in a source will show up as broadband noise in a power-law form, distinct from the Poisson white noise. Especially relevant to X-ray astronomy is red noise, or Brownian noise, for which the power density increases towards low frequencies proportional to $1/f^2$ and is the expected noise to be observed from an accretion disc (see Section 1.3.3).

As mentioned before, the overall fractional variability of the source can be estimated by integrating over the power spectrum of the frequency range of interest when it is presented in fractional rms normalisation. With sufficient data available, the distribution of variability with energy can be probed by producing a power spectrum for a number of energy bands and calculating the fractional rms for each, allowing the fractional rms to be plotted against energy. This rms spectrum allows the identification of spectral components whose underlying processes dominate the variability of the source.

1.3 Accretion onto compact objects

The magnitude of the X-ray luminosities that we observe from X-ray point sources in our Galaxy and beyond require a highly energetic physical source, the accretion of matter onto compact objects. We describe these objects in Section 1.3.1. For accretion to occur, a fuel source is required, which we discuss in Section 1.3.2. Next, we introduce the process of accretion itself (Section 1.3.3) as well as two other physical processes important to the X-ray spectra we observe: Comptonisation (Section 1.3.4) and absorption (Section 1.3.5).

1.3.1 Compact objects: neutron stars and black holes

Compact objects are a class composed for the most part of stellar remnants – objects that are formed at the end of a star's lifetime when it can no longer support itself against the force of gravity by nuclear fusion – and include white dwarves, neutron stars and black holes (e.g. Shapiro & Teukolsky 1983). This investigation is primarily concerned with the remnants of massive stars ($M \gtrsim 8\,\mathrm{M}_\odot$) that undergo a core-collapse supernova explosion (or simply a direct collapse for very high-mass stars) at the end of their lifetimes (e.g. Smartt 2009). These remnants, neutron stars and black holes (for which we will henceforth use 'compact objects' to refer to these two classes of such, for simplicity), are the most extreme gravitational environments in the Universe.

In the case of progenitor stars with $8 < M < 25\,\mathrm{M}_\odot$ or $\gtrsim$solar metallicity (e.g. Heger et al. 2003), the remnant object is extremely dense, with a mass of 1.4–3 $\mathrm{M}_\odot$ enclosed within a radius of ~ 10 km. It is made up mostly of neutrons held together by self-gravity, and the gravitational force is only balanced by neutron degeneracy pressure (e.g. Shapiro & Teukolsky 1983). Such an object is called a neutron star (NS). The angular momentum of the stellar matter not blown away by the supernova explosion is conserved so that a newly formed NS, having a radius far smaller than its progenitor star, spins very rapidly, with an initial period of $\sim$ 10–100 ms (e.g. Migliazzo et al. 2002; Kaplan et al. 2004). Additionally, the magnetic flux is also conserved when the star collapses to a small radius, so that the moderately strong magnetic fields (~ 100 G) of the young, massive progenitor stars result in NS magnetic field strengths of $\gtrsim 10^{12}$ G (e.g. Gold 1968; Ostriker & Gunn 1969).

The strong magnetic field is not necessarily aligned with the axis of rotation of the NS, so these properties mean that a NS may manifest observationally as a regularly pulsing source called a pulsar, including in the radio (e.g. Hewish et al. 1968) or X-ray (e.g. Giacconi et al. 1971a) electromagnetic regimes. Pulsars are observed as radiation is beamed along the direction of the open magnetic field lines, creating a lighthouse-like effect as the magnetic poles periodically pass across an observer's line of sight (e.g. Lorimer & Kramer 2004).

In cases of very high mass progenitor stars with low metallicity (e.g. Mirabel 2017), the mass of the compact remnant can be sufficiently high ($\gtrsim 3M_{\odot}$) that neutron degeneracy pressure cannot balance the gravitational force. No other stronger pressure force is known to exist to prevent further in-fall of matter, therefore the object is thought to collapse entirely into an infinitely dense singularity (e.g. Shapiro & Teukolsky 1983). Rather than a surface, this object has an event horizon, at which the escape velocity exceeds the speed of light and thus no matter or information can be retrieved from beyond it – for this reason, it is called a black hole (BH), as not even light can emerge from within it. For a non-rotating BH, the event horizon occurs at the Schwarzschild radius R_s which is double the gravitational radius R_g, a result of an exact solution to Einstein's field equations (Einstein, 1915; Schwarzschild, 1916):

$$R_s = 2R_g = \frac{2GM}{c^2}, \tag{1.3.3}$$

where G is the gravitational constant, M is the mass of the object, and c is the speed of light. Kerr (1963) later found a rotating solution to Einstein's field equations, which is more physically realistic in that a BH would be expected to retain some of the angular momentum of its progenitor, in which the event horizon depends on both the mass and the angular momentum per unit mass. Two surfaces become relevant in this scenario – the event horizon at $r = (R_s + \sqrt{R_s^2 - 4a^2})/2$ and an outer ergosphere surface at $r = (R_s + \sqrt{R_s^2 - 4a^2\cos^2\theta})/2$, where a is the angular momentum per unit mass (e.g. Visser 2007). Between these surfaces, within the ergosphere, is a region of spacetime where particles are forced to corotate with the BH.

The mass, angular momentum and charge of a BH are its only three properties that affect the Universe around it, and therefore the only three things that can actually be

known about any BH – this is known as the 'no-hair theorem' (e.g. Misner et al. 1973). Since the electrical charge is likely to be neutralised in the case of astrophysical BHs, the properties relevant to astronomy are the mass and the angular momentum. The mass of a stellar-remnant BH is limited by the mass of its progenitor star (and the mass of the companion it accretes from), which in turn is limited by the metallicity of the environment the star originally formed in. In most cases, this means that the BH will have mass $M_{\rm BH} \lesssim 20\,{\rm M}_{\odot}$, although it is possible for BHs formed from very low-metallicity stars to have $M_{\rm BH} \sim 80\,{\rm M}_{\odot}$ (Belczynski et al., 2010). The existence of massive stellar-remnant BHs was directly confirmed in 2015 with the detection of gravitational waves from the merger of two BHs in a binary system with masses 36 and $29\,{\rm M}_{\odot}$ respectively (Abbott et al., 2016). Aside from gravitational waves, however, BHs themselves cannot be directly observed – what we observe instead is the accreting matter outside of the event horizon.

1.3.2 The fuel: companion stars

For a compact object to accrete matter onto itself, it requires a source of said matter. For the non-nuclear objects that this work is concerned with, this fuel source is a companion star which, along with the compact object, is part of an X-ray binary (XRB) system, in which one member of a binary star system has become a BH or NS and has begun to accrete matter from its less-evolved companion (e.g. Verbunt 1993).

The type of companion star affects how the XRB system behaves and where in a galaxy it is likely to be found. Systems with low-mass companion stars ($\lesssim 1\,{\rm M}_{\odot}$) are known as low-mass X-ray binaries (LMXBs) and are found in old regions of galaxies where star-formation occurred in the past. In these regions, sufficient time has passed for the low-mass companion star (which may have begun as such, may have been an intermediate-mass star that lost much of its mass during the supernova that formed the primary compact object, or may have been gravitationally captured by a solitary compact object in a dense stellar environment) to evolve to a giant phase (e.g. Li 2015). Additionally, the compact object and companion star will have obtained a close binary separation, either due to friction within a common envelope at the point that the primary star was in its own giant phase (e.g. Taam & Ricker 2010), or due to tidal interaction of the compact object with the star during gravitational capture or by the transfer of angular momen-

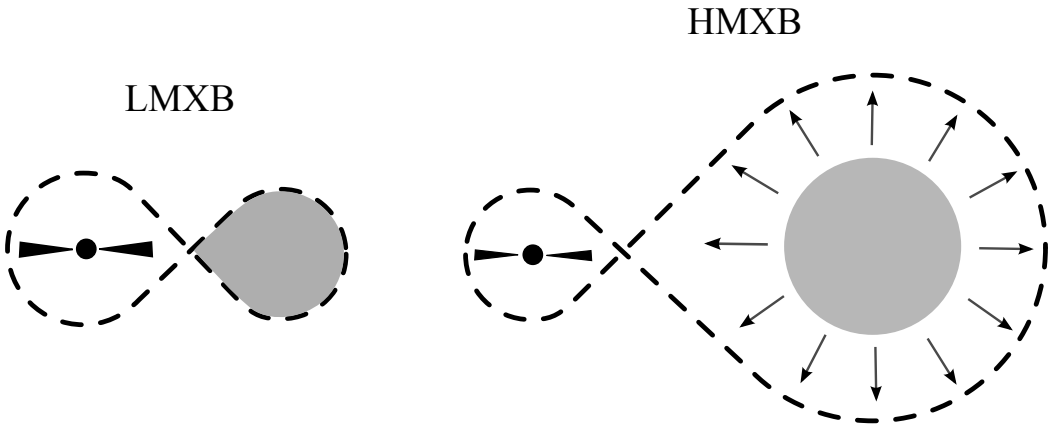

Figure 1.12: A schematic of a low-mass (*left*) and a high-mass (*right*) X-ray binary. The compact object and accretion disc are shown in black, the companion star is shown in grey, and the Roche lobes are indicated with a dashed line – the point at which they meet is the first Lagrange point. In the low-mass X-ray binary, the companion star fills its Roche lobe, causing mass transfer to occur. In the high-mass X-ray binary, a stellar wind is emitted from the companion star, some of which is then captured by the compact object.

tum through encounters with other stars that results in a close binary being formed (e.g. Ivanova 2013). The combination of these scenarios causes the companion star to fill its Roche lobe, the point at which the outer layers of the star are no longer gravitationally bound to it, and mass transfer takes place as matter passes through the first Lagrange point into the compact object's Roche lobe (e.g. Tauris & van den Heuvel 2006).

Systems with high-mass ($\gtrsim 10\,\mathrm{M}_{\odot}$), O- or B-type companion stars are known as high-mass X-ray binaries (HMXBs) and since these stars are short-lived, they are found in star-forming regions (e.g. Grimm et al. 2002, 2003; Lutovinov et al. 2005). Accretion is fuelled by capture of the stellar wind that is driven off the companion star by radiation pressure or from the gaseous disc around a Be star, although it can also occur through Roche lobe overflow when the companion star evolves to a giant stage (e.g. Chaty 2011). A schematic of LMXB and HMXB systems is given in Fig. 1.12.

In the case of HMXBs, the companion star can be observed in the optical; in LMXB systems, the accretion disc dominates the optical emission of the system while in outburst (e.g. Charles & Coe 2003), although the star can be observed when the source is in quiescence (see Section 1.4). An optical spectrum of the companion star allows the radial velocity of the star to be measured from its absorption lines. The semi-amplitude of the radial velocity curve, K_{C}, and the orbital period P can then be inserted into the binary

mass function (e.g. van Paradijs & McClintock 1995):

$$f = \frac{(M_{\rm X} \sin i)^3}{(M_{\rm C} + M_{\rm X})} = \frac{PK_{\rm C}^3}{2\pi G}, \tag{1.3.4}$$

where $M_{\rm X}$ and $M_{\rm C}$ are the masses of the compact object and companion star respectively, and i is the inclination of the system. $M_{\rm C}$ can usually be estimated by identifying the stellar classification from its colour and magnitude. While i is often unknown (unless it can be determined due to X-ray source eclipses), this allows a lower limit to be placed on the mass of the compact object. For example, Cyg X-1 was first confirmed to be a BH in this manner due to having a mass lower limit $\sim 5\,{\rm M}_\odot$ – too large to be a NS (Webster & Murdin, 1972; Bolton, 1972).

The optical counterparts of ULXs (see Section 1.5) are generally harder to identify and characterise than Galactic sources due to their distance. They are often found in crowded fields and require the use of the excellent angular resolution of the Hubble Space Telescope (*HST*) to resolve them from other stars (e.g. Terashima et al. 2006; Gladstone et al. 2013). They tend to be very bright and blue sources, which would make them at first glance consistent with OB-supergiants or Wolf-Rayet stars (and this can be spectrally confirmed in some cases e.g. Motch et al. 2011), making the ULX systems HMXBs. However, in many cases the spectral energy distribution is power-law-shaped rather than a black body, and the optical emission may also be highly variable – these indicate that the emission is more likely dominated by the accretion disc, either by direct emission, or by the reprocessing of X-rays from the centre of the system in the outer disc (e.g. Tao et al. 2011).

1.3.3 Accretion

Matter from the companion star that falls into the Roche lobe of a compact object will not fall directly onto the object, as it will still possess a large amount of angular momentum from the initial circular motion of the binary system itself. Instead it will go into orbit around the object, forming an accretion disc through which angular momentum is transported outwards, allowing the matter in the centre of the disc to accrete onto the compact object (Pringle, 1981). This angular momentum is transported outwards through

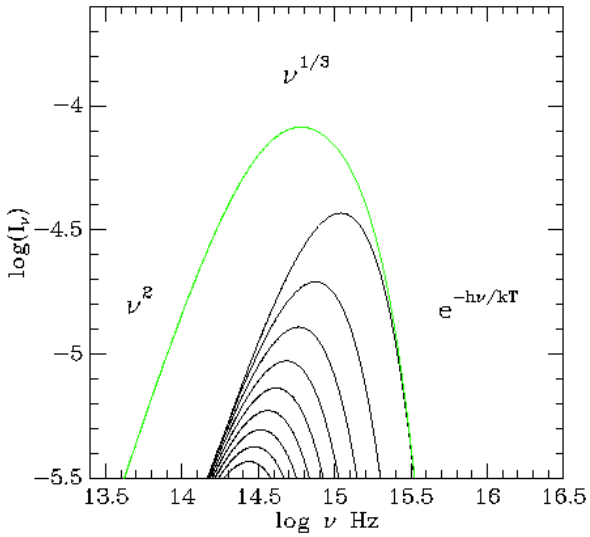

Figure 1.13: An example of how the black-body-emitting segments of an accretion disc (black) combine to produce a multicolour accretion disc spectrum (green).[5]

turbulence within the disc from magnetorotational instability, causing friction between the different orbits of matter and allowing them to move inwards towards the centre. This frictional heating causes the disc to emit radiation that, for stellar-mass compact objects, peaks in the X-ray regime. In the case of high opacity and relatively low accretion rate, the density of the accretion disc drops rapidly with the scale height, making the disc optically thick and geometrically thin (the 'thin disc model'; Shakura & Sunyaev 1973).

The closer to the inner regions of the accretion disc, the faster the disc material is moving, and therefore the frictional heating is greater. The heated material emits thermal radiation, increasing in energy with the increase in temperature towards the centre of the disc. If each infinitesimal annulus that makes up the thin accretion disc is considered to radiate as a black body, then the total radiation from the accretion disc is the sum of all of these black bodies – a spectrum known as a multicolour disc (MCD; Mitsuda et al. 1984). The MCD spectrum has a power-law shape up to its peak, then takes on the Wien portion of the innermost part of the accretion disc at the highest energies (see Fig. 1.13). The energy of the peak of the spectrum then depends upon the innermost radius of the accretion disc. Since the luminosity of a black body depends upon its temperature, this also applies to the accretion disc, and the luminosity of the disc can be related to its apparent temperature with $L \propto T^4$.

In the case of a NS, the accretion disc would extend to the surface of the star were it not for the magnetic field, which causes inflowing material to be dragged along the magnetic field lines instead, accreting along the poles of the NS (e.g. Davidson & Ostriker 1973). This causes the brightest X-ray radiation to be anisotropic, so that pulsations can be observed in the X-ray regime. For a BH, the accretion disc can extend down to the innermost stable circular orbit (ISCO; Misner et al. 1973) at:

$$R_{\rm ISCO} = 3R_s = \frac{6GM}{c^2} \tag{1.3.5}$$

For a spinning BH, the ISCO may be closer, as low as R_g for a maximally spinning BH. Inside the ISCO, particles will rapidly spiral into the BH. If it is assumed that an accretion disc extends to the ISCO, this allows the BH mass or spin to be estimated from the peak temperature of the MCD, although this only holds true for states in which the accretion disc is not truncated (see Section 1.4) and black-body-like emission is not expected from a different source such as outflowing winds (see Section 1.5.3).

1.3.3.1 The Eddington luminosity

The process of accretion is essentially the conversion of gravitational potential energy to kinetic energy to heat. The power generated by the accretion of free-falling matter (at a free-fall velocity of $v_{\rm ff} = \sqrt{2GM/R}$) onto an object of mass M at an accretion rate of $\dot{M}$ and at radius R is given by:

$$L = \frac{1}{2}\dot{M}v_{\rm ff}^2 = \frac{G\dot{M}M}{R} = \frac{1}{2}\dot{M}c^2\left(\frac{R_s}{R}\right) \equiv \eta\dot{M}c^2, \tag{1.3.6}$$

where $\eta = R_s/2R$ is an efficiency factor – the fraction of the rest mass energy of the matter being accreted that can be radiated away – depending on how compact the object is. For a BH, this is the most efficient process in the Universe, with $\eta \sim 0.1$–0.4, depending upon its spin.

Since the luminosity scales with the mass accretion rate, one could naively assume that the luminosity has no upper limit, as long as the mass accretion rate is high enough.

[5] Image from http://www.astro.utu.fi/~cflynn/astroII/l6.html

In reality, a limit is placed upon the mass accretion rate by the radiation pressure exerted by the high luminosity. For a proton-electron pair at a distance r from an object of mass M, the gravitational force is given by:

$$F_{\text{grav}} \approx \frac{GMm_p}{r^2}, \tag{1.3.7}$$

where m_p is the mass of the proton, which dominates the total mass of the proton electron pair. The force due to radiation pressure depends upon the Thomson cross-section, for which the term is dominated by the electron because of its far lower mass compared to the proton, and is thus given by:

$$F_{\text{rad}} \approx \frac{\sigma_{\text{T}} L}{4\pi r^2 c}, \tag{1.3.8}$$

where σ_{T} is the Thomson cross-section of the electron.

The proton-electron pair is bound by electrostatic forces, so both forces apply to the pair as a whole and can therefore be equated. Making the luminosity the subject of the equation gives the Eddington luminosity (e.g. Frank et al. 2002) – the theoretical maximum luminosity that can result from an accreting source before it blows away the in-falling material and loses its fuel source:

$$L_{\text{Edd}} = \frac{4\pi GMm_p c}{\sigma_{\text{T}}} \tag{1.3.9}$$

This theoretical upper limit carries a number of assumptions, such as that the in-falling material is made up purely of ionised hydrogen[6], and that the system is spherically symmetric. In reality it is evident from the accretion disc alone that the system is anisotropic, and if accreting matter and outward radiation occur in different parts of the system and in different directions, this can allow the Eddington luminosity to be exceeded.

At luminosities that are a significant fraction of the Eddington luminosity, the accretion flow becomes geometrically thick due to internal radiation pressure and the thin disc model no longer holds, with a 'slim disc' model of accretion applying instead (Abramowicz et al., 1988). In such a model, the time it takes for radiation to propagate through

[6]While the electron and proton we consider are not directly bonded as in atomic hydrogen, it is assumed that electrostatic forces will keep the population together overall, so the above reasoning still works.

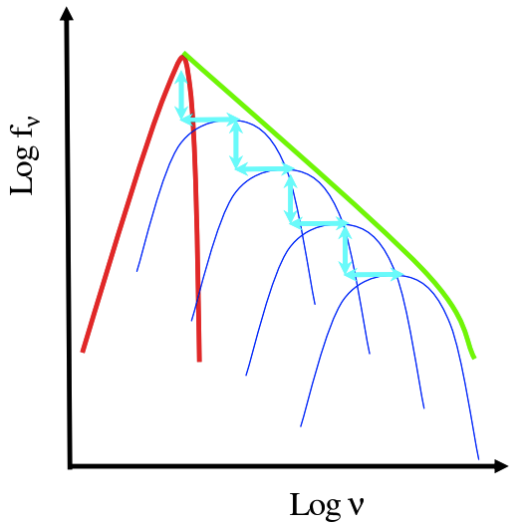

Figure 1.14: An example of how multiple orders of Compton up-scattering (blue) of a MCD spectrum (red) combine to form power-law emission with a cut-off at high energies (green), from Done (2010).

the disc is greater than the time it takes for the matter to accrete, essentially trapping a proportion of the energy within the disc so that it is accreted rather than emitted. This radiative inefficiency allows for faster accretion of matter since the luminosity is lower than it would be for a thin disc. This process becomes important in models of super-Eddington accretion (see Section 1.5.3).

1.3.4 Comptonisation

Comptonisation is the name given to the interaction between a high-energy photon and a low-energy electron, changing the momentum of the electron and the energy of the photon such that the electron is accelerated and the photon loses energy. In a hot plasma containing relativistic electrons, low-energy photons can instead gain energy (be up-scattered) by the same mechanism, called inverse Comptonisation (e.g. Rybicki & Lightman 1979).

This Comptonising medium, often called a Comptonising 'corona', can cause an initial low-energy spectrum (for example, emission from a MCD) to become distorted as a fraction of the photon distribution is up-scattered to higher energies (e.g. Gilfanov 2010). Furthermore, a photon that has been up-scattered once can be further up-scattered if the electron population is still able to impart it energy, which means that a fraction of the up-scattered photon distribution is itself up-scattered, and so on up to the limit of the energy

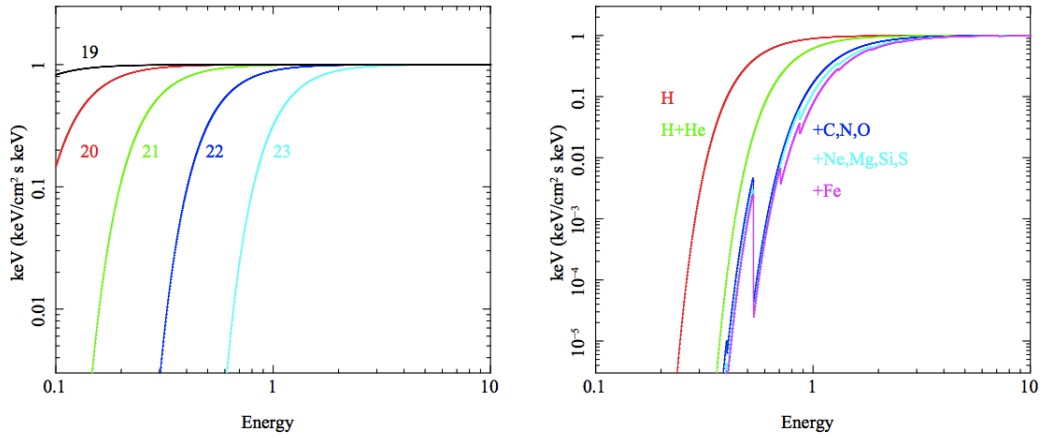

Figure 1.15: Examples of how photoelectric absorption affects a flat ($\Gamma = 2$) PL spectrum, from Done (2010). *Left*, photoelectric absorption from pure hydrogen, in increasing increments of $\log N_{\rm H}$. As the column density increases, progressively higher energies are absorbed from the spectrum. *Right*, photoelectric absorption at a column density of $\log N_{\rm H} = 22$, as heavier elements are added to the absorbing medium, adding complexity to the spectrum.

of the electron population. This creates a power-law (PL) shaped spectrum (see Fig. 1.14) which cuts off at three times the electron temperature, with a slope that depends upon the electron temperature and the optical depth. In many cases, this spectrum cut-off occurs well outside of the energy range of telescopes such as *XMM-Newton* and *Chandra* and so a simple PL model can be – and is often – used to describe the emission, but in some cases a more physical model is required to accurately characterise the spectrum.

1.3.5 Absorption

The emission from XRBs has to travel through intervening interstellar gas, both in the host galaxy and our own, before it reaches the observer. Incoming photons can be absorbed by electrons in atoms and ions, the absorbed energy allowing them to transition from one bound state to another or to become unbound completely in ionisation. In the former case, the energy difference between bound states is very specific, and only photons of that energy will be absorbed. In the latter case, the energy equal to the binding energy of the electron frees it from its orbit, and any further energy imparted to the electron by the photon provides it with kinetic energy – this process is called photo-electric absorption.

The amount of absorption depends upon the optical depth of the intervening material,

$\tau = \sigma(E)N_{\rm H}$, where $\sigma(E)$ is the energy-dependent cross-section and $N_{\rm H}$ is the column density of neutral hydrogen along the line of sight (e.g. Done 2010). The cross-section for neutral hydrogen is zero below 13.6 eV, where it peaks and drops off towards higher energies, allowing more higher-energy X-ray photons to pass through. The higher the column density, the higher the energy of X-ray photons absorbed; typical values for the column density have $N_{\rm H} > 10^{20}\,{\rm cm}^{-2}$ (see Fig. 1.15, left). In reality, the intervening material is not purely hydrogen, and heavier elements will add further absorption features to the spectrum (see Fig. 1.15, right). Usually (and in this work) the abundance of heavier elements in the interstellar medium is assumed to be close to solar (e.g. Wilms et al. 2000) and $N_{\rm H}$ alone is sufficient to characterise the absorption, unless the soft X-ray data are of excellent quality or very high resolution spectroscopy is being utilised.

1.4 Sub-Eddington accretion

LMXBs exhibit transient behaviour as the accretion rate onto the compact object changes over time. In doing so, their X-ray spectra take a number of different shapes, but most can be very basically characterised as various combinations of the MCD and PL components. The different spectral behaviours are categorised into different accretion states (McClintock & Remillard, 2006).

The low/hard state is, as the name suggests, a usually low-flux accretion state with a hard (that is, peaking at high energies) spectrum, dominated by a PL component with photon index $\Gamma \sim 1.7$ which cuts off at very high energies (~ 100 keV). It also exhibits a steady radio jet. The high/soft state is a high-flux accretion state dominated by soft, thermal emission with temperature ~ 1 keV (and therefore often called the thermal dominant or simply thermal state), and also exhibiting a faint PL tail. That the thermal emission is from a MCD is supported by the luminosity-temperature behaviour expected from a disc (see Section 1.3). The thermal state does not exhibit any radio emission. The very high, or steep PL, state also peaks at low energies, but has a steep PL tail with $\Gamma \sim 2.5$ at a similar flux to the disc. Examples of these three states are shown in Fig. 1.16 (left). As well as these main states, there is also the quiescent state, a very faint state dominated by PL emission, and intermediate states which are associated with transition between the

main accretion states – it is now thought that the steep PL state is an intermediate state itself. The steep PL/intermediate states are often associated with an intermittent radio jet as the source transitions between the hard and thermal states.

These accretion states tend to occur in a sequence over time during an outburst event, marking out a 'q' shape when plotted on a hardness-intensity diagram (see Fig. 1.17, left). Beginning from quiescence, the intensity increases significantly with the source in a hard state. At a high intensity, the spectrum softens, going through a high-flux intermediate spectral state (that is, the steep PL state) before entering the thermal dominant state. The intensity then begins to decrease with fluctuating hardness, before the source finally returns through a low-flux intermediate state to the hard state and then to quiescence.

The timing properties of the source also change between states (Remillard & McClintock, 2006), marking a similar 'q' shape on an rms-intensity diagram (e.g. Muñoz-Darias et al. 2011), see Fig. 1.17 (right). The hard state is highly variable, exhibiting band-limited noise (with a high- and low-frequency break in the power spectrum) with high rms ($\gtrsim 10\%$), and the possible presence of QPOs. As the intensity increases, the rms decreases. The thermal state is weakly variable, with low rms ($\sim 1\%$) and a red noise power spectrum cutting off at high frequencies. The steep PL/intermediate states tend to have QPOs in the power spectrum and moderate rms. Example power spectra for these states are shown in Fig. 1.16 (right), in which QPOs are seen in the hard and steep PL states.

The physical cause of these accretion states and the cycling between them can be explained using a truncated disc model (Done et al., 2007; Fender & Belloni, 2012; Zhang, 2013). The accreting source begins at a low accretion rate with an accretion disc truncated at a very high ($\gg$ISCO) radius, with emission being dominated by a central corona, possibly a radiatively inefficient advection-dominated accretion flow, with most energy accreted with the flow rather than radiated. The hard PL emission results from soft photons originating in the cool accretion disc interacting with the hot inner electrons in thermal and/or bulk motion Comptonisation. The hot inner flow is also the region from which the radio jet is launched.

As the accretion rate increases, the edges of the inner flow are cooled by the process of Comptonisation and condense into the disc, bringing the inner radius in towards the ISCO, disrupting and eventually stopping the production of the jet. At this point, the

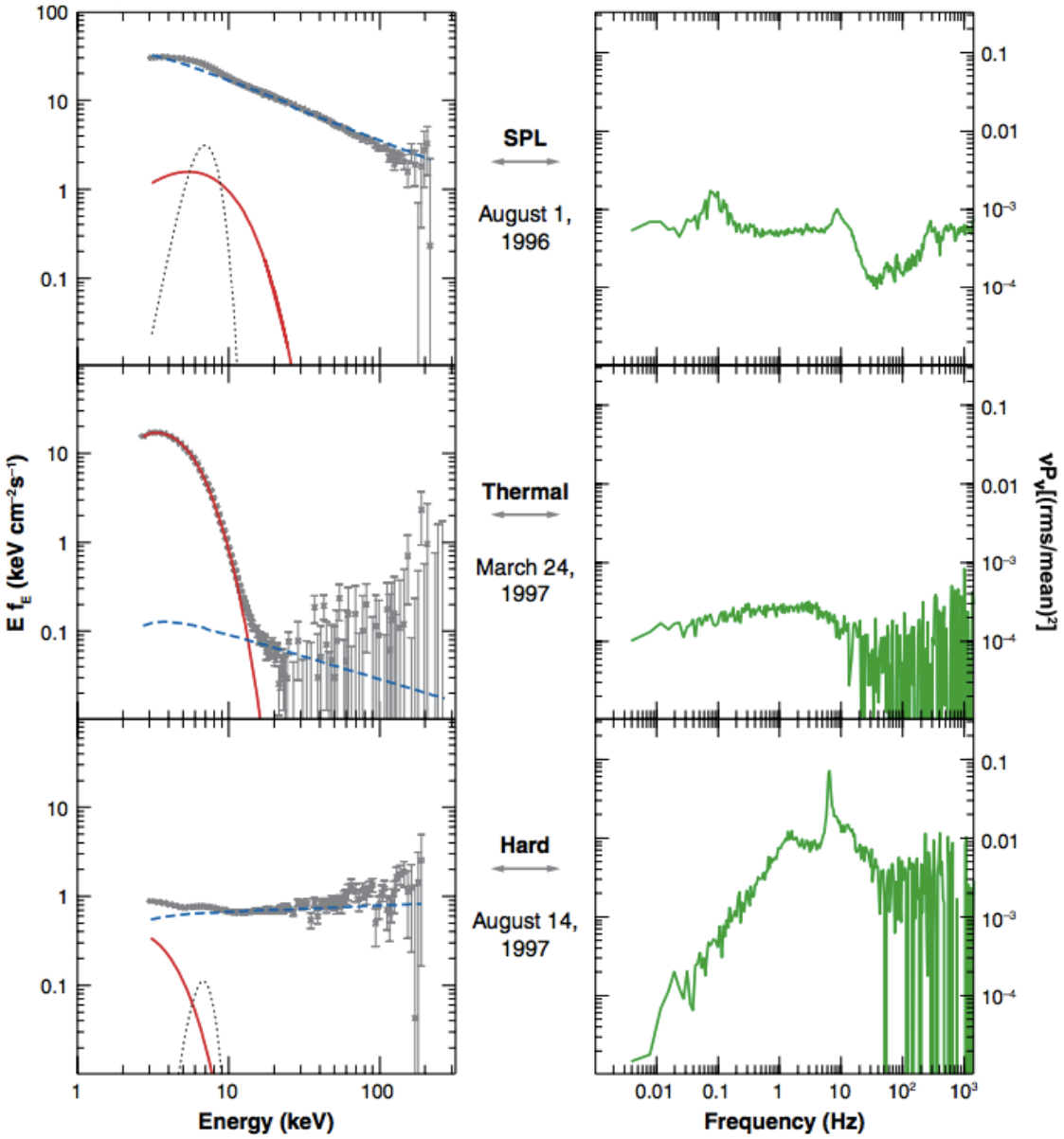

Figure 1.16: The energy spectra (*left*) and power spectra (*right*) of Galactic BH binary GRO J1655-40 in the steep PL (*top*), thermal (*centre*) and hard (*bottom*) sub-Eddington accretion states, from Remillard & McClintock (2006). The energy spectra, plotted in grey, are decomposed into the MCD (red) and PL (blue) components. The power spectra are plotted in green.

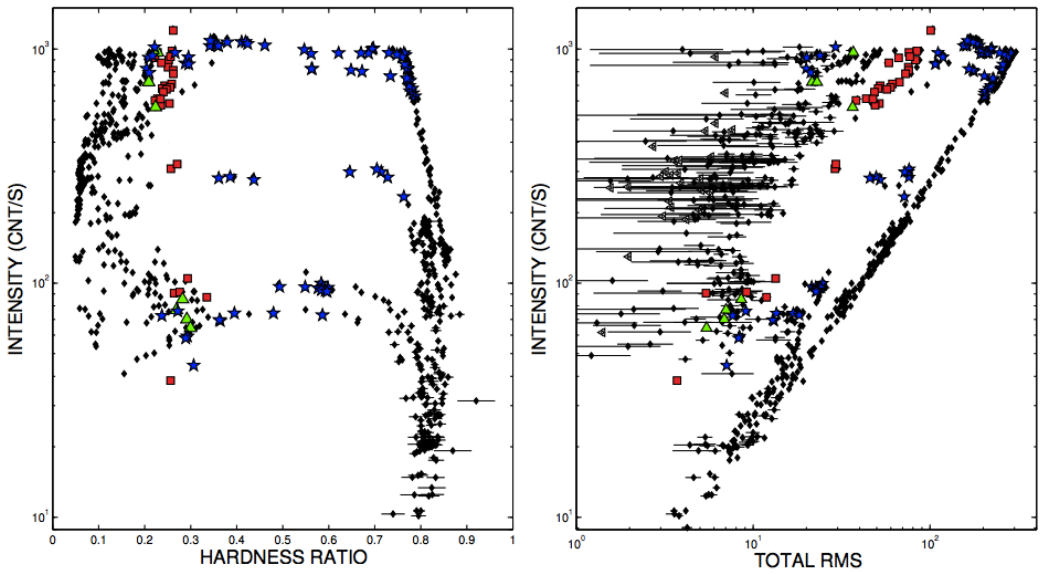

Figure 1.17: The hardness-intensity (*left*) and rms-intensity (*right*) diagrams showing the progress of four outbursts of Galactic BH binary GX 339-4, with each point representing a single observation, adapted from Motta et al. (2011). Coloured symbols represent states in which different types of QPO are observed in the power spectrum. In each outburst, the source begins in the hard state and rises up the right side of each plot, increasing in luminosity and variability, before transitioning to the soft and low-variability thermal state (the luminosity at which this happens is not necessarily consistent between outburts, as evidenced by the multiple horizontal tracks). The source then decreases in luminosity, its hardness and variability fluctuating as it does so, before returning to the hard/quiescent state.

source is in the thermal state, with emission dominated by the hot inner accretion disc but still possessing a contribution from a corona of hot electrons, creating the hard PL tail seen in this state. In the steep PL state, both disc and Comptonising corona significantly contribute to the emission. As the accretion rate decreases again, the local accretion rate at the inner disc is higher than the supply, causing the inner accretion disc to be eaten away, and the source returns to the hard state.

These transitions are reasonably sudden, due to thermal and viscous instability in the disc associated with the ionisation of hydrogen – between 10^4 and 10^5 K, a small increase in temperature (caused by an increase in mass accretion rate from the companion star) leads to a dramatic change in disc opacity as hydrogen is ionised, which in turn reinforces the temperature change and rapidly propagates through the disc during an accretion state change. The increase in temperature then affects the viscosity, allowing for a faster local

accretion rate. When the input rate decreases, this fast local accretion rate decreases the pressure and therefore temperature of the disc, causing the hydrogen to recombine and the opacity to dramatically drop due to the thermal instability (Done et al., 2007).

While the truncated disc model is commonly accepted for explaining the various sub-Eddington accretion states and the transitions between them, there also exist a number of alternative models. For example, instead of the hard state possessing a disc truncated at a large radius, it may in fact still reach the ISCO and directly fuel a corona which acts as the base of the radio jet (e.g. Miller et al. 2006). Or, rather than the inner disc radius evolving during accretion state changes, the spectral hardening factor that governs the inference of the physical parameters of the disc changes instead (Salvesen et al., 2013), which could be due to inhomogeneity or magnetisation of the accretion disc.

Accretion in HMXB systems driven by the stellar wind allows for a far more consistent accretion rate onto the compact object, so that the temperature is constantly above the hydrogen reionisation instability regime and the source persistently accretes rather than undergoing outburst cycles. Persistent sources can still move between accretion states, although these states will be of comparable luminosity and the sources do not drop back into quiescence.

1.5 Ultraluminous X-ray sources

During studies of the X-ray populations of other galaxies, it was found that a number of X-ray sources outside of the centre of their host galaxy had luminosities $L \geq 10^{39}$ erg s^{-1} – these subsequently became known as ultraluminous X-ray sources (ULXs). Since the Eddington luminosity of a 10 $M_{\odot}$ BH is $\sim 1.3 \times 10^{39}$ erg s^{-1}, and furthermore sub-Eddington sources are not expected to regularly reach very high fractions of the Eddington luminosity, this would imply that these BHs were either particularly massive, that their emission is highly beamed, or that they are accreting at super-Eddington rates (Feng & Soria, 2011). A recent and comprehensive review of ULXs can be found in Kaaret et al. (2017).

1.5.1 Intermediate-mass black holes

At first glance, the possibility that ULXs are intermediate-mass BHs (IMBHs; $10^2 < M_{\rm BH} < 10^5\,{\rm M}_\odot$; Colbert & Mushotzky 1999) accreting at sub-Eddington rates seems a simple enough solution. Since the Eddington luminosity is directly related to the mass of the BH (see Equation 1.3.9), a more massive BH is capable of reaching higher luminosities. This interpretation can be supported by fitting ULXs with the same MCD and PL treatment as applied to sub-Eddington accreting XRBs – such a model often gives very cool accretion discs (~ 0.1 keV). Assuming that we are indeed seeing the peak emission of a thin accretion disc that extends to the ISCO, this would imply that the ISCO is at a large radius and therefore the BH has a high mass (e.g. Miller et al. 2004; see Equation 1.3.5).

Such massive BHs are a challenge for formation scenarios as they cannot be formed simply as the result of normal stellar evolution. Massive stellar-mass BHs up to $\sim 80\,{\rm M}_\odot$ can form at very low metallicities (Belczynski et al., 2010), however creating BH masses $\gtrsim 100\,{\rm M}_\odot$ requires either very large ($> 260\,{\rm M}_\odot$), zero-metallicity population III stars as progenitors (e.g. Madau & Rees 2001), or the BH to be grown via mergers within very dense star clusters (e.g. Vesperini et al. 2010). Alternatively, the core of a dwarf galaxy could be absorbed by the current host galaxy in a minor merger (Farrell et al., 2012; Mapelli et al., 2012), so that the BH began its life as a central BH rather than being formed in its current host galaxy. While these are acceptable explanations for individual objects, they are problematic for explaining the entire ULX population, especially in star-forming galaxies containing a large number of ULXs, since an unrealistic production rate of IMBHs is required to match observations (King, 2004).

Examination of the luminosity function of X-ray sources in galaxies shows that it extends as a power-law up to $\sim 10^{40}\,{\rm erg\,s^{-1}}$, where it breaks and drops off steeply (Grimm et al., 2003; Swartz et al., 2004). This indicates an apparent upper limit to the X-ray luminosity of these sources which is equivalent to $\sim 10\%$ of the Eddington luminosity for a $1{,}000\,{\rm M}_\odot$ BH. This is unrealistic for a population composed mainly of IMBHs, since there is no reason why IMBHs should have a limit to their luminosity below their Eddington limit when stellar-mass BHs can be observed to accrete up to their Eddington limit (Roberts, 2007). Also, the luminosity functions of HMXBs and LMXBs themselves extend into the ULX regime, implying that most ULXs are simply the high-luminosity tail

of the XRB population rather than a separate population of sources (Swartz et al., 2011; Walton et al., 2011; Mineo et al., 2012).

Another problem for the majority-IMBH interpretation comes from the spectral properties of ULXs. Examination of the highest quality ULX data shows the presence of spectral curvature at $\sim 5\,\mathrm{keV}$ (Stobbart et al., 2006; Gladstone et al., 2009; Miyawaki et al., 2009) that sits at odds with the usual PL treatment of hard emission from sub-Eddington XRBs at these energies. It implies that the Comptonising corona responsible for the hard emission is optically thick rather than optically thin, or that there is a different source of hard emission altogether, both of which indicate an accretion state distinct from the sub-Eddington states. Also, when an MCD model is fitted to soft ULX spectra which appear to resemble the sub-Eddington thermal accretion state, there can often be inconsistencies between the apparent temperature of the disc and the luminosity we would expect for the thermal accretion state (Soria & Kong, 2016; Urquhart & Soria, 2016a) or, equivalently, between the mass scaling implied by the luminosities compared with the mass scaling implied by fitted disc temperatures (e.g. Colbert & Mushotzky 1999). Additionally, the fitted MCD model does not always follow the luminosity-temperature relation expected of a thin accretion disc (Kajava & Poutanen 2009; see Section 1.3.3).

The very brightest ULXs, called hyperluminous X-ray sources (HLXs) with $L_{\mathrm{X}} > 10^{41}\,\mathrm{erg\,s^{-1}}$, might still be good candidates for genuine IMBHs since they are too bright to easily explain with other methods (e.g. Gao et al. 2003; Farrell et al. 2009; Sutton et al. 2012). The best example of a candidate IMBH is ESO 243-49 HLX-1, henceforth referred to as HLX-1, which has been observed in multiple states similar to sub-Eddington accretion states (Godet et al., 2009; Servillat et al., 2011) and has exhibited radio flaring that confirms its mass to be in the IMBH range (Webb et al., 2012). HLXs must be carefully investigated, however, to make sure they are genuine residents of their apparent host galaxy, since some have been found to be background quasars (e.g. Sutton et al. 2015). Other good candidates for IMBHs are sources that demonstrate unambiguous features of sub-Eddington accretion states, particularly the hard state, such as a hard PL spectrum that does not turn over up to very high energies, or the presence of a powerful radio jet (Mezcua et al., 2013, 2015).

1.5.2 Beamed emission

A second explanation for the high apparent luminosities of ULXs may be the beaming of emission from an otherwise ordinary XRB (e.g. Okada et al. 1998; King et al. 2001). If the source's emission is not isotropic, and the majority of the emission is in the direction of an observer, it can give the appearance of exceeding the Eddington luminosity even if the source is in a sub-Eddington accretion state. The luminosity may be enhanced in this way by a very powerful jet, whose relativistic motion with respect to the observer can cause it to appear at a very high luminosity (Urry & Shafer, 1984; Körding et al., 2002).

However this explanation is inconsistent with the ULX luminosity function – we would expect to see far more ULXs with $L_X \sim 10^{39}\,\mathrm{erg\,s^{-1}}$ than we do for the number of ULXs with $L_X \sim 10^{40}\,\mathrm{erg\,s^{-1}}$ observed (Davis & Mushotzky, 2004), whereas in reality the luminosity function is shallower than that (e.g. Swartz et al. 2004; Walton et al. 2011). Also, the morphology of photoionised nebulae observed around some ULXs is inconsistent with the X-ray sources being narrowly beamed (e.g. Kaaret et al. 2004).

1.5.3 Super-Eddington accretion

The highest quality ULX spectra in the energy range of *XMM-Newton* and *Chandra* display a number of qualities that distinguish them from the sub-Eddington accretion states and can be roughly divided into three groups. The first group, at the lowest ULX luminosities, shows broad disc-like curvature over the whole energy band. The second and third groups possess a distinctive two-component spectrum, with an excess at low energies and a spectral turnover at $\sim 5\,\mathrm{keV}$ (Stobbart et al., 2006), with the hard and soft components dominant respectively with increasing luminosity. Examples of these spectral regimes are shown in Fig. 1.18. The spectral turnover was confirmed by *NuSTAR* observations of ULXs to be a genuine feature (e.g. Bachetti et al. 2013; Walton et al. 2015a), and it has been found to drop off as a steep PL rather than the Wien tail of a black body spectrum. These spectral behaviours, distinct from the sub-Eddington accretion states, could be explained as a new super-Eddington accretion regime (Gladstone et al., 2009), containing a supercritically accreting BH with mild geometric beaming through the funnel of a geometrically thick disc and strong radiatively driven winds (Poutanen et al., 2007).

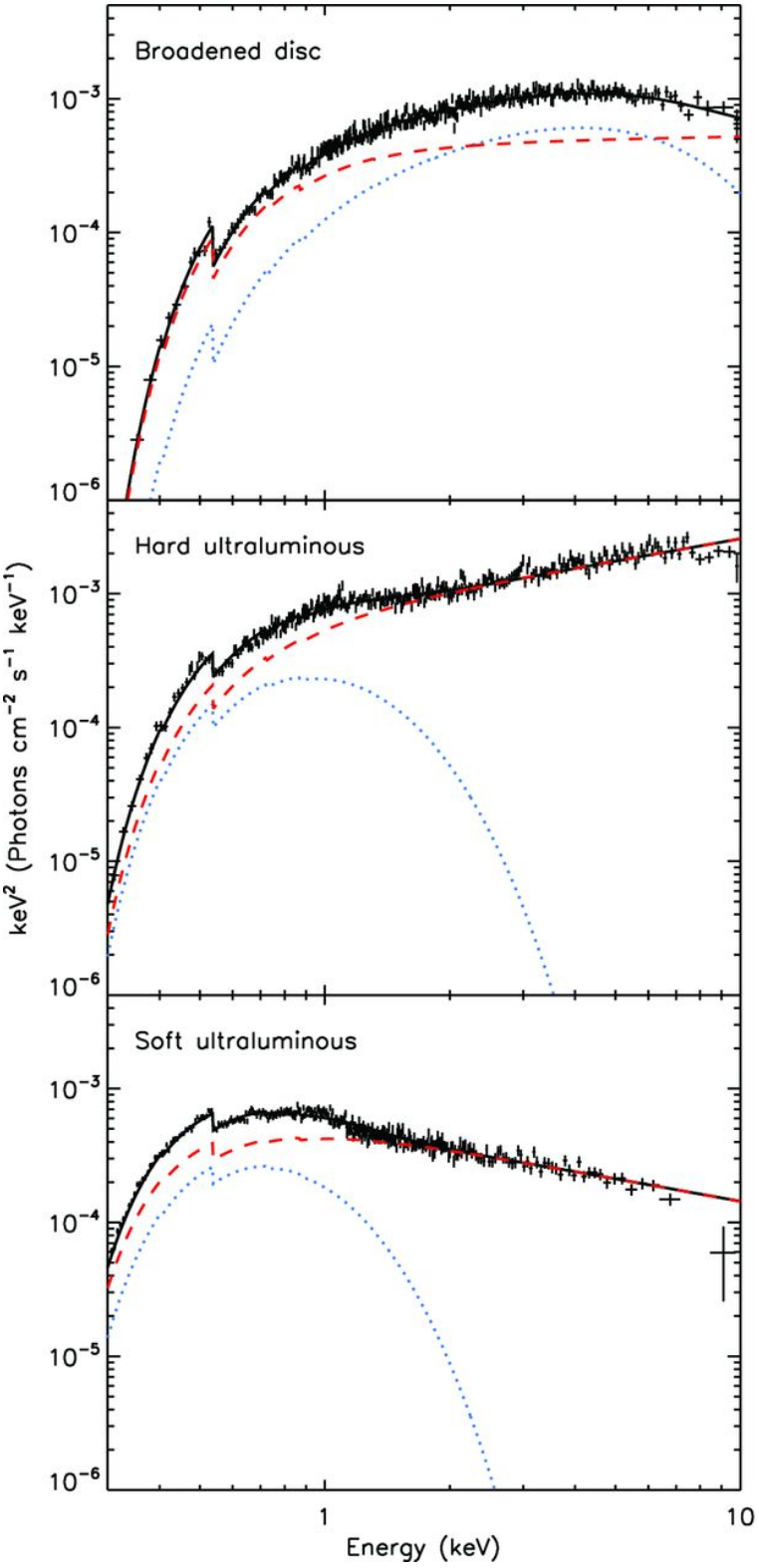

Figure 1.18: Examples of the three regimes of the ultraluminous state, from Sutton et al. (2013b). *Top*, NGC 1313 X-2 in the broadened disc regime. *Centre*, Ho IX X-1 in the hard ultraluminous regime. *Bottom*, NGC 5408 X-1 in the soft ultraluminous state. All spectra are shown with the best-fitting MCD (blue) and PL (red) model, and exhibit obvious spectral curvature above ~ 5 keV.

The first group, named the broadened disc regime, can be fitted with models of slim discs accreting at or around the Eddington limit. They can be considered to be an intermediate stage between a purely disc-dominated spectrum and the two-component spectrum seen in brighter ULXs with the emergence of a radiatively driven wind (e.g. Middleton et al. 2011). Their connection to the two-component states can be further supported by strong hard variability in some examples of this regime, similar to the soft ultraluminous state (see below). The other groups are the hard and soft ultraluminous regimes, the result of super-Eddington accretion. Unlike the sub-Eddington hard accretion state, the hard ultraluminous state does not tend to be very variable. Conversely, while the soft sub-Eddington thermal state is not highly variable, the soft ultraluminous state is. Additionally, this variability appears to be associated with the hard component of emission (Sutton et al., 2013b; Middleton et al., 2015a).

These various ultraluminous accretion regimes can be unified in a model in which a clumpy, optically thick wind is radiatively driven off a geometrically thick, supercritical accretion disc, creating a funnel structure orientated along the poles of the accreting system. At low inclinations, allowing the observer to see into the central funnel of the wind, the hard central emission – originating from the inner disc and up-scattered by a hot corona into a PL tail (e.g. Walton et al. 2015b) – dominates the spectrum. At higher inclinations, the spectrum is dominated by a soft, clumpy wind that absorbs and down-scatters the hard emission, with variability imprinted upon the high-energy component by the clumpy wind crossing the observer's line of sight to the centre of the system (Middleton et al., 2015a). A schematic of this model is shown in Fig. 1.19.

Spectral variation between these states, observed in sources such as NGC 1313 X-1, NGC 5204 X-1 and Ho IX X-1, may be caused by the angle of the funnel closing at higher accretion rates, precession of the accretion disc (Luangtip et al., 2016) or by the effective radius of geometric beaming moving outwards at higher accretion rates (Walton et al., 2016). Additional support for such a model with an outflowing wind has come from recent high-resolution spectroscopy of ULXs using the high-resolution RGS instrument on *XMM-Newton* to resolve and confirm the presence of blue-shifted absorption lines in the soft emission of ULXs, indicating the presence of a relativistic outflow at $\sim 0.2c$ (Pinto et al., 2016).

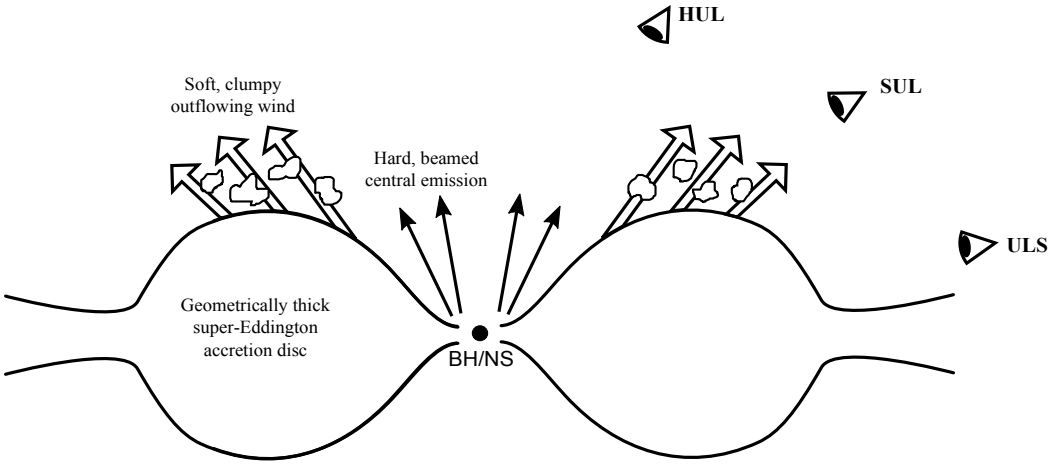

Figure 1.19: A schematic of a super-Eddington accretion state that may unify the hard and soft ultraluminous regimes, as well as the ultraluminous supersoft regime. The compact object is in the centre, surrounded by a geometrically thick accretion disc from which a clumpy outflowing wind is driven off. A spectrum observed at low inclinations would be dominated by hard central emission, manifesting as the hard ultraluminous (HUL) regime. At higher inclinations, the soft wind dominates the spectrum and high energy emission is variably occulted, the soft ultraluminous (SUL) regime. At the highest inclinations, all central emission is obscured, leaving an ultraluminous supersoft (ULS) spectrum.

Such a model may also extend to ultraluminous supersoft sources (ULSs; Di Stefano & Kong 2004). These are characterised by a very luminous ($L_{\rm bol} > 10^{39}\,{\rm erg\,s^{-1}}$) and very soft ($kT \sim 0.1\,{\rm keV}$) black body spectrum with little to no hard emission at all. These may be due to observing a supercritically accreting BH system as described above at a relatively high inclination angle (see Fig. 1.19), such that virtually all central emission is obscured and down-scattered, or through an optically thick photosphere formed by the outflowing wind that completely envelops the source when the accretion rate is at its highest (Feng et al., 2016; Soria & Kong, 2016; Urquhart & Soria, 2016a).

1.5.4 Neutron star ULXs

The very high luminosities of ULXs led to the assumption that the central compact objects were as high in mass as was reasonable (even though there was disagreement on what exactly constituted a reasonable high mass), and thus were most likely BHs. However, in recent years further complexity has been added to our interpretation of ULXs with

the discovery of coherent pulsations in the *NuSTAR* data from the ULX M82 X-2, unambiguous evidence that the source is a highly super-Eddington NS (Bachetti et al., 2014). M82 X-2 exhibits a spectrum with a moderately high-energy turnover compared to other ULXs ($\sim 14\,\mathrm{keV}$ compared with the usual $\sim 5\,\mathrm{keV}$; Brightman et al. 2015); however, subsequently two further ULXs with pulsations and spectra that appear closer to 'normal' ULX behaviour (see Section 1.5.3) have been discovered: NGC 7793 P13 (Fürst et al., 2016; Israel et al., 2017b) and NGC 5907 ULX-1 (Israel et al., 2017a). This would imply that any number of ULXs could potentially harbour a NS rather than a BH.

A big difference between BHs and NSs is the ability of the latter to sustain a powerful magnetic field. The presence of a strong magnetic field alters the electron cross-section and thus effectively raises the Eddington luminosity of the NS, allowing technically sub-Eddington accretion to occur at luminosities well above the normal Eddington limit for an object the mass of a NS (Mushtukov et al., 2015). The presence of a magnetic field also affects the geometry of the system – instead of an accretion disc reaching down to the surface of the NS, matter is accreted along the magnetic field lines and onto the surface of the NS via the poles (Dall'Osso et al., 2015). However, the mostly sinusoidal pulse profiles seen in NS ULXs observed so far imply that their emission is not tightly beamed (Fürst et al., 2016).

NS ULXs are also subject to the 'propeller effect' whereby in cases when the magnetospheric radius is larger than the corotation radius (the radius at which material within a Keplerian disc is rotating at the same angular velocity as the spinning NS), accretion is stopped and material may even be ejected from the system (Stella et al., 1986). This could be an explanation for the wide range of luminosities these sources are observed at (which, in the case of M82 X-2, are in a bimodal distribution; Tsygankov et al. 2016), with the periods of low luminosity being due to the source entering the propeller regime. This may also mean that transience in a ULX is potential evidence for a NS nature.

1.6 Thesis overview

The aim of this thesis is to create a new sample of extragalactic XRBs using recent data in order to investigate both the ULX population and sources at the Eddington Threshold,

which we define as the luminosity range $10^{38} < L_{\rm X} < 3 \times 10^{39}\,{\rm erg\,s^{-1}}$, and in doing so gain a better understanding of the extreme accretion scenarios found in these objects.

In Chapter 2, we describe the creation of this new catalogue of sources, using an improved version of the method presented in Walton et al. (2011), and examine sample properties, such as hardness ratios and luminosities, and how they change across different types of host galaxy. In Chapter 3, we focus on one unusual object, M51 ULX-7, which possesses atypical spectral and timing properties for a ULX and may be an IMBH candidate or another NS ULX. In Chapter 4, we investigate a small sample of soft Eddington Threshold sources with good data quality, finding that even the softest Eddington Threshold sources are a heterogeneous population including the highest-luminosity sub-Eddington accreting sources, ULSs, and extreme examples of the soft ultraluminous regime. In Chapter 5, we search for evidence of the most down-scattered super-Eddington sources by looking for ultraluminous ultraviolet sources (ULUVs) in a similar manner to Chapter 2, comparing different UV missions for suitability for such a study and locating potential candidates for *HST* follow-up. Finally, we draw up the conclusions of this thesis and suggest avenues for future work building upon the research in this investigation.

CHAPTER 2

A new, clean catalogue of extragalactic non-nuclear X-ray sources in nearby galaxies

Abstract

We have created a new, clean catalogue of extragalactic non-nuclear X-ray sources by correlating the 3XMM-DR4 data release of the *XMM-Newton* Serendipitous Source Catalogue with the Third Reference Catalogue of Bright Galaxies and the Catalogue of Neighbouring Galaxies, using an improved version of the method presented in Walton et al. (2011). Our catalogue contains 1,464 sources, of which 372 are ultraluminous X-ray sources (ULXs). Our resulting catalogue improves upon previous catalogues in its handling of contaminants by taking into account *XMM-Newton* quality flags, and we estimate the contamination to be 19.8%. We define a 'complete' subsample as those ULXs in galaxies for which the sensitivity limit is below $10^{39}\,\mathrm{erg\,s^{-1}}$ and use it to examine the hardness ratio properties between ULX and non-ULX sources, and ULXs in different classes of host galaxy. We find that ULXs have a similar hardness ratio distribution to lower-luminosity sources, consistent with previous studies. We also find that ULXs in spiral and elliptical host galaxies have similar distributions except for a hard subpopulation found in spirals, which we postulate is due to high levels of absorption within the host galaxy rather than any intrinsic difference in spectral shape. Our catalogue contains further interesting subpopulations for further study, including Eddington Threshold sources, variable sources and transient ULXs. We also examine the highest-luminosity ULXs in our catalogue in search of IMBH candidates, and find eight new possible candidates.

2.1 Introduction

Over the past decade, ULXs have proved to be a fruitful laboratory for challenging and refining our understanding of extreme accretion onto compact objects. The extreme luminosity of these objects has two possible implications: either they are IMBHs accreting at sub-Eddington rates and likely in similar accretion states to those we observe in stellar-mass BH binaries (e.g. Miller et al. 2004), or they are stellar-mass compact objects undergoing a non-standard form of accretion – either undergoing beaming (e.g. King et al. 2001) sufficient to make a sub-Eddington source appear to have a luminosity above Eddington, or accreting in a genuinely super-Eddington mode (e.g. Poutanen et al. 2007) which may also involve mild beaming (see Section 1.5).

Although it has been established that the properties of the majority of ULXs can be explained by super-Eddington accretion onto stellar-mass BHs or NSs (e.g. Gladstone et al. 2009; Swartz et al. 2011; Bachetti et al. 2014; Middleton et al. 2015a), the most luminous of the population, HLXs ($L_{\rm X} > 10^{41}\,{\rm erg\,s^{-1}}$), are challenging to explain even with highly super-Eddington accretion, and thus are a good place to look for genuine IMBH candidates. It is also possible to find plausible IMBH candidates in the main ULX population if they show strong evidence of accreting in a sub-Eddington rather than a super-Eddington state, such as radio detection of steady jet emission (e.g. NGC 2273-3c, Mezcua et al. 2015) or strong band-limited noise and a hard spectrum (e.g. M51 ULX-7, Earnshaw et al. 2016) indicating a source accreting in the low/hard state. Together with the ambiguity between BH and NS ULXs, the presence of IMBHs in the ULX population shows it to be a complex and heterogeneous one.

While closely studying the properties of individual well-known ULXs can provide us with detailed insight into the accretion mechanisms of this population, this is only possible for a small number of sources for which, through a combination of high luminosity, relative proximity, and lengthy observing campaigns, there is a wealth of high-quality data available. Insight into the properties of the ULX population as a whole requires the creation of large samples of ULXs, which has been made possible through the collected observations of X-ray space telescopes, especially *ROSAT*, *Chandra* and *XMM-Newton* (Roberts & Warwick, 2000; Colbert & Ptak, 2002; Swartz et al., 2004; Liu & Mirabel, 2005; Liu & Bregman, 2005; Swartz et al., 2011; Walton et al., 2011). These samples

have allowed us to investigate this population's characteristics – for example, it appears to be the case that ULXs are more numerous and luminous in star-forming galaxies than in non-star-forming galaxies (Swartz et al., 2004; Liu & Bregman, 2005), which would imply different ULX populations depending upon the nature of their host environment. The association of one population with star-forming galaxies makes them likely to be in HMXBs with a high-mass, short-lived stellar companion such as an OB-supergiant acting as the fuel supply. Those ULXs in elliptical galaxies and non-star-forming regions of spiral galaxies are more likely to be LMXBs with smaller companion stars that begin accreting long after star formation has ended. This notion of two populations of ULXs is tentatively supported by the differing luminosity functions of ULXs found in spiral and elliptical host galaxies, with a shallower power-law slope for those in spiral (i.e. star-forming) galaxies indicating the presence of a greater number of higher luminosity ULXs (e.g. Walton et al. 2011).

Aside from their extreme luminosities, ULXs do not differ a great deal from lower-luminosity X-ray sources, possessing much the same bulk X-ray properties as non-ULXs in terms of spectral shape and colour (Swartz et al., 2004). However, different subgroups of objects within the general X-ray source population such as HMXBs and LMXBs, as well as supernova remnants and supersoft sources, are suggested to have different distributions in X-ray colour (Prestwich et al., 2003). Subgroup differences may also be evident in the ULX population, where it has been suggested that the hard and soft ultraluminous regimes can be distinguished by X-ray colour (Pintore et al., 2014).

Samples of ULXs are also useful for identifying extreme or otherwise unusual sources for further study. The most obvious example is the search for HLXs that could potentially be viable IMBH candidates (e.g. Sutton et al. 2012, examining high-luminosity ULXs in the catalogue presented in Walton et al. 2011; see Section 1.5.1). However, the ability to select sources based upon other properties, such as their spectral shape or their variability properties, allows other routes for locating objects of interest. In this respect, the *XMM-Newton* Serendipitous Source Catalogue is an excellent resource for constructing a ULX sample, containing for every detected source the fluxes in various energy bands and hardness ratios between bands. In addition, it benefits from the large collection area, good sensitivity and wide field of view of the mission which makes the telescope effective at

making serendipitous detections (see Section 1.1.1 for more details on the *XMM-Newton* telescope). It also contains a number of quality indicators which assist in reducing sample contamination by camera artefacts or detections likely to have unreliable fluxes.

In this chapter we create a new, clean sample of ULXs using the recent 3XMM-DR4 data release of the *XMM-Newton* Serendipitous Source Catalogue. We describe our sample creation in Section 2.2, and examine the bulk properties of our sample and some significant subsets in Section 2.3. We present our conclusions in Section 2.4.

2.2 Data & sample selection

We produced our catalogue of ULXs using the 3XMM-DR4 data release of the *XMM-Newton* Serendipitous Source Catalogue (Rosen et al., 2015, 2016). Images were taken using the EPIC instrument of *XMM-Newton* between the dates of 3 February 2000 and 8 December 2012, with a coverage of $\sim 2\%$ of the total sky. The survey catalogue contains 531,261 detections of 372,728 unique sources, a $\sim 50\%$ increase from the previous 2XMMi-DR3 data release, and features improvements in the instrument calibration, data processing algorithms and the Science Analysis Software available for data reduction. It is therefore an ideal resource for creating a large sample of ULXs that can be used for statistical studies of these rare and extreme objects, as well as for obtaining large numbers of lower luminosity objects. We note that further 3XMM data has been released since this project's inception, with the latest data release being 3XMM-DR7 in 2017 (Rosen et al., 2016) and that future projects will benefit from using the most up-to-date version of the catalogue available.

The 2XMM-DR1 release of the *XMM-Newton* Serendipitous Source Catalogue was used by Walton et al. (2011) (henceforth referred to as W11) to create a catalogue of ULXs. Our method is based heavily on that used in W11, applied to the 3XMM-DR4 release, but containing a number of improvements and extended to lower-luminosity extragalactic X-ray sources. This section describes the process of catalogue creation and the basic properties of the final sample, but we also recommend that the reader refer to W11 for further details.

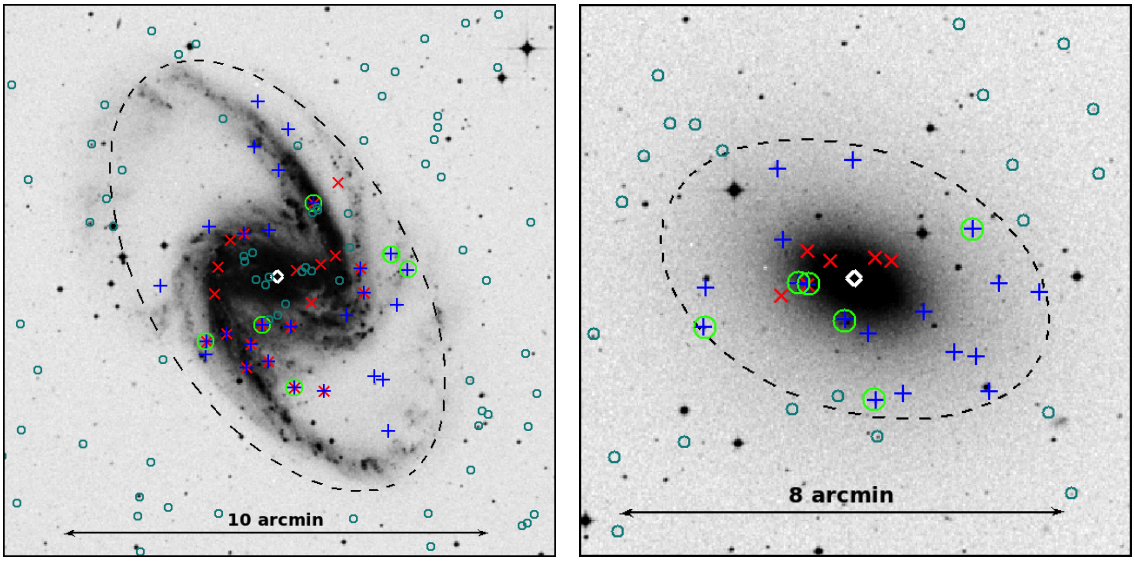

Figure 2.1: Examples of the catalogue selection method for NGC 1365 (*left*) and NGC 4697 (*right*). Sources are overlaid on DSS optical images of the galaxies. Sources from 3XMM-DR4 are marked with small dark cyan circles. The D25 ellipses of the galaxies are marked in black, and significant detections of point sources falling inside them are marked either with a blue cross for a source with no major detection quality flags, or with a red cross for a flagged detection (see Section 2.2.3). For sources with multiple detections, it is possible for one detection to have a major quality flag and another not to. The central AGN is marked with a white diamond and ULXs are marked with large green circles.

2.2.1 Sample creation

We began by cross-correlating 3XMM-DR4 with a list of galaxies from the Third Reference Catalogue of Bright Galaxies (RC3; de Vaucouleurs et al. 1991), as in W11. RC3 is an all-sky galaxy catalogue with the aim of being mostly complete in galaxies with diameters greater than 1 arcminute, B-band magnitudes greater than 15.5 and redshifts below 15,000 km s^{-1} (11,897 objects), and including over 10,000 additional galaxies to bring the total to 23,022 individual galaxies. We supplemented RC3 with the Catalogue of Neighbouring Galaxies (CNG; Karachentsev et al. 2004), which contains 451 galaxies with distance $D \lesssim 10$Mpc, in order to build a more complete picture of the local population of X-ray binaries in other galaxies. We added the 366 galaxies in CNG that are not already included in RC3 to our list, then updated the central position coordinates and recessional velocities of all galaxies with their values according to the NASA Extragalactic

Database (NED)[1]. A small number of nearby galaxies extend over a greater area of the sky than the *XMM-Newton* field of view, which means that we cannot guarantee that these galaxies were observed completely – additionally, we expect that the X-ray source population of these galaxies is heavily contaminated by background sources, given their low distance and large area on the sky. Therefore we removed from our list all galaxies with a D_{25} isophotal major axis greater than 25 arcminutes – these 13 galaxies are Andromeda, the Large and Small Magellanic Clouds, M33, M54, M81, M101, NGC 55, NGC 253, NGC 5128, Draco Dwarf, Sculptor Dwarf, and Sextans Dwarf Spheroidal. While this removes a number of known ULXs and X-ray binaries from our sample, the X-ray populations of these galaxies are well-studied already, so we are unlikely to miss discovering new sources by not including them.

In order to obtain the most accurate distances for the galaxies, we first used data from the NED Distances Database (NED-D). If a galaxy had distance measurements within NED-D obtained from Cepheid variables, the tip of the red giant branch or Type Ia supernovae (in that order of precedence), we took the mean of the distances calculated using that method to obtain the best galaxy distance. The distances of remaining galaxies with recessional velocity $cz < 1000$ km s^{-1} were obtained from the Catalogue of Nearby Galaxies (NBG; Tully & Fisher 1988). Any galaxies with $cz < 1000$ km s^{-1} and no NED-D or NBG distance were discarded, as the velocities of nearby galaxies will be dominated by peculiar motion and an accurate distance cannot be obtained using the recessional velocity alone. The velocity of galaxies with $cz > 1000$ km s^{-1} and no NED-D or NBG distance we considered to be dominated by the Hubble flow and were calculated with Hubble's law, using $H_0 = 75$ km s^{-1} for consistency with Tully & Fisher (1988). Finally, we ran an initial correlation of this galaxy list with the 3XMM-DR4 summary of observations to find all galaxies that fall within the sky coverage of 3XMM-DR4, which gave us a final list of 1,957 3XMM-DR4 field galaxies.

This list of field galaxies was matched with all significantly-detected point sources in the 3XMM-DR4 catalogue, defined as those objects with extent < 6 arcseconds and a maximum likelihood of detection > 8 (equivalent to a 3.5σ detection). As in W11, we

[1] http://nedwww.ipac.caltech.edu/

performed this matching using the TOPCAT[2] software to find all point sources that fell (to within their catalogue position error, which corresponds to a 63% confidence radius) inside the D_{25} isophotal ellipse of each galaxy, or within a circular match using the minor axis where there was no position angle data. This left us with an initial sample of 2,975 X-ray point sources. For an example of the execution of this method, see Fig. 2.1.

The luminosity of each detection was calculated using the EPIC flux over all energy bands (0.2–12 keV), and the calculated distance to the host galaxy as described above. The error on the luminosity was derived from the error on the flux, as while we expect that the error will be dominated by the uncertainty in the distance measurement, it is not well quantified. We defined ULXs as those sources with $L_X \geq 10^{39}$ erg s^{-1} or luminosity within 1σ of the cut-off luminosity, however we retain lower luminosity sources in our sample as an extension of the catalogue.

2.2.2 Removal of known contaminants

A large number of contaminants are still present in the sample at this stage. The majority of contaminants are the active galactic nuclei (AGNs) of the host galaxies. To ensure that our sample only contains the non-nuclear objects, these host AGNs must be removed. While many AGNs will be much more luminous even than most ULXs, a cut cannot be made on the basis of luminosity alone, since ULX luminosities can overlap with those of low luminosity AGNs (LLAGNs), which may have luminosities as low as $\sim 10^{38}$ erg s^{-1} (e.g. Ghosh et al. 2008, Zhang et al. 2009). Instead, we removed possible AGNs based on their separation from the centre of the host galaxy as defined by NED.

We defined a minimum separation $r_{\rm min}$ as the separation between the object's source position and the galaxy centre, minus three times the source position error, a slightly more conservative metric than that used by W11. We set aside all objects with $L_X > 10^{42}$ erg s^{-1} into a separate sample of sources which we are confident are AGNs. We found that $> 95\%$ of this AGN sample had $r_{\rm min} < 1$ arcsecond. Therefore we initially removed all objects with $r_{\rm min} < 1$ arcsecond, which made up $\sim 25\%$ of the sample. However, visual inspection of the remaining high luminosity objects ($L_X > 10^{41}$ erg s^{-1}) led us to believe

[2]Tool for Operations on Catalogues and Tables; http://www.star.bris.ac.uk/mbt/topcat/

that a significant proportion of AGNs were still retained by this cut, so we extended the conditions of removal to $r_{\rm min} < 3$ arcseconds, which we found gave a good balance of excluding probable AGNs and retaining as many candidate ULXs as possible. This cut removed $\sim 30\%$ of the sample in total, leaving 2,105 sources, and the removed objects were added to the AGN sample which was retained for the purpose of comparison.

To remove any remaining known contaminants, we cross-correlated the remaining objects with the Véron-Cetty & Véron (2010) catalogue of quasars to remove background QSOs, and the Tycho-2 catalogue (Høg et al., 2000) to remove foreground stars. We then cross-correlated all remaining objects with NED, and removed all supernovae, supernova remnants (SNRs) and background QSOs. These cross-correlations were all performed within 10 arcseconds and removed a total of 80 sources (a further $\sim 4\%$ of the sample). At this point, being confident that known background contaminants have been removed, we resolved any duplicated detections caused by the overlapping of the D_{25} isophotes between different galaxies by assuming that the source lies in the foreground galaxy, as the foreground galaxy is likely to cause a significant amount of absorption to anything lying behind it, or in the galaxy it is closest to the centre of in the case of systems at an equal distance. In subsequent closer examination of some of the more extreme objects of the sample (for example, objects with high luminosity or very hard spectra; see Section 2.3.2) we also removed all detections of nine sources which coincided with the AGN of their host galaxy but had a separation of $r_{\rm min} > 3$ arcseconds due to an inaccurate position, or coincided with background objects of known redshift. The sample at this stage contains 3,288 detections of 2,026 sources.

2.2.3 Flagged detections

While we have made a number of minor refinements to W11's method in previous stages, the primary difference between our selection method and that of W11 is our consideration of detections assigned quality flags by the *XMM-Newton* pipeline. The *XMM-Newton* flagging system highlights problematic detections, however we want to strike a good balance between only including good quality data in the sample and retaining as many sources as possible for a large sample size. In this section we give a summary of the flagging system and our justification for the exclusion of sources marked with some types

of flag. A detailed description of the various flags and their meanings can be found in the 2XMM and 3XMM User Guides to the Catalogue[3].

There are twelve quality flags that can be assigned to a detection, and a further summary flag field that takes values between 0 and 4 depending upon the state of the quality flags. Flags 1, 2, 3 and 9 are automatically triggered when a source has low detector coverage, is near another source, is within extended emission, or is near the bright corner of the EPIC-MOS1 detector respectively, and therefore may have some problems with its recorded parameters. If any of these flags are true, the summary flag is given the value 1. Flags 4, 5 and 6 are automatically triggered in various circumstances that indicate that the source detection is possibly spurious, and if at least one of these flags is set to true, flag 7 is set as well. Flag 8 is triggered if the source is on the bright EPIC-MOS1 corner or a low-gain column on the EPIC-pn detector. If either flag 7 or flag 8 are true, the summary flag is increased to 2.

The remaining flags are handled differently between the 2XMM and 3XMM pipelines. In 2XMM, flag 10 is unused, and flag 11 is manually triggered on visual inspection of the observation if the source lies within a region where a spurious detection is likely – for example, regions of bright extended emission, out-of-time events or 'spiderleg' artefacts caused by the reflection grating array (RGA) – with flag 12 indicating the bright source which is often the cause for these regions. For detections with flag 11 set to true, the summary flag is increased to 3. If flags 7 or 8 are also true, the summary flag is instead increased to 4. In 3XMM, flag 10 is put to use as an automatically triggered flag in the case of out-of-time events, although if only flag 10 is set, then the summary flag is only given the value 1. Visual inspection of the observations continue to be used to set flag 11, but rather than flag 12 exempting bright sources, flag 11 simply isn't set in these cases.

Approximately 45% of all detections have at least one quality warning flag attached to them and thus have a summary flag value greater than zero. Of the flagged detections, about 36% have a summary flag of 1, and 62% have a summary flag of 3, with only a handful having a summary value of 2 or 4 (see Fig. 2.2). Therefore the main drivers of a detection being flagged are either minor problems with its source parameters, or it lying

[3]http://xmmssc-www.star.le.ac.uk/Catalogue/2XMM/UserGuide_xmmcat.html and http://xmmssc-www.star.le.ac.uk/Catalogue/3XMM-DR4/UserGuide_xmmcat.html

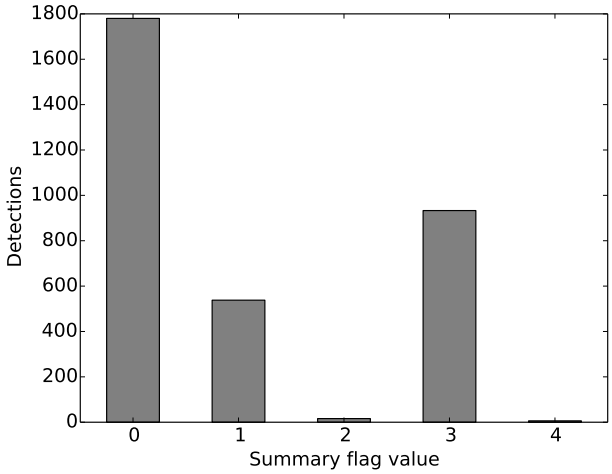

Figure 2.2: Bar chart of the occurrence of summary flag values throughout the sample after contaminants have been removed in Section 2.2.2.

in a region where spurious detections are likely. We decided that removing all flagged detections would decrease the size of our sample by too much, so we kept sources with a summary flag of 1. Sources with a summary flag of 3 have a reasonable possibility of being spurious even without flags 7 and 8, which only consider limited scenarios that may cause a detection to be spurious, and there is no easy way of identifying which sources may be genuine without further visual inspection of each observation. Additionally, even those sources that are genuine but embedded within bright extended emission will have their source fluxes erroneously increased and their spectra distorted by the presence of contaminating soft emission. Therefore we removed all detections with a summary flag of 2, 3 or 4, as well as sources with quality flag 10 set to true which are also likely to be artefacts or out-of-time events rather than genuine detections.

We acknowledge that removing these flagged detections introduces some bias in the sample based upon the environment of the sources. Sources with a summary flag of 3 are more likely to be located near the centre of galaxies, since that is where either bright extended emission or RGA artefacts caused by bright AGNs are located. We show the bias against more centrally-located sources in Fig. 2.3, where it is clear that sources with a summary flag value greater than 1 are more likely to be centrally located than sources with no flag or a minor flag, which have a mostly flat distribution with fractional distance from the galaxy centre. There is also some bias against sources located in large, bright elliptical galaxies due to their extended X-ray emission, which can be seen in Fig. 2.4 in which

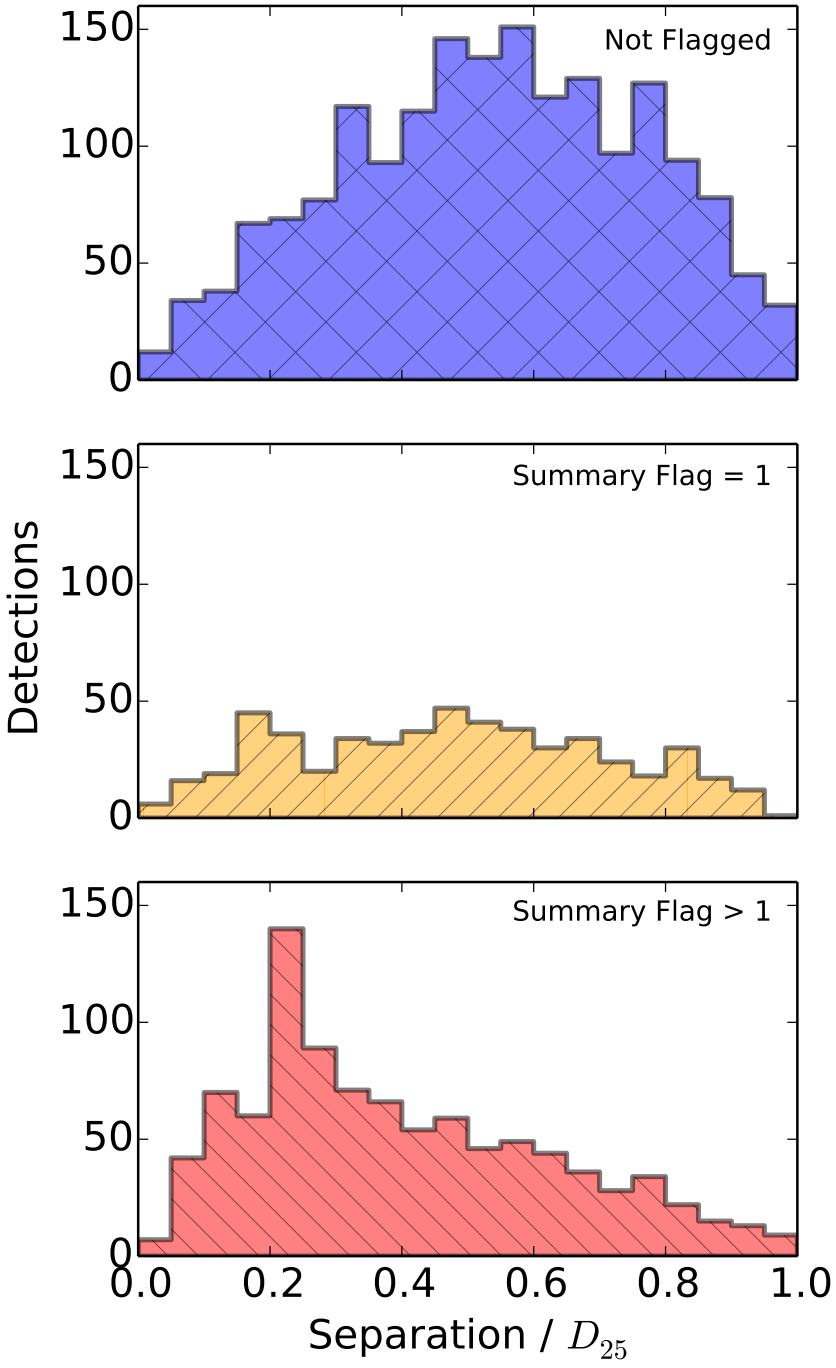

Figure 2.3: Histogram of flag occurrence by the fractional separation of the detection from the centre of its host galaxy. Unflagged sources are shown in blue, sources with summary flag equal to 1 are shown in yellow, and all other flagged sources are shown in red.

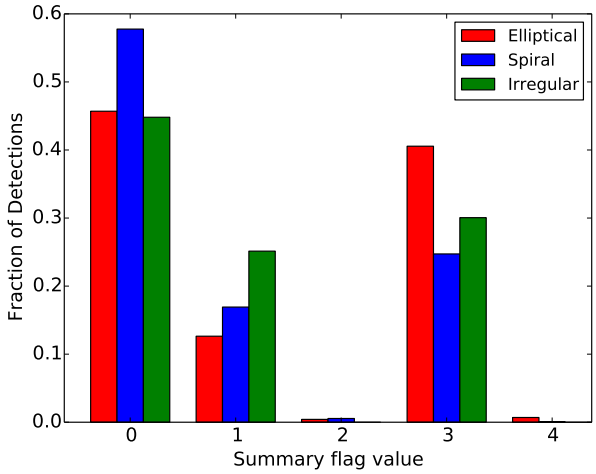

Figure 2.4: Bar chart of the fractional occurrence of summary flag values by host galaxy type. Values for elliptical galaxies are plotted in red, spiral galaxies in blue and irregular galaxies in green.

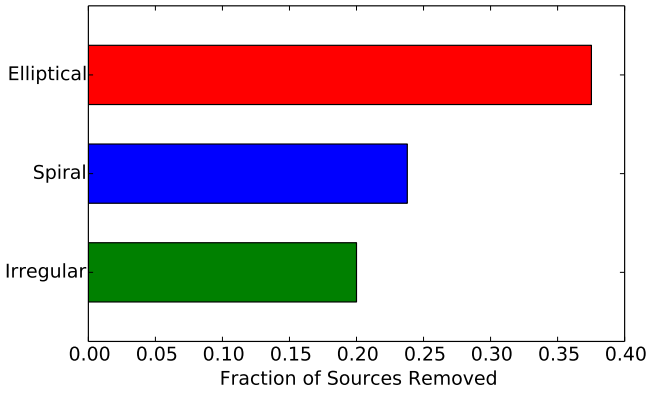

Figure 2.5: Bar chart of the fraction of sources removed completely from the sample by the flag cut, by host galaxy type.

elliptical galaxies are slightly over-represented for summary flag values greater than 1. This bias is confirmed when we examine the number of sources removed completely from the sample (rather than only having a fraction of their detections removed), and break them down by galaxy type – nearly 40% of sources in elliptical galaxies are removed, compared with about 25% of sources in spirals and 20% of sources in irregular galaxies (Fig. 2.5).

However, we expect there to be fewer ULXs in elliptical environments than in star-forming environments from previous studies (Swartz et al., 2004; Liu & Bregman, 2005), and upon inspection of some objects discarded for this reason we conclude that many are more likely to be background QSOs than genuine ULXs. Therefore we are confident

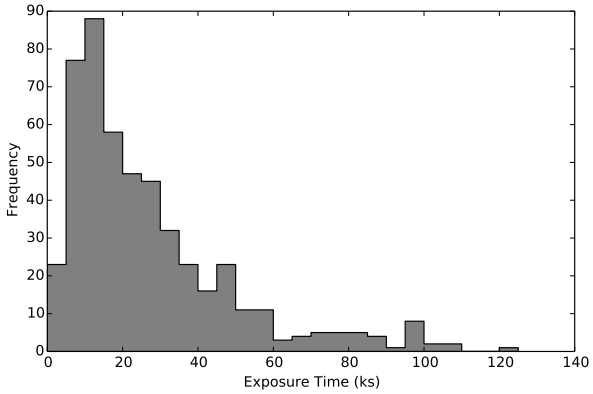

Figure 2.6: The distribution of exposure times for the observations that went into creating our sample.

that removing those detections with a summary flag greater than 1 strikes a good balance between creating a clean and reliable sample and still retaining a good sample size. After applying this flag cut, the final sample contains 2,256 detections of 1,464 sources.

2.2.4 Sample properties

The final sample contains 2,256 detections of 1,464 sources, located within 349 host galaxies. Of these sources, 372 are candidate ULXs, defined as having at least one detection with $L_X > 10^{39}\,\mathrm{erg\,s^{-1}}$ or else having L_X within 1σ of $10^{39}\,\mathrm{erg\,s^{-1}}$. This data was obtained from 1,808 unique *XMM-Newton* observations with a median duration of 20 ks (although observations are concentrated below the median, the exposure time distribution has a tail that extends to over 120 ks – see Fig. 2.6). The median distance for the host galaxies of the sources in our sample is 19.8 Mpc, with the distribution of distances similarly concentrated at relatively low distances with a long tail out to very distant galaxies (see Fig. 2.7). Given the sensitivity of *XMM-Newton*, for a typical 20 ks observation of a galaxy 20 Mpc away, we can expect to detect sources down to $\sim 10^{38}\,\mathrm{erg\,s^{-1}}$, depending on the spectral shape. Indeed, while there are several hundred ULXs, the majority of detections we include are of sources with luminosities in the range $10^{37} < L_X < 10^{39}\,\mathrm{erg\,s^{-1}}$ (see Fig. 2.8). This makes the catalogue a good resource for sampling X-ray populations of interest with luminosities below the ULX regime, such as the Eddington Threshold (see Section 2.3.3).

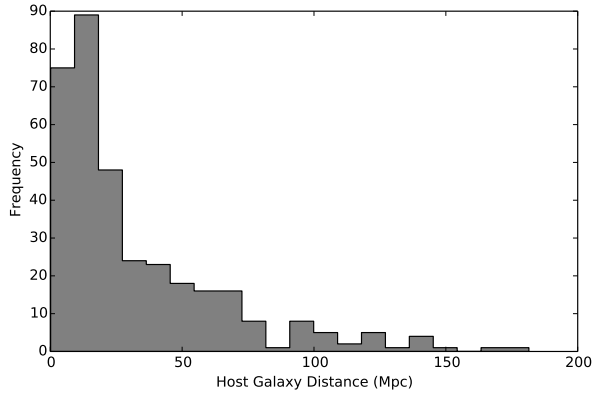

Figure 2.7: The distribution of distances for the host galaxies of our sample.

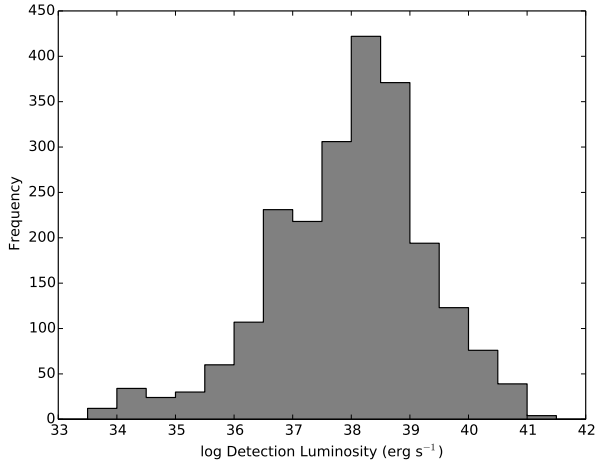

Figure 2.8: The distribution of luminosities for the detections in our sample.

We divide our sources between different galaxy types in order to investigate potential differences in the ULX population in different galactic environments. To do this we use the Hubble stage T given in the catalogue, which is a numerical classification of the galaxy morphology based on the Hubble sequence (de Vaucouleurs, 1994). We define elliptical galaxies as galaxies with Hubble stage $T < 0$ in RC3 or CNG, spiral galaxies as those with $0 \geq T \geq 9$, and irregular galaxies as those with $T > 9$. We present sample numbers in these galaxy groupings in Table 2.1, both for the full-luminosity sample and for those sources identified as ULXs (including detections of ULXs that do not in themselves reach ULX luminosities).

There is a common association of ULXs with star-forming regions that might suggest we would expect to find a greater number of ULXs in spiral or irregular (mostly star-

Table 2.1: Catalogue numbers for all sources and for ULXs, broken down by galaxy type and including the complete subsample (see Section 2.2.5).

	Full sample	Spiral	Elliptical	Irregular	Complete
Field galaxies	1,957	1,179	679	99	435
Detections	2,256	1,725	418	108	2,048
Sources	1,464	1,029	350	76	1,305
- with multiple detections	362	310	37	15	342
Host galaxies	349	231	86	32	222
- containing multiple sources	172	118	37	17	152
ULX detections	539	417	94	28	298
ULXs	372	272	80	20	227
- with multiple detections	87	67	13	7	55
ULX host galaxies	248	178	56	14	122
- containing multiple ULXs	103	82	14	7	59

forming) galaxies than in elliptical (mostly non-star-forming) galaxies. Indeed, we find that the majority of extragalactic non-nuclear X-ray sources are found in spiral or irregular galaxies regardless of luminosity, with $\sim 20\%$ of all spiral galaxies and $\sim 30\%$ of all irregular galaxies containing at least one non-nuclear X-ray source, compared with $\sim 13\%$ of elliptical galaxies. Similarly, while fewer galaxies contain a ULX than contain X-ray sources in general, we find more in spirals and irregulars: $\sim 15\%$ of field galaxies contain at least one ULX in both cases, compared with $\sim 8\%$ of ellipticals. This appears to be consistent with the association of ULXs with star-forming environments. We do note our previously-identified bias against bright elliptical galaxies in flagging, which will reduce the number of sources in elliptical galaxies that make it into our sample (see Section 2.2.3), however when we correct for the proportion of flagged detections removed, as well as for the reduced number of elliptical galaxies in the field to begin with, we still find that spiral and irregular galaxies contain greater numbers of non-nuclear X-ray sources than elliptical galaxies do.

We present a selection of average host galaxy properties in Table 2.2, both for the entire list of field galaxies, those galaxies containing any good detections of X-ray sources, and ULX host galaxies. ULX host galaxies are on average more distant than the overall population of those containing non-nuclear X-ray sources, illustrating the relative scarcity

Table 2.2: The median host galaxy properties for the catalogue, broken down by galaxy type and including the complete subsample (see Section 2.2.5).

Field Galaxies	All	Spiral	Elliptical	Irregular	Complete
$\tilde{d}^a$	$66.9^{+24.2}_{-21.6}$	$71.3^{+22.0}_{-19.9}$	$66.2^{+25.2}_{-19.9}$	$21.2^{+10.7}_{-13.0}$	15.3 ± 3.7
$\tilde{M_{\rm B}}^b$	$-15.3^{+0.5}_{-0.8}$	$-15.3^{+0.6}_{-0.5}$	$-15.5^{+0.6}_{-0.5}$	$-12.1^{+0.5}_{-0.9}$	$-14.3^{+1.0}_{-0.7}$
Source Host Galaxies	All	Spiral	Elliptical	Irregular	Complete
$\tilde{d}^a$	$19.8^{+12.5}_{-6.0}$	$20.6^{+15.8}_{-5.5}$	$22.0^{+12.0}_{-7.7}$	$4.1^{+17.6}_{-0.7}$	$13.8^{+2.5}_{-4.7}$
$\tilde{M_{\rm B}}^b$	$-15.1^{+0.7}_{-0.6}$	-15.1 ± 0.6	-15.3 ± 0.6	$-12.1^{+0.7}_{-1.0}$	$-14.6^{+0.9}_{-0.7}$
$\tilde{\rm N}^c$	1^{+1}_{-0}	2^{+1}_{-1}	1^{+1}_{-0}	2^{+0}_{-1}	2^{+2}_{-0}
$\bar{\rm N}^d$	6.4 ± 1.0	7.4 ± 1.5	4.9 ± 1.0	3.4 ± 0.6	5.9 ± 0.7
ULX Host Galaxies	All	Spiral	Elliptical	Irregular	Complete
$\tilde{d}^a$	$31.3^{+19.4}_{-10.7}$	$31.3^{+15.0}_{-13.9}$	$36.3^{+13.9}_{-13.4}$	$26.9^{+10.6}_{-18.1}$	$16.3^{+4.4}_{-1.7}$
$\tilde{M_{\rm B}}^b$	$-15.4^{+0.6}_{-0.5}$	$-15.4^{+0.6}_{-0.5}$	$-15.8^{+0.5}_{-0.3}$	$-13.5^{+1.0}_{-0.4}$	$-15.0^{+0.6}_{-0.7}$
$\tilde{\rm N}^c$	1 ± 0	1 ± 0	1 ± 0	1^{+1}_{-0}	1^{+1}_{-0}
$\bar{\rm N}^d$	1.95 ± 0.19	2.05 ± 0.13	1.66 ± 0.24	1.86 ± 0.30	1.86 ± 0.12

[a]Median galaxy distance in Mpc, along with the inter-tercile range.
[b]Median absolute magnitude in the *B* system, corrected for Galactic and internal extinction, along with the inter-tercile range.
[c,d]Median/mean number of sources/ULXs located in the host galaxy, along with the inter-tercile range/standard error on the mean.

of ULXs and also that they can be detected at larger distances than lower luminosity X-ray sources. In general though, galaxies containing non-nuclear X-ray sources have a lower average distance than field galaxies because of the limitations of *XMM-Newton's* sensitivity and spatial resolution – at higher distances it is not only hard to detect any but the very brightest sources, but it is also more likely that a non-nuclear X-ray source within a galaxy will be indistinguishable from an AGN due to the positional uncertainty extending over the central 3 arcsecond region that we use to define AGNs, and thus filtered out of our catalogue.

In order to determine how many of the ULX candidates that we identify are new, we matched our sources with the following previous ULX catalogues: Colbert & Ptak (2002), Swartz et al. (2004), Liu & Mirabel (2005), Liu & Bregman (2005), Swartz et al. (2011) and W11. These previous catalogues use data from *ROSAT*, *Chandra* and *XMM-Newton*, and various slightly different methods between them. The largest, W11, contains 470 ULX candidates. We find in our sample 165 new candidate ULXs which do not appear in any of these catalogues, 86 of which are sources new to the 3XMM-DR4 release.

Additionally we find 251 of the sources identified in the W11 catalogue in our own as well. The discrepancy in numbers between our catalogue and W11's is mostly due to two main factors: the first being the changes between the 2XMM and 3XMM pipelines, leading to a large number of the W11 objects either not being significantly detected in 3XMM or their newly-calculated luminosities found to be slightly below the ULX definition, and the second being the removal of certain flagged detections.

While our sample is smaller than the largest previous catalogue (although still large), due to our handling of flags and contaminants we are confident that it is cleaner than previous catalogues and also contains a large number of ULXs that have not yet been considered in most ULX population studies.

2.2.5 A complete subsample

In order to perform statistical studies of the ULX population of our sample of extragalactic X-ray sources, we require a complete subsample – that is, a sample made up of all ULXs within galaxies for which we are confident that all ULXs they possess have been detected. This is to ensure that the ULXs we examine are representative of the population as a whole rather than biased towards the brightest objects. The method we use is presented in detail in W11, so we provide only a brief summary here.

We begin by using the 3XMM sensitivity maps for *XMM-Newton* to find the minimum count rate at a certain position on the detector for each observation, $f_{\rm obs}$, such that a source could be detected with maximum likelihood > 10 across the energy range 0.5–12 keV. At the same position, we calculate the minimum ULX flux in the same band, $f_{\rm ULX}$, emitted by a source with luminosity $L_{\rm X} = 10^{39}\,{\rm erg\,s^{-1}}$ and an average ULX spectral shape which we define as an absorbed PL spectrum with $\langle N_{\rm H}\rangle = 2.4 \times 10^{21}\,{\rm cm^{-2}}$ and $\langle\Gamma\rangle = 2.2$, as determined from Gladstone et al. (2009). We compare $f_{\rm obs}$ and $f_{\rm ULX}$ for each observation of the galaxy across its entire area, excluding chip gaps and the circular region excluded to filter out AGNs, and for each *XMM-Newton* detector. An observation of a galaxy is determined complete if $f_{\rm ULX} > f_{\rm obs}$ for at least one of the detectors and thus we can be confident that all ULXs in the galaxy have been detected at least once and will therefore appear in the catalogue.

This first-pass complete subsample contains 298 detections of 227 ULXs across 435

galaxies, 222 of which contain at least one non-nuclear X-ray source (although the sample is not complete below $L_X \approx 10^{39}\,\mathrm{erg\,s^{-1}}$) and 122 of which host at least one ULX. Complete galaxies are of course at much lower distances than the galaxy list as a whole, with all complete galaxies within 52 Mpc and at a median distance of 15.3 Mpc. We give properties for the complete subsample in Tables 2.1 and 2.2, including the total number of X-ray sources, although we note that there is no guarantee that all sources with luminosities below the ULX regime will have been detected.

2.2.6 Quantifying unknown contamination

While we have taken care to remove known contaminants (see Section 2.2.2), some fraction of the remaining sources will be made up of unknown contaminants, in this case background quasars that have not been identified as such. While these cannot be removed from the sample, we can attempt to quantify the extent of the contamination by estimating the number of background sources we expect to appear in the catalogue. This method is also very similar to that used in W11, so we again briefly summarise it here and direct the reader to W11 for further details.

We took a typical quasar spectrum to be an absorbed PL with $\Gamma = 1.59$ (Piconcelli et al., 2003) and with a column density equal to the Galactic column density in the direction of the host galaxy under consideration. We defined a limiting flux f_{lim} as the highest of the minimum ULX flux f_{ULX} calculated using the quasar spectrum and the minimum detection sensitivity flux f_{obs}, as defined in Section 2.2.5. Using the Moretti et al. (2003) distribution of background sources that should be resolved at a flux sensitivity S, $N(>S)$, we converted the f_{lim} maps to maps of the number of background contaminants expected to be observed for each pixel. The total expected number of contaminants observed is the sum of the background contaminants across the area of each galaxy, again excluding chip gaps and the inner AGN region.

We compared this number with the number of sources in our sample we detected with maximum likelihood > 10 in the hard band (2–12 keV), which was found to be more reliable than a soft band in W11, subtracting background contaminants we already identified and removed (see Section 2.2.2), and calculated a fractional background contamination of 19.8% across the entire sample. Divided into galaxy types, ellipticals suffer a larger

amount of contamination with a fractional contamination of 37.2% compared to 13.2% for spirals, which is due to their greater cumulative area on the sky. These percentages are upper limits (particularly in the case of dusty spiral galaxies) as we do not take absorption intrinsic to the host galaxy into account, which background sources will be subject to.

This contamination estimate was performed before and separately to the removal of detections based upon *XMM-Newton* quality flags (see Section 2.2.3). While further contaminants due to badly constrained fluxes and camera artefacts were removed at that step, we expect that the fractional contamination due to background objects remained similar after the flag cut.

2.2.7 Catalogue limitations

Given the similarities of our method to that of W11, our catalogue shares some of its limitations, including the presence of contamination due to background sources (although we improve on removing contaminants due to artefacts or badly constrained source flux), incompleteness due to the limited number of galaxies observed by *XMM-Newton* and the limited observation depth, and loss of some ULXs near the centre of their host galaxy due to our AGN cut. In addition to this, we also introduce a further radial bias by filtering on *XMM-Newton* quality flags (see Section 2.2.3).

We also note that in a number of cases, the angular resolution of *XMM-Newton* is not sufficient to resolve ULX candidates that are close together in space. In some cases, the source appears in our catalogue as a particularly bright ULX, which can be resolved using *Chandra* into separate sources which may or may not be ULXs themselves (e.g. a luminous ULX in NGC 2276, Sutton et al. 2012). It is also possible that some clusters of unresolved ULXs, or simply ULXs embedded in a bright extended star-forming region, may have been identified as extended sources and thus filtered out of our sample.

Since the publication of 3XMM-DR4 in 2013 there have been a number of subsequent data releases of the 3XMM catalogue, the latest being 3XMM-DR7 in 2017. Each data release brings with it an additional quantity of data, as well as corrections to errors identified in previous versions of the catalogue. In particular, the 3XMM-DR5 data release came with the identification of problems in the 3XMM-DR4 release, including a number of corrupted event lists from mismatched mosaic mode sub-pointings (although no ob-

servations included in our sample were affected by this), and erroneously over-estimated errors in some detection positions, fluxes and hardness ratios (Rosen et al., 2016). This affects the overall derived values of these quantities as they are an error-weighted combination of values from the EPIC-MOS and EPIC-pn cameras. Additionally, erroneously large position errors may cause sources near the centre of galaxies to be incorrectly identified as AGN. Therefore, while 3XMM-DR4 was the most up-to-date catalogue at the beginning of this project, it is no longer the largest and most reliable dataset available today.

Finally, we note that a handful of famous ULXs do not make it into our catalogue, for reasons that mainly relate to the galaxy-matching stage. For example, HLX-1 is absent from our sample because its host galaxy, ESO 243-49, does not appear in the RC3 and CNG galaxy catalogues, and Ho IX X-1 does not appear because no position angle data is available for its host galaxy, meaning that our matching algorithm only matched within the minor axis of the galaxy, which the source lies outside of. Occurrences such as these mean that other ULXs could have been missed due to incompleteness in our galaxy data.

2.3 Catalogue applications: analysis & discussion

A large, clean sample of ULX candidates provides an ideal resource for studying the bulk properties of the ULX population and identifying trends, as well as for picking out unusual objects that warrant further investigation. The *XMM-Newton* source catalogue that forms the basis of our sample contains a large number of science fields populated through its analysis pipeline, including count rates and fluxes in five different energy bands (and combinations thereof) and hardness ratios between these bands. These properties are useful for preliminary characterisation of the ULX population using only products from the *XMM-Newton* pipeline without further time-intensive analysis. In this section, we present an overview of the hardness ratios, luminosity and variability of the ULXs in our sample, and whether these properties show any dependence upon the nature of the host galaxies of these sources.

2.3.1 Properties of the complete subsample

If we examine the entire ULX sample indiscriminately, we become subject to bias as the most luminous sources become overrepresented in the sample due to the flux limitations of the observations. Therefore we created a complete subsample representative of the ULX population as a whole (see Section 2.2.5). In this section we first examine the hardness ratio (HR; i.e. X-ray colour index) and luminosity distributions of this complete subsample of ULXs, for which we can be confident that we have detected all ULXs within their host galaxies and not simply the brightest from each galaxy.

The *XMM-Newton* pipeline records source count rates in five different energy bands: 0.2–0.5, 0.5–1.0, 1.0–2.0, 2.0–4.5 and 4.5–12.0 keV. From these five bands, four HRs are defined by:

$$\mathrm{HRn} = (\mathrm{RATE\_}b - \mathrm{RATE\_}a)/(\mathrm{RATE\_}b + \mathrm{RATE\_}a), \tag{2.3.1}$$

where a and b are adjacent energy bands. Where the count rate of one of the bands is zero, the HR takes an upper or lower limit of 1 or -1 respectively, therefore we only consider HRs where $-1 < \mathrm{HR} < 1$ in our analysis. We also exclude those HRs with error > 0.2, as it causes the object's position on HR plots to be very unconstrained.

We first compare the population of ULXs as a whole with the lower luminosity sources in the sample, as well as the AGNs we filtered out in Section 2.2.2, in a set of HR-HR plots, to determine how the overall spectral shape of ULXs compares with other sources (Fig. 2.9). On the whole, the ULXs have a very similar HR-HR distribution to lower-luminosity X-ray sources, matching the underlying distribution of lower-luminosity sources almost exactly except for the softest with very low HR2 and HR3 values. This further supports findings in Swartz et al. (2004) showing that the general X-ray properties of ULXs are statistically indistinguishable from the lower-luminosity population and the interpretation that the majority of ULXs are the highest luminosity objects within the stellar-mass BH population of their host galaxies.

AGNs, however, have a very obviously different distribution of HRs, tending to have low HR2 values, indicating a steep spectrum at low energies, and are more likely to have high HR3 and HR4 values, indicating a hard high-energy tail. However, ULXs cannot be distinguished from AGNs by HRs alone, with the AGN population overlapping signifi-

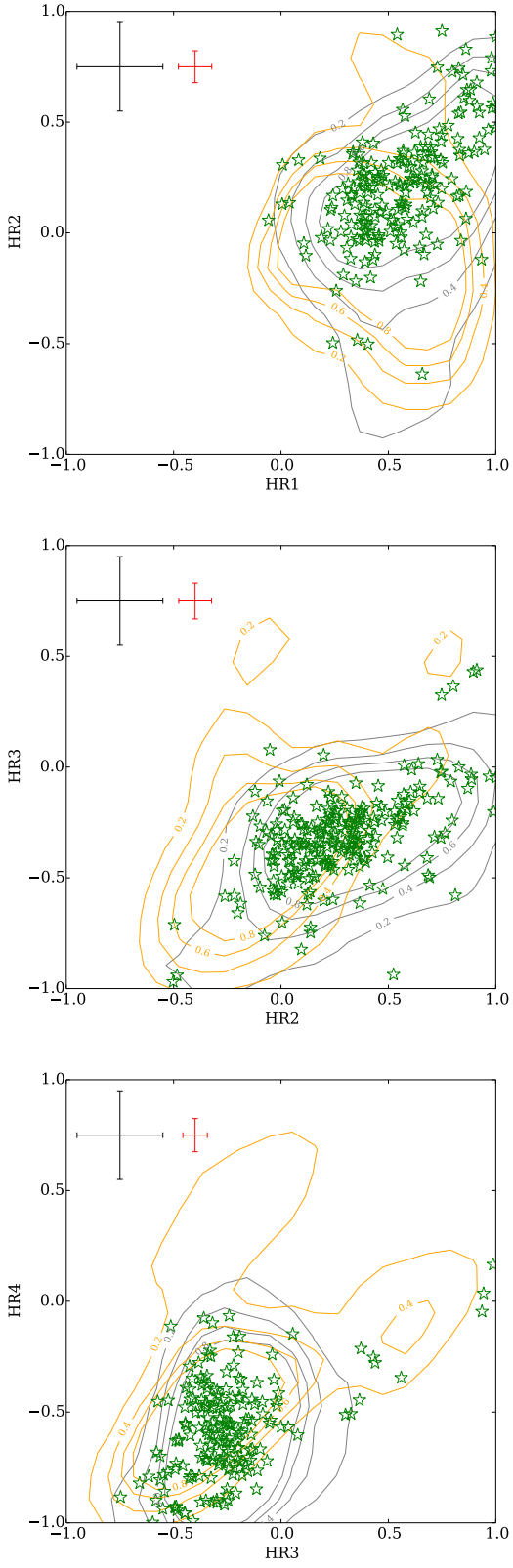

Figure 2.9: Hardness ratio plots for the complete ULX subsample (green stars) compared with the lower luminosity extragalactic X-ray sources (grey contours) and AGNs (yellow contours). Average error bars are shown in red, with the maximum errors (± 0.2) shown in black.

cantly with the majority of the ULX population.

The majority of ULXs lie within a reasonably tight locus with $0 < \mathrm{HR1} < 0.75$, $-0.25 < \mathrm{HR2} < 0.5$, $-0.5 < \mathrm{HR3} < 0$ and $-1 < \mathrm{HR4} < -0.25$. The exception is a small branch of harder sources with primarily high HR1 and HR2 values, with $\mathrm{HR1}, \mathrm{HR2} > 0.5$, although some of these also have unusually high HR3 values.

We further investigate the distribution of ULXs in HR space by dividing the sample into two groups based upon the nature of their host galaxy. ULXs in elliptical galaxies form one group, and ULXs in spiral galaxies form a second. We also place ULXs in irregular galaxies into the spirals group, since the sample size of irregular-hosted ULXs is very low, and we would expect both irregular and spiral galaxies to be primarily star-forming environments. We refer to this group containing ULXs in both spiral and irregular galaxies purely as spiral-hosted for convenience.

When we divide the ULX sample into elliptical- and spiral-hosted sources in this way (Fig. 2.10), we find that the high-HR2 hard tail is made up exclusively of ULXs located in spiral galaxies. Since the number of ULXs in elliptical galaxies is smaller than the number of ULXs in other environments, we need to test whether this is simply due to having a smaller sample size. Therefore we selected ULXs equal to the number of elliptical-hosted ULXs from the spiral ULX population and checked to see if any from that selection had $\mathrm{HR2} > 0.5$. We repeated this 10,000 times and found that the null hypothesis probability of both populations having the same underlying distribution in HR2 was $p = 0.019$. Therefore we are only confident at the $\sim 2.3\sigma$ level that this high-HR2 population is peculiar to the spiral galaxy environment.

A positive value of HR1 is a natural consequence of X-ray absorption below 0.5 keV, so it is unsurprisingly the case for the vast majority of all types of X-ray source. However, a high value of HR2 can result in the case of highly absorbed sources. Of the spiral-hosted sources with $\mathrm{HR2} > 0.5$, a handful are located in galaxies subject to high Galactic absorption with Galactic column density $N_{\mathrm{H}} \gtrsim 10^{21}\ \mathrm{cm}^{-2}$ (such as IC 342 and IC 4596), but many are subject to high local column densities. Winter et al. (2007) found that the hydrogen columns in the direction of most ULXs are consistent with belonging to the host galaxy rather than being intrinsic to the source. Upon visual inspection of the host galaxies of our high-HR2 population, we found that most of the spiral galaxies that host these high-

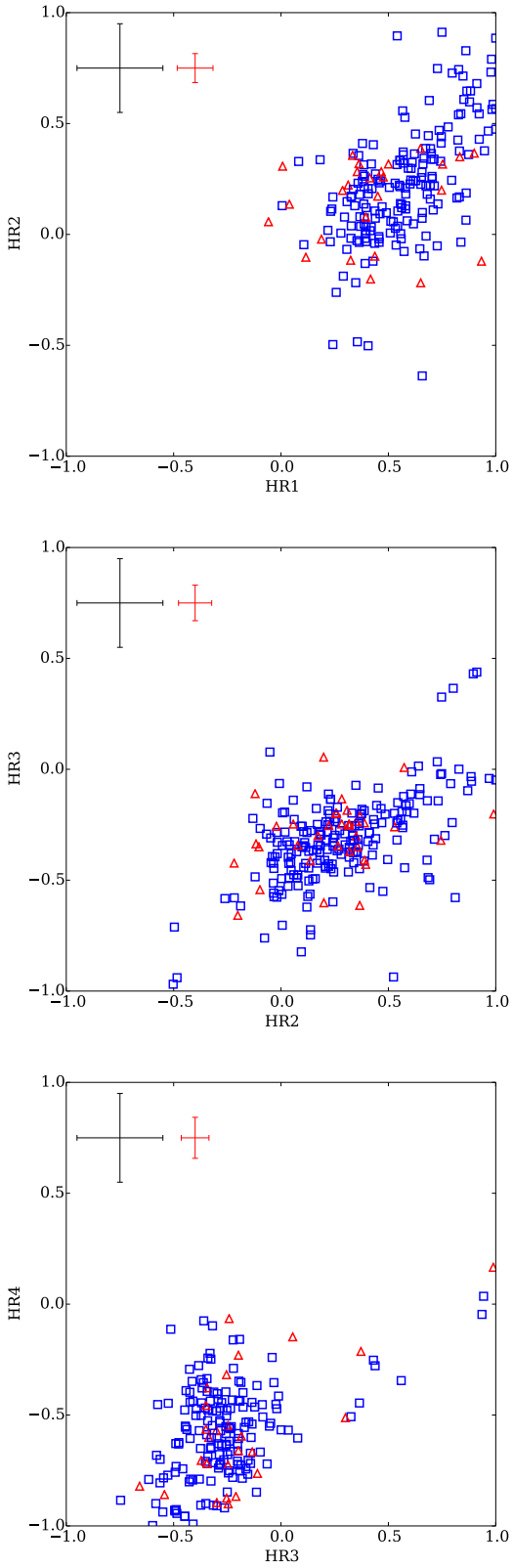

Figure 2.10: Hardness ratio plots for the complete ULX subsample, divided into sources located in elliptical host galaxies (red triangles) and those located in spiral or irregular galaxies (blue squares). Example error bars are as in Fig. 2.9.

HR2 objects are highly inclined or edge-on. Therefore it is likely that this main population difference in colour, while it may be dependent upon the host galaxy morphology, it is unlikely to represent a major difference in the underlying spectral properties of the sources or their immediate surroundings and more likely due to the dust and obscuration within the host galaxy itself.

Pintore et al. (2014) (henceforth P14) also examined X-ray colours to attempt to characterise the variability behaviour of ULXs between observations when fitted with a disc and corona model. They produced a soft X-ray vs. hard X-ray colour plot that appeared to indicate that the ULX population lay in a sequence from a high hard colour and low soft colour to a low hard colour and high soft colour, and could be divided loosely into two groups. The first, hard group was made up of less luminous and more absorbed sources, with the normalisation of the soft component and the parameters of the hard corona component driving the spectral changes. The second contained more luminous and less absorbed sources, with variations in $N_{\rm H}$ and the normalisation of the soft component being more significant than the corona in driving spectral changes. The first group contained sources in the broadened disc and hard ultraluminous accretion regimes as classified by Sutton et al. (2013b), and the second contained sources in the soft ultraluminous regime – it was suggested that X-ray colour, and the soft colour in particular, could be used to distinguish between the two groups in cases of lower-quality data.

In order to test whether this is indeed the case, we make an approximation of the P14 colour-colour plots with our own ULX sample (Fig. 2.11), although the energy bands directly available to us from the 3XMM-DR4 catalogue are not identical to those used in P14, therefore the plots are not precisely comparable. The high-hard/low-soft to high-soft/low-hard ULX sequence seen in P14 is still present in our plots, although there is a greater amount of scatter and a few objects that have similarly high values for both colours. The far left of the plot is populated by the most highly-absorbed ULXs in spirals, as discussed earlier in this section, and bears similarity with the positioning of IC 342 X-1 in P14. However, the overall distribution cannot as easily be divided into two based on the soft colour as in P14. The general trend of where the various super-Eddington accretion regimes appear on the plot may well hold – example sources from Sutton et al. (2013b) marked in Fig. 2.11 fall roughly into the expected regions, with a soft ultralumi-

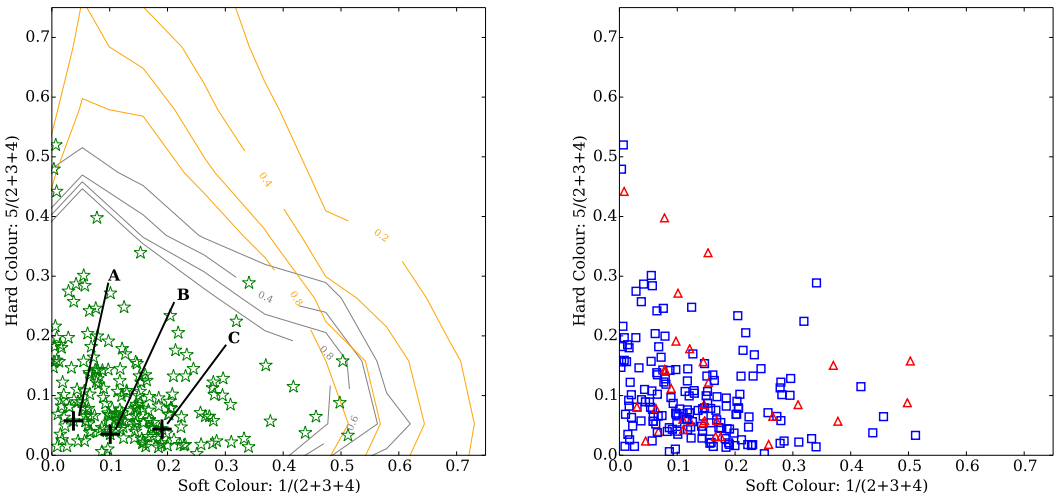

Figure 2.11: Colour-colour plots based on those introduced in Pintore et al. (2014), with the energy bands of *XMM-Newton* numbered from 1 to 5, for the complete ULX subsample compared with lower luminosity extragalactic X-ray sources and with AGN as in Fig. 2.9 (left), and with the ULX sample divided into elliptical and spiral/irregular galaxies as in Fig. 2.10 (right). Three sources from (Sutton et al., 2013b) are marked with black crosses on the left plot. A = NGC 2403 X-1 (detection classified as a broadened disc in Sutton et al. 2013b), B = NGC 6946 X-1 (detection classified as hard ultraluminous), C = NGC 4559 ULX2 (detection classified as soft ultraluminous).

nous source having a higher soft colour than a hard ultraluminous and a broadened disc source – however these different accretion regimes form a spectrum across colour space rather than into easily divisible groups.

We can investigate the host galaxy dependence of ULX properties from a different angle by plotting the HRs against the detection luminosity for the elliptical and spiral populations (Fig. 2.12). The majority of ULX detections have a luminosity below 10^{40} erg s^{-1}. The harder subset found in spiral galaxies have a similar luminosity distribution to the rest of the ULXs, however there is a different subset of ULXs with luminosities greater than 10^{40} erg s^{-1} which are also only seen in spiral galaxies. We perform a similar statistical test to determine whether it is significant that we only see sources of very high luminosity in spiral galaxies, and found a null-hypothesis probability of $p = 0.07$. Therefore we are only confident to $\sim 1.8\sigma$ that the elliptical and spiral ULX populations have different luminosity distributions.

The ULX population in spiral galaxies is, on the whole, more luminous than that in

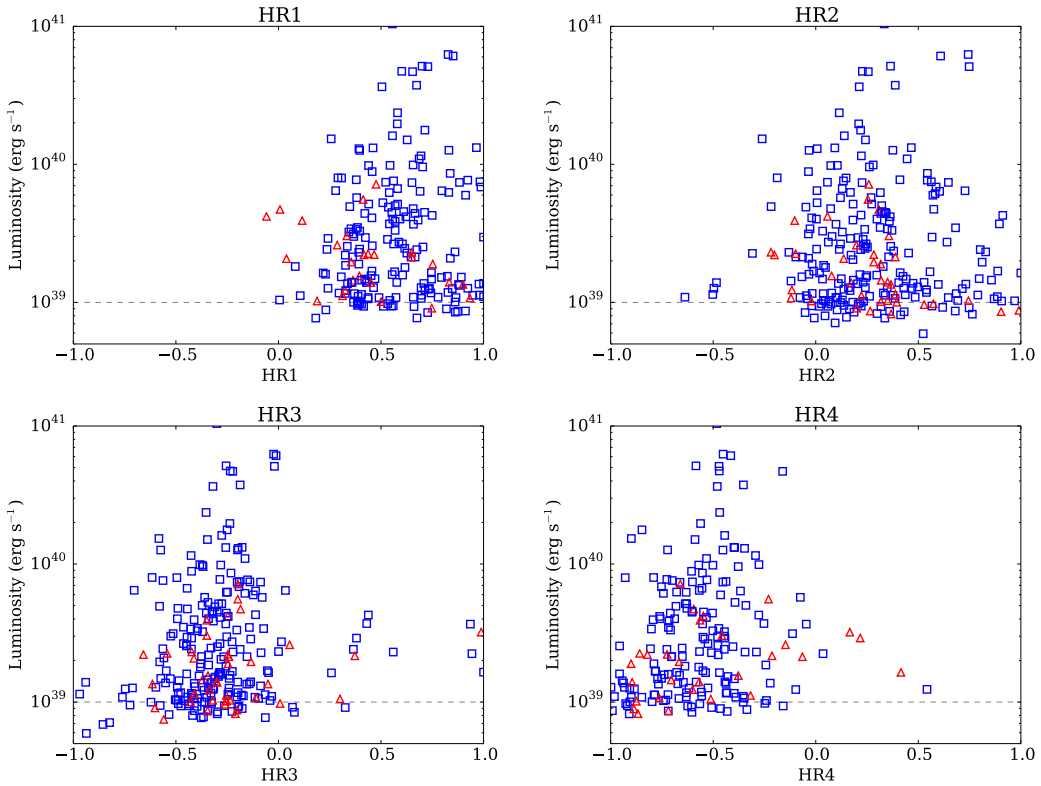

Figure 2.12: The hardness ratios plotted against luminosity for the complete ULX subsample, divided into elliptical and spiral/irregular galaxies as in Fig. 2.10.

elliptical galaxies. Given the lower sample size of elliptical-hosted ULXs, this is not a statistically significant population difference on the basis of our sample alone, however it is consistent with indications in Walton et al. (2011) that the luminosity function for X-ray sources in elliptical galaxies is steeper than that for spiral galaxies.

The ULX groups can be further divided into bins of their Hubble stage T, for which we produce a box plot of the luminosity (Fig. 2.13), both for every detection in the ULX range and for the average luminosity of each individual source. Plotted in this way, we can see that the most luminous ULXs occur in the more loosely wound spirals with $T \geq 4$, and there is very tentative evidence that ULXs in the most diffuse, Magellanic spirals ($T = 8, 9$) and irregular galaxies ($T = 10$–99) are brighter on average than those in tighter spirals, although the sample size is too small to draw any definite conclusions, and the luminosity distributions of ULXs between different spiral classifications are not found to be significantly different using a KS-test.

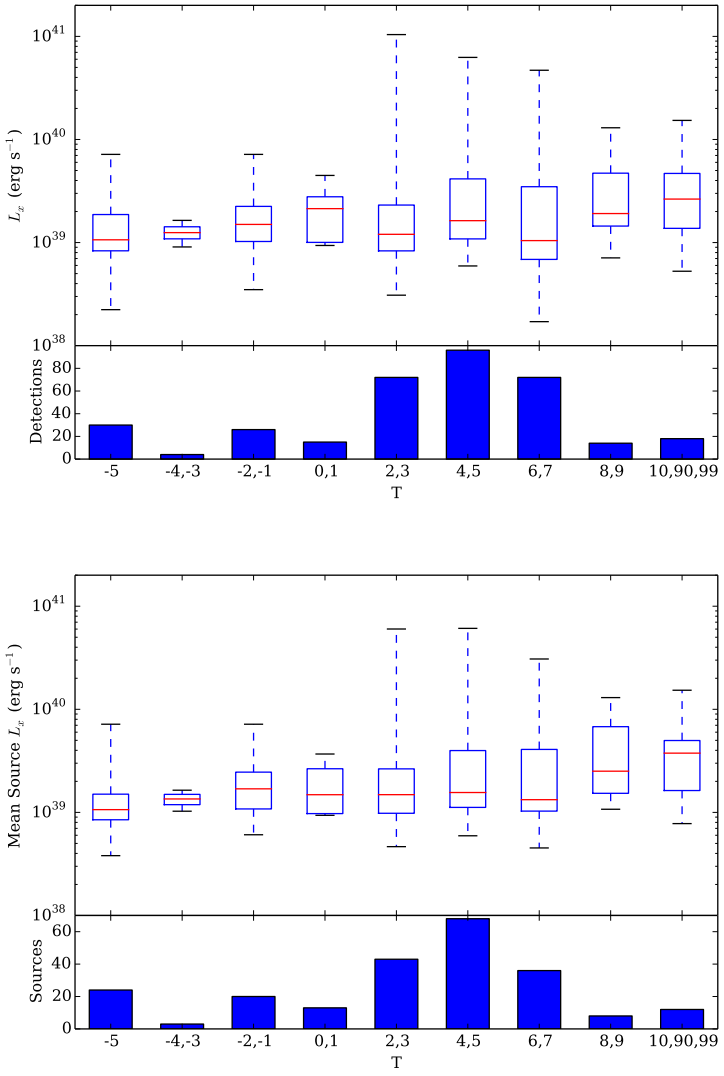

Figure 2.13: Box plots of ULX luminosity for host galaxies with Hubble Stage T, for every detection of a source classed as a ULX in the complete sample (*top*) and for the average luminosity of each individual ULX in the complete sample (*bottom*). Boxes span from the first to the third quartile, with the median marked in red and whiskers extending to the maximum and minimum values. A bar plot beneath each box plot shows the number of detections or sources in each T bin.

2.3.2 The most luminous ULXs

One motivation for constructing samples of ULXs is the search for hyper-luminous X-ray sources (HLXs; $L_{\rm X} > 10^{41}\,{\rm erg\,s^{-1}}$), which are difficult to explain even with super-Eddington accretion onto a moderately-sized black hole, and thus represent the best candidates for IMBHs. The *XMM-Newton* Serendipitous Source Catalogue has previously

been used in dedicated searches for HLXs (e.g. Zolotukhin et al. 2016).

While there are no HLXs in our complete subsample, our wider sample contains 22 sources with at least one detection above $5 \times 10^{40}\,\mathrm{erg\,s^{-1}}$, which we investigated on an individual basis to discover whether any viable new candidates for IMBHs had been identified. We list these sources in Tables 2.3 and 2.4, separated into sources which are either already well-studied or poor candidates for IMBHs, and the sources which are the most likely to be genuine IMBH candidates.

To produce these lists, we first ran these sources past previous studies of highly luminous ULXs to establish which had already been studied and which were potential new IMBH candidates. We also examined the optical data (from SDSS where available, and DSS where not) to determine whether there were optical counterparts to these sources, which may identify further background or foreground contaminants.

Five of these objects, located in NGC 470, NGC 2276, NGC 5907, IC 4320 and NGC 7479 are already well-studied sources, examined by Sutton et al. (2012) as some of the brightest sources in the W11 catalogue. Notable among these sources is NGC 2276 ULX, in fact a blended source of three separate ULXs which can only be resolved using the high spatial resolution of the *Chandra* telescope, one of which remains an IMBH candidate (Mezcua et al., 2015), and NGC 5907 ULX-1, subsequently found to be a NS ULX (Israel et al., 2017a). Another is the ULX in IC 4320, confirmed to be a background AGN at $z \sim 2.8$ by Sutton et al. (2015). HLX-1 is not identified due to its host galaxy not appearing in RC3 or LV (see Section 2.2.7).

Of the remaining high-luminosity sources, nine have optical counterparts when examined with DSS or SDSS data. Four of these, in IC 1623B, IC 2431, ARP 148 and UGC 12127, are likely AGNs of their host galaxies. IC 1623B and ARP 148 are both halves of complex merger systems, for which the NED position of the galaxy is offset from the position of the AGN. IC 2431 is a system of four interacting galaxies, at such a distance that the PSF of the X-ray emission encompasses most of the optical extent of the system, therefore it is likely formed of contributions from the AGNs of several if not all of these galaxies. For UGC 12127, the NED position of the galaxy is slightly offset from the geometric centre of the optical data, potentially due to the presence of bright regions within the galaxy ellipse in addition to the galaxy core.

Table 2.3: The 14 high-luminosity sources within the full (non-complete) version of the catalogue that have previously been discovered or are otherwise poor IMBH candidates.

Name	Host Galaxy	D^a	$C^b_{\mathrm{X,max}}$	$L^c_{\mathrm{X,max}}$
Notes		(Mpc)	(ct s^{-1})	($\times 10^{40}$ erg s^{-1})
3XMM J003937.5+005110	NGC 201	60.5	0.078 ± 0.002	5.9 ± 0.4
Optical counterpart in SDSS, redshift unknown				
3XMM J010746.7−173026*	IC 1623B	81.2	0.128 ± 0.004	41 ± 2
AGN of IC 1623B				
3XMM J011942.7+032422	NGC 470	30.5	0.48 ± 0.01	12.2 ± 0.05
Examined in Sutton et al. (2012)				
3XMM J020937.6+354728	UGC 1651	154.9	0.046 ± 0.007	25 ± 4
Optical counterpart in DSS, redshift unknown				
3XMM J072648.0+854550	NGC 2276	36.8	0.123 ± 0.006	8.0 ± 0.4
3 blended ULXs (Sutton et al., 2012)				
3XMM J080728.0+391135*	NGC 2528	52.4	0.034 ± 0.007	8 ± 2
Background AGN at $z = 0.13$ (Abazajian et al., 2004)				
3XMM J090434.7+143539*	IC 2431 NED02	199.3	0.120 ± 0.006	63 ± 5
AGN(s) of IC 2431				
3XMM J091502.2+294314*	NGC 2789	84.6	0.030 ± 0.003	5 ± 1
Background AGN at $z = 0.32$ (Geller et al., 2014)				
3XMM J110353.9+405100*	ARP 148	138	0.048 ± 0.003	14 ± 1
AGN of ARP 148				
3XMM J113355.4+490348	IC 708	130.0	0.020 ± 0.006	7 ± 3
Optical counterpart in SDSS, redshift unknown				
3XMM J134404.2−271410*	IC 4320	83.5	0.117 ± 0.006	22 ± 2
Background AGN at $z \sim 2.8$ (Sutton et al., 2015)				
3XMM J151558.6+561810	NGC 5907	16.4	0.583 ± 0.007	5.15 ± 0.09
Well-studied (Sutton et al., 2013a; Walton et al., 2015a)				
3XMM J223829.4+351947*	UGC 12127	110.3	0.160 ± 0.003	24.2 ± 0.6
AGN of UGC 12127				
3XMM J230457.6+122028	NGC 7479	32.4	0.248 ± 0.007	6.8 ± 0.3
Examined in Sutton et al. (2012)				

[a]The host galaxy distance in Mpc.
[b]The maximum count rate across all energy bands.
[c]The maximum source luminosity.
*These sources were unambiguously identified as contaminants and thus removed from the final catalogue (see Section 2.2.2).

For two of the other five sources with optical counterparts, in NGC 2528 and NGC 2789, the optical counterparts have redshifts associated with them, confirming them to be background AGNs. Therefore we removed these sources from the sample altogether, as well as the others above confirmed to be AGNs. For the three with optical counterparts but no recorded redshifts (in NGC 201, UGC 1651 and IC 708), we retained them in the sample as it is not in the scope of this study to confirm them as background sources one way or

Table 2.4: The eight high-luminosity sources from the catalogue that are the best new IMBH candidates.

Name	Host Galaxy	D (Mpc)	$C_{\mathrm{X,max}}$ ($\mathrm{ct\,s^{-1}}$)	$L_{\mathrm{X,max}}$ ($\times 10^{40}\,\mathrm{erg\,s^{-1}}$)
3XMM J022748.9+003023	UGC 1934	168.2	0.006 ± 0.001	8 ± 3
3XMM J104414.4+064541	NGC 3356	84.6	0.006 ± 0.001	8 ± 3
3XMM J120438.4+014716	NGC 4077	97.4	0.072 ± 0.005	10 ± 2
3XMM J121117.8+392430	UGC 7188	93.8	0.014 ± 0.005	14 ± 7
3XMM J132727.7−271932	IC 4252	181.5	0.03 ± 0.01	12 ± 7
3XMM J161604.0−223726	IC 4596	103.7	0.021 ± 0.001	10 ± 1
3XMM J223843.9+353223	NGC 7345	124.7	0.028 ± 0.006	9 ± 5
3XMM J233843.6−562849	ESO 192-GI 011	135.7	0.012 ± 0.003	7 ± 3

Columns as in Table 2.3.

another, however we note that, especially in the cases of NGC 201 and UGC 1651, the counterparts look like background galaxies upon visual inspection and are unlikely to be realistic IMBH candidates.

After these considerations, eight high-luminosity sources remain, none of which feature in previous ULX catalogues we have compared our sample to. All are at relatively large distances, with the nearest in NGC 3356, 84.6 Mpc away. All also have low count rates – distance is a factor in this, but also high off-axis angle in some cases such as the source in UGC 1934 – with the highest rate recorded for the source in NGC 4077, $0.072 \pm 0.005\,\mathrm{ct\,s^{-1}}$, requiring ~ 14 ks of good time to observe ~ 1000 counts. Their low count rates does not necessarily put them completely beyond further study, but detailed investigations will require lengthy dedicated observing campaigns. We show the locations of these eight sources on DSS images in Fig. 2.14. Even among these sources, the ULXs in NGC 4077, IC 4252, and IC 4596, while insufficiently close to their galaxy centre to be automatically removed as AGNs in our selection method, are close enough to potentially be offset AGN, especially if the position errors of either the X-ray source or the galaxy have been underestimated, since at the high distances we are considering, the difference of a few arcseconds is a significant fraction of the angular size of the galaxy. Even if they are genuine non-nuclear sources, the PSF of *XMM-Newton* is large enough to overlap with the galaxy centre, so to be confident that the source emission is not contaminated by the presence of an AGN, these three sources would need to be observed with the high spatial resolution capabilities of *Chandra* – currently, only IC 4252 has been covered by

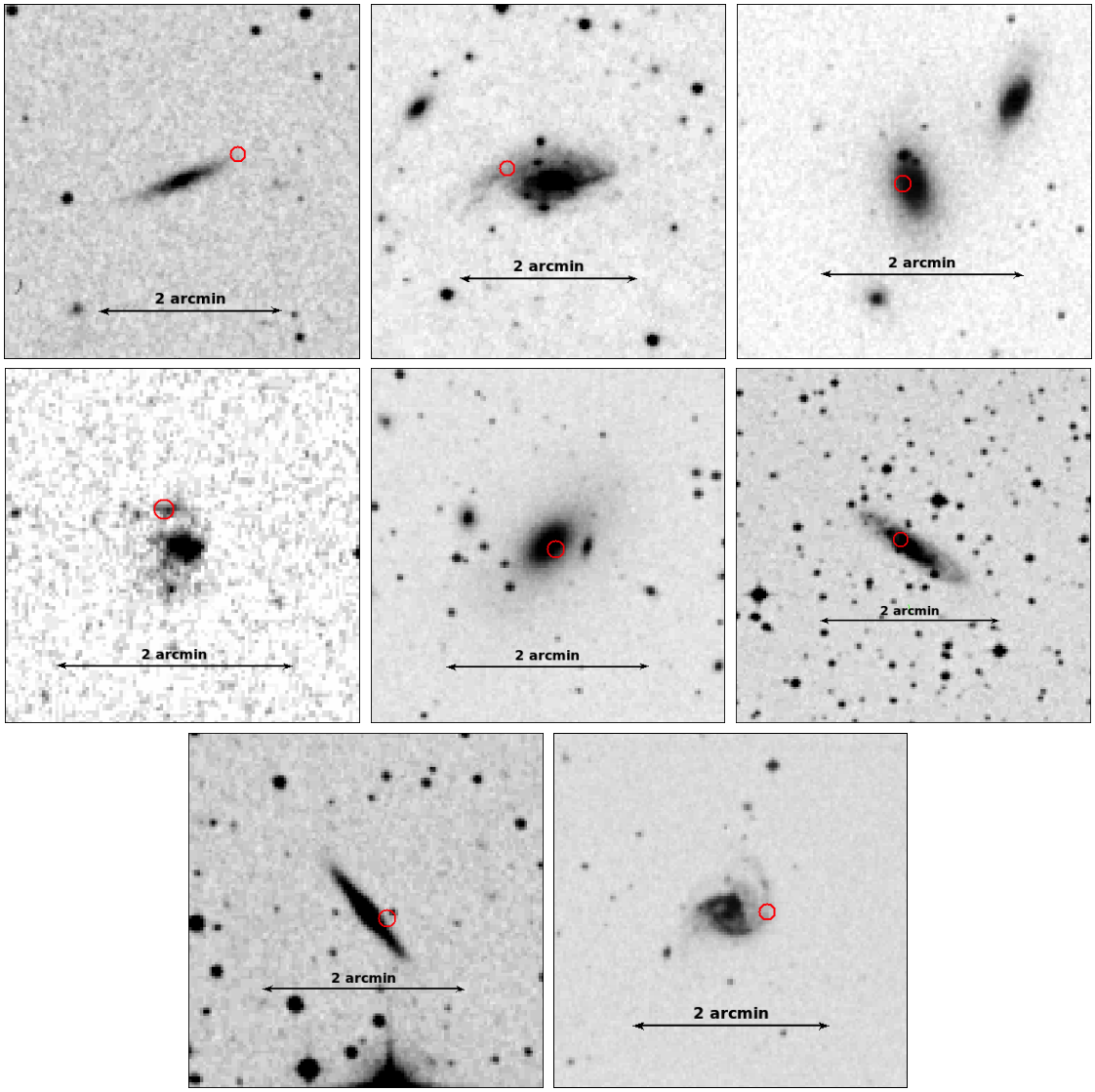

Figure 2.14: The positions of eight potential IMBH candidates (see Table 2.4), marked on DSS images of their host galaxies by a 5 arcsecond red circle. *Top left*, UGC 1934, *centre top*, NGC 3356, *top right*, NGC 4077, *centre left*, UGC 7188, *centre*, IC 4252, *centre right* IC 4596, *bottom left*, NGC 7345, *bottom right*, ESO 192-GI 011.

a *Chandra* observation, which was too short for the source to be detected.

The five remaining candidates which are not close to their host galaxy centre have less than 120 counts observed each. Therefore, while these sources represent our best candidates for possible IMBHs, the collection of a significant amount of additional data is required before we can make any further claims as to their nature.

2.3.3 The Eddington Threshold

At the other end of the luminosity range of ULXs is the Eddington Threshold, the luminosity regime $10^{38} < L_X < 3 \times 10^{39}$ erg s^{-1}. A sample of sources at these luminosities is valuable for a number of different reasons – they provide a potential resource for studying sources accreting at or just below the Eddington limit or possibly transitioning between sub- and super-Eddington accretion, and also house objects related to ULXs such as ultraluminous supersoft sources (ULSs). They also have cosmological significance, as the flat X-ray luminosity function of star-forming galaxies indicates that the bulk of the energy from X-ray emission within star-forming galaxies is emitted in this regime, which potentially makes the feedback from Eddington Threshold sources significant in the formation history of these galaxies. As a population within our catalogue they also have the ideal qualities of being more numerous than ULXs, and still at a comfortable luminosity for *XMM-Newton* to detect in a typical observation, making them the most numerous luminosity group in our sample (see Section 2.2.4).

Our catalogue contains 666 sources with detections at luminosities in the Eddington Threshold regime. Many of these sources are in nearby and well-studied galaxies, so while their fluxes are lower than ULXs at an equivalent distance, it is still possible to obtain good data on individual objects as well as the population as a whole. Four Eddington Threshold objects with particularly good data are examined in Chapter 4 (Earnshaw & Roberts, 2017), and reveal that the softest objects in this luminosity regime are a heterogeneous population that includes the highest-luminosity examples of sub-Eddington accretion as well as ultraluminous supersoft sources and potential intermediate objects between the soft ultraluminous and the ultraluminous supersoft accretion regimes.

Given the generally low flux of these objects, it is difficult to obtain sufficient data for in-depth studies of individual sources for the majority of these objects. Therefore techniques such as spectral stacking, which we are employing in a new study (Roberts et al. in prep), will also prove invaluable in further probing this population of extragalactic X-ray sources.

2.3.4 Variable and transient ULXs

Another potentially interesting subset of our sample are variable ULXs. Under the models of super-Eddington accretion for sources in the ultraluminous regime, it is expected that strong variability is more likely to be found in those sources dominated by soft emission, as hard central emission is thought to be intermittently obscured by a soft, clumpy and fast-moving outflowing wind (e.g. Middleton et al. 2015a).

We can perform a basic search for varying ULXs by finding sources variable enough to trigger being flagged as such (VAR_FLAG = True) in 3XMM-DR4. This occurs when the χ^2 probability of a source having a constant brightness over the course of an observation has a value $p < 10^{-5}$ for at least one exposure in any of the cameras. This measure is conservative but it is easy to select on and provides a small list of highly-variable targets we can follow up on.

We find 12 sources in our sample flagged as variable in 3XMM-DR4 in at least one observation, five of which are ULXs. Two of these ULXs are well-studied and known to be variable, NGC 1313 X-1 (Heil et al., 2009) and NGC 5408 X-1 (Strohmayer et al., 2007). Out of the remaining three, one particularly interesting variable ULX discovered in this way is M51 ULX-7, which not only is highly variable but has a hard spectrum, which goes against the prediction that variable ULXs will have predominantly soft spectra. An in-depth investigation into M51 ULX-7, which we cover in Chapter 3, revealed that it has spectral and timing properties similar to a source accreting in the sub-Eddington low/hard state, and may therefore be a candidate IMBH (Earnshaw et al., 2016).

The existence of multiple *XMM-Newton* observations of the host galaxies of many of the ULXs in our catalogue also allows for the identification of transient objects. This is increasingly relevant as multiple ULXs are being found to actually host pulsars – that is, rotating NSs with strong magnetic fields – rather than BHs. One behaviour expected from pulsars is the so-called 'propeller effect', which occurs if the magnetosphere radius is greater than the corotation radius of the accretion disc, and has the effect of stopping accretion at the magnetosphere radius. This has been put forward as a possible explanation for the extreme range of luminosities exhibited by ULX pulsars discovered to date, in M82 X-2 (Dall'Osso et al., 2015) and NGC 7793 P13 (Fürst et al., 2016). Therefore, transient ULXs showing evidence of accretion switching on or off may be good targets to

investigate in order to search for more ULX pulsars.

We produced a list of transient ULXs by running the ULX source positions through FLIX[4], which produces an estimate of the flux or a flux upper limit in the case of non-detections for every observation of that location by *XMM-Newton*. We defined transient objects as those with at least an order of magnitude's difference between the maximum known flux and the minimum flux or upper limit. Our catalogue contains 33 transient ULXs by this definition, including NGC 5907 ULX-1, recently discovered to be a ULX pulsar (Israel et al., 2017a), so there is plenty of scope for follow-up investigations into transient ULXs as possible pulsar candidates.

2.4 Conclusions

Using an improved version of the method introduced in Walton et al. (2011), we have produced a new, clean catalogue of 1,464 extragalactic non-nuclear X-ray sources from the 3XMM-DR4 data release of the *XMM-Newton* Serendipitous Source Catalogue, of which 372 are ULXs. This is one of the largest ULX samples to date and is a significant improvement to previous ULX catalogues in terms of cleanness. We confirm previous findings that ULXs are more commonly found in spiral or irregular star-forming galaxies than in non-star-forming elliptical galaxies, and that this also applies to lower-luminosity objects.

By studying the HR properties of a complete subsample of the ULX catalogue, we have found that ULXs have very similar colour properties to the extragalactic X-ray binary population as a whole, and have a different (although overlapping) distribution to AGNs, which are generally softer in HR2 and HR3 and extend to higher values of HR4. ULXs in spiral or irregular host galaxies and ULXs in elliptical host galaxies are mostly indistinguishable in HR space except for a subset of spiral-hosted sources that have higher values of HR2 – this can likely be attributed to high amounts of absorption from the host galaxy or Galactic extinction rather than any intrinsic difference between the source populations. Producing a similar colour-colour plot to that introduced in Pintore et al. (2014), we see that while the ULX population cannot be easily divided into distinct groups based

[4]http://www.ledas.ac.uk/flix/flix_dr5.html

on colour, there is tentative evidence that it can still be used to distinguish between the different ultraluminous accretion regimes.

Upon examination of the 22 ULXs in our catalogue with X-ray luminosity $L_{\rm X} > 5 \times 10^{40}\,{\rm erg\,s^{-1}}$, we find four previously-identified extreme-luminosity ULXs, and eight new objects which are our best possible candidates for the discovery of more IMBHs. Our catalogue also possesses other sub-populations of interest, including 666 sources at the Eddington Threshold ($10^{38} < L_{\rm X} < 3 \times 10^{39}\,{\rm erg\,s^{-1}}$) and 33 transient ULXs, making it an ideal resource for exploring the nature of accreting objects within the nearby Universe.

CHAPTER 3

A variable ULX and possible IMBH candidate in M51a

Abstract

ULX-7, in the northern spiral arm of M51, demonstrates unusual behaviour for an ultraluminous X-ray source, with a hard X-ray spectrum but very high short-term variability. This suggests that it is not in a typical ultraluminous state. We analyse the source using archival data from *XMM-Newton*, *Chandra* and *NuSTAR*, and by examining optical and radio data from *HST* and *VLA*. Our X-ray spectral analysis shows that the source has a hard power-law spectral shape with a photon index $\Gamma \sim 1.5$, which persists despite the source's X-ray luminosity varying by over an order of magnitude. The power spectrum of the source features a break at $6.5^{+0.5}_{-1.1} \times 10^{-3}$ Hz, from a low-frequency spectral index of $\alpha_1 = -0.1^{+0.5}_{-0.2}$ to a high-frequency spectral index of $\alpha_2 = 0.65^{+0.05}_{-0.14}$, making it analogous to the low-frequency break found in the power spectra of low/hard state black holes (BHs). We can take a lower frequency limit for a corresponding high-frequency break to calculate a BH mass upper limit of $1.6 \times 10^3\,M_\odot$. Using the X-ray/radio fundamental plane we calculate another upper limit to the BH mass of $3.5 \times 10^4\,M_\odot$ for a BH in the low/hard state. The hard spectrum, high rms variability and mass limits are consistent with ULX-7 being an intermediate-mass BH; however we cannot exclude other interpretations of this source's interesting behaviour, most notably a neutron star with an extreme accretion rate.

3.1 Introduction

While the majority of sources that make up the ULX population are now thought to be stellar-mass BHs with super-Eddington accretion rates (see Section 1.5.3), there are cur-

rently a small number of good candidates for IMBHs. These tend to be objects too luminous to be explained by super-Eddington accretion onto stellar-mass BHs, in particular hyper-luminous sources (HLXs; $L_{\rm X} > 10^{41}\,{\rm erg\,s^{-1}}$; Gao et al. 2003; Farrell et al. 2009; Sutton et al. 2012), or ULXs with powerful radio jets (e.g. Mezcua et al. 2013, 2015). For example, one of the best HLX candidates, HLX-1, has been observed in different spectral states similar to the hard and thermal dominated states seen in stellar-mass BH binaries (Godet et al., 2009; Servillat et al., 2011). This strongly supports the interpretation of HLX-1 as a sub-Eddington accreting source scaled up to higher masses. If further IMBHs do exist, then we might expect that some are accreting at lower rates and have a similar luminosity to stellar-mass ULXs, although distinguishing them from stellar-mass ULXs would be difficult and dependent on the spectral and timing properties of the source.

The interacting galaxy system M51 (NGC 5194/5, also known as the Whirlpool Galaxy) is a pair of galaxies at a distance of 7.85 Mpc[1], containing the face-on spiral galaxy M51a which has high rates of star formation and a large population of X-ray sources, including nine ULXs (Terashima et al., 2006). While looking for highly variable sources in our catalogue of ULXs (Chapter 2), we discovered that one such ULX located in the northern spiral arm of M51a, henceforth referred to as ULX-7, has a hard X-ray spectrum and high levels of variability. Its variability was first investigated by Liu et al. (2002), who found a tentative period of 7620 s. Later studies (e.g Dewangan et al. 2005; Terashima & Wilson 2004; Terashima et al. 2006) found significant long- and short-term variability, although they did not find a period, suggesting that the variability is instead due to aperiodic noise from stochastic processes. The source is near to a young massive star cluster with age $T \sim 12\,{\rm Myr}$ (Abolmasov et al., 2007) and has previously been found to have a changing spectral shape by Yoshida et al. (2010), ranging from fairly flat ($\Gamma < 1.5$) to soft ($\Gamma \sim 2-3$), although any contribution from the host galaxy to the emission was not considered in their study.

While they often demonstrate spectral variability between observations (e.g. Kajava & Poutanen 2009), strong short term variability is not a common feature of ULXs (e.g. Feng & Kaaret 2005; Heil et al. 2009). In the broadened disc/hard ultraluminous/soft

[1]The mean distance given by the NASA/IPAC Extragalactic Database (http://ned.ipac.caltech.edu/).

ultraluminous classification of ULX accretion regimes, high ($> 10\%$) fractional variability is predominantly seen in the soft ultraluminous state in which the X-ray spectrum is dominated by soft thermal emission (Sutton et al., 2013b). Furthermore, the variability is limited to the hard component of emission (Middleton et al., 2015a). A proposed mechanism for this is a soft clumpy wind radiatively driven off an accretion disc during super-Eddington accretion – for more details, see Section 1.5.3. However in the case of ULX-7, the spectrum is hard, which suggests that this source does not fit this model and may be in an accretion state more analogous to the low/hard state of stellar-mass BHs – in which case, this object might instead be a candidate IMBH, albeit emitting at a lower luminosity than other candidate IMBHs we are aware of to date.

Here we conduct our own analysis of ULX-7, examining its X-ray spectral and timing properties, as well as optical and radio data, to attempt to better characterise this fascinating source. In Section 3.2 we detail the reduction of archival data from *XMM-Newton*, *Chandra*, *NuSTAR*, the Hubble Space Telescope (*HST*) and the Very Large Array (*VLA*) telescopes. We present the results of our analysis in Section 3.3, and discuss the possibility of this source being a background AGN, a neutron star or an IMBH in Section 3.4, before presenting our conclusions in Section 3.5.

3.2 Reduction of archival data

In this chapter we investigate this object from a multi-wavelength perspective, using archival data from a range of missions. We assume a source position of 13:30:01.0 +47:13:44 (J2000; Kilgard et al. 2005).

3.2.1 X-ray observations

There were six observations of M51 by the *XMM-Newton* observatory over the course of eight years, between 2003 and 2011. The durations of observations with *XMM-Newton* are limited by visibility due to the position of M51 in the sky and the orbit of the telescope. The longest observation to date is ~ 52 ks. Data reduction was performed using v13.5.0 of the *XMM-Newton* Scientific Analysis System (SAS) and up-to-date calibration files. We used EPPROC and EMPROC to produce calibrated event lists for the pn and MOS

detectors. The event lists were filtered for high-energy background flaring in accordance with the standard *XMM-Newton* SAS threads[2], excluding intervals for which the > 10 keV count rate was $\geq 0.35\,\mathrm{ct\,s^{-1}}$ in the EPIC-MOS data and the 10–12 keV count rate was $\geq 0.4\,\mathrm{ct\,s^{-1}}$ in the EPIC-pn data.

XMM-Newton spectra and light curves were extracted using EVSELECT from 20 arcsecond radius regions around the source, filtering for `pattern` ≤ 12 for the EPIC-MOS camera and `pattern` ≤ 4 for the EPIC-pn camera. Background counts were extracted from an equally-sized region outside of the galaxy on the same chip, at a similar distance from the readout node. Redistribution matrices and auxiliary response files were generated using RMFGEN and ARFGEN respectively, and spectral data were grouped into bins of at least 25 counts, making sure not to oversample *XMM-Newton*'s intrinsic energy resolution by a factor more than three. Corrected lightcurves for EPIC-MOS and EPIC-pn were generated using EPICLCCORR with a bin size of 50 s and added together, using the same start and end times. All six observations have a quality warning flag due to the source being located within bright extended emission, which we characterise in Section 3.2.1.

While *Chandra* does not have the collecting area of *XMM-Newton*, it has not been limited by visibility in the same way, and its orbit allows for far longer observations of M51. There have been eleven *Chandra* observations of M51 taken over the course of twelve years, between 2000 and 2012, the longest being ~ 190 ks (see Table 3.1) during a set of five deep observations in 2012. The *Chandra* data were reduced using V4.7 of the Chandra Interactive Analysis of Observations (CIAO) software package and reprocessed to produce up-to-date event lists.

Chandra spectra and light curves were extracted using the SPECEXTRACT and DMEXTRACT routines respectively from 3 arcsecond radius regions, with the same binning as the *XMM-Newton* data. Since ULX-7 is a point source, we set `weight=no` and `correctpsf=yes`. Background counts were collected from an annulus around the source between 3 and 20 arcseconds. This same annulus was also used to characterise diffuse emission surrounding the object in order to correct the *XMM-Newton* spectra – the background region in this case was taken from an equally-sized region outside of the

[2]See the SAS User Manual at http://xmm.esac.esa.int/sas

galaxy. Between *XMM-Newton* and *Chandra*, we can examine the long-term variability of the source, as well as its short-term properties.

The advent of the *NuSTAR* mission allows us to probe spectral energies of > 10 keV for resolved sources. To date there is one observation of M51 using *NuSTAR*, performed in 2012, in which ULX-7 is detected along with the low-luminosity AGN and one other ULX in the galaxy. We reduced the *NuSTAR* data using the standard pipeline, NUPIPELINE, part of the *NuSTAR* Data Analysis Software (NUSTARDAS, v1.4.1; included in the HEASOFT distribution), with the instrumental calibration files from CALDB V20140414. The unfiltered event files were cleaned with the standard depth correction, significantly reducing the internal high-energy background, and passages through the South Atlantic Anomaly were removed. Source spectra and instrumental responses were produced for each of the two focal plane modules (FPMA/B) using NUPRODUCTS. Source spectra were extracted from a circular region of radius 25 arcseconds in order to avoid contamination from a potential nearby X-ray source, while background was estimated from a much larger region on the same detector as the source, avoiding all the other bright X-ray sources in M51. In order to maximise the good exposure, in addition to the standard (mode 1) data, we also reduced the available mode 6 data; see Walton et al. and Fuerst et al. (in preparation) for a description of *NuSTAR* mode 6. This provides an additional $\sim$15% exposure, resulting in a total on-source time of 19 ks per FPM. Finally, owing to the low signal-to-noise, we combined the data from FPMA and FPMB using ADDASCASPEC. The resulting *NuSTAR* spectrum provides a detection up to $\sim$20–25 keV, and is rebinned to a minimum of 20 counts per bin for our spectral analysis.

A list of all X-ray observations is presented in Table 3.1. We calculate the flux between 0.3–10 keV (3.0–10 keV and 3.0–20 keV for the *NuSTAR* data) using the best-fitting absorbed PL model if there are sufficient counts for a spectral fit. In the cases where there are a small number of data points we use WebPIMMS[3] and the count rate to predict the flux, assuming a photon index of $\Gamma = 1.5$ (the average photon index of the best-fitting models to the data we were able to fit – see Section 3.3.1). In the case of *XMM-Newton* observation X6, it should be noted that the flux is likely dominated by the surrounding diffuse emis-

[3]https://heasarc.gsfc.nasa.gov/cgi-bin/Tools/w3pimms/w3pimms.pl

Table 3.1: Dates, durations and fluxes for X-ray observations of M51 with *XMM-Newton*, *Chandra* and *NuSTAR*.

ID[a]	Observation ID	Instrument	Observation Date	Exposure[b] (ks)	Flux[c] ($\times 10^{-13}$ erg cm^{-2} s^{-1})
			XMM-Newton		
X1	0112840201	MOS1	2003-01-15	20.66	1.9 ± 0.1
		MOS2		20.67	
		pn		19.05	
X2	0212480801	MOS1	2005-07-01	35.04	7.6 ± 0.2
		MOS2		35.77	
		pn		24.94	
X3	0303420101	MOS1	2006-05-20	39.60	5.9 ± 0.1
		MOS2		39.66	
		pn		30.90	
X4	0303420201	MOS1	2006-05-24	29.77	8.5 ± 0.2
		MOS2		29.76	
		pn		23.18	
X5	0677980701	MOS1	2011-06-07	9.80	5.2 ± 0.4
		MOS2		9.51	
		pn		5.13	
X6	0677980801	MOS1	2011-06-11	1.60	1.1 ± 0.1[d]
		MOS2		1.60	
		pn		2.30	
			Chandra		
C1	354	ACIS-S	2000-06-20	15.05	4.5 ± 0.5
C2	1622	ACIS-S	2001-06-23	27.15	0.5 ± 0.1[d]
C3	3932	ACIS-S	2003-08-08	48.61	4.7 ± 0.2
C4	12562	ACIS-S	2011-06-12	9.75	0.8 ± 0.1[d]
C5	12668	ACIS-S	2011-07-03	10.12	4.0 ± 0.6
C6	13812	ACIS-S	2012-09-12	159.54	7.1 ± 0.2
C7	13813	ACIS-S	2012-09-09	181.57	8.6 ± 0.2
C8	13814	ACIS-S	2012-09-22	192.36	5.5 ± 0.1
C9	13815	ACIS-S	2012-09-23	68.07	3.6 ± 0.2
C10	13816	ACIS-S	2012-09-26	74.07	0.8 ± 0.1
C11	15496	ACIS-S	2012-09-19	41.51	6.0 ± 0.3
C12	15553	ACIS-S	2012-10-10	38.07	0.3 ± 0.1[d]
			NuSTAR		
N1	60002038002	FPMA/B	2012-10-29	19	3.8 ± 0.7
					5.6 ± 0.9

[a] A short ID used elsewhere within this paper for clarity.

[b] Sum of the good time intervals after removal of background flaring events.

[c] Deabsorbed flux in the energy range 0.3–10 keV for *XMM-Newton* and *Chandra*, and the ranges 3–10 keV and 3–20 keV for *NuSTAR*. The flux is determined from the best-fitting PL model, excluding contribution from soft diffuse emission in the *XMM-Newton* observations (see Section 3.3.1). The *NuSTAR* fluxes are calculated from the best-fitting PL model ($N_{\rm H} = 1 \times 10^{21}$ cm^{-2}) to the 3–10 keV and 3–20 keV data respectively.

[d] Where there is insufficient data to calculate flux from a best-fitting model, we use WebPIMMS to find the deabsorbed flux, using the detected count rate and a PL model with $N_{\rm H} = 1 \times 10^{21}$ cm^{-2} and $\Gamma = 1.5$.

sion rather than the source itself. The source flux varies between 3.0×10^{-14} erg cm^{-2} s^{-1} and 8.6×10^{-13} erg cm^{-2} s^{-1} in the 0.3–10 keV energy band over the course of all observations (i.e. its luminosity varies between 2.2×10^{38} erg s^{-1} and 5.1×10^{39} erg s^{-1}). This is an unusually high amount of flux variation for a ULX, even if we disregard fluxes calculated using WebPIMMS, in which case we still see variation of over an order of magnitude.

3.2.2 Radio observations

In order to search for core radio emission from the ULX, we retrieved archival *VLA* A-array data at 1.5 GHz (project 11A142, August 2011). The data flagging and calibration was performed following standard procedures with the Common Astronomy Software Applications (CASA) software. The data were calibrated in amplitude using 3C286 as flux calibrator, while delay and phase solutions were derived from the phase calibrator J1327+4326 and interpolated and applied to the target source. The calibrated data were imaged in CASA using the CottonSchwab algorithm and natural weighting. The resulting beam has a size of 1.5 arcseconds $\times$ 1.4 arcseconds oriented at a position angle of 36.9 degrees. No radio emission is detected at the *Chandra* position of the source within a positional error of 1 arcsecond. An upper limit on the 1.5 GHz radio flux density of 87 μJy beam^{-1} is derived from the local rms at the *Chandra* position. The 1.5 GHz radio image is shown in Fig. 3.1. Other studies of the radio emission in M51 have also not detected a counterpart to ULX-7 (Maddox et al., 2007; Rampadarath et al., 2015).

3.2.3 Optical observations

M51 has been well observed by *HST* over the course of the mission's lifetime, and was mapped in 2005 with the ACS/WFC camera as part of the Hubble Heritage project. We collected pre-processed data from the Hubble Legacy Archive, made up of exposures combined using the MULTIDRIZZLE routine. We used images in the F435W (*B*), F555W (*V*) and F814W (*I*) bands to locate possible optical counterparts to ULX-7. The 90% confidence circle for the *Chandra* ACIS-S instrument is 0.6 arcseconds, however it is also necessary to align the relative astrometry of the *HST* and *Chandra* images. We did this by

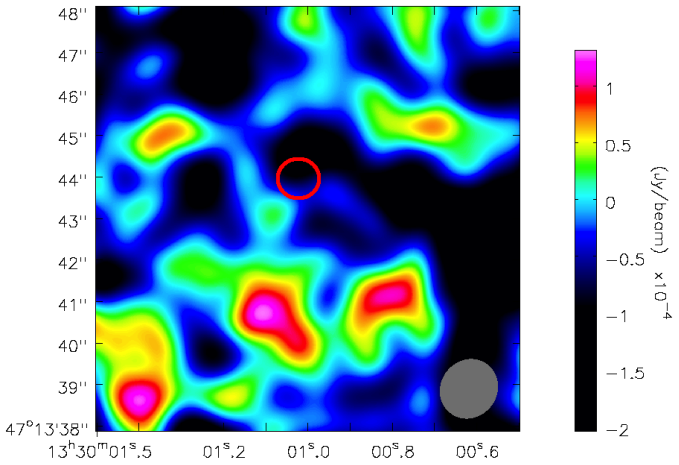

Figure 3.1: The 1.5 GHz radio image surrounding the source location, which is marked with a 1 arcsecond error circle (red) and does not coincide with a radio detection. The rms is 8.73×10^{-5} Jy/beam, therefore the fluctuations shown are all consistent with noise. The beam size is marked in grey.

selecting *2MASS* objects within the M51 field and using the IRAF tools CCFIND, CCMAP and CCSETWCS to find the necessary corrections to the right ascension and declination. We found an offset of 0.1 arcseconds in the right ascension direction and 0.7 arcseconds in declination.

The source is located near to a young star cluster and has a number of possible optical counterparts. We performed photometry on these objects using the DAOPHOT II/ALLSTAR software package (Stetson, 1987), a PSF-fitting routine (see Section 3.3.3), although due to the crowded nature of the field, we were only able to obtain limited constraints on the magnitudes in each band. Where the magnitude of an object was unconstrained, we used the various sources of detector noise to place a lower limit on the magnitude.

3.3 Analysis & results

We analysed the archival data described in Section 3.2 in order to determine the properties of ULX-7. Optical and X-ray images of M51 from the *HST*, *XMM-Newton*, *Chandra* and *NuSTAR* telescopes, along with the location of ULX-7, are shown in Fig. 3.2. The source lies within diffuse X-ray emission in the northern spiral arm of its host galaxy.

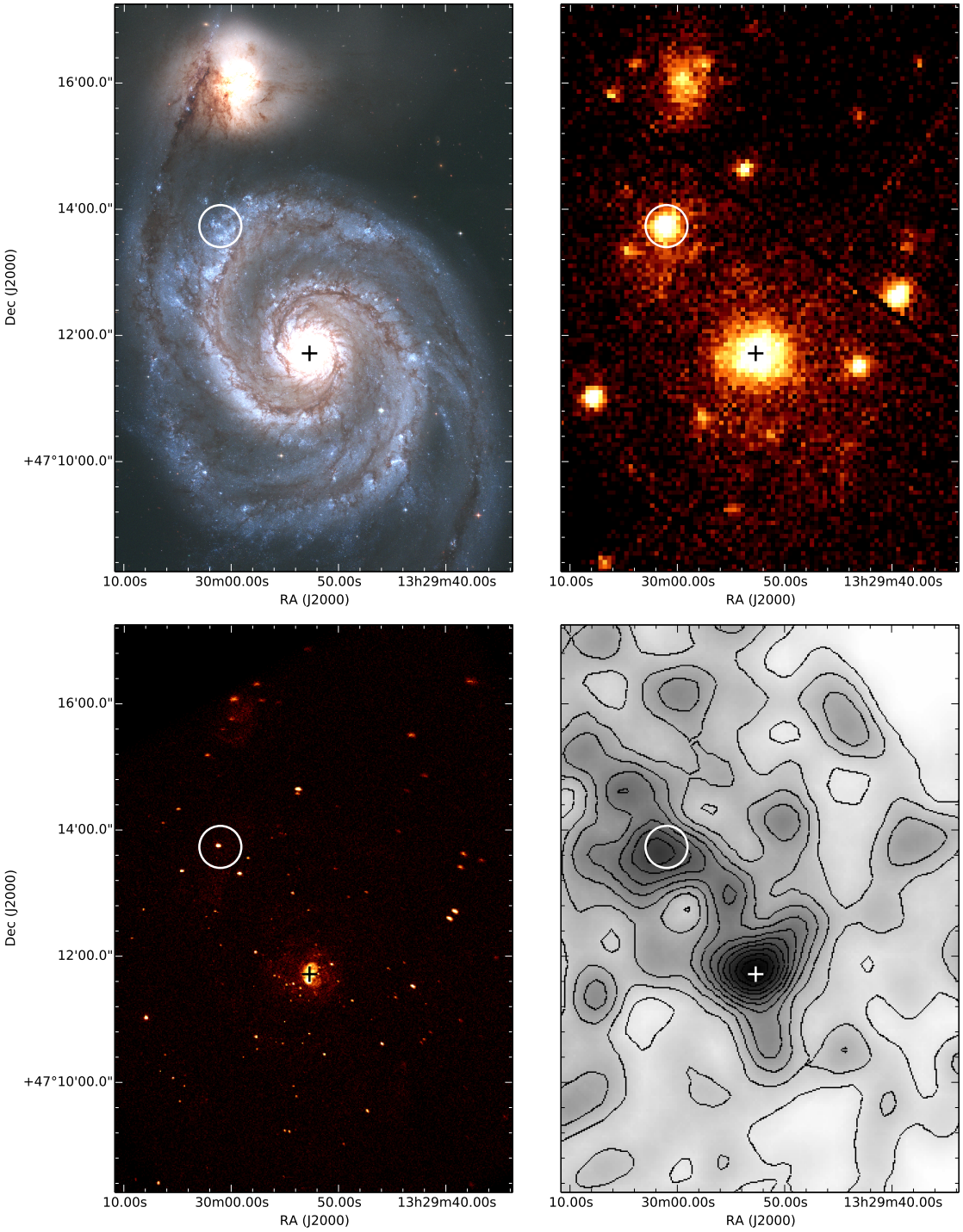

Figure 3.2: Images of the M51 system, centred for convenience on 13:29:52.3 +47:12:45.3 (J2000). In all images, the position of the centre of M51a is marked with a cross, and ULX-7 is indicated by a 20 arcsecond radius white circle. *Top left*, *HST* true-colour image with the red, green and blue channels corresponding to the F814W, F555W and F435W bands respectively. *Top right*, *XMM-Newton* EPIC-pn image in the energy range 0.3–10 keV from observation X4. *Bottom left*, *Chandra* ACIS-S image in the energy range 0.3–10 keV from observation C8. *Bottom right*, *NuSTAR* image in the energy range 3–24 keV, smoothed with a 14 arcsecond Gaussian and with contours to aid visibility only.

Table 3.2: The temperature, flux and χ^2 goodness of fit for the two `mekal` components used to fit the diffuse emission around ULX-7 in the deepest *Chandra* observations.

ID[a]	kT_1 (keV)	F_1 ($\times 10^{-14}$ erg cm^{-2} s^{-1})	kT_2 (keV)	F_2 ($\times 10^{-14}$ erg cm^{-2} s^{-1})	χ^2/dof
C6	$0.25^{+0.08}_{-0.07}$	1.3 ± 0.3	$0.6^{+0.4}_{-0.1}$	1.3 ± 0.3	54.3/60
C7	$0.22^{+0.05}_{-0.04}$	1.5 ± 0.4	$0.7^{+0.2}_{-0.1}$	1.0 ± 0.2	84.2/73
C8	$0.17^{+0.10}_{-0.09}$	1.0 ± 0.3	$0.4^{+0.2}_{-0.1}$	1.4 ± 0.2	76.2/71
C9	< 0.27	2.5 ± 0.4	< 1.0	0.5 ± 0.2	14.1/21
C10	$0.24^{+0.05}_{-0.06}$	2.0 ± 0.4	$0.8^{+0.6}_{-0.2}$	0.5 ± 0.3	34.4/24
All[b]	$0.26^{+0.03}_{-0.05}$	1.9 ± 0.1	0.8 ± 0.2	0.6 ± 0.1	279.9/258

[a]The short observation ID as defined in Table 3.1.
[b]The best-fitting parameters when fitting all five observations simultaneously.

3.3.1 X-ray imaging & spectral analysis

The *XMM-Newton* image of the source and its environment (see Fig. 3.2) shows that it lies within extended diffuse emission. Therefore the *XMM-Newton* source spectra are likely to be contaminated by a soft thermal component. In order to characterise this component, we first examine archival data from the *Chandra* observatory, since its high spatial resolving power allows us to separate out the spectra of the source and of the surrounding gas.

To obtain sufficient counts from the *Chandra* data for analysis, we used only the five observations with exposure time > 50 ks. We extracted diffuse emission spectra from an annulus with an inner radius of 3 arcseconds around the source, and an outer radius of 20 arcseconds to be the same as the *XMM-Newton* footprint used for source analysis. There are no resolved point sources within the annulus. We took a background spectrum from a 20 arcsecond radius region centred to the north of the galaxy in an area with minimal diffuse emission.

All spectral fitting was performed with v12.8.2 of XSPEC (Arnaud, 1996), and all *Chandra* and *XMM-Newton* observations are fitted in the 0.3–10 keV energy range with errors given at 90% confidence intervals. The data is binned (see Section 3.2.1) such that fitting can be performed using χ^2 minimisation, and χ^2 statistics used to determine the goodness-of-fit. The abundance tables of Wilms et al. (2000) are used throughout.

The diffuse emission spectra were well-fitted using two `mekal` thermal plasma com-

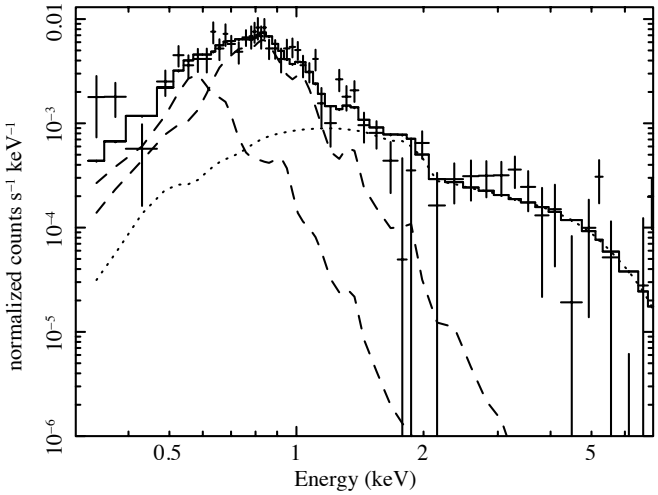

Figure 3.3: The X-ray spectrum of the diffuse emission surrounding ULX-7 from observation C8, together with the best-fitting `mekal+mekal+tbabs*powerlaw` model, with `mekal` parameters as given in Table 3.2. The `mekal` components are plotted with dashed lines and the `tbabs*powerlaw` component with a dotted line. Events are grouped into 20 counts per bin.

ponents: a cooler component at ~ 0.2 keV and a second warmer component at ~ 0.7 keV, consistent with previous studies into the diffuse emission of the galaxy (e.g. Owen & Warwick 2009). We also detected hard emission, requiring an additional hard component in the spectrum since attempting to fit the data without it causes one of the `mekal` components to take on an unrealistically high temperature. This hard component may be due to unresolved hard sources within the annulus, therefore we fitted it with an absorbed PL (`tbabs*powerlaw`), allowing the photon index to vary. We set the hydrogen column density to $N_{\rm H} = 1 \times 10^{21}$ cm^{-2} since preliminary fits to the ULX-7 source spectrum gave $N_{\rm H}$ of approximately this value and we would expect absorption by the surrounding interstellar medium (ISM) to be similar in the near vicinity. The power-law has $\Gamma \sim 1$–2 and would contribute $< 0.1\%$ of the total flux when combined with the source spectrum. For this reason, we expect that its effect on the spectrum of ULX-7 is negligible, so we do not include it in our characterisation of the diffuse emission itself.

The fit results for the diffuse emission are given in Table 3.2. Given that the temperature parameters are all consistent within the errors, and that we do not expect the diffuse emission to vary between observations if it originates in the ISM of M51, we

performed a simultaneous fit of all five observations and used the best-fitting parameters (see Table 3.2) when fitting the *XMM-Newton* source spectra. An example of the diffuse emission spectrum is shown in Fig. 3.3.

While six *XMM-Newton* observations of ULX-7 exist, there is only sufficient data quality for spectral analysis from the first five. We fit the spectra of each of these first five observations with an absorbed power-law model and two additional `mekal` components to account for contamination from the diffuse emission (`mekal+mekal+tbabs*powerlaw`). We set the lower bound of $N_{\rm H}$ for the `tbabs` component to the Galactic foreground value[4] of $N_{\rm H} = 1.8 \times 10^{20}\,{\rm cm}^{-2}$ and fixed the `mekal` parameters and normalisations to the average values determined from the *Chandra* results, which we take as a good first-order approximation to the contribution of diffuse emission to the spectrum. Most of the *XMM-Newton* source spectra are well-fitted by this model and exhibit fairly hard ($\Gamma \sim 1.5$–1.6) PL emission. The exception is observation X3 for which we reject a simple absorbed PL at $> 4\sigma$ significance. The fit for X3 undergoes moderate improvement ($\Delta\chi^2 \sim 17$ for 2 fewer degrees of freedom) by the addition of a MCD component (`mekal+mekal+tbabs*(diskBB+powerlaw)`), although it is still rejected at $\sim 3.5\sigma$ significance. It is unclear from the residuals what a better model might be, so we are unable to find an acceptable fit for the data from this observation. It is possible that ULX-7 exhibits similar soft atomic features to those seen in other ULXs (e.g. Middleton et al. 2015b), however the presence of diffuse emission in the host galaxy complicates more detailed study of the soft end of the spectrum.

We also fit the *Chandra* source observations of sufficient data quality with an absorbed PL model to ensure that they are consistent with the *XMM-Newton* results (we do not include the `mekal` components as we assume that the contribution from surrounding diffuse emission is negligible in the *Chandra* source data). As in the case of *XMM-Newton*, $N_{\rm H}$ is given a lower limit of the Galactic foreground value and allowed to vary, except for observation C10 for which we set $N_{\rm H}$ to 1×10^{21} cm^{-2} (the average value found from fits to other observations) since there is insufficient data to constrain it further. We find that the spectra are consistent with the same hard ($\Gamma \sim 1.5$) PL shape as the *XMM-*

[4]Foreground $N_{\rm H}$ was obtained from the HEASARC $N_{\rm H}$ calculator at http://heasarc.gsfc.nasa.gov/cgi-bin/Tools/w3nh/w3nh.pl, using results from Kalberla et al. (2005).

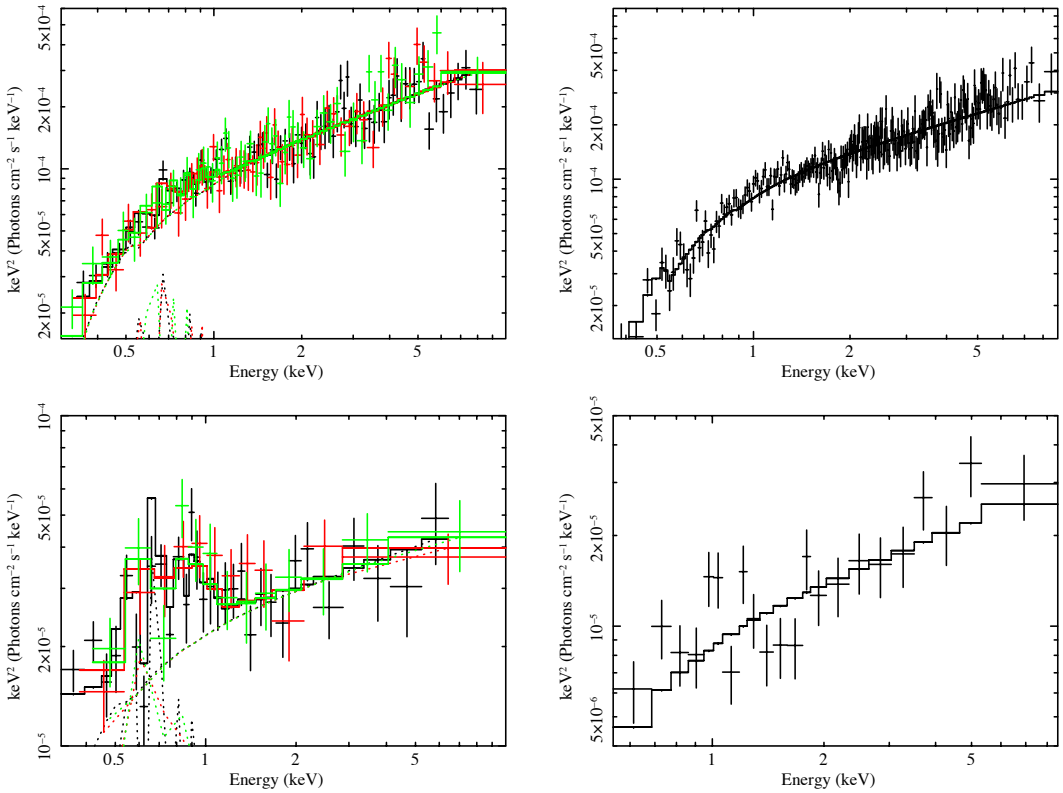

Figure 3.4: Example spectra of ULX-7 from *XMM-Newton* and *Chandra* at high and low fluxes, unfolded from the detector response and plotted between 0.3 and 10 keV, along with the best-fitting absorbed PL model and the contribution from diffuse emission in the case of *XMM-Newton*. Fluxes can be found in Table 3.1, the diffuse emission parameters in Table 3.2, and best-fitting source parameters in Table 3.3. For the *XMM-Newton* spectra, pn data is plotted in black, MOS1 data in red and MOS2 in green. *Top left*, high-flux *XMM-Newton* observation X4. *Top right*, high-flux *Chandra* observation C7. *Bottom left*, low-flux *XMM-Newton* observation X1. Diffuse emission can be seen to be dominant at the soft end of this spectrum (< 1 keV). *Bottom right*, low-flux *Chandra* observation C10.

Newton observations.

Best fit parameter values for *XMM-Newton* and *Chandra* are given in Table 3.3, and examples of high- and low-flux spectra and their power-law fits are shown in Fig. 3.4.

ULX-7 is strongly detected in the 8–24 keV band in the *NuSTAR* observation (Fig. 3.2), with a good signal found up to ~ 20 keV (Fig. 3.5). The data quality is insufficient to perform in-depth analysis, however we are still able to extract a spectrum from a circular region with radius of 25 arcseconds. The *NuSTAR* spectrum is plotted alongside the *XMM-Newton* observation X2 and the *Chandra* observation C6 in Fig. 3.6. These are the obser-

Table 3.3: The parameter values and goodness of fit for the *XMM-Newton* and *Chandra* source spectra when fitted with an absorbed PL model (and a PL with a MCD in the case of X3).

ID[a]	$N_{\rm H}$ ($\times 10^{21}$ cm^{-2})	Γ	$T_{\rm in}$ (keV)	χ^2/dof
		XMM-Newton		
X1	$0.6^{+0.6}_{-0.5}$	1.7 ± 0.2	...	47.9/53
X2	1.1 ± 0.2	1.59 ± 0.06	...	231.2/177
X3	1.1 ± 0.2	$1.57^{+0.07}_{-0.06}$	...	260.5/174
	1.2 ± 0.4	1.2 ± 0.2	0.4 ± 0.1	243.7/172
X4	0.8 ± 0.2	$1.45^{+0.06}_{-0.05}$	...	172.3/182
X5	$0.6^{+0.6}_{-0.5}$	$1.5^{+0.2}_{-0.1}$	...	30.5/39
		Chandra		
C1	$1.5^{+0.9}_{-0.8}$	1.3 ± 0.2	...	26.2/28
C3	1.4 ± 0.4	1.5 ± 0.1	...	67.2/94
C5	$0.4^{+4.0}_{-0.4}$	$1.3^{+0.5}_{-0.3}$	...	13.7/12
C6	1.2 ± 0.2	1.49 ± 0.05	...	244.1/215
C7	1.4 ± 0.2	$1.48^{+0.05}_{-0.04}$	...	273.1/245
C8	$1.6^{+0.3}_{-0.2}$	$1.54^{+0.06}_{-0.05}$	...	203.6/203
C9	$1.2^{+0.6}_{-0.5}$	1.4 ± 0.1	...	65.9/69
C10	1.0[b]	1.5 ± 0.2	...	32.4/20
C11	1.0 ± 0.5	1.5 ± 0.1	...	89.3/94

[a]The short observation ID as defined in Table 3.1.
[b]$N_{\rm H}$ frozen at 1×10^{21} cm^{-2}.

vations closest in flux to the *NuSTAR* observation with the 3–10 keV flux of the best-fitting absorbed PL model being $(3.80 \pm 0.09) \times 10^{-13}$ and $(3.9 \pm 0.2) \times 10^{-13}$ erg cm^{-2} s^{-1} for X2 and C6 respectively. The *NuSTAR* 3–10 keV data has a flux of $(3.8 \pm 0.7) \times 10^{-13}$ erg cm^{-2} s^{-1} when fitted with an absorbed PL model, having $\Gamma = 1.3 \pm 0.7$ (with $N_{\rm H}$ fixed at 1×10^{21} cm^{-2}, the average value found from *XMM-Newton* and *Chandra* observations, since the *NuSTAR* data is too high-energy to constrain it).

The full 3–20 keV *NuSTAR* data demonstrates a softer spectrum when fitted with a power-law model, with $\Gamma = 2.1 \pm 0.3$. This suggests that the spectrum turns over at the higher energies we observe with *NuSTAR*. Therefore we fit the *NuSTAR* data simultaneously with observations X2 and C6, with an absorbed PL model (and a background modelled with `mekal` components for the *XMM-Newton* observation as before). We also fit a model replacing the `powerlaw` component with a `cutoffpl` component to char-

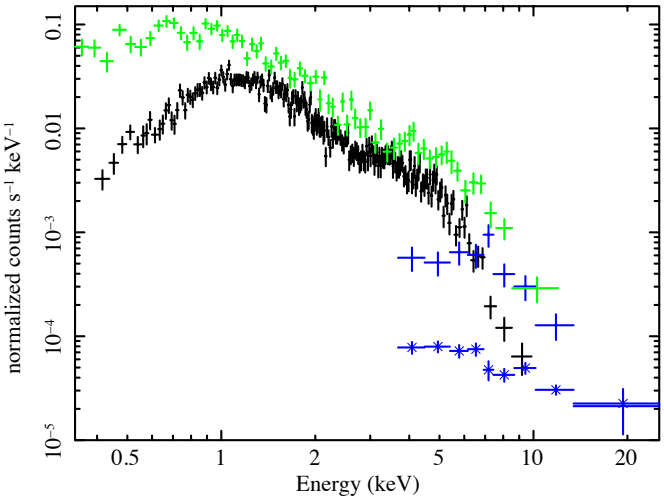

Figure 3.5: The data spectra of the source from *XMM-Newton* observation X2 (green – only EPIC-pn data is shown for clarity), *Chandra* observation C6 (black) and combined FPMA and FPMB data from *NuSTAR* (blue), along with the *NuSTAR* background spectrum (blue crosses). We detect a good signal from *NuSTAR* up to ~ 20 keV.

acterise any potential turnover. In both cases we also included a multiplicative constant to the absorbed PL component of the models, which we allowed to vary freely to account for any difference in normalisation between *NuSTAR* and the other telescope. The fit parameters with *NuSTAR* data included are given in Table 3.4, although it is important to note that neither of these observations are contemporaneous with the *NuSTAR* observation and so we cannot be certain that the source is in the same spectral state between them.

While both observations are consistent with a cut-off to the energy spectrum at 18 keV, we find that a cut-off PL model offers no improvement over a PL model for either observation X2 or C6. This is not entirely unexpected, as the appearance of a turnover is mainly driven by a single *NuSTAR* data point. Further observations with *NuSTAR* simultaneous with observations from *XMM-Newton* are required to better constrain the high-energy spectral shape of this source.

3.3.2 Timing analysis

All observations of ULX-7 with *XMM-Newton* are flagged as variable in the *XMM-Newton* Serendipitous Source Catalogue, and all have fractional rms at $\sim$30-40% according to an initial examination of the light curves using the LCSTATS routine in FTOOLS. Previous

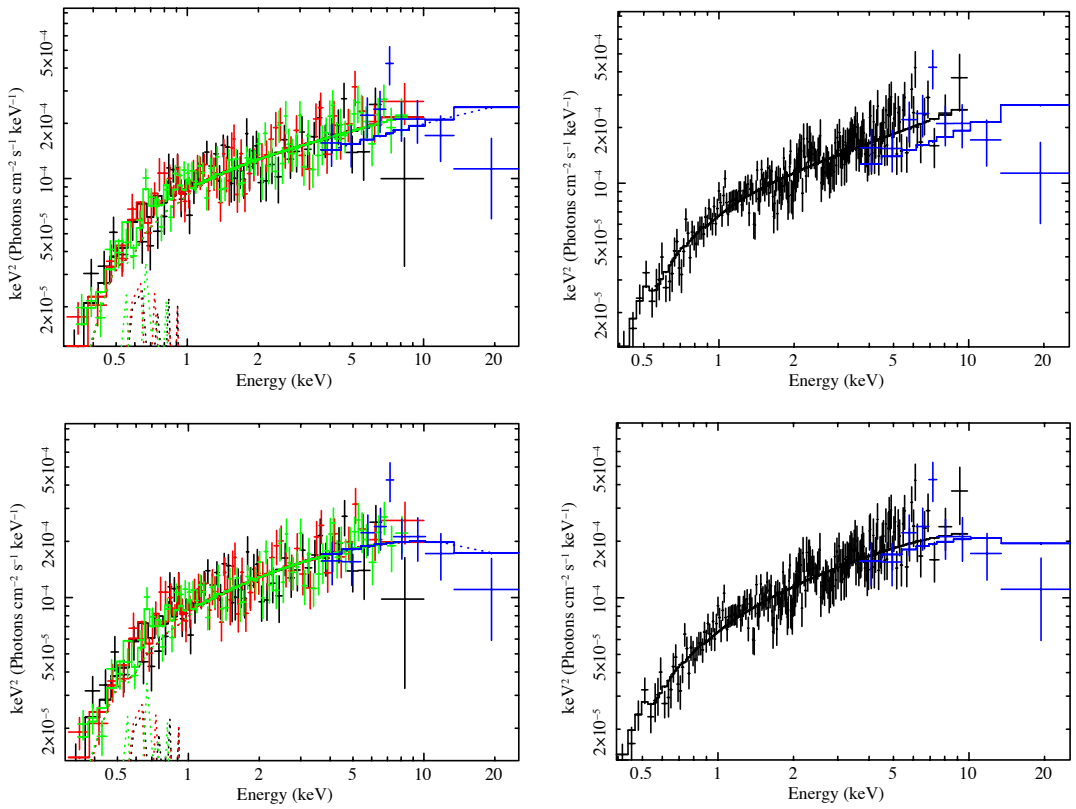

Figure 3.6: Spectra of ULX-7 from *XMM-Newton* observation X2 and *Chandra* observation C6, unfolded from the detector response and plotted between 0.3 and 10 keV, with the combined FPMA and FPMB data from *NuSTAR* plotted between 3 and ∼20 keV (blue). *XMM-Newton* spectra colours are as Fig. 3.4. *Top left*, X2 and *NuSTAR* data, fitted with a `mekal+mekal+tbabs*powerlaw` model. *Top right*, C6 and *NuSTAR* data, fitted with a `tbabs*powerlaw` model. *Bottom left*, X2 and *NuSTAR* data, fitted with a `mekal+mekal+tbabs*cutoffpl` model. *Bottom right*, C6 and *NuSTAR* data, fitted with a `tbabs*cutoffpl` model.

Table 3.4: Parameter values and goodness of fit for the *NuSTAR* spectrum fitted simultaneously with the closest-flux observations X2 and C6, with both a PL (top) and a cut-off PL (bottom) model.

ID	$N_{\rm H}$ ($\times 10^{21}$ cm^{-2})	Γ	$E_{\rm cut}$ (keV)	χ^2/dof
X2	1.4 ± 0.3	1.64 ± 0.06	...	245.0/184
	1.1 ± 0.3	1.5 ± 0.1	18^{+51}_{-8}	239.9/183
C6	1.3 ± 0.2	1.51 ± 0.05	...	264.5/223
	1.1 ± 0.3	1.3 ± 0.1	18^{+43}_{-8}	258.8/222

studies have attempted to find a period in this variability, with Liu et al. (2002) suggesting a period of 7620 s using EFSEARCH and Dewangan et al. (2005) similarly declaring

a period of 5925 s with $\sim 2\sigma$ significance. However, a subsequent study by Terashima et al. (2006) found no evidence of periodic variation, instead suggesting that the source variability is due to stochastic noise.

The source also undergoes significant long-term variation, with the dynamic range of its flux encompassing well over an order of magnitude, even over the course of a single month when observed using *Chandra* in 2012. The long-term lightcurve, along with an example of short-term variability from observation X3, is shown in Fig. 3.7. However, despite this variation in flux there is no evidence for a flux-hardness relation, given the consistent shape of the spectrum found in Section 3.3.1.

We created power spectra for the *XMM-Newton* and *Chandra* observations of ULX-7 by taking the periodogram of fixed-length segments in each observation taken from good time intervals and averaging over all segments for each telescope. We used 3,200 s segments for the *XMM-Newton* observations and 12,800 s segments for the *Chandra* observations. The greater length of the *Chandra* observations allows us to probe down to $\sim 10^{-4}$ Hz, although at higher frequencies the data is dominated by noise, whereas the *XMM-Newton* data, while not having the low-frequency range, has far less contribution from white noise up to $\sim 8 \times 10^{-3}$ Hz. The two datasets are therefore very complementary and allow us access to two decades of frequency space.

The power spectra are normalised so that the power is given in units of the squared fractional rms per frequency interval. We combined all observations for each telescope, given that the overall shape of the power spectrum remained consistent from observation to observation, except for *Chandra* observations C4 and C5, which did not have good time intervals long enough for our chosen segment length, and C12, which contributed a lot of noise to the power spectrum due to a very low count rate.

We first rule out a simple PL shape to the power spectrum by performing a simultaneous fit to the *XMM-Newton* and *Chandra* data using the `whittle` statistic in XSPEC and a `powerlaw` model, disregarding frequency bins consistent with the white noise level of the power spectrum. The best-fitting PL has $\alpha = 0.4$ (for $P(\nu) \propto \nu^{-\alpha}$) which has $\chi^2 = 54.8/28$ and we reject at $> 3\sigma$ significance, so we can be confident that the power spectrum shape requires a more complex model to fit it. We next fit the power spectrum with a broken PL model. This is an excellent fit to the data, with goodness-of-fit

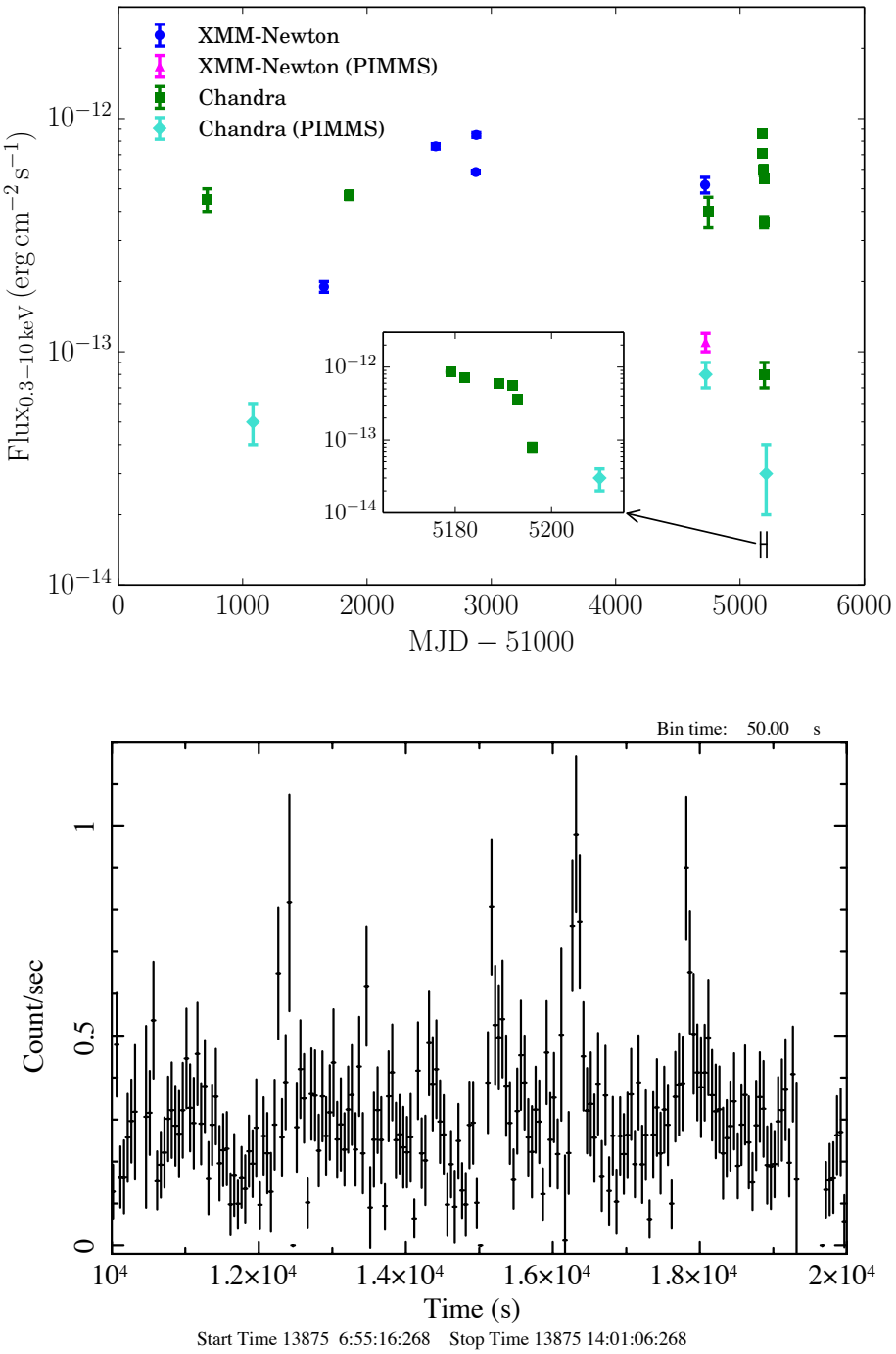

Figure 3.7: *Top*, the long-term lightcurve for ULX-7 showing the 0.3–10 keV flux over time as measured using the *XMM-Newton* and *Chandra* telescopes. Points identified as PIMMS are fluxes calculated from the count rate assuming a PL spectrum with $N_{\mathrm{H}} = 1 \times 10^{21}$ cm^{-2} and $\Gamma = 1.5$. See Table 3.1 for details and values. *Bottom*, a 10 ks segment of the pn + MOS light curve of observation X3, binned into 50 s intervals.

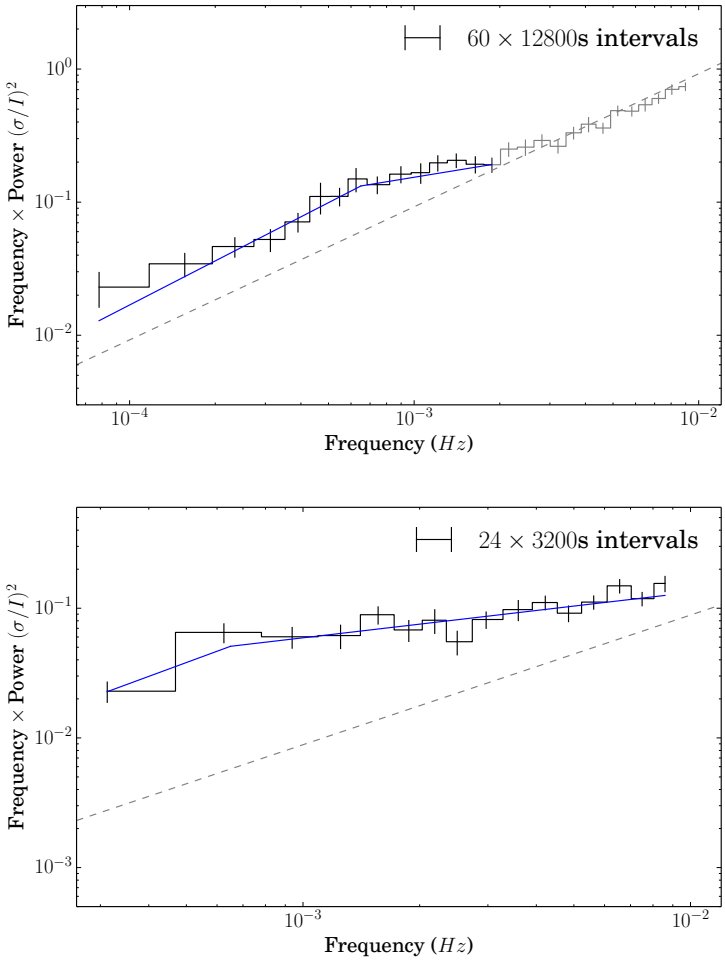

Figure 3.8: The power spectra for *Chandra* (top) and *XMM-Newton* (bottom) observations, along with the best-fitting broken PL model in blue (for which $\nu_b = 6.5 \times 10^{-4}$ Hz, $\alpha_1 = -0.1$ and $\alpha_2 = 0.65$), normalised so that power is in units of the squared fractional rms per frequency interval. The white noise level is marked by the dashed grey line, and the bins discounted from analysis due to being dominated by white noise are also coloured grey. The data is geometrically rebinned with a co-efficient of 1.1, and error bars represent the standard error on the mean for each frequency bin.

$\chi^2 = 23.0/25$, however the fit parameters are not highly constrained. We find that the power spectrum exhibits a break at $\nu_b = 6.5^{+0.5}_{-1.1} \times 10^{-4}$ Hz, with a low-frequency slope of $\alpha_1 = -0.1^{+0.5}_{-0.2}$ and a high-frequency slope of $\alpha_2 = 0.65^{+0.05}_{-0.14}$ (errors were found using a Monte Carlo Markov Chain method with a chain length of 100,000). Since the break is at the overlap of the two power spectra and its frequency can only be constrained with the *Chandra* data, it is likely that future long observations with *XMM-Newton* will help to better characterise the break. The two power spectra are shown in Fig. 3.8.

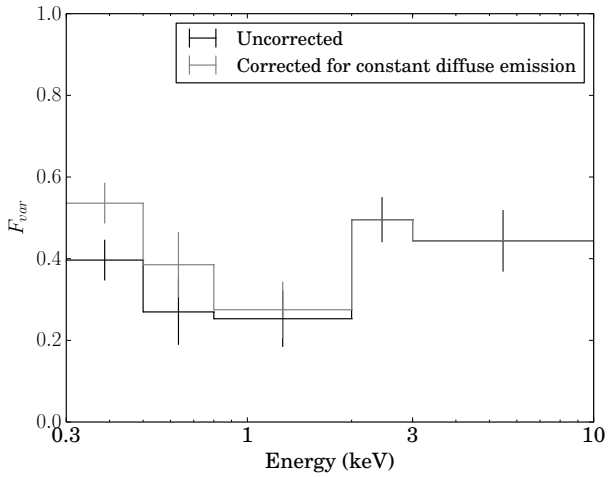

Figure 3.9: The fractional rms spectrum for ULX-7, both uncorrected (black) and corrected to discount the contribution from non-variable diffuse emission (grey). The energy bands are: $0.3-0.5$ keV, $0.5-0.8$ keV, $0.8-2.0$ keV, $2.0-3.0$ keV and $3.0-10.0$ keV. The error bars represent the standard error on the mean across all 19 3200 s segments.

In order to see how the fractional variability of ULX-7 changes as a function of energy, we created a fractional rms spectrum using five energy bands by integrating over the power spectrum for each energy band, averaging over all *XMM-Newton* segments. Since the source flux is contaminated by diffuse emission that we do not expect to be variable, we also correct for the flux contribution from the diffuse emission, giving the intrinsic fractional variability of the source. The source exhibits a high amount of variability across all energy bands, especially at low and high energies, although we find the spectrum to be statistically consistent with constant fractional rms at all energies. The fractional rms spectrum is shown in Fig. 3.9.

We also checked for an rms-flux relation by ordering intervals by flux and grouping them into bins of at least 10 before creating an unnormalised power spectrum for each bin and integrating over a decade in frequency to find the rms. The data was sufficient to confirm that ULX-7 exhibits a positive linear rms-flux relation as expected for an accreting source (Heil et al., 2012), with a significance of $> 10\sigma$ for a positive slope. The rms-flux relations are shown in Fig. 3.10. ULX-7 is the third ULX to date for which a positive linear rms-flux relation has been confirmed (Hernández-García et al., 2015).

Finally, we also examine the data from the *XMM-Newton* EPIC-pn camera, which has a time resolution of 73.4 ms in full-frame mode, for evidence of coherent pulsations such

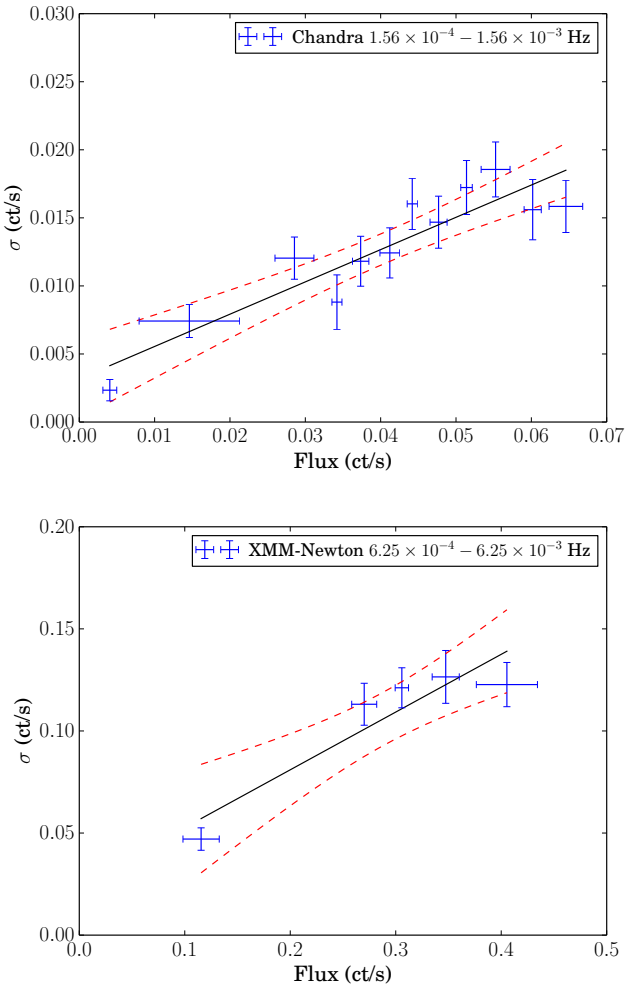

Figure 3.10: The rms-flux relation for *Chandra* (top) and *XMM-Newton* (bottom) observations, along with a line of best fit (black) and 90% confidence intervals (red dashed). The error bars are the standard deviation of the rms and flux.

as those produced by pulsars. To do this we use the H-test (de Jager et al., 1989). In brief, the H-test is a test for a periodic signal that is especially useful in the case where there is no a priori information about the shape of the light curve available. The H statistic is based on the Z^2_m statistic (Buccheri et al., 1983), and defines the optimal number of harmonics, M, such that:

$$H \equiv \max_{1 \leq m \leq 20} \left(Z^2_m + 4m + 4 \right) = Z^2_M + 4M + 4 \geq 0 \tag{3.3.1}$$

We apply the H-test to the five longest *XMM-Newton* observations, examining a range of frequencies from 6.85 Hz (approximately the Nyquist frequency for EPIC-pn data) to

Table 3.5: Periods with $p < 10^{-3}$ found in *XMM-Newton* EPIC-pn data when using the H-test to search for pulsations.

ID[a]	Period (s)	p^b ($\times 10^{-4}$)
X2	0.1833	9.62
X2	0.3003	4.71
X3	0.6211	2.60

[a]The short observation ID as defined in Table 3.1.
[b]The probability of the null hypothesis that there is no periodic signal for this period.

0.1 Hz. We found no evidence of a pulsation period to high significance (that is, the commonly quoted condition of $H > 23$), although we found three marginally significant periods with $H > 17$, equivalent to a probability of $p \lesssim 10^{-3}$ that these H values were produced by chance, which are listed in Table 3.5. It should be noted that a period of 0.3003 s is approximately 4 times the time resolution of the EPIC-pn camera and may therefore be due to an instrumental effect.

3.3.3 Optical counterparts

We mark the *Chandra* position of ULX-7 on a true color *HST* image with a 0.6 arcsecond radius 90% confidence circle in Fig. 3.11. Using DAOPHOT II, we were able to obtain photometric data for 11 objects within the circle, although visual inspection reveals that there are other possible counterparts that are too faint or unresolved to characterise. A list of objects and their locations is given in Table 3.6, and their magnitudes as determined by DAOPHOT II are given in Table 3.7. Given the faint and crowded nature of the field, we do not expect the values we obtain to be better than approximations.

Using the distance modulus for M51, $\mu = 29.45$, we can calculate an absolute magnitude for each object. We plot M_V against the $B-V$ colour in Fig. 3.12. Most of the objects that we are able to characterise have low absolute magnitudes (that is, high luminosities) and $B-V$ colours consistent with OB supergiants (Roberts et al., 2008) – suitable companion stars for a HMXB – for which we would expect values of M_V of between -7 and -4, and $B-V \sim -0.2$ (Wegner, 2006; Roberts et al., 2008). This appears to be consistent with previous findings indicating that ULX optical counterparts are often consistent with

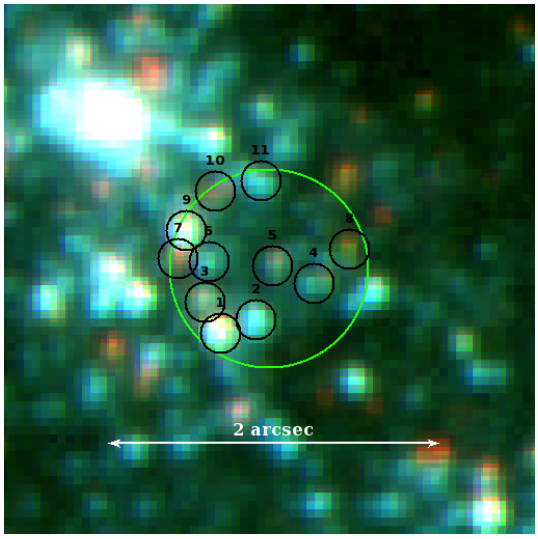

Figure 3.11: *HST* true-colour image around the position of ULX-7, with the red, green and blue channels corresponding to the F435W, F555W and F814W bands respectively. A 0.6 arcsecond radius circle of 90% confidence is shown around the source position 13:30:01.0 +47:13:44. The numbered objects correspond to those listed in Table 3.6.

being OB-type stars (e.g. Gladstone et al. 2013). We might also expect these properties from an X-ray irradiated disc (e.g. Madhusudhan et al. 2008; Tao et al. 2011). The two exceptions are objects 1 and 9, which are significantly brighter and redder than expected for a OB-type star, and too luminous to be red supergiants (for which we would expect $M_V \sim -6$; Heida et al. 2014). Because of this, it is likely that objects 1 and 9 are small, unresolved clusters of multiple stars. This may also be the case for object 2, as it is also unusually bright.

While the colours for the rest of the objects are consistent with OB-type stars, we would also expect background quasars at intermediate redshifts to appear blue, and it would be reasonable to detect them at similar apparent magnitudes to these objects. Therefore we also calculated an X-ray/optical ratio for the objects, using the highest 2–10 keV flux recorded from ULX-7 and calculating the optical flux using the formula $F_{\rm opt} = 8 \times 10^{-6} \cdot 10^{-m_V/2.5}\,{\rm erg\,cm^{-2}\,s^{-1}}$ (e.g. Shtykovskiy & Gilfanov 2005). These ratios are given in Table 3.7. For any potential counterpart within the error circle that is not characterised by DAOPHOT II, including the faint red objects for which we were unable to determine a *B*- or *V*-band magnitude, the optical flux would be lower therefore the ratio would be higher. The same applies to the brightest characterised counterparts,

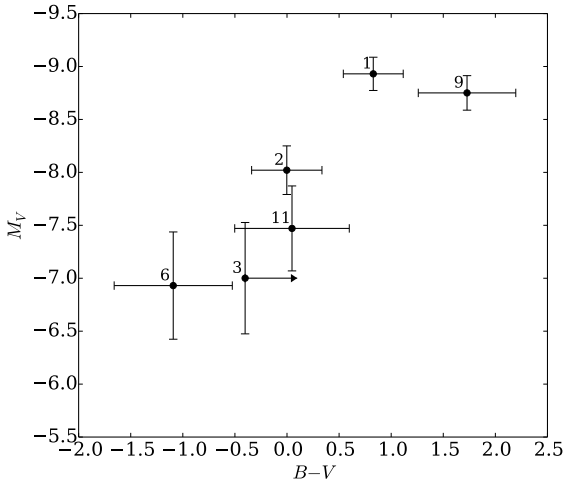

Figure 3.12: $B-V$ colour against the V-band magnitude for 6 of the 11 potential optical counterparts within 0.6 arcseconds of ULX-7, for which we were able to calculate a magnitude for the B- and/or V-band. Numbers correspond to the ID column of Table 3.6. Errors are the estimated standard error from DAOPHOT II results.

Table 3.6: The positions of optical counterparts found within a 0.6 arcsecond error circle of 13:30:01.0 +47:13:44.

ID[a]	R.A. (J2000)	Dec. (J2000)
1	13 30 01.05	47 13 43.62
2	13 30 01.03	47 13 43.70
3	13 30 01.06	47 13 43.80
4	13 30 00.99	47 13 43.91
5	13 30 01.02	47 13 44.03
6	13 30 01.06	47 13 44.04
7	13 30 01.07	47 13 44.07
8	13 30 00.97	47 13 44.12
9	13 30 01.07	47 13 44.23
10	13 30 01.05	47 13 44.47
11	13 30 01.03	47 13 44.52

[a]ID for the purposes of reference within this chapter only.

for although they have the lowest ratios, they are likely to be collections of less luminous objects which will all individually have higher ratios.

Table 3.7: The magnitudes and colours of optical counterparts found within a 0.6 arcsecond error circle of 13:30:01.0 +47:13:44, characterised using DAOPHOT II. IDs correspond to the ID column of Table 3.6.

ID	m_B^a	m_V^a	m_I^a	M_V^b	$B-V^b$	$V-I^b$	F_X/F_{opt}^c
1	22.1 ± 0.2	21.43 ± 0.09	21.04 ± 0.07	-8.9 ± 0.2	0.8 ± 0.3	0.5 ± 0.2	11.7 ± 0.4
2	22.2 ± 0.2	22.3 ± 0.2	22.8 ± 0.3	-8.0 ± 0.2	0.0 ± 0.3	-0.4 ± 0.4	27.0 ± 0.9
3	>22.8	23.4 ± 0.5	22.6 ± 0.3	-7.0 ± 0.5	>-0.4	0.8 ± 0.6	69 ± 2
4	>22.8	>23.5	23.3 ± 0.4	>-6.9	...	>0.3	>76
5	>22.8	>23.5	23.0 ± 0.3	>-6.9	...	>0.6	>76
6	22.2 ± 0.2	23.4 ± 0.5	>23.9	-6.9 ± 0.5	-1.1 ± 0.5	<-0.4	73 ± 3
7	>22.8	>23.5	22.2 ± 0.2	>-6.9	...	>1.3	>76
8	>22.8	>23.5	23.0 ± 0.4	>-6.9	...	>0.5	>76
9	23.2 ± 0.4	21.6 ± 0.1	21.5 ± 0.1	-8.8 ± 0.2	1.7 ± 0.5	0.3 ± 0.3	13.8 ± 0.5
10	>22.8	>23.5	22.7 ± 0.3	>-6.9	...	>0.8	>76
11	22.8 ± 0.3	22.9 ± 0.4	>23.9	-7.5 ± 0.4	0.0 ± 0.5	<-0.9	45 ± 2

[a]Observed magnitude and estimated standard error from DAOPHOT II results, or lower limits where the source was able to be characterised with DAOPHOT II.
[b]Absolute magnitude and colours, corrected for foreground extinction using $E(B-V) = 0.0301 \pm 0.0007$, found using the IRSA online calculator for Galactic dust and reddening (http://irsa.ipac.caltech.edu/applications/DUST). Values used are from Schlafly & Finkbeiner (2011).
[c]X-ray/optical flux ratio based on the highest detected 2–10 keV flux from ULX-7.

3.4 Discussion

The high luminosity of ULX-7 places it firmly into the category of ULXs, albeit at a luminosity that is not particularly remarkable within that class of sources. What makes ULX-7 remarkable is its unusual spectral and timing properties compared with the majority of ULXs. According to the classification of super-Eddington accretion regimes by Sutton et al. (2013b), sources in the hard ultraluminous regime have very low levels of variability if it is present at all, with high variability only featuring in sources in the soft ultraluminous regime. Middleton et al. (2015a) suggests that the observed spectrum and variability of sources in ultraluminous accretion states depend on the inclination and accretion rate of the source, with the main driver of these differences being a radiatively-driven, massive and inhomogeneous wind, that imprints the variability on the hard component of the spectrum if it rises into the line-of-sight.

The energy spectrum of ULX-7 could be argued to be consistent with a hard ultraluminous accretion regime, with the characteristic two-component shape expected in the

spectrum smeared out by insufficient data quality, except for a hint of a soft excess from *XMM-Newton* observation X3 and a putative high energy turnover in the *NuSTAR* data. However, were the source to truly be in this regime, we would not expect the high levels of variability that we observe across all observations. This is furthermore unusual given that variability is high at all observed energies, unlike the observed higher variability above 1 keV in the soft ultraluminous regime. Additionally, the observed luminosity of ULX-7 varies by over an order of magnitude, but we see no evidence of the accretion properties changing. Therefore a soft, clumpy wind is unlikely to be the cause of this variability.

It is possible that our understanding of the hard ultraluminous regime of ULXs is as yet incomplete, and that ULX-7 is an unusually variable specimen of this accretion mode. However, as the data quality is insufficient to prefer a more complex spectral model over a PL, we have examined other interpretations for the nature of this object that have PL-like spectra, in particular considering the scenarios of a background AGN, a super-Eddington NS and an IMBH.

3.4.1 Background AGN

An occasional occurrence in studies of ULXs is the discovery that the object is a background AGN (e.g. Dadina et al. 2013; Sutton et al. 2015), rather than located within the galaxy it appears coincident with. The hard PL spectrum that we observe is not inconsistent with ULX-7 being an AGN (e.g. Reeves & Turner 2000; Mateos et al. 2010), so we need to look to other source properties to confirm its location.

Examining the possible optical counterparts suggests that this source is likely located within the galaxy. The sources that we are able to characterise are consistent either with OB supergiant type stars, or with clusters of cooler stars. While background quasars at intermediate redshifts could be consistent with the $B-V$ colour and magnitude, we find that for the OB-type stars the X-ray/optical ratios are high, with $F_{\rm X}/F_{\rm opt} > 10$ in all cases. We would expect the majority of AGNs to have optical/X-ray flux ratios between 0.1 and 10 (e.g. Krautter et al. 1999; Hornschemeier et al. 2001), so it is unlikely that any of these potential optical counterparts are background AGNs. We are only able to characterise the very brightest potential optical counterparts of ULX-7, given the limitations of the data, but since the X-ray/optical relationship would be even higher for the fainter objects we

cannot characterise, these are even less likely to be a background AGN.

The X-ray/optical relation alone comes with the caveat that we only have one epoch of *HST* data and assume the same optical flux for the highest X-ray flux observation. If the optical emission also varies over time, this conclusion does not necessarily hold. It is also possible that a very highly obscured QSO would have an extreme X-ray/optical flux ratio. However, the proposal that ULX-7 is not a background AGN is also supported by the X-ray timing properties of the source, since there is a high amount of variability on timescales of ~ 100 s. This is shorter than expected for an AGN, for which noise tends to extend only down to timescales of tens of minutes to hours (e.g. González-Martín & Vaughan 2012). Additionally, the low-frequency break feature we see is also not often seen in AGNs – one exception being Ark 564, which has a break at 7.5×10^{-7} Hz in the 2–8.8 keV band (McHardy et al., 2007), a much lower frequency than the one we see for ULX-7.

3.4.2 Neutron star

Given the recent discovery that M82 X-2 is in fact a highly super-Eddington pulsar (Bachetti et al., 2014) and the subsequent discovery of two other NS ULXs (Fürst et al., 2016; Israel et al., 2017a), another possible interpretation for ULX-7's unusual behaviour may be that it is a NS rather than a BH. To this end, we searched for coherent pulsations within the *XMM-Newton* data, but found no strong evidence for any between 6.85 Hz and 0.1 Hz with significance comparable to other studies (that is, with $H > 23$). With that said, the absence of pulsations in an H-test do not necessarily mean that there is no stellar surface – using a similar method, Doroshenko et al. (2015) were unable to detect pulsations from M82 X-2 in the *XMM-Newton* data for the source. It could instead mean that that either the pulsation amplitude was too low to be detected, or the spin-down rate and/or orbital modulation of the signal is significant enough to require an accelerated epoch folding search to detect pulsations.

The NS equivalent to super-Eddington accreting BHs are Z-sources, the most luminous NSs, accreting close to or above their Eddington limit (Hasinger & van der Klis, 1989). They can also exhibit high amounts of variability, although at very low frequencies their power spectra exhibit a steep PL shape with $\alpha \sim$1–2, inconsistent with the power

spectrum of ULX-7, which exhibits a low break and a flatter slope. A comparison with the very luminous extragalactic Z-source LMC X-2 further reveals that its energy spectrum is harder than that of ULX-7 as well (Barnard et al., 2015), so the properties of ULX-7 appear to be inconsistent with what we would expect from Z-sources.

However, the spectral properties of M82 X-2 (Brightman et al., 2015) indicate that it is possible for a highly super-Eddington NS ULX to show similar properties to ULX-7. Examination of the pulsed spectrum in *NuSTAR* shows that the spectrum of M82 X-2 has a high energy turnover at 14^{+5}_{-3} keV (other NS ULXs discovered so far, NGC 5907 and NGC 7793 P13, show spectra with lower-energy curvature more typical of ULXs in general). Further observations using *NuSTAR* would help to confirm whether ULX-7 exhibits a similar spectral shape at high energies.

Additionally, the NS ULXs we know of all have long-term flux variation over about two orders of magnitude, similar to ULX-7. This may indicate that this extreme flux variation is due to a NS entering and leaving the so-called propeller regime, in which accretion is halted and matter is ejected from the system (see Section 1.5.4). It is possible then that ULX-7 shows the characteristics of a NS ULX instead, with its detections at a low flux being due to it entering such a state.

3.4.3 Intermediate mass black hole

Another possible interpretation is that ULX-7 is instead a BH accreting in a hard state analogous to lower luminosity BH binaries (BHBs). This would imply an unusually high BH mass due to its high luminosity, despite a low assumed accretion rate, and would manifest a hard power-law shaped spectrum with high variability across all energy bands (e.g. Grinberg et al. 2014) like we see in ULX-7. The irradiated disc of an IMBH would also be consistent with most of the possible optical counterparts we detect (Madhusudhan et al., 2008).

This interpretation is supported by the presence of a break in the power spectrum from a spectral index of $\alpha \sim 0$ to $\alpha \sim -1$, a feature that we would expect from the low-frequency break in the power spectrum of a source in the hard state, which takes the form of band-limited noise and can be modelled by two Lorentzians or, more simply, a doubly-broken PL (e.g. Done & Gierliński 2005), whose high-frequency break scales with the

BH mass. While we see no evidence of a high-frequency break, we can take the lower limit of such a break to be the white noise level of the *XMM-Newton* power spectrum, at $\nu_b = 9 \times 10^{-3}$ Hz. We can use the relationship between the high-frequency break and BH mass found to apply to BHs of all size scales by McHardy et al. (2006), with the offset for BHs in the hard state from Körding et al. (2007), to calculate an upper limit on the BH mass using the following equation: $\log \nu_b = 0.98 \log \dot{M} - 2.1 \log M_{\rm BH} - 15.38$. We calculate $\dot{M}$ from $L_{\rm bol}/\eta c^2$, assuming an accretion efficiency of $\eta = 0.1$ for the highest-flux observation, and obtain $L_{\rm bol}$ by applying a bolometric correction of 5 to the 2–10 keV luminosity of that observation (Körding et al., 2006). In this way, we find an upper limit of $M_{\rm BH} < 1.6 \times 10^3\,{\rm M}_\odot$, which means that ULX-7 is consistent with being an IMBH.

We would expect an IMBH accreting in the hard state to also exhibit radio emission from a jet. Since there is no radio detection of ULX-7, we can use the calculated flux density upper limit of $87\,\mu{\rm Jy\,beam}^{-1}$ to establish an upper limit on the BH mass independent of that calculated from the timing analysis, using the fundamental plane in BH mass, radio and X-ray luminosity which has been found to apply to BHBs and AGNs as well as intermediate sources (e.g. Mezcua et al. 2015). We use the fundamental plane equation described in Gültekin et al. (2009), which has been calibrated for low mass AGNs in the range 10^5–$10^7\,{\rm M}_\odot$ (Gültekin et al., 2014), and assume a flat radio spectral index of $\alpha = 0.15$ to find $L_{5\,\rm GHz}$. We calculate a mass upper limit of $M_{\rm BH} < 3.5 \times 10^4\,{\rm M}_\odot$, which also allows for an IMBH interpretation.

It is also possible to place a lower limit on the BH mass of an IMBH by taking the maximum observed flux of $8.6 \times 10^{-13}\,{\rm erg\,cm^{-2}\,s^{-1}}$ and assuming a maximum accretion rate for the low/hard state, given that ULX-7 is a persistent source. The maximum luminosity of a low/hard state tends to be $\sim$2% of Eddington[5], with the highest Eddington ratios observed being $\sim$5% (Maccarone, 2003). Therefore we use an Eddington ratio of 5% to place a lower limit on the BH mass of $M_{\rm BH} > 1.0 \times 10^3\,{\rm M}_\odot$, which is consistent with our previously calculated upper limits and places the source firmly within the IMBH regime.

[5]It is possible for transient BHs in the hard state to reach up to 100% of Eddington before a transition to the soft thermal state (Dunn et al., 2010), however given that we see no evidence of state transitions for ULX-7, we calculate the lower limit using a more typical value for persistent hard states.

We can compare our results for ULX-7 with HLX-1, currently the best candidate for an IMBH due to its extreme luminosity and evidence of state transitions. When first discovered, it had a spectrum consistent with an absorbed PL (Farrell et al., 2009), albeit a softer one than we see in ULX-7. Further studies have revealed it to have a very high dynamic range, as we see for ULX-7, although its spectrum changes shape and it appears to demonstrate state transitions (Godet et al., 2009) whereas ULX-7 appears to remain in a single state. In its third *XMM-Newton* observation, HLX-1 appeared to enter a hard state, with a lower luminosity and a spectral index of $\Gamma = 1.6 \pm 0.4$ when compensating for the host galaxy's contribution to the soft emission and fitted alongside an accretion disc (Servillat et al., 2011). No significant intrinsic variability was detected, although since the power was not well constrained, a high fractional variability was not ruled out. Additionally, there have also been radio detections of HLX-1 while in this state (Cseh et al., 2015), making it analogous to the hard state seen in stellar-mass BHBs.

From this, we can conclude that it is reasonable to suggest that ULX-7 could also be an IMBH in a hard state, its large mass being the cause of its high luminosities, although unlike HLX-1, it does not appear to undergo state transitions as it changes luminosity.

The association of ULX-7 with a young stellar population implies that it is a short-lived source if it was formed there (Roberts, 2007), and in this respect it bears similarity to the wider ULX population which is found predominantly in star-forming regions. This would be a point in favour of a more standard stellar remnant ULX interpretation. However, there are possible formation scenarios for an IMBH in a young stellar environment. For example, an IMBH could have formed through runaway mergers within a dense stellar cluster and subsequently been ejected, or the cluster dissipated into the disc of the galaxy, leaving the IMBH accreting within a dense molecular cloud (e.g. Miller & Hamilton 2002) or retaining a young stellar population around itself (e.g. Farrell et al. 2012). This is an unlikely formation scenario for the ULX population as a whole (King, 2004), but still a possibility for an individual object, as a very rare occurrence.

Another possibility is a minor merger of a dwarf galaxy with the main galaxy, a mechanism that has been suggested for HLX-1 (Farrell et al., 2012; Mapelli et al., 2012) and NGC 2276-3c (Mezcua et al., 2015). A recent minor merger could be identified by evidence of disruption in the spiral arm around the source and increased levels of star for-

mation, however these are seen in the northern spiral of M51 anyway due to M51a's interaction with M51b. Therefore any evidence for a minor merger that could have formed ULX-7 would likely be eclipsed by the disruption of the current interaction.

3.5 Conclusions

We have undertaken a case study of M51 ULX-7, a source with moderate luminosity and very high variability for a ULX, and a consistently hard spectrum. This is in contrast to expected ULX variability behaviour, in which we might expect to see high variability in sources with soft spectra. We find that the source is generally well-fitted by a PL with a spectral photon index that remains steady at $\Gamma \sim 1.5$ while the source luminosity varies by over an order of magnitude over the course of 12 years. ULX-7 also demonstrates very high fractional variability between 0.3 and 10.0 keV, with a broken PL shape to its power spectrum analogous to the low-frequency break in the power spectrum of an X-ray binary accreting in the hard state. We find solid evidence for a positive linear rms-flux relation, making ULX-7 the third ULX for which this feature is confirmed. We find no evidence of coherent pulsations, however.

Taken together, these properties are unusual for a ULX, and are suggestive of an alternative explanation to the broadened disc or ultraluminous regimes that describe the majority of ULXs for which we have reasonable data (Gladstone et al., 2009; Sutton et al., 2013b). By examining the possible optical counterparts in *HST* data, we consider it unlikely that this source is a background AGN. No significant pulsations are detected, although its spectrum may possibly bear similarities to that of the NS ULX M82 X-2 and it demonstrates high flux variability that is also seen in the NS ULXs known to date. Therefore it is possible that ULX-7 is another instance of a highly super-Eddington NS, although there is not yet solid evidence for this being the case.

Our results are consistent with ULX-7 being an IMBH accreting in the hard state. Using the absence of a high-frequency break and a radio detection, we can calculate upper limits on the BH mass of $M_{\rm BH} < 1.55 \times 10^3\,{\rm M}_\odot$ and $M_{\rm BH} < 3.5 \times 10^4\,{\rm M}_\odot$ respectively, and by taking the maximum accretion rate to be 5% of the Eddington limit, we can calculate a lower mass limit of $M_{\rm BH} > 1.0 \times 10^3\,{\rm M}_\odot$. All of these limits show the source to

be consistent with an IMBH interpretation if we assume it is accreting in the hard state. There remains weak evidence of a possible high energy turnover in the spectrum when considering the *NuSTAR* data on this source, which would imply that this source may be exhibiting some permutation of the ultraluminous state after all, but simultaneous deep observations with *XMM-Newton* and *NuSTAR* will be required to confirm or rule out the existence of these features.

CHAPTER 4

Soft extragalactic X-ray binaries at the Eddington Threshold

Abstract

The luminosity range at and just below the 10^{39} erg s^{-1} cut-off for defining ultraluminous X-ray sources (ULXs) is a little-explored regime. It none-the-less hosts a large number of X-ray sources, and has great potential for improving our understanding of sources with $\sim$Eddington accretion rates. We select a sample of four sources in this Eddington Threshold regime with good data for further study; these objects possess a variety of soft spectral shapes. We perform X-ray spectral and timing analysis on the *XMM-Newton* and *Chandra* data for these objects to gain insight into their accretion mechanisms, and also examine their optical counterparts using *HST* images. NGC 300 X-1 is a highly luminous and well-known example of the canonical steep power-law accretion state. M51 ULS exhibits a cool blackbody-like spectrum and is consistent with being an ultraluminous supersoft source (ULS), possibly a super-Eddington accreting object viewed at a high inclination through an optically thick outflowing wind. NGC 4395 ULX-1 and NGC 6946 ULX-1 have unusually steep power-law tails, for which we discuss a variety of possible physical mechanisms and links to similar features in Galactic microquasars, and we conclude that these sources are likely intermediate objects between the soft ultraluminous regime of ULXs and classic ULSs.

4.1 Introduction

Our understanding of super-Eddington accretion has developed profoundly with the study of ULXs, the majority of which can be explained either as stellar-mass BHs accreting at

rates above the Eddington limit (e.g. Gladstone et al. 2009) or as highly super-Eddington NSs (e.g. Bachetti et al. 2014; Fürst et al. 2016; Israel et al. 2017a). A number of different X-ray spectral shapes and timing properties observed in ULXs can be unified with a model in which a clumpy, optically thick wind is driven off a geometrically thick, supercritical accretion disc, obscuring the hard central source at high accretion rates and/or high inclinations to the line of sight, and reprocessing its emission (Poutanen et al., 2007; Sutton et al., 2013b; Middleton et al., 2015a). This model can also extend to ULSs, whose near complete lack of hard emission may be due to observing the source at relatively high inclinations or through an optically thick photosphere formed by the wind that completely envelops the source when the accretion rate is at its highest (e.g. Urquhart & Soria 2016a; Feng et al. 2016). For more details, see Section 1.5.3.

The highest luminosity ULXs are natural sources of interest as potential candidates for IMBHs and also simply because their luminosity allows for easier collection of sufficient data for in-depth analysis of nearer objects. However, there are a large number of sources in nearby galaxies at low ULX luminosities, or just below the ULX regime, that are less well-studied and a largely untapped resource for furthering our understanding of the lower-luminosity manifestations of super-Eddington accretion, as well as transitions from sub-Eddington to super-Eddington accretion regimes. We refer to this luminosity regime as the Eddington Threshold, encompassing objects with X-ray luminosity in the range $10^{38} < L_{\rm X} < 3 \times 10^{39}\,{\rm erg\,s^{-1}}$.

The main roadblock to the study of such objects is the relatively low amount of data we can collect using current missions, due to the generally low fluxes of these objects. Therefore for this study we select the best datasets available of this population at the Eddington Threshold as a proof of concept study for the science that could be achieved with next-generation missions such as *Athena*, whose larger collection area and higher sensitivity will make this class of objects far more accessible to investigation.

In Section 4.2 we detail how we selected our sample and summarise previous literature on these objects. We describe the data reduction process and analysis techniques in Section 4.3, and describe the results of X-ray spectral and timing analysis as well as optical counterpart photometry in Section 4.4. We discuss the implications of our results and draw comparisons between our sources and other known accretion regimes in Section 4.5,

Table 4.1: The properties of the soft Eddington Threshold sources and their host galaxies.

Name	R.A. & Dec. (J2000)	d^a (Mpc)	N_H^b ($\times 10^{20}$ cm^{-2})	$E(B-V)^c$
NGC 300 X-1	00 55 10.0 −37 42 12	1.83	4.04	0.0111
NGC 4395 ULX-1	12 26 01.5 +33 31 31	3.98	1.86	0.0150
M51 ULS	13 29 43.3 +47 11 35	8.55	1.82	0.0309
NGC 6946 ULX-1	20 35 00.3 +60 09 07	6.28	18.4	0.2944

[a]The distance to the host galaxy, found by averaging the entries in the NED Redshift-Independent Distances database obtained from Cepheid standard candles for NGC 300 and NGC 4395, and from the tip of the red giant branch for M51 and NGC 6946.
[b]The Galactic absorption column in the direction of this source, obtained by using HEASARC's N_H tool (https://heasarc.gsfc.nasa.gov/cgi-bin/Tools/w3nh/w3nh.pl; Kalberla et al. 2005).
[c]The Galactic extinction in the direction of the source, obtained by using the NASA/IPAC Infrared Science Archive's DUST tool (http://irsa.ipac.caltech.edu/applications/DUST/; Schlafly & Finkbeiner 2011).

and present our conclusions in Section 4.6.

4.2 Sample selection

From our catalogue of extragalactic non-nuclear X-ray sources, the creation of which is described in Chapter 2, we selected objects with peak luminosities at the Eddington Threshold ($10^{38} < L_X < 3 \times 10^{39}$ erg s^{-1}) according to the fluxes given in 3XMM-DR4, but with sufficient data for reasonably in-depth analysis. We defined this to be at least four *XMM-Newton* observations of the source, with multiple of these observations having counts in the thousands. We filtered this further to sources with variability of factor ~ 2, to increase the chance of finding changes in accretion behaviour that could further increase the scientific value of the investigation.

These selection criteria leave us with four objects, all with soft spectra. We acknowledge this as an obvious selection bias, since extragalactic sources in the luminosity range we specify are only likely to have large numbers of counts available if they are dominated by soft emission due to the instrumental response. We summarise what is currently known about these sources below. A list of the sources and their host galaxy properties is provided in Table 4.1.

Table 4.2: The *XMM-Newton* and *Chandra* observations for the sample of Eddington Threshold sources.

ID[a]	Observation ID	Instrument	Date	Exposure[b] (ks)	Off-axis Angle (arcmin)
			NGC 300 X-1		
X1	0112800101	MOS1/MOS2/pn	2001-01-01	43.78/43.79/39.95	2.28
X2	0112800201	MOS1/MOS2/pn	2000-12-26	33.63/33.64/29.95	2.23
X3	0305860301	MOS1/MOS2/pn	2005-11-25	36.49/36.47/34.85	2.27
X4	0305860401	MOS1/MOS2/pn	2005-05-22	34.62/34.93/29.69	3.93
X5	0656780401	MOS1/MOS2/pn	2010-05-28	16.21/16.32/12.16	1.30
C1	9883	ACIS-S	2008-07-08	10.20	3.49
C2	12238	ACIS-I	2010-09-24	63.83	4.85
C3	16028	ACIS-I	2014-05-16	65.09	3.93
C4	16029	ACIS-I	2014-11-17	62.08	2.96
			NGC 4395 ULX-1		
X1	0112521901	MOS1/MOS2/pn	2002-05-31	15.08/15.10/10.08	3.07
X2	0112522701	MOS1/MOS2/pn	2003-01-03	8.18/8.19/6.57	2.26
X3	0142830101	MOS1/MOS2/pn	2003-11-30	103.65/104.06/98.16	1.89
X4	0200340101	MOS1/MOS2/pn	2004-06-02	75.88/76.69/68.43	13.24
C1	5014	ACIS-I	2004-08-07	33.14	12.4
			M51 ULS		
X1	0112840201	MOS1/MOS2/pn	2003-01-15	20.66/20.67/19.05	1.65
X2	0212480801	MOS1/MOS2/pn	2005-07-01	35.04/35.77/24.94	1.18
X3	0303420101	MOS1/MOS2/pn	2006-05-20	39.60/39.66/30.90	0.66
X4	0303420201	MOS1/MOS2/pn	2006-05-24	29.77/29.76/23.18	2.82
C1	3932	ACIS-S	2003-08-07	48.61	2.52
C2	13812	ACIS-S	2012-09-12	159.54	3.32
C3	13813	ACIS-S	2012-09-09	181.57	3.32
C4	13814	ACIS-S	2012-09-20	192.36	3.56
C5	13815	ACIS-S	2012-09-23	68.07	3.64
			NGC 6946 ULX-1		
X1	0200670101	MOS1/MOS2/pn	2004-06-09	12.30/12.40/8.30	1.10
X2	0500730101	MOS1/MOS2/pn	2007-11-08	27.85/28.28/20.21	0.89
X3	0500730201	MOS1/MOS2/pn	2007-11-02	32.47/32.48/29.72	0.90
X4	0691570101	MOS1/MOS2/pn	2012-10-21	110.52/112.21/98.23	1.23
C1	1043	ACIS-S	2001-09-07	59.03	3.30
C2	4404	ACIS-S	2002-11-25	30.33	1.00
C3	4631	ACIS-S	2004-10-22	30.12	2.83
C4	4632	ACIS-S	2004-11-06	28.33	2.93
C5	4633	ACIS-S	2004-12-03	26.96	3.04

[a]A short source-specific observation ID, used for the remainder of this paper. An X prefix stands for an *XMM-Newton* observation, and a C prefix stands for a *Chandra* observation.
[b]Sum of the good time intervals after removal of background flaring events. *XMM-Newton* values given as MOS1/MOS2/pn.

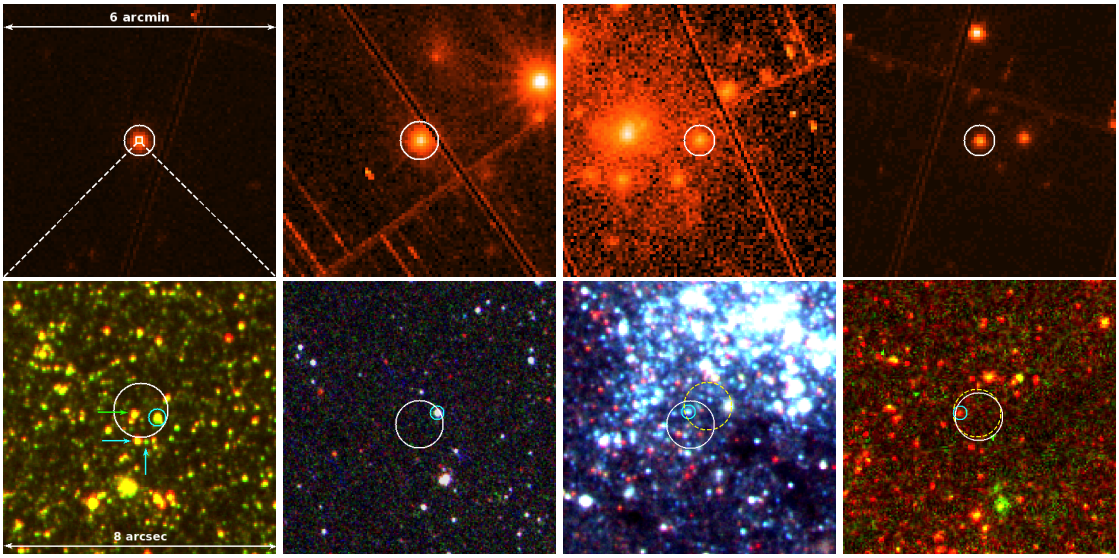

Figure 4.1: The *XMM-Newton* EPIC-pn images (top) and astrometrically corrected *HST* images (bottom) for our sample of sources. The *XMM-Newton* boxes are 6×6 arcminutes in size and the *HST* boxes are 8×8 arcseconds, so fit well within the source positions in the top images. Source locations are as given in Table 4.1. *Far left*, NGC 300 X-1 is marked with a 25 arcsecond white circle on *XMM-Newton* observation X1. The source position is marked with a 0.8 arcsecond white error circle on the *HST* image, with the *F*814W band shown in red and the *F*606W band shown in green. The WR candidate is marked with a cyan circle. We indicate the other two possible counterpart candidates identified by Binder et al. (2015) with cyan arrows, and one further bright star and possible candidate within our error circle with a green arrow. *Centre left*, NGC 4395 ULX-1 is marked with a 25 arcsecond white circle on *XMM-Newton* observation X3. The AGN in this galaxy can be seen towards the top right of the image. The source position is marked with a 0.7 arcsecond white error circle on the UV *HST* image, with the *F*438W band shown in red, the *F*336W band in green and the *F*275W band in blue. The one counterpart we see, the same as identified in Vinokurov et al. (2016), is marked with a cyan circle. *Centre right*, M51 ULS is marked with a 20 arcsecond white circle on *XMM-Newton* observation X2. The LLAGN can be seen on the left. The source position is marked with a 0.7 arcsecond white error circle and an alternate 0.7 arcsecond dashed yellow error circle on the *HST* image, with the *F*814W band shown in red, the *F*555W band in green and the *F*435W band in blue. We indicate the counterpart identified in Terashima et al. (2006) with a cyan circle. *Far right*, NGC 6946 ULX-1 is marked with a 20 arcsecond white circle on *XMM-Newton* observation X3. The AGN in this galaxy can be seen to the right and X-1 (Pinto et al., 2016) to the top. The source position is marked with a 0.7 arcsecond white error circle and an alternate 0.7 arcsecond dashed yellow error circle on the *HST* image, with the *F*814W band shown in red and the *F*658N band in green. A single possible counterpart is marked with a cyan circle.

4.2.1 NGC 300 X-1

Of our sample, 2XMM J005510.0-374212 (henceforth NGC 300 X-1, from Carpano et al. 2007) is by some margin the best-studied object. It is a well-known Wolf-Rayet/BH binary within the eastern spiral arm of its host galaxy. The radial velocity obtained from optical spectroscopic observations has been used to place limits on the mass function of the system, and derive a BH mass of $20 \pm 4\,\mathrm{M}_{\odot}$ (Crowther et al., 2010). Its high mass and low distance, coupled with the fact that it has most frequently been observed in the very luminous steep power-law state (e.g. Carpano et al. 2007, Binder et al. 2011), makes it unsurprising that it has the luminosity and data quality sufficient to appear in our sample.

NGC 300 X-1 has been observed five times with *XMM-Newton*, for a total observing time of approximately 170 ks. It has also been observed five times with *Chandra* for a total of over 220 ks and, recently, with the Hubble Space Telescope (*HST*) Advanced Camera for Surveys (ACS) in the *F*606W and *F*814W bands. While it has previously been assumed that the Wolf-Rayet star is the binary companion, the *HST* images also show a number of other possible companion stars, including an AGB star candidate and a high-mass main sequence star (Binder et al., 2015).

4.2.2 NGC 4395 ULX-1

While the least variable source of our sample between *XMM-Newton* observations, 2XMM J122601.4+333131 (henceforth NGC 4395 ULX-1, from Liu & Bregman 2005) has a large amount of *XMM-Newton* data available, with four *XMM-Newton* observations not dominated by background flaring, each with source counts in the multiples of thousands and one in excess of 30,000, with a total observing time of ~ 214 ks. It is also detected in three *Chandra* observations for a total of ~ 44 ks. It has previously been identified as a ULX in the catalogues of Roberts & Warwick (2000), Liu & Bregman (2005) and Swartz et al. (2011), and found to have a soft power-law-like spectrum by several studies, albeit one with significant residuals, possibly from hot diffuse gas (Feng & Kaaret, 2005; Stobbart et al., 2006). It shows significant long-term variability according to *Swift* data (Kaaret & Feng, 2009), and was recently found to exhibit a period of 62.8 days (Vinokurov et al., 2016).

The south-east portion of the galaxy containing NGC 4395 ULX-1 has been previously imaged by *HST* in six bands with the WFC3 and ACS instruments, although for the optical bands *F*814W, *F*555W and *F*435W, the source lies within the Advanced Camera for Surveys' chip gap. NGC 4395 ULX-1 has a singular optical counterpart with a blue power-law spectral energy distribution over the *F*275W, *F*336W and *F*438W bands. Its optical spectrum shows evidence of broad He II emission, consistent with other ULX counterparts (Vinokurov et al., 2016).

4.2.3 M51 ULS

2XMM J132943.2+471134 (henceforth M51 ULS, also called M51 ULX-2 in Terashima & Wilson 2004 but not to be confused with M51 ULX-2 in Urquhart & Soria 2016b) is located in the western spiral arm of M51, a very well-studied galaxy with a large population of ULXs and an abundance of multi-wavelength data. It has been observed six times with *XMM-Newton* although M51 ULS is only detected in four of them, totalling ~ 154 ks of observing time. It has also been the subject of a deep *Chandra* observing campaign, placing the total observing time at just under 750 ks. Previous studies analysing the ULX population of M51 have discovered this source to be very soft (Di Stefano & Kong, 2004), able to be fit with a cool MCD model (~ 0.1 keV; Terashima & Wilson 2004) with a small amount of additional hard emission that can be fit with a combination of a PL tail and a `mekal` thermal plasma component (Dewangan et al., 2005).

A deep *HST* observation as part of the Hubble Heritage Project in 2005 allowed the identification of a probable optical counterpart to M51 ULX-2, found to be consistent with being an OB-supergiant type star, making M51 ULS a HMXB (Terashima et al., 2006).

4.2.4 NGC 6946 ULX-1

Finally, 2XMM J203500.1+600908 (henceforth NGC 6946 ULX-1, from Liu & Bregman 2005, but not to be confused with NGC 6946 X-1 in Pinto et al. 2016) is a soft source in an inner eastern spiral arm of its host galaxy, and the only object of our sample with peak luminosity in the traditional ULX range ($L_{\rm X} > 10^{39}$ erg s^{-1}) according to the 3XMM-DR4 data. While the galaxy has been observed by *XMM-Newton* 11 times, the source is only

detected with sufficient data for spectral analysis in four of them, although those four observations total over 185 ks of observing time. Additionally, it has been observed for ~ 210 ks with *Chandra* over six observations. Like NGC 4395 ULX-1, it has previously been found to be a soft source, by Devi et al. (2008) who claim it to be an IMBH due to being acceptably fitted with a cool MCD model.

NGC 6946 ULX-1 has been observed in two *HST* bands with the ACS instrument, *F*814W and *F*658N.

4.3 Data reduction and analysis

We conducted our analysis on the objects listed in Section 4.2 using archival *XMM-Newton* and *Chandra* observations. A list of the observations used in this investigation – those where the source is detected with enough data for spectral analysis, approximately 400 counts at minimum – is given in Table 4.2.

We reduced the *XMM-Newton* data using V13.5.0 of the *XMM-Newton* Science Analysis System (SAS) software package. We first created calibrated and clean event lists by running the tasks EMPROC and EPPROC, then removed intervals dominated by background flaring, defined as a > 10 keV count rate greater than $0.35\,\mathrm{ct\,s^{-1}}$ for the EPIC-MOS data and a 10–12 keV count rate greater than $0.4\,\mathrm{ct\,s^{-1}}$ for the EPIC-pn data. Using EVSELECT, we selected source events for spectra and light curves with `pattern` ≤ 12 for the MOS cameras and `pattern` ≤ 4 and `flag == 0` for the pn camera from a circular region around the source with radius 20 arcseconds for M51 ULS and NGC 6946 ULX-1, and 25 arcseconds for NGC 300 X-1 and NGC 4395 ULX-1. Background counts were taken from equally-sized regions outside the host galaxy and on the same chip at a similar distance from the readout node. Redistribution matrices and auxiliary response files were generated using the RMFGEN and ARFGEN tasks respectively. The spectral data was grouped into at least 20 counts per bin to allow for Gaussian statistics, and oversampling limited to a maximum of three groups per spectral resolution FWHM by setting `oversample` $= 3$ in the SPECGROUP task.

The *Chandra* data was reduced using V4.7 of the Chandra Interactive Analysis of Observations (CIAO) software package and reprocessed using CHANDRA_REPRO to produce

up-to-date event lists. Spectra and light curves were extracted using the SPECEXTRACT and DMEXTRACT routines respectively, with the same binning as the *XMM-Newton* data, using the settings `weight=no` and `correctpsf=yes` given that each of our objects is a point source. We extracted source counts from 3 arcsecond radius circular regions around the source, except for one instance of an extended PSF when the source was off-axis, when we used a source region of 5 arcseconds. Background counts were extracted from an annulus around the source with inner radius equal to the radius of the source region and outer radius of 20 arcseconds.

As well as exhibiting significant long-term variability, each of our sources except for NGC 4395 ULX-1 have at least one *XMM-Newton* observation flagged as variable in 3XMM-DR4 (having a χ^2 probability of constant rate $< 1 \times 10^5$). We examined the timing properties of the sources by creating power spectra. We checked that the power spectrum was stationary across all observations, then we divided all of the available lightcurves for a source from a single telescope into approximately 20 equal-length segments. Then we averaged over the periodograms of each segment to obtain a power spectrum for each of *XMM-Newton* and *Chandra*, which we normalised into units of squared fractional rms per frequency interval. In the case of NGC 300 X-1, for which there is sufficient signal above the white noise level, we repeated this procedure for five different energy bands and integrated the resultant power spectra to create an rms spectrum.

In order to examine potential optical counterparts for our sources, we used pre-processed drizzled data from the Hubble Legacy Archive or the MAST distribution centre for all sources. So that we could match the *Chandra* source positions with *HST* images, we refined the *HST* astrometry by aligning the WCS with sources from the USNO 2.0 catalogue using the IRAF tools CCFIND, CCMAP and CCSETWCS. We found the 1σ rms error on the astrometric corrections, converted these errors into 90% confidence intervals, and combined them in quadrature with the 90% confidence interval for the overall astrometric accuracy of *Chandra* (0.6 arcseconds). This gave us error circles of radius 0.8 arcseconds for NGC 300 X-1, and 0.7 arcseconds for M51 ULS, NGC 4395 ULX-1 and NGC 6946 ULX-1 (rounded to the nearest 0.1 arcsecond). In the cases of M51 and NGC 6946, we found a small number of direct *Chandra* and *HST* coincidences (three background AGNs and a foreground star, and three foreground stars respectively). We

used these to calculate alternate astrometric corrections and 90% confidence regions – both have a radius of 0.7 arcseconds – and kept the results of both of these methods for comparison.

We performed aperture photometry with GAIA on the NGC 6946 ULX-1 counterpart we identify, as it is the only source in our sample without a previous investigation into possible optical counterparts. We used the aperture correction method and STMAG zero-points given in Sirianni et al. (2005), and corrected for foreground extinction using the $E(B-V)$ value given in Table 4.1, with extinction ratios from Sirianni et al. (2005) assuming an O5 SED.

We show the *XMM-Newton* EPIC-pn images and corresponding astrometrically corrected *HST* images for all four sources in Fig. 4.1, with solid circles on the *HST* images representing the error region from correcting the astrometry by aligning with USNO sources, and dashed sources the error region obtained by matching *HST* and *Chandra* directly. We retrieve most previously identified optical counterparts to these sources and identify a potential counterpart for NGC 6946 ULX-1 for the first time.

4.4 Results

4.4.1 X-ray spectral fitting

Spectral fitting was performed using v12.8.2 of XSPEC (Arnaud, 1996) in the energy range of 0.3–10 keV, with errors calculated at the 90% confidence interval. The best-fitting model parameters were found using χ^2 minimisation, and χ^2 statistics were used to determine the goodness-of-fit. We used the abundance tables of Wilms et al. (2000) throughout. We began with simple single-component models and refined the models if necessary as described in Sections 4.4.1.2 and 4.4.1.3. All models also contain an absorption component frozen to the Galactic column (see Table 4.1). An example of the spectral fitting process is shown in Fig. 4.2.

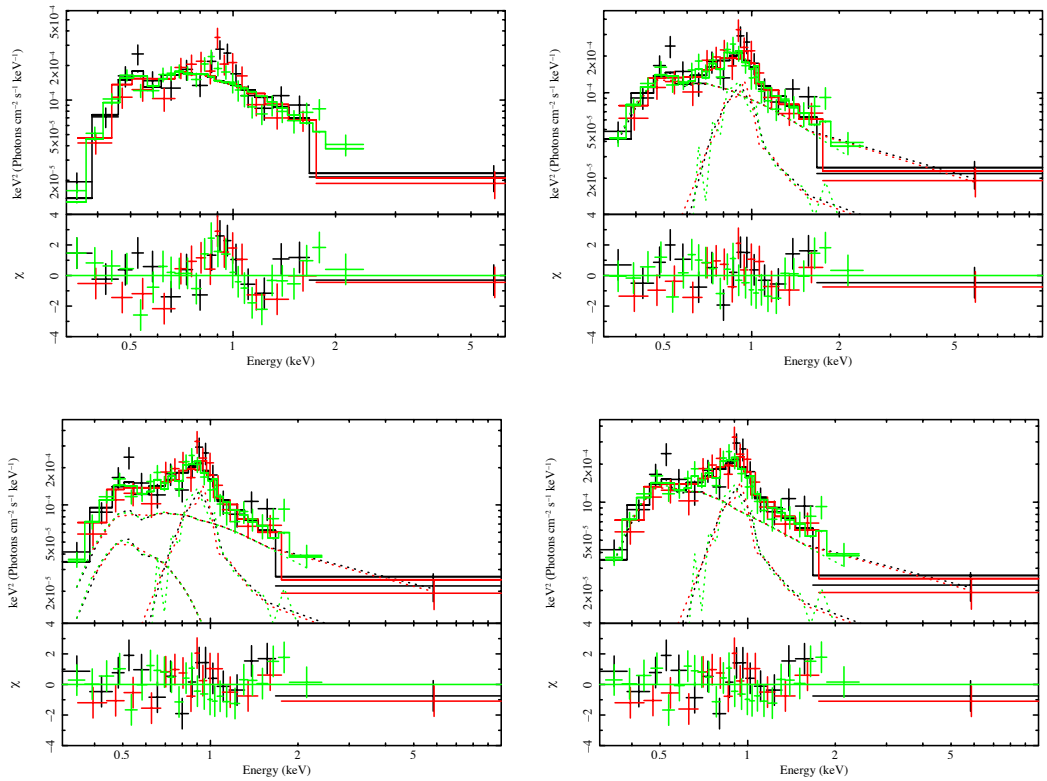

Figure 4.2: The spectral fitting process, showing the unfolded spectrum and $\Delta\chi^2$ residuals for various models fitted to *XMM-Newton* observation X2 of NGC 4395 ULX-1. *Top left*, fitted with a single absorbed PL model, with $N_{\rm H} = (29 \pm 5) \times 10^{20}\,{\rm cm}^{-2}$ and $\Gamma = 4.3 \pm 0.3$, $\chi^2 = 96.3/56$. *Top right*, fitted with an absorbed PL model with $N_{\rm H} = 12^{+6}_{-5} \times 10^{20}\,{\rm cm}^{-2}$ and $\Gamma = 3.7 \pm 0.4$, and a MEKAL thermal plasma component with $kT = 0.69^{+0.08}_{-0.07}\,{\rm keV}$, $\chi^2 = 61.0/54$. *Bottom left*, fitted with an absorbed MCD with $N_{\rm H} = 17^{+10}_{-8} \times 10^{20}\,{\rm cm}^{-2}$ and $T_{\rm in} = 0.1^{+0.2}_{-0.1}\,{\rm keV}$, a PL with $\Gamma = 3.5^{+0.6}_{-0.5}$ and a MEKAL component with $kT = 0.69^{+0.09}_{-0.07}\,{\rm keV}$, $\chi^2 = 59.6/52$. *Bottom right*, fitted with an absorbed MCD with $N_{\rm H} = 13^{+20}_{-6} \times 10^{20}\,{\rm cm}^{-2}$ and $T_{\rm in} = 0.1 \pm 0.06\,{\rm keV}$, convolved with a `simpl` convolution with $\Gamma = 3.5^{+0.4}_{-0.5}$ and scattered fraction > 0.05, and a MEKAL component with $kT = 0.70 \pm 0.08\,{\rm keV}$, $\chi^2 = 59.5/52$.

4.4.1.1 Single-component models

We began by fitting the source spectra with absorbed single-component models, either a MCD (`tbabs*diskbb`) or a PL (`tbabs*powerlaw`).

We present the results of a first pass of single-component fitting in Table 4.3. The first thing we find is that all four sources are very soft, with MCD models taking on low temperatures and PL models having high photon indices. However, only M51 ULS is better fitted by a MCD model than by a PL, with three of its *XMM-Newton* observations accept-

ably fit by a MCD without any additional components in the model, although additional spectral features are seen in the residuals of most of the observations.

The majority of observations of both NGC 300 X-1 and NGC 6946 ULX-1 show very significant hard residuals when fitted with a MCD, but are well-fitted by a PL model, with photon index $\Gamma \sim 2.5$ for NGC 300 X-1 and a high photon index $\Gamma \sim 3.5$–5.5 for NGC 6946 ULX-1. Examination of the residuals of the NGC 300 X-1 spectra, especially those for which a single-component model was not an adequate fit, reveal that there is a peaked excess around 0.9 keV in the *XMM-Newton* data. This is consistent with the findings of Carpano et al. (2007) who find that the inclusion of a Gaussian line at that energy significantly improves the spectral fit. Observation X4 of NGC 6946 ULX-1 also shows distinctive soft residuals around 1 keV as seen in other ULX spectra (e.g. Middleton et al. 2015b). We therefore refined our models for NGC 300 X-1 and NGC 6946 ULX-1 to include an additional broad Gaussian line to fit the excess at ~ 0.9 keV if it offered a significant improvement to the fit. For other observations of NGC 6946 ULX-1, while well-fitted by a single-component PL model, many of them still exhibit residuals potentially indicative of hot gas emission or absorption edges.

The observations for NGC 4395 ULX-1 were fitted better by a PL model than by a MCD, but unlike NGC 300 X-1 and NGC 6946 ULX-1, only the observation with the lowest amount of data was acceptably fit with a single-component model. The other observations exhibited strong residuals suggesting the presence of a thermal plasma component.

4.4.1.2 Fitting the residuals

Since many of the observations showed significant residuals when fitted with single-component models, we next attempted to fit these residuals by adding a `mekal` or `edge` component to the model to test for contributions from thermal plasma or ionised absorption features. In the case of NGC 300 X-1, we used a Gaussian line at ~ 0.9 keV as in Carpano et al. (2007). The observations for which the fit was significantly improved ($\Delta\chi^2 > 10$ per d.o.f. over the original single-component fit) by the addition of such a component are given in Tables 4.4 and 4.5.

In the case of M51 ULS, the MCD fit can be improved either by the addition of a

Table 4.3: The best-fitting parameters of a single-component (MCD or PL) model fit to the sample of Eddington Threshold sources.

ID[a]	tbabs*tbabs*diskbb			tbabs*tbabs*powerlaw			
	$N_{\rm H}^{b}$ ($\times10^{20}$ cm^{-2})	$T_{\rm in}^{c}$ (keV)	χ^2/d.o.f.	$N_{\rm H}^{b}$ ($\times10^{20}$ cm^{-2})	Γ^{d}	χ^2/dof	$L_{\rm X}^{e}$ ($\times10^{38}$ erg s^{-1})
NGC 300 X-1							
X1	0	(0.4)	1057.7/170	$\mathbf{4\pm1}$	$\mathbf{2.52\pm0.06}$	**227.1/170**	$2.01^{+0.05}_{-0.06}$
X2	0	(0.3)	541.9/101	0	$\mathbf{2.57\pm0.06}$	**117.1/101**	0.86 ± 0.02
X3	0	(0.4)	987.0/166	5 ± 1	2.60 ± 0.06	278.2/166	2.15 ± 0.05
X4	0	(0.4)	770.6/149	3 ± 1	$2.55^{+0.08}_{-0.07}$	205.0/149	1.75 ± 0.04
X5	0	(0.3)	241.0/67	$\mathbf{3\pm2}$	$\mathbf{2.7\pm0.1}$	**83.2/67**	$1.60^{+0.07}_{-0.08}$
C1	0	$0.46^{+0.06}_{-0.05}$	66.1/27	$\mathbf{8\pm7}$	$\mathbf{2.6\pm0.3}$	**31.9/27**	$1.7^{+0.3}_{-0.2}$
C2	0	(0.6)	264.6/86	$<\mathbf{4.6}$	$\mathbf{2.4\pm0.1}$	**69.4/86**	$1.9^{+0.1}_{-0.2}$
C3	0	0.77 ± 0.05	228.2/89	$\mathbf{8^{+6}_{-5}}$	$\mathbf{2.5\pm0.1}$	**99.0/89**	2.0 ± 0.1
C4	0	0.78 ± 0.06	166.9/63	$<\mathbf{7.7}$	$\mathbf{2.3\pm0.1}$	**67.2/63**	$2.01^{+0.1}_{-0.3}$
NGC 4395 ULX-1							
X1	4 ± 2	0.29 ± 0.02	151.2/83	28 ± 4	4.2 ± 0.2	123.6/83	6.1 ± 0.3
X2	3^{+3}_{-2}	0.28 ± 0.02	109.3/56	29 ± 5	4.3 ± 0.3	96.3/56	6.6 ± 0.3
X3	(0.5)	(0.3)	913.4/187	(0.2)	(4.0)	649.4/187	(7.4)
X4	6 ± 2	0.27 ± 0.01	203.7/79	33 ± 4	4.5 ± 0.2	178.7/79	8.1 ± 0.2
C1	0	$\mathbf{0.48\pm0.04}$	**29.5/27**	$\mathbf{50\pm30}$	$\mathbf{3.8\pm0.4}$	**19.8/27**	12.2^{+2}_{-1}
M51 ULS							
X1	$<\mathbf{8}$	$\mathbf{0.16^{+0.03}_{-0.02}}$	**25.4/16**	30^{+2}_{-1}	$5.8^{+1.2}_{0.8}$	33.5/16	$8.0^{+1.0}_{-0.9}$
X2	7 ± 3	0.15 ± 0.01	107.8/57	30^{+7}_{-6}	6.1 ± 0.5	152.9/57	9.0 ± 0.4
X3	$<\mathbf{13}$	$\mathbf{0.24^{+0.04}_{-0.06}}$	**37.8/26**	$\mathbf{20^{+20}_{-10}}$	$\mathbf{4\pm1}$	**34.6/26**	1.6 ± 0.2
X4	$\mathbf{3\pm3}$	$\mathbf{0.16\pm0.01}$	**45.6/40**	$\mathbf{23^{+6}_{-5}}$	$\mathbf{5.7\pm0.5}$	**58.4/40**	6.6 ± 0.3
C1	10^{+6}_{-5}	$0.16^{+0.02}_{-0.01}$	58.0/29	60^{+20}_{-10}	7 ± 1	85.4/29	$6.5^{+0.5}_{-0.6}$
C2	10^{+8}_{-6}	0.14 ± 0.01	95.1/38	70 ± 20	9 ± 1	110.4/38	4.4 ± 0.5
C3	12^{+9}_{-7}	0.12 ± 0.01	78.5/34	(58)	(8.8)	105.5/34	3.6 ± 0.4
C4	17^{+6}_{-5}	0.14 ± 0.01	163.5/56	(74)	(8.8)	173.9/56	6.2 ± 0.3
C5	20 ± 10	0.13 ± 0.02	46.2/20	(85)	(9.4)	62.6/20	5.2 ± 0.6
NGC 6946 ULX-1							
X1	0	0.28 ± 0.03	35.9/15	$\mathbf{30\pm20}$	$\mathbf{4.5^{+0.9}_{-0.7}}$	**31.4/15**	$3.8^{+0.5}_{-0.4}$
X2	$<\mathbf{4.6}$	$\mathbf{0.34^{+0.02}_{-0.03}}$	**98.1/69**	$\mathbf{38^{+7}_{-6}}$	$\mathbf{4.3\pm0.3}$	**71.3/69**	6.2 ± 0.3
X3	<0.6	$0.47^{+0.02}_{-0.01}$	235.7/121	$\mathbf{29\pm3}$	$\mathbf{3.4\pm0.1}$	**132.8/121**	13.6 ± 0.3
X4	(5)	(0.3)	515.0/140	$4.0^{+0.4}_{-0.3}$	4.5 ± 0.2	349.8/140	5.1 ± 0.1
C1	11 ± 5	0.31 ± 0.03	131.0/64	$\mathbf{51\pm7}$	$\mathbf{4.7\pm0.3}$	**88.7/64**	$5.6^{+0.2}_{-0.3}$
C2	9^{+9}_{-8}	$0.30^{+0.05}_{-0.04}$	84.3/33	$\mathbf{50\pm10}$	$\mathbf{4.7^{+0.6}_{-0.5}}$	**63.9/33**	5.3 ± 0.4
C3	<13	$0.32^{+0.02}_{-0.06}$	41.3/19	$\mathbf{40\pm20}$	$\mathbf{4.6^{+0.9}_{-0.8}}$	**35.5/19**	3.5 ± 0.4
C4	(37)	(0.2)	50.1/16	80^{+30}_{-20}	6 ± 1	40.0/16	$2.8^{+0.4}_{-0.3}$
C5	$\mathbf{20^{+20}_{-10}}$	$\mathbf{0.27^{+0.06}_{-0.05}}$	**29.3/15**	$\mathbf{70^{+30}_{-20}}$	$\mathbf{5.5^{+1.1}_{-0.9}}$	**19.3/15**	$2.8^{+0.4}_{-0.2}$

Notes: Statistically acceptable fits (confidence within 3σ based on χ^2 statistic) are displayed in bold. Values given in brackets are not constrained due to a poor fit.

[a]The short observation ID given in Table 4.2. [b]The intrinsic column density of the source. The Galactic column density is accounted for in the first, frozen `tbabs` component; see Table 4.1. Models for which no further absorption component was required are indicated with $N_H = 0$. [c]The accretion disc temperature at the inner disc radius. [d]The photon index of the PL model. [e]The source luminosity calculated using the best-fitting single-component model (a MCD for M51 ULS and a PL for the other sources) from the observed flux between 0.3 and 10 keV.

Table 4.4: The best-fitting parameters of multi-component (a MCD or PL component plus one or more residual components) model fits, for observations for which of a *mekal* or *gauss* component offered a significant improvement to the goodness-of-fit (i.e. $\Delta\chi^2 > 10/\text{d.o.f.}$). MCD and PL parameters as in Table 4.3.

ID	`tbabs*tbabs*(diskbb`		`+mekal`	`+mekal`	`+gauss`		`)`	
	$N_{\rm H}$ ($\times 10^{20}\,{\rm cm}^{-2}$)	$T_{\rm in}$ (keV)	kT_1^a (keV)	kT_2^a (keV)	E_L^b (keV)	σ_L^c (keV)	F^d	$\Delta\chi^2/\Delta$dof
				M51 ULS				
X2	6^{+6}_{-4}	0.12 ± 0.02	$0.50^{+0.08}_{-0.12}$	...	...	...	0.34	29.7/2
C2	<12	0.11 ± 0.02	$0.55^{+0.04}_{-0.08}$	...	...	...	0.30	33.5/2
C4	16^{+10}_{-8}	0.10 ± 0.01	0.59 ± 0.05	...	...	...	0.15	76.8/2
ID	`tbabs*tbabs*(powerlaw`		`+mekal`	`+mekal`	`+gauss`		`)`	
	$N_{\rm H}$ ($\times 10^{20}\,{\rm cm}^{-2}$)	Γ	kT_1^a (keV)	kT_2^a (keV)	E_L^b (keV)	σ_L^c (keV)	F^d	$\Delta\chi^2/\Delta$dof
				NGC 300 X-1				
X1	2 ± 1	2.42 ± 0.06	...	...	$0.93^{+0.02}_{-0.03}$	0.07 ± 0.03	0.03	56.6/3
X2	0	3.1 ± 0.2	(12.2)	...	...	...	0.50	41.4/2
X3	2 ± 1	2.46 ± 0.07	...	...	0.93 ± 0.02	0.08 ± 0.02	0.05	76.9/3
X4	<1	$2.41^{+0.08}_{-0.06}$	...	...	$0.90^{+0.02}_{-0.03}$	0.07 ± 0.02	0.03	58.6/3
				NGC 4395 ULX-1				
X1	20 ± 5	$3.9^{+0.4}_{-0.3}$	0.8 ± 0.1	...	...	...	0.14	20.9/2
X2	12^{+6}_{-5}	3.7 ± 0.4	$0.69^{+0.08}_{-0.07}$	...	...	...	0.42	35.3/2
X3*	14 ± 1	3.63 ± 0.08	0.75 ± 0.03	...	...	...	0.34	379.2/2
	13^{+2}_{-1}	$3.8^{+0.2}_{-0.1}$	0.68 ± 0.03	$1.5^{+0.3}_{-0.2}$	...	...	0.38	397.9/4
X4	21^{+5}_{-4}	4.1 ± 0.3	$0.77^{+0.10}_{-0.06}$	...	...	...	0.29	68.5/2
				NGC 6946 ULX-1				
X4	20 ± 4	3.6 ± 0.2	...	...	$0.92^{+0.02}_{-0.03}$	0.13 ± 0.02	0.34	182.8/3
C2	20 ± 10	$3.3^{+0.7}_{-0.6}$	0.7 ± 0.1	...	...	...	0.36	22.7/2
C4	70^{+60}_{-50}	(7.7)	0.8 ± 0.2	...	...	...	0.72	22.2/2

Notes: *Both refined fits of X3 are major improvements on a single-component fit, but are not in themselves statistically acceptable.
[a]The plasma temperature of a first and, optionally, second `mekal` component.
[b]Energy of Gaussian emission line.
[c]Line width of Gaussian emission line.
[d]Flux fraction of the residual component(s).

~ 0.5 keV thermal plasma or a ~ 1 keV absorption edge, the latter offering slightly better improvement to the reduced χ^2 statistic. Including an absorption edge results in a slightly higher temperature for the underlying disc, at around 0.2 keV compared to around 0.1 keV in the case of adding a `mekal` component.

Three of the *XMM-Newton* observations of NGC 300 X-1 are significantly improved by the addition of a broad Gaussian line at ~ 0.9 keV. One exception was observation X2, which showed curvature in its residuals which we were able to fit with an ill-constrained

Table 4.5: The best-fitting parameters of multi-component model fits, for observations for which the convolution with an absorption edge offered a significant improvement to the goodness-of-fit (as in Table 4.4). MCD and PL parameters as in Table 4.3.

ID	`tbabs*tbabs*(diskbb`		`*edge`		)
	$N_{\rm H}$ ($\times 10^{20}$ cm^{-2})	$T_{\rm in}$ (keV)	E_c^a (keV)	τ^b	$\Delta\chi^2/\Delta$dof
			M51 ULS		
X2	< 3	$0.21^{+0.01}_{-0.02}$	0.97 ± 0.03	1.7 ± 0.6	33.7/2
C1	< 4	0.22 ± 0.03	$1.10^{+0.05}_{-0.04}$	$1.7^{+0.7}_{-0.6}$	24.4/2
C2	< 5	$0.20^{+0.01}_{-0.02}$	0.99 ± 0.02	$1.8^{+0.6}_{-0.5}$	41.1/2
C3	0	$0.18^{+0.02}_{-0.01}$	0.95 ± 0.03	$2.1^{+0.8}_{-0.5}$	38.2/2
C4	3^{+4}_{-3}	0.21 ± 0.02	1.04 ± 0.02	1.8 ± 0.4	83.0/2
C5	0	0.23 ± 0.04	1.06 ± 0.03	$2.0^{+0.6}_{-0.5}$	23.2/2
ID	`tbabs*tbabs*(powerlaw`		`*edge`		)
	$N_{\rm H}$ ($\times 10^{20}$ cm^{-2})	Γ	E_c^a (keV)	τ^b	$\Delta\chi^2/\Delta$dof
			NGC 300 X-1		
X5	3 ± 2	2.5 ± 0.1	1.39 ± 0.05	0.6 ± 0.2	26.3/2
			NGC 6946 ULX-1		
C1	54 ± 7	4.6 ± 0.3	$1.20^{+0.09}_{-0.05}$	0.5 ± 0.2	21.3/2
C2	50 ± 10	$4.5^{+0.5}_{-0.4}$	1.17 ± 0.04	0.8 ± 0.3	20.0/2
C4	80^{+30}_{-20}	$5.3^{+1.0}_{-0.8}$	$1.18^{+0.07}_{-0.05}$	$1.3^{+0.6}_{-0.5}$	20.0/2

[a] Threshold energy of absorption edge.
[b] Absorption edge depth.

high-temperature `mekal` component, but is likely more indicative of there being two underlying components to its emission similar to the canonical BH accretion states (see Section 4.4.1.3). Observation X5 was also not improved by the addition of a Gaussian line, instead exhibiting an absorption feature at $E_c = 1.39 \pm 0.05$ keV which is unique to that observation. The *Chandra* observations, on the other hand, showed no evidence of additional spectral features on top of the underlying PL.

All *XMM-Newton* observations of NGC 4395 ULX-1 are improved by the addition of a 0.7–0.8 keV `mekal` component. In particular, the fit to observation X3 is dramatically improved by the addition of the thermal plasma component, but is still statistically unacceptable, with null hypothesis probability $p = 4.4 \times 10^{-5}$. The fit can be improved further, with diminishing returns, by adding more `mekal` components, but the residuals are too complex to be well-described by this method.

While most observations of NGC 6946 ULX-1 do not undergo significant improvements to their fit with the inclusion of additional components, three of the *Chandra* ob-

servations appear to exhibit an absorption feature at ~ 1.2 keV. In two of these cases, the spectrum can also be fitted with a warm `mekal` component, although in the case of C4, it has the effect of dramatically steepening the PL to the point that it becomes very unconstrained, and the thermal plasma component dominates the emission. Observation X4 exhibits strong soft residuals that are not well-described either by an absorption edge or `mekal` components, and instead resemble residual peaks at $\sim$1 keV that are found in ULX spectra, therefore we fit these with a Gaussian component (we also note that two Gaussian absorption components can be used to produce a similar improvement in fit as in Middleton et al. 2015b, but for simplicity we only use a single Gaussian emission component in our analysis).

We show a typical example of a spectrum of each source fitted with a single underlying component plus residuals in Fig. 4.3.

4.4.1.3 Towards physically motivated models

While a PL model, combined with a characterisation of any complex residuals, is a good empirical description of the spectrum for the sources NGC 300 X-1, NGC 4395 ULX-1 and NGC 6946 ULX-1, it is not in itself suitable for a physical explanation of the system. We therefore attempted to fit these sources with a combined MCD and PL model, for comparison with the canonical BH accretion states defined by an accretion disc and an additional hard Comptonised component.

In the case of *XMM-Newton* observations of NGC 300 X-1, the spectra can be fitted using a MCD with $T_{\rm in} \sim 0.1$ keV, a PL with $\Gamma \sim 2.4$ and a Gaussian line, for those observations that exhibited the line in their residuals. The other two *XMM-Newton* observations are once again exceptions, with X2 exhibiting a harder PL with $\Gamma = 2.0 \pm 0.1$, and X5 exhibiting a hotter accretion disc with $T_{\rm in} = 0.24^{+0.03}_{-0.04}$ keV. Fits to the *Chandra* spectra tend to prefer slightly warmer discs of $T_{\rm in} \sim 0.2$ keV, however these are far less well-constrained than in the *XMM-Newton* observations. The *Chandra* PL photon indices are all consistent with $\Gamma = 2.4$ but similarly not well constrained.

NGC 4395 ULX-1 and NGC 6946 ULX-1 can be treated in a similar way, although it is unusual to see PL slopes this steep. To begin with, we tried to fit the spectra with a MCD, using additional `mekal` components to account for the hard excess. We found

Table 4.6: The best-fitting parameters of physically-motivated fits to the spectra with an underlying PL shape. Parameters as in Table 4.3.

ID[a]	tbabs*tbabs*diskbb		*simpl		+comptt		)	
	$N_{\rm H}$ ($\times10^{20}$ cm^{-2})	$T_{\rm in}$ (keV)	Γ	$F^a_{\rm scat}$	kT^b (keV)	τ^c	χ^2/dof	R[d]
NGC 300 X-1								
X1	7^{+5}_{-4}	$0.09^{+0.02}_{-0.01}$	2.44 ± 0.08	$0.3^{+0.4}_{-0.1}$	...	...	170.9/165	G
	6 ± 5	$0.08^{+0.01}_{-0.02}$	...	...	<17.5	5^{+1}_{-3}	165.2/164	G
X2	0	0.16 ± 0.03	2.0 ± 0.2	0.29 ± 0.09	...	...	70.7/98	
X3	2^{+4}_{-3}	$0.12^{+0.05}_{-0.03}$	$2.42^{+0.07}_{-0.09}$	$0.5^{+0.2}_{-0.3}$	...	...	208.0/161	G
	<5	0.10 ± 0.03	...	...	<33.9	$5.4^{+0.4}_{-4.9}$	197.1/160	G
X4	7 ± 4	$0.10^{+0.03}_{-0.02}$	2.3 ± 0.1	$0.2^{+0.2}_{-0.1}$	...	...	128.6/144	G
	8^{+6}_{-5}	0.10 ± 0.02	...	...	<9.9	$5.6^{+0.4}_{-4.0}$	126.1/143	G
X5	0	$0.21^{+0.02}_{-0.03}$	$2.3^{+0.1}_{-0.3}$	$0.34^{+0.08}_{-0.10}$	...	...	68.2/63	E
C1	<12	$0.20^{+0.10}_{-0.07}$	$2.0^{+0.6}_{-0.9}$	$0.3^{+0.4}_{-0.2}$	...	...	27.9/25	
	<21	$0.19^{+0.10}_{-0.07}$	...	...	<109	<21.4	27.7/24	
C2	<33	$0.17^{+0.07}_{-0.04}$	$2.3^{+0.1}_{-0.2}$	$0.4^{+0.3}_{-0.2}$	...	...	62.8/84	
	<15	$0.17^{+0.06}_{-0.03}$	...	...	<28.9	<7.0	60.9/83	
C4	<75	$0.13^{+0.08}_{-0.03}$	$2.4^{+0.2}_{-0.3}$	$0.1^{+0.6}_{-0.1}$	...	...	63.7/61	
	<51	$0.14^{+0.06}_{-0.03}$	...	...	<100	$5.9^{+0.7}_{-5.0}$	60.9/60	
NGC 4395 ULX-1								
X1	14 ± 10	0.12 ± 0.05	...	...	<130	<4.4	98.1/78	M
X2	14^{+13}_{-9}	$0.10^{+0.06}_{-0.08}$	$3.5^{+0.4}_{-0.5}$	>0.05	...	...	59.5/52	M
X3	11 ± 1	$0.041^{+0.01}_{-0.004}$	$3.55^{+0.05}_{-0.08}$	>0.08	...	...	269.5/183	M
	9^{+2}_{-1}	0.090 ± 0.001	$3.7^{+0.2}_{-0.1}$	>0.45	...	...	246.1/181	M+M
	8 ± 3	$0.073^{+0.008}_{-0.2}$	...	...	<3.5	$3.5^{+0.1}_{-1.2}$	264.3/182	M
	8 ± 3	$0.07^{+0.02}_{-0.01}$	...	...	<3.5	$3.3^{+0.2}_{-1.9}$	243.4/180	M+M
X4	13^{+5}_{-4}	0.16 ± 0.03	3.6 ± 0.8	$0.2^{+0.3}_{-0.1}$	...	...	104.3/75	M
	12^{+5}_{-3}	$0.16^{+0.03}_{-0.06}$	...	...	<135	4^{+1}_{-3}	103.6/74	M
C1	40^{+100}_{-10}	<0.41	$3.7^{+0.4}_{-2.7}$	>0.22	...	...	19.1/25	
NGC 6946 ULX-1								
X1	<55	0.17 ± 0.09	3^{+2}_{-1}	>0.08	...	...	28.6/13	
X2	22^{+20}_{-7}	<0.22	$3.9^{+0.4}_{-0.6}$	>0.18	...	...	68.9/67	
	21^{+20}_{-9}	$0.15^{+0.06}_{-0.04}$	...	...	<103	<4.1	68.5/66	
X3	11^{+4}_{-9}	$0.23^{+0.06}_{-0.05}$	$3.2^{+0.1}_{-0.4}$	>0.33	...	...	130.5/119	
	33^{+7}_{-5}	$0.03^{+0.02}_{-0.01}$	...	...	90^{+10}_{-90}	<0.89	123.6/118	
X4	60^{+20}_{-30}	0.07 ± 0.02	$3.8^{+0.2}_{-0.3}$	<0.12	...	...	159.5/135	G
	50 ± 30	0.07 ± 0.01	...	...	<7.5	$3.3^{+0.3}_{-3.0}$	158.7/134	G
C1	11^{+10}_{-4}	$0.32^{+0.04}_{-0.02}$	>4.1	>0.5	...	...	63.8/60	E
C2	<54	$0.2^{+0.1}_{-0.2}$	$1.8^{+1.6}_{-0.8}$	>0.05	...	...	39.9/29	M
C3	60^{+40}_{-30}	$0.15^{+0.08}_{-0.05}$	3 ± 2	$0.04^{+0.20}_{-0.02}$	...	...	28.9/17	

Notes: *XMM-Newton* observations with particular cameras excluded are the same as in Table 4.3. Residual components were used in the fits as appropriate, although their parameters are largely the same as in Tables 4.4 and 4.5, so we do not display them here. We also only show the fit results for observations where we could obtain minimal constraints for all parameters; observations for which at least one parameter was completely unconstrained are not included.

[a]The fraction of input photons that are scattered. [b]The plasma temperature. [c]The plasma optical depth. [d]The residual component used used in this fit: M = `mekal`, E = `edge`, G = `gauss`.

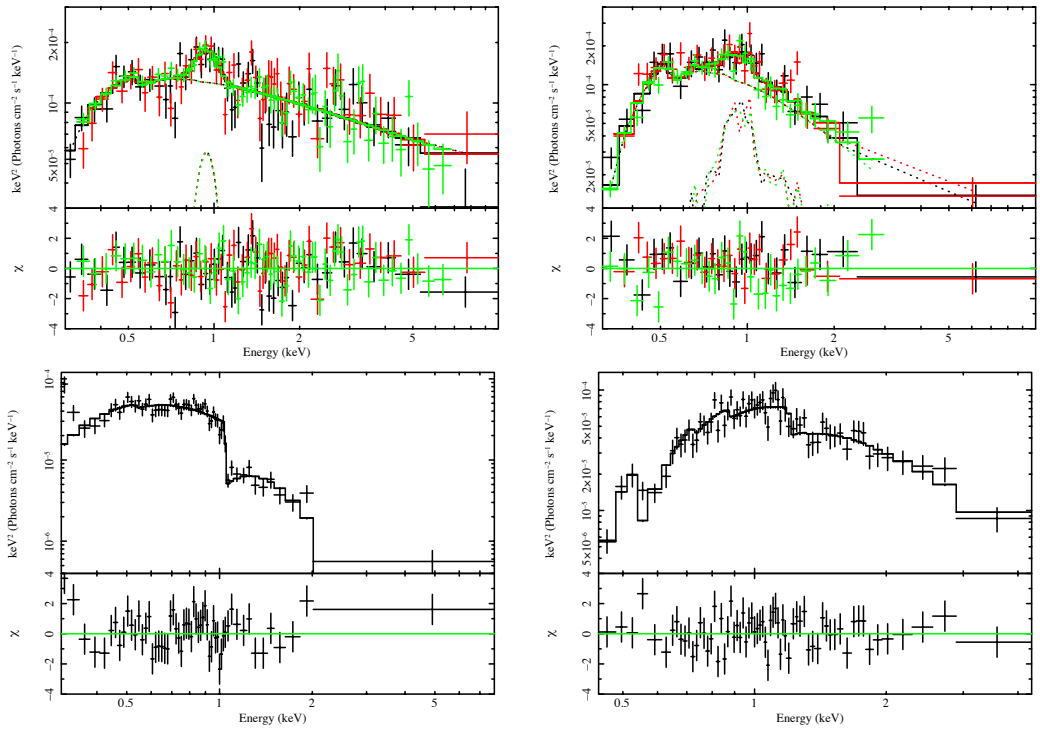

Figure 4.3: The unfolded spectrum and $\Delta\chi^2$ residuals for the best-fitting absorbed single component plus residuals model, for a typical observation of each source. *Top left*, NGC 300 X-1 observation X3 fitted with an absorbed PL model with $N_{\rm H} = 2 \pm 1 \times 10^{20}\,{\rm cm}^{-2}$ and $\Gamma = 2.46 \pm 0.07$, and an additional Gaussian line with $E_L = 0.93 \pm 0.02\,{\rm keV}$ and $\sigma_L = 0.08 \pm 0.02\,{\rm keV}$, $\chi^2 = 201.3/163$. *Top right*, NGC 4395 ULX-1 observation X1, fitted with an absorbed PL model with $N_{\rm H} = 20 \pm 5 \times 10^{20}\,{\rm cm}^{-2}$ and $\Gamma = 3.9^{+0.4}_{-0.3}$, and an additional `mekal` component with $kT = 0.8 \pm 0.1\,{\rm keV}$, $\chi^2 = 102.7/81$. *Bottom left*, M51 ULS observation C4, fitted with an absorbed MCD model with $N_{\rm H} = 3^{+4}_{-3} \times 10^{20}\,{\rm cm}^{-2}$ and $T_{\rm in} = 0.21 \pm 0.02\,{\rm keV}$, with an absorption edge at $E_c = 1.04 \pm 0.02\,{\rm keV}$ with depth $\tau = 1.8 \pm 0.4$, $\chi^2 = 80.5/54$. *Bottom right*, NGC 6946 ULX-1 observation C1, fitted with an absorbed PL model with $N_{\rm H} = 54 \pm 7 \times 10^{20}\,{\rm cm}^{-2}$ and $\Gamma = 4.6 \pm 0.3$, with an absorption edge at $E_c = 1.20^{+0.09}_{-0.05}\,{\rm keV}$ with depth $\tau = 0.5 \pm 0.2$, $\chi^2 = 67.4/62$.

that subsequent `mekal` components preferentially fitted low-energy residuals and did not account for most of the high-energy tail. Since we were unable to characterise the hard excess with hot diffuse emission, we continued with a traditional combined MCD and PL approach. However, since the PL slopes are still steep ($\Gamma > 3$ in most cases) even when a MCD component is included, the PL component dominates the spectral continuum at low energies. This has the effect of potentially artificially reducing the MCD component's temperature and normalisation, and therefore distorting our picture of the physical processes (which could also be happening to a lesser extent to the NGC 300 X-1

spectra, since the PL slopes observed for that source are still fairly steep).

Therefore we instead made use of the `simpl` convolution model component (Steiner et al., 2009), which self-consistently generates a PL tail from the Compton up-scattering of seed photons from an input model, for which we used `diskbb` as before. In the cases where there was sufficient data to put constraints upon the parameters, we also fitted the spectra with a MCD plus `comptt` model, with the input temperature kT tied to the MCD temperature. We show the results of these fits in Table 4.6.

While there is not sufficient data quality to put good constraints on the `simpl` or `comptt` parameters for the majority of observations, we can still glean some overall trends. For all three objects, a cool accretion disc temperature is favoured, with disc temperatures for the most part < 0.2 keV. The slopes of the PL tails obtained once the contribution from an accretion disc is properly considered are slightly harder than a PL model on its own, but still unusually soft in the cases of NGC 4395 ULX-1 and NGC 6946 ULX-1. For those observations for which we were able to make a `comptt` fit, the parameters for a Comptonising corona are for the most part very unconstrained, but the majority are consistent with optically thick material and a cool plasma temperature.

4.4.2 Timing analysis

In order to characterise the long-term variability of each source, we created a long-term light curve (Fig. 4.4) by using the best-fitting single component model to calculate the 0.3–10 keV flux of the object in each observation, then using the galaxy distance given in Table 4.1 to calculate the source luminosity (Table 4.2), assuming $L_{\rm X} = 4\pi d^2 f_{\rm X}$ in the absence of direct information on the viewing angle and geometry of the system, where d is the distance to the host galaxy in Mpc, and $f_{\rm X}$ is the X-ray flux between 0.3 and 10 keV. We do not correct for absorption since extending steep PLs to low energy might misrepresent (i.e. overestimate) the true luminosity hidden by the absorption – doing so gives an estimated intrinsic luminosity up to an order of magnitude higher than the observed luminosity, which is most pronounced in the case of NGC 6946 ULX-1.

All four sources do not exhibit large amplitude long-term variability between most of their *XMM-Newton* and *Chandra* observations. NGC 300 X-1 and M51 ULS both only show one departure from their dominant luminosity which is significantly less bright

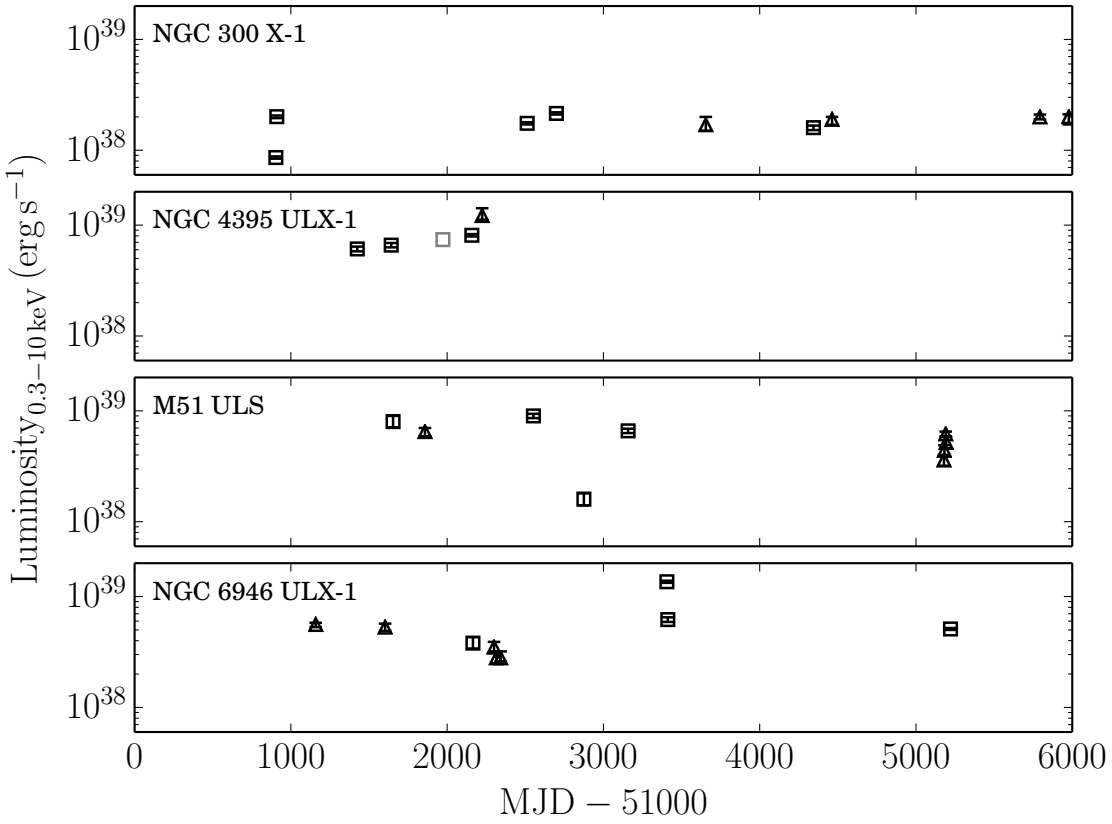

Figure 4.4: The long term light curve for the sample of Eddington threshold sources using the observed luminosity from *XMM-Newton* and *Chandra* data, as tabulated in Table 4.3. *XMM-Newton* observations are marked with squares, *Chandra* observations with triangles. The grey square for NGC 4395 ULX-1 without error bars is the observation for which the flux could not be well-constrained.

than the other observations (X2 and X4 for each source respectively). NGC 4395 ULX-1 and NGC 6946 ULX-1 both have a single brighter observation which exceeds $L_X = 1 \times 10^{39}\,\mathrm{erg\,s^{-1}}$ (C1 and X3 for each source respectively).

We show the luminosity-temperature relation for the `diskbb` component across the various physically-motivated models for our sources in Fig. 4.5. The bolometric luminosity was calculated from the model normalisation of the `diskbb` fit. For M51 ULS, we make a distinction between those models which used a `mekal` component to fit the residuals, those that used an `edge` component, and those that were not improved with an additional residual component. None of the groups show any evidence of a trend except for the three observations fitted only with a MCD, which shows a very tentative inverse relation between the disc luminosity and temperature. For the other sources, we distin-

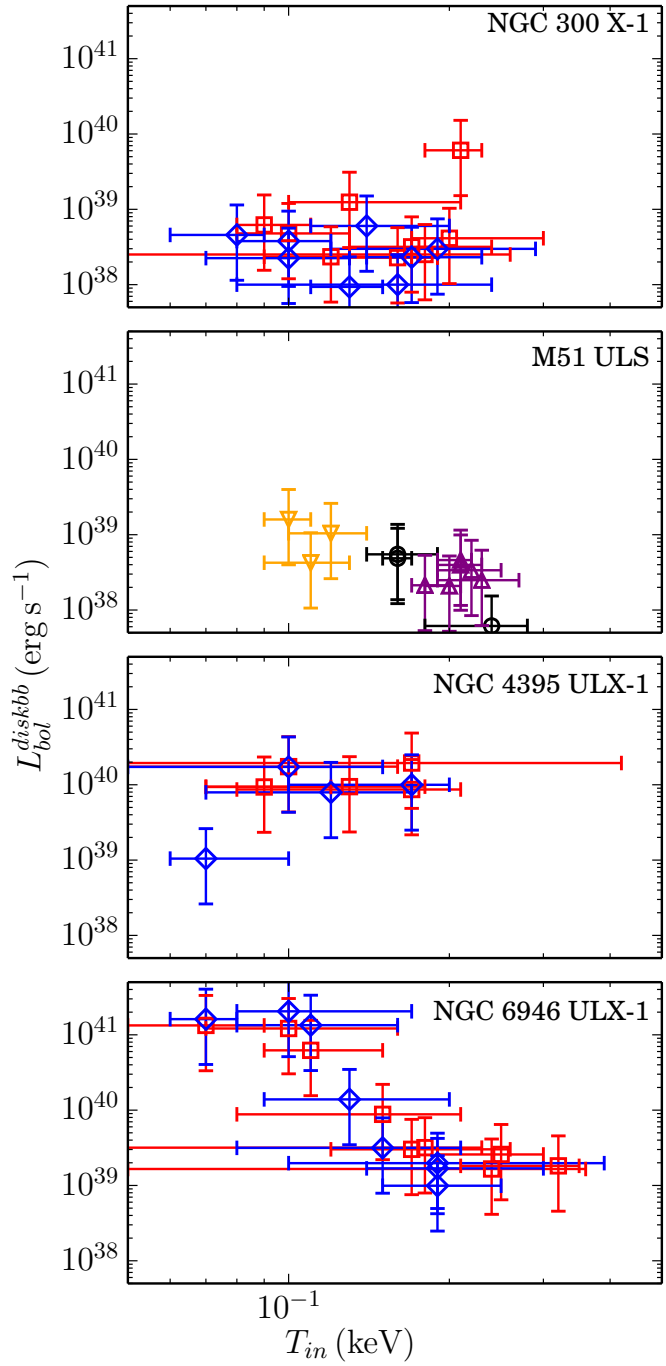

Figure 4.5: The inner disc temperature and bolometric luminosity of the fitted accretion disc component of the best-fitting MCD models for M51 ULS, and the best-fitting physically-motivated models for NGC 300 X-1, NGC 4395 ULX-1 and NGC 6946 ULX-1. Black circles indicate a simple MCD model, yellow downward-pointing triangles indicate a MCD model with an additional `mekal` component, purple upward-pointing triangles indicate a MCD model with an `edge` component, red squares indicate a `diskbb*simpl` model with suitable residual components, and blue diamonds indicate a `diskbb+comptt` model with suitable components.

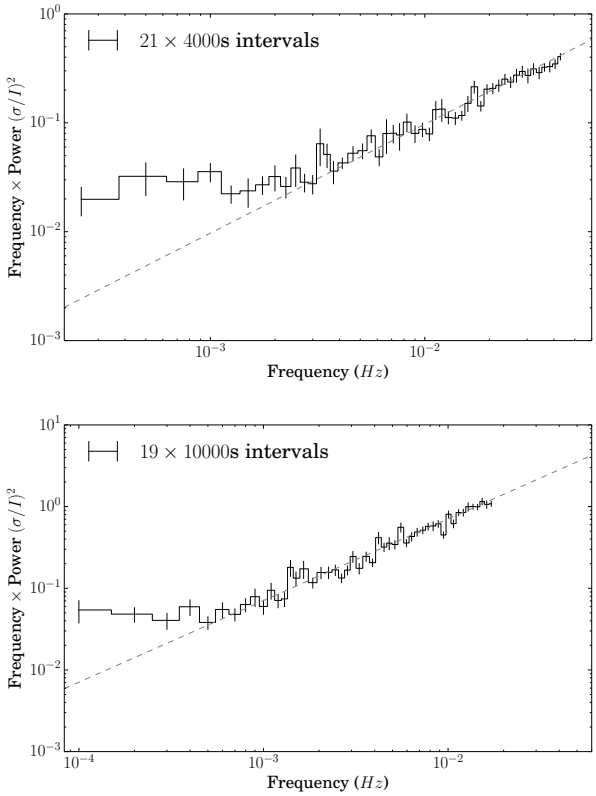

Figure 4.6: The *XMM-Newton* (top) and *Chandra* (bottom) power spectra of NGC 300 X-1, normalised so that the power is in units of the squared fractional rms per frequency interval. The grey dashed line indicates the white noise level, and error bars are the standard error on the mean. The spectrum is geometrically rebinned with a rebinning co-efficient of 1.05.

guish between the models that use a `simpl` component and those that use a `comptt` component. Neither NGC 300 X-1 nor NGC 4395 ULX-1 show a strong relation, however NGC 6946 ULX-1 shows a clear, statistically significant ($> 3\sigma$) inverse relationship between disc luminosity and temperature for both types of model. Linear regression analysis shows the relations to be $L_{\rm bol} \propto T_{\rm in}^{-3.5\pm0.5}$ for `simpl` models and $L_{\rm bol} \propto T_{\rm in}^{-5.8\pm0.9}$ for `comptt` models. (A similar inverse relationship exists if the spectra are instead fitted with a `bbody` model, with more-or-less consistent slopes).

The power spectra for NGC 4395 ULX-1 and NGC 6946 ULX-1 across all of their observations are consistent with the Poisson noise level down to $\sim 10^{-4}$ Hz. At the longest timescales, $< 10^{-4}$ Hz, we see some evidence for red noise in the *Chandra* power spectrum of M51 ULS. NGC 300 X-1 is the only source where there is sufficient signal to see a clear red noise component in both the *XMM-Newton* and *Chandra* power spectra (Fig. 4.6) with slope $\alpha \sim 1$ for $P(\nu) \propto \nu^{-\alpha}$, consistent with the findings by Barnard et al.

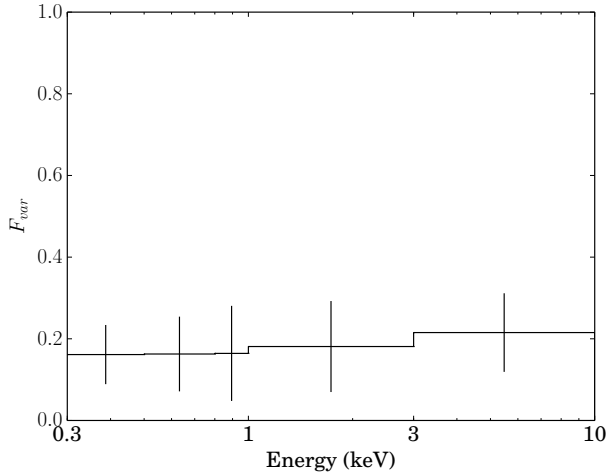

Figure 4.7: The *XMM-Newton* fractional rms variability spectrum for NGC 300 X-1, using the energy bands 0.3–0.5, 0.5–0.8, 0.8–1.0, 1.0–3.0 and 3.0–10.0 keV. The errors are calculated by propagating the standard error on the mean for each power spectrum bin summed to find the fractional variability.

(2008) and characteristic of an accretion disc.

Since the timing data quality for M51 ULS, NGC 4395 ULX-1 and NGC 6946 ULX-1 is poor, we are not able to place good constraints on the fractional rms for most observations. We obtain upper limits on the fractional rms of $\lesssim 0.35$ for M51 ULS, with *XMM-Newton* observations X2 and X4 having 0.39 ± 0.06 and 0.33 ± 0.04 respectively, consistent with most observations having a high variability of $\sim 30\%$. Likewise, most observations of NGC 4395 ULX-1 and NGC 6946 ULX-1 give upper limits of < 0.3, with observation X3 for NGC 4395 ULX-1 having fractional rms 0.09 ± 0.01 and observation X4 for NGC 6946 ULX-1 having an upper limit to the fractional rms of < 0.15. This could be consistent either with the sources being moderately variable, or having little to no variability at all.

Since NGC 300 X-1 has sufficient variability power for further analysis, we created a fractional rms spectrum to examine the variability across different energy bands (Fig. 4.7). We did this by integrating over the *XMM-Newton* power spectrum in five different energy bands. Across the entire energy range we examine, the fractional variability remains constant at ~ 0.2, showing no evidence of strong energy-dependence.

4.4.3 Optical counterparts

Using our own astrometric corrections and error circles, we successfully identify the same stellar counterparts for our sample that previous studies do, except for NGC 6946 ULX-1 for which we present the first identified counterpart. In all cases we use STMAG units.

For NGC 300 X-1, we identify the Wolf-Rayet star but not the other stars suggested in Binder et al. (2015) as potential counterparts. We see one other bright possible counterpart, but since we also find the Wolf-Rayet star, it is likely that it is the genuine companion star. We find a single counterpart to NGC 4395 ULX-1, the same as identified in Vinokurov et al. (2016). For M51 ULS, we comfortably identify the counterpart found in Terashima et al. (2006) using both methods of astrometry matching, therefore we conclude that this is most likely to be the genuine counterpart. We do however note that the error circle obtained from USNO-matching also contains a number of other bright blue stars, as well as probable red giants or AGB stars, and the error circle obtained from direct *Chandra* and *HST* matching contains further blue sources and a probable star cluster, so there do exist a number of other legitimate ULX counterparts for this source.

For NGC 6946 ULX-1, we identify a single star as a possible counterpart within the error circle, which is only detected in the $F814$W band, with magnitude $m_{F814W} = 22.3 \pm 0.7$ after correcting for extinction, which corresponds to an absolute magnitude of $M_{F814W} = -6.4$ using the distance to NGC 6946 given in Table 4.1. Given that we only have access to data in the I band and the narrow Hα band, we acknowledge that it is possible that a very blue optical counterpart may also be present within the error circle but undetected. Shorter-wavelength optical and UV bands would be required to further characterise potential companion stars to NGC 6946 ULX-1.

4.5 Discussion

We have identified a heterogeneous sample of four soft, bright sources observed with luminosities just below the Eddington luminosity for a $\sim 10\,M_{\odot}$ BH. Since we are only looking at the sources with the highest-quality data and selection effects bias us towards soft sources, these objects are not representative of this luminosity range as a whole. Despite this they are still of interest, and even within this small sample we observe different

Table 4.7: The properties of the most likely optical counterparts of the sample of Eddington Threshold sources.

Name	Optical R.A. & Dec. (J2000)	m^a_{435}	m^a_{555}	m^a_{606}	m^a_{814}	M^b_V	M^c_I
NGC 300 X-1	00 55 09.99 −37 42 12.65	...	...	22.41	22.33	−4.2	−4.0
M51 ULS	13 29 43.31 +47 11 34.73	23.20	24.01	...	25.50	−5.5	−4.2
NGC 6946 ULX-1	20 35 00.42 +60 09 07.1	...	...	...	22.3	...	−6.2
		m^a_{275}	m^a_{336}	m^a_{438}	m^a_{547}		
NGC 4395 ULX-1	12 26 01.44 +33 31 31.1	19.97	20.50	22.08	22.26	−6.2	...

References: NGC 300 X-1 – Binder et al. (2015); M51 ULS – Terashima et al. (2006); NGC 6946 ULX-1 – this work; NGC 4395 ULX-1 – Vinokurov et al. (2016).
[a]Extinction-corrected stellar magnitudes of the brightest optical counterpart in STMAG.
[b]Absolute magnitude in the V band, either calculated from the photometry (M51 ULS, NGC 4395 ULX-1) or estimated from spectral type (NGC 300 X-1).
[c]Absolute magnitude in the I band calculated from the photometry.

accretion behaviours, including the highest-luminosity canonical sub-Eddington accretion states and potential ultraluminous supersoft sources.

4.5.1 NGC 300 X-1: the highest luminosity canonical states

The soft PL-dominated spectrum of NGC 300 X-1 with $\Gamma \sim 2.5$ and a fairly high fractional rms of ~ 0.2 are typical features of the canonical very high/steep PL accretion state of stellar mass BHs. The observation that appears to be an exception to this interpretation is X2, whose lower luminosity and harder PL slope when fitted with a MCD and PL model potentially indicate the source dropping into a hard state.

The broad Gaussian line at 0.9 keV offers a significant improvement in the spectral fit in the case of three of the *XMM-Newton* observations. Carpano et al. (2007) suggest that these could be unresolved emission lines, possibly from reprocessing by a photoionised stellar wind – they are not present in all observations, but tend to be present in the higher-luminosity ones. Binder et al. (2015) find similar improvements in the fit to ours using an `apec` thermal plasma model. This feature is consistent with being a combination of emission and absorption lines produced by an extended hot gas corona.

As NGC 300 X-1 is already a well-studied source, we do not go into much further discussion of its properties. Binder et al. (2015) suggest that while spectral models find low inner disc temperatures, since the mass of the BH is known and this would thus imply

a strong retrograde BH spin, it is more likely that there is a hot inner disc covered by an extended corona that is able to access cooler seed photons from further out in the accretion disc. Fitted accretion discs appearing cooler and less luminous than expected due to accretion energy being emitted through the corona is a normal feature of the steep PL state observed in other sources (e.g. Kubota & Done 2016), as well as an amount of disc truncation compared to the standard thermal-dominant state. This may also be why there does not seem to be a clear accretion disc luminosity-temperature relationship.

While in Galactic sources the steep PL state is often considered to be a transitional state between the low/hard state and the thermal dominant state, it is possible that in NGC 300 X-1 the high mass of the companion star means that the stellar wind can provide it with a persistent rapid rate of fuel supply and therefore enable it to possess a stable accretion rate, at $\sim 10\%$ of the Eddington luminosity.

4.5.2 A selection of highly luminous supersoft sources

The remaining three sources all show behaviour distinct from the canonical sub-Eddington accretion states. NGC 4395 ULX-1 and NGC 6946 ULX-1 both show a very steep PL spectrum, with $\Gamma > 3$ even when considering the presence of an accretion disc and accounting for residuals. M51 ULS is consistent with a single thermal component spectrum, and does not feature the steep hard tail found in the other sources.

The first obvious comparison that can be drawn is with ULSs, such as M101 ULX-1 (Soria & Kong, 2016) and NGC 247 ULS (Feng et al., 2016). Characterised by super-Eddington bolometric luminosities and dominated by a low temperature thermal component with $T \sim 0.1\,\mathrm{keV}$, ULSs may at first glance seem to be evidence of IMBHs in a thermal-dominated accretion state. However, the luminosity, temperature and expected accretion rate for the thermal-dominated accretion state are not consistent with an IMBH interpretation. Instead, Soria & Kong (2016) suggest that these sources are examples of the supercritical ULX model (Poutanen et al., 2007) viewed through very optically thick outflowing winds, at very extreme accretion rates and/or viewed at a high inclination, such that all hard photons from the central source are downscattered in the wind, removing any hard tail in the spectrum. This means that the blackbody shape in the spectrum does not actually originate from the disc but from the wind – with very low peak temperatures,

a MCD model and a standard blackbody model are statistically indistinguishable in the *XMM-Newton* data, so this is acceptable in the context of our spectral fitting.

We note here that in the case of an interpretation as a super-Eddington accreting compact object, the object's underlying nature could be either a BH or a NS (as a small number of ULXs have been discovered to be pulsars e.g. Bachetti et al. 2014; Fürst et al. 2016; Israel et al. 2017a). The detection of pulsations is to date the only definitive method of confirming the presence of a NS rather than a BH, and since we do not detect them in any of our sources we continue our discussion under the assumption of super-Eddington accretion onto a BH while conceding that there is a possibility that these sources are NSs – a possibility we are unable to test at this time.

For M51 ULS, it is not likely that we are viewing the accretion disc of an IMBH, since the luminosity is too low to be in the sub-Eddington thermal-dominant accretion state for the disc temperature we observe. Additionally, while no strong trend is observed, there is tentative evidence of an inverse relationship between the disc component's luminosity and temperature, as opposed to the $L_{\rm disc} \propto T_{\rm in}^4$ expected from an accretion disc in the thermal dominant state, and similar to inverse relationships seen in other ULSs (e.g. Urquhart & Soria 2016a) and in the soft component of some ULXs (e.g. Feng & Kaaret 2007; Soria 2007; Kajava & Poutanen 2009). The spectrum is consistent with viewing a supercritically accreting source through an optically thick wind that has down-scattered the seed photons into a thermal spectrum. While it is hard to constrain the source variability, the fractional rms upper limit for M51 ULS is generally around 0.3, consistent with the strong short-term variability seen in other ULSs. It exhibits an absorption edge at ~ 1 keV in some of our observations of the source, and we note that transient absorption edges are a feature seen in a number of ULSs as well (e.g. Feng et al. 2016; Urquhart & Soria 2016a) and are further evidence of absorption in an effectively optically thick outflow wind. All these features are consistent with M51 ULS being a normal member of the ULS population – and indeed it makes an appearance as one of seven ULSs examined in Urquhart & Soria (2016a).

What may be more challenging to explain are the PL spectral shapes of NGC 4395 ULX-1 and NGC 6946 ULX-1. For most ULSs that sometimes exhibit hard residuals (e.g. M101 ULX-1), these are transient – in the case of M101 ULX-1, Soria & Kong (2016) fit

them with multiple `mekal` components and suggest that they may be the result of central source emission being observed through gaps in the clumpy wind that makes up the outflow. However, the steep slopes of our two sources are persistent and cannot simply be fitted with additional `mekal` components, instead requiring a PL shaped model.

Perhaps more similar is NGC 247 ULS, which is observed to have a steep PL slope with $\Gamma = 3.9 \pm 0.4$ in its 2014 observation. Feng et al. (2016) suggest that this may be an extreme example of the soft ultraluminous regime, with the hard emission very suppressed so that it manifests as a steep PL and no spectral turnover is evident (either because it is not present, or else because the hard flux is far too low for one to be detected). They also observe moderate short-term variability, which appears to originate from the soft component itself, rather than variability observed primarily in the hard emission as the hard central emission is occulted by a clumpy wind, as in the soft ultraluminous regime (Middleton et al., 2015a).

While there is no strong relationship between the bolometric luminosity and the temperature of the disc component for NGC 4395 ULX-1, there is an inverse relationship between those properties for NGC 6946 ULX-1, which is inconsistent with being produced by an accretion disc. It could, however, be produced instead by an expanding and contracting photosphere, and bears similarity with 'standard' ULS behaviour and that of the soft excess in ULXs, which would lend support to these very steep PL sources being intermediate objects between a soft ultraluminous ULX and a ULS.

If this is the case, the question remains of why M51 ULS and other typical ULSs have such high levels of variability compared to this moderately variable steep PL ultraluminous state we see in NGC 4395 ULX-1 and NGC 6946 ULX-1 if little to no hard emission emerges at all. Middleton et al. (2015a) predicts that at very high inclinations, the density of the clumps in the wind would smooth out any variability caused by obscuration of the central source. It is possible then that at extreme accretion rates, while the hard central emission is completely obscured, the outflowing wind varies in temperature by radius such that the clumpy edge of the wind still imprints variability upon the spectrum by occulting deeper parts of the wind at different temperatures to the clumps. Alternatively, Feng et al. (2016) suggest that at very high inclinations, the wind or photosphere itself may be masked by an uneven occulter at much larger radii, such as the outer edges of a

warped accretion disc or even a circumbinary disc.

It is appealing to explain NGC 4395 ULX-1 and NGC 6946 ULX-1 as a special case of the soft ultraluminous regime, in which the hard central photons are mostly but not completely downscattered, leaving a steep PL tail and therefore placing them within an ultraluminous unified model. However, the steepness of the PL tail of their spectra and the lack of a spectral turnover brings into question whether the explanation is that simple. These two ULSs, as well as the similar observation of NGC 247 ULS, exhibit PL slopes with $\Gamma = 3$–4, whereas the majority of soft ultraluminous sources have a slope of $\Gamma = 2$–3 when fitted either with a single-component PL or a MCD+PL model (Gladstone et al., 2009). Even an exception found by Gladstone et al. (2009) to have $\Gamma > 3$ (NGC 5408 X-1) very clearly exhibits a high-energy turnover as well as a steep PL slope.

NuSTAR data of ULXs has shown that at energies above the hard spectral turnover, the spectrum is consistent with a steep PL, with $\Gamma \sim 3$ (e.g. Walton et al. 2014, 2015a; Mukherjee et al. 2015). Therefore it is possible that instead of being absent in NGC 4395 ULX-1 and NGC 6946 ULX-1, this hard turnover is present at an unusually low energy ($\sim$ 1 keV) and is therefore masked by the soft component and possibly also residual features present in the spectrum. The issue is then why the turnover is at such a low energy, instead of why the PL is so steep. In order to produce such a spectrum using a `comptt` model, the plasma temperature is required to be very cool with $kT < 1$ keV (below the general applicability of the `comptt` model). Rather than as actual Comptonisation, this component is often interpreted as a distorted hot accretion disc – however, in this case, this would imply a observed disc temperature not much higher than the temperature of the outflowing wind, which is not unexpected for a system in which we do not see the hot inner regions of the disc. In any case, we do not have the statistics to test either of these scenarios at the present time, so we also examine a number of other possible interpretations of this steep, unbroken PL tail for completeness.

It could be possible that these steep PL tails are direct emission from the centre of the accreting system and are the result of Compton up-scattering in addition to a down-scattering outflowing wind, in which case the `comptt` model fits indicate that the Comptonising medium is optically thick and in most cases low temperature. However, it is unclear how this medium, if similar to the accretion disc corona observed in the steep PL

state in sub-Eddington sources, could possibly be seen if the source is at a high inclination or otherwise dominated by the outflowing wind. Additionally, it would require a source of low-temperature photons to be up-scattered in the first place – we would expect the central source to be high-energy, with the low-energy photons originating in the outflowing wind, outside the Comptonising medium.

Alternatively, as it expands, the outflowing wind could eventually disperse and become optically thin. If the material beyond the photosphere is still very hot and ionised, it may be sufficient for Compton up-scattering of the soft emission from the outer regions of the accretion disc or wind photons from its optically thick phase. There is some degeneracy in the parameters of the `comptt` model in that a similarly steep PL slope can be produced with an optically thin, high-temperature plasma, although model fits tend to prefer optically thick, low-temperature parameter values. However, this would require the wind to be at a very high temperature, inconsistent with current measurements.

Another possibility is that the hard emission is caused by shocks within the expanding envelope of the outflow between shells and/or clumps of different densities produced as the wind varies, or a collision between the outflow and a dense interstellar medium generated by the stellar wind from the companion star. Collisional shocks have been suggested as a mechanism in ULXs before, in the context of explaining the origin of soft emission line residuals within the spectra (e.g. Pinto et al. 2016), however these shocks appear to produce a thermal, emission-line rich spectrum and not a non-thermal PL-shaped spectrum.

It may be illuminating to consider soft Galactic objects with similarly steep PL spectra for insight into the underlying physics of our sources. We can draw parallels with Galactic microquasars that enter a hypersoft state, such as Cyg X-3 and GRO J1655-40, characterised by very steep PL slopes with $\Gamma = 4$–8. Study of Cyg X-3's hypersoft state revealed that while there was no hard X-ray emission detected, the source did emit γ-rays while in that state, indicating that highly-energetic processes were still taking place albeit obscured in the hard X-rays (Koljonen et al., 2010). SED modelling of GRO J1655-40 suggests that its unusually steep spectrum is caused by a powerful Compton-thick and ionised disc wind, driven by a source accreting at a near- or super-Eddington intrinsic luminosity (Uttley & Klein-Wolt, 2015; Shidatsu et al., 2016). This interpretation ties the hypersoft state

into the ULX family in a similar fashion to ULSs, and demonstrates that such sources can manifest with steep PL slopes, just as NGC 4395 ULX-1 and NGC 6946 ULX-1 do. Additionally, the absorption edges observed in the spectra of NGC 6946 ULX-1 indicate high levels of ionisation.

The main difference between the hypersoft accretion state and our very steep PL objects is the transience of the hypersoft state, compared with our sources which are for the most part persistent in their steepness. This could be attributed to their companion stars allowing persistent accretion through Roche lobe overflow, keeping the source in a single accretion state across years of observation. Additionally, a direct comparison of these sources with GRO J1655-40 shows the Galactic source to have a much higher blackbody temperature of ~ 0.4 keV, making drawing direct parallels between the objects tricky.

We must also consider that NGC 4395 ULX-1 and NGC 6946 ULX-1 may be similar to NGC 300 X-1, in a sub-Eddington steep PL state, albeit with a steeper PL than is usually expected in such a source, implying a particularly low plasma temperature in the Comptonising corona. They are consistent with having moderately high variability and a cool disc temperature similar to NGC 300 X-1. However, their luminosities are for the most part 3–5 times higher that that observed for NGC 300 X-1 while in the steep PL state, therefore we must conclude that for this analogy to hold, the sources either have a higher BH mass (60–100 $M_{\rm BH}$) or are consistently accreting at a higher Eddington fraction than NGC 300 X-1 (30–50%).

In Table 4.7 we collate previous studies of the optical counterparts of our sources with this work. All sources have very bright counterparts, similar to ULX counterparts, whose absolute magnitudes tend to lie in the range of $-4 > M_V > -8$, with most having $M_V \approx -6$ (Vinokurov et al., 2016). Those counterparts for which we have a value of M_V lie in this range and have possible supergiant spectral types, with the magnitudes of M51 ULS and NGC 300 X-1 being consistent with an OB supergiant and WR star respectively. NGC 4395 ULX-1 has an optical spectrum with similar features to other ULX spectra (Vinokurov et al., 2016), which are very blue and show features such as broadened He II, Hα and Hβ emission lines. While these spectra are similar to late-nitrogen WR star or OB supergiant spectra, Fabrika et al. (2015) suggest that these may actually be dominated by emission from an irradiated supercritical accretion disc wind, similar to Galactic

source SS 433. If this is the case, this would be further support for NGC 4395 ULX-1 being a super-Eddington accreting object. For the counterpart to M51 ULS, at a less extreme magnitude, it is more ambiguous as to whether the counterpart is dominated by a supergiant star or a supercritical disc – optical spectroscopy would be required to make this distinction, and to determine whether the spectrum is suitable for dynamical mass measurements.

The *I*-band magnitude of the counterpart of NGC 6946 ULX-1 is much brighter than the other counterparts we observe. This could possibly be an indication of a red supergiant companion star, found in some ULX systems (e.g. Heida et al. 2014, 2016). Red supergiant companion stars are useful for radial velocity measurements as they are expected to be dominant over the accretion disc in the near infrared, since the contribution from the accretion disc is lower in that regime than in the optical. Therefore if this counterpart is indeed a red supergiant, it could prove a good target for spectroscopic mass measurements.

4.6 Conclusions

We have searched our catalogue of extragalactic, non-nuclear X-ray point sources for luminous objects with peak luminosity below $3 \times 10^{39}\,\mathrm{erg\,s^{-1}}$ in order to find sources at the Eddington Threshold and to probe the nature of accretion at or just below super-Eddington rates. We identified a heterogeneous sample of four sources, all very soft due to the nature of our selection methods:

• NGC 300 X-1 is a well-known example of a BH accreting in a persistent steep PL state, made possible by its high-mass WR companion star. Its selection does not come as a surprise given that we would expect the highest-luminosity examples of the canonical sub-Eddington BH accretion states to appear at Eddington threshold luminosities.

• M51 ULS is best fitted with a MCD disc model, with a blackbody-shaped spectrum. This spectral shape and its likely fairly high levels of fractional variability make it similar to ULSs, so this may be a super-Eddington accreting source viewed at high inclinations and/or through an optically thick outflowing wind, which causes both the lack of high-energy photons, which are beamed away or down-scattered, and the lower than expected

luminosity.

• NGC 4395 ULX-1 and NGC 6946 ULX-1 both exhibit a very steep PL tail, a complication that does not make them immediately comparable with ULSs. We consider a number of possible physical scenarios, including Compton-up-scattering at the point the wind becomes optically thin, shocks within the wind or where the wind meets the interstellar medium, or manifestations of the steep PL state with relatively low corona temperatures. However, we conclude that it is most likely that they are an intermediate stage between ULSs and the soft ultraluminous regime in ULXs, in which most but not all of the hard central emission is down-scattered, leaving a very steep PL tail. They also bear similarities with the hypersoft state observed in a handful of Galactic microquasars, which may also be associated with super-Eddington accretion driving a Compton-thick wind.

Even with the best-quality data sets, many of these sources are not luminous enough to provide sufficient data for highly in-depth investigation unless they are targeted by long dedicated observation campaigns. Additionally, due to selection bias, our sample is not representative of the Eddington Threshold population as a whole. However we have demonstrated even with this limited sample that the Eddington Threshold population exhibits a variety of accretion behaviours that are not well understood, and would be an excellent regime for investigation by future X-ray missions such as *Athena*.

CHAPTER 5

In search of ultraluminous ultraviolet sources

Abstract

Models of ULXs as supercritically accreting BHs driving an optically thick outflowing wind are predicted to be UV-bright when observed at high inclinations. Therefore, searching for ultraluminous ultraviolet sources (ULUVs) may uncover further examples of super-Eddington accreting sources as well as ULXs. We investigate the *GALEX* source catalogue for its suitability to construct a sample of ULUVs and find that the source detection algorithm used in the *GALEX* pipeline makes it unsuitable for detecting point sources in other galaxies. We then create a sample of possible ULUV candidates from the *Swift* UVOT source catalogue and make the case for *HST* follow-up of these objects.

5.1 Introduction

Various models of super-Eddington accretion now exist, presenting ways that extreme amounts of matter can be accreted either onto stellar-mass BHs or NSs. According to some models of super-Eddington accretion onto a stellar-mass BH, the different X-ray spectral shapes and variability behaviours of super-Eddington accreting sources depend heavily upon a fast, optically thick outflowing wind driven off the accretion disc and its position in relation to the line-of-sight of an observer (Poutanen et al., 2007; Sutton et al., 2013b; Middleton et al., 2015a). If an observer is able to see the hard central emission, the source manifests as either a hard or a soft ULX. The wind obscures and downscatters the hard central emission from the inner accretion disc and the spectrum gains a soft excess from emission of the wind and outer accretion disc, which dominates the spectrum if the

wind flows into the line-of-sight between the observer and the centre of the system. This depends upon the mass accretion rate, which drives the size of the funnel for which there is a direct line-of-sight to the centre, and on the angle of inclination of the system with respect to the observer.

In cases with a extremely high mass accretion rate and/or inclination angle, the central emission is completely obscured and down-scattered by the wind, generating an X-ray spectrum with little to no hard emission and a single bright thermal component in the soft X-rays, which may be the cause of ultraluminous supersoft sources (ULSs; e.g. Urquhart & Soria 2016a; Feng et al. 2016). If this is the case, it is possible that the most extremely down-scattered sources will have the peak of their thermal emission occur in the UV regime rather than in the soft X-rays, and manifest as an ultraluminous UV source (ULUV) rather than, or as well as, a ULX or ULS – this is suggested to be the case for Galactic microquasar SS 443 (Begelman et al., 2006; Poutanen et al., 2007).

One such ULUV that has already been observed is NGC 6946 ULX-3 (Liu & Bregman, 2005), a compact X-ray source with ULX luminosities ($L_X > 10^{39}\,\mathrm{erg\,s^{-1}}$) located within a nebula MF 16 in NGC 6946 at 20:35:00.7 +60:11:31 (J2000; Swartz et al. 2004). The optical spectrum of the nebula contains strong emission lines which, as well as indicating the presence of shock heating, require a strong UV source of photoionisation more luminous even than the observed X-ray luminosities (Blair et al., 2001; Abolmasov et al., 2008). Kaaret et al. (2010) found a bright UV counterpart to the source (henceforth NGC 6946 ULUV) using *HST*, with a monochromatic luminosity of $\lambda L_\lambda \approx 1 \times 10^{40}\,\mathrm{erg\,s^{-1}}$ at 1533 Å. Fitting the optical and UV SED from *HST* photometry they found two potential solutions that provided the necessary energetics to produce the photoionisation observed: either two blackbody emitters at 26,000 K and 140,000 K (2.2 eV and 12.1 eV respectively, consistent with an OB-supergiant star and an additional blackbody, perhaps from an outflowing wind), or a single MCD model with a temperature of 16,000–21,000 K, depending upon the disc profile. Berghea & Dudik (2012) also found equally good fits between an irradiated disc model and an OB star and accretion disc model (although they did not consider the scenario in which the soft X-ray emission originates from an outflowing wind in a supercritical disc model). Distinguishing between all of these scenarios is difficult without further data points, especially in the

far- to extreme-UV, however the discovery of this object does demonstrate that it may be reasonable to expect to find further ULUVs elsewhere.

In this investigation, we attempt to perform a search for ULUVs using a similar method to that used to find ULXs (see Chapter 2). We attempt this first with the *Galaxy Evolution Explorer* (*GALEX*) source catalogue from data release GR6/7 (Bianchi et al., 2014), then with the *Swift* Ultraviolet/Optical Telescope (UVOT; Page et al. 2014) Serendipitous Source Catalogue, and describe our methods and the suitability of each catalogue in Section 5.2. We make the case for *HST* follow-up in Section 5.3 and give our conclusions and plan for further study in Section 5.4.

5.2 Data & sample selection

We select our samples of candidate ULUVs similarly to the way we selected our extragalactic X-ray source sample in Chapter 2, so we only give a brief description of our method here. We began with a UV source catalogue and matched it with the Third Reference Catalogue of Bright Galaxies (RC3; de Vaucouleurs et al. 1991) and Catalogue of Neighbouring Galaxies (CNG; Karachentsev et al. 2004), with host galaxy properties and distances corrected as in Section 2.2.1 of Chapter 2. We filtered out AGNs in the centres of host galaxies by removing all sources that were within three times their position error plus 3 arcseconds of the galaxy centre in NED, using the same method as we used for the X-ray catalogue given that the position errors of *GALEX* and *XMM-Newton* are similar.

For this investigation we had the added complication of wanting to avoid simply selecting regions of high star formation rate, which would also appear bright in the UV. We therefore added the condition of selecting sources that demonstrated variability over the course of multiple observations, since we would not expect star forming regions to have strong long-term variability on timescales of days to years. However, it is possible that changes in the behaviour of an accretion-powered ULUV could cause its flux to change significantly between observations. This does mean that our ULUV sample is from the outset limited only to those sources that have multiple observations and demonstrate variable flux over those observations – we are not currently able to distinguish ULUVs accreting at a steady luminosity over a long period of time from bright star formation.

A possible exception to the lack of stellar variability would be the presence of a luminous blue variable (LBV) star, which have been observed to reach $L \sim 10^{38}\,\mathrm{erg\,s^{-1}}$ in the FUV (Shore, 1992), and can be variable up to a factor of 1.5 over timescales of days to weeks (van Genderen, 2001). Therefore we make sure to choose our definition of variability to exceed these values (see below) in order to minimise the possibility of our ULUV candidates being LBVs.

5.2.1 Matching using GALEX

The *Galaxy Evolution Explorer* mission was an orbiting UV telescope launched in 2003, capable of imaging and spectroscopy in a near-UV (NUV; 1750-2750Å, effective wavelength 2271Å) and a far-UV (FUV; 1350-1750Å, effective wavelength 1528Å) band. It has a field of view of 1.2 degrees and with an angular resolution of ~ 5 arcseconds (Martin et al., 2003, 2005). The first UV catalogue that we chose to use to create a ULUV sample was the GR6/7 data release of the *GALEX* Merged Catalog of sources, the latest version of which was released in 2013 and contains over 210,000,000 source measurements taken over the course of the *GALEX* mission (Bianchi et al., 2014). It includes NUV and FUV data compiled from the Nearby Galaxies Survey (Gil de Paz et al., 2007), and the Deep, Medium and All-Sky Imaging Surveys (Morrissey et al., 2007), including extensive photometry data for each source. Combined, these surveys cover over 50% of the UV sky and the distribution of pointings ensures that a large number of sources are observed on multiple occasions, allowing us to select based upon flux variability. These factors, along with the availability of both NUV and FUV data meant that *GALEX* initially seemed like an ideal catalogue to use to search for ULUV sources in other galaxies.

We performed our matching of sources to galaxies by accessing the Virtual Observatory with the TOPCAT software, using the maximum of the NUV and FUV position errors as the overall detection position error, and removed sources with the flag CHKOBJ_TYPE=1, which are known bright stars used for aligning *GALEX*'s position on the sky. The *GALEX* catalogue detections were not grouped into sources in the initial pipeline, so we matched the detections located within RC3 and CNG galaxies with themselves, using the matches within the maximum detection position error to identify detections likely to originate from the same source.

We corrected the NUV and FUV fluxes for host galaxy and Galactic extinction by combining the intrinsic $A_{\rm B}$ value from the RC3/CNG catalogues, and the $E(B-V)$ value given in the *GALEX* catalogue. These were converted into a total $E(B-V)$ value and then into absolute extinction for each band using the equations $A_{\rm NUV} = 7.24E(B-V)$ and $A_{\rm FUV} = 4.89E(B-V)$ (Yuan et al., 2013), and used to calculate an intrinsic flux for the detections in each band. The monochromatic luminosity in each band was calculated from the intrinsic flux and the corrected host galaxy distance. Finally, we defined candidate ULUVs as those sources with a luminosity greater than $5 \times 10^{38}\,{\rm erg\,s^{-1}}$ in at least one of the UV bands, and a factor 1.5 flux variability between their detections. The resulting sample of objects contained 14 sources with 42 detections between them.

Upon inspection, we found major issues with this sample of ULUV candidates, due to the fact that the SExtractor routine used to identify sources in the *GALEX* pipeline is not good at detecting extragalactic point sources, tending instead to extract properties from large, elliptical source regions that extend over large areas of the host galaxy, or in some cases the entire galaxy. Therefore the high UV luminosities of our sample are simply due to picking up a large amount of the UV flux from the entire host galaxy, not a single source, and the variability originates from the source regions changing from observation to observation (see Fig. 5.1).

For comparison, we examined the *GALEX* sources detected in NGC 6946 to see if the pipeline was able to pick up the location of MF 16. We found no source region in either band that matched the location of NGC 6946 ULUV, nor of many other bright regions in the galaxy that are identifiable by eye. Most of the FUV source regions identified are highly extended, and the main NUV source region extends over the entire galaxy (see Fig. 5.2, left). We also examined the well-known spiral galaxy M51, which contains a large number of X-ray sources and star formation regions, and found that while bright regions are better identified in this galaxy, there is still a tendency for the source regions to be extended and highly elliptical (see Fig. 5.2, right). Therefore we conclude that the *GALEX* source catalogue is unsuitable for the serendipitous discovery of ULUV candidates, although it does have value in the UV follow-up of sources with known locations.

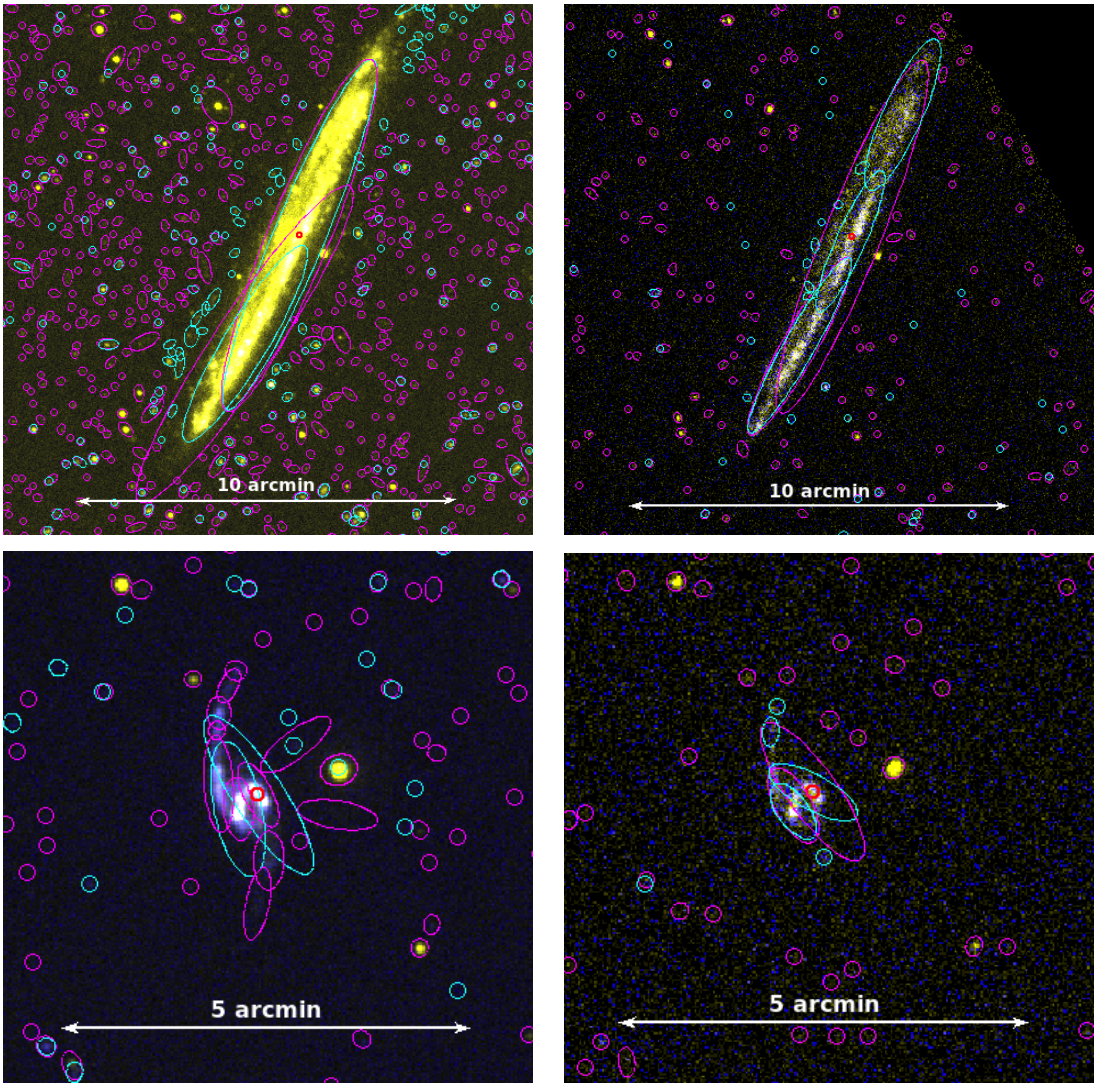

Figure 5.1: *GALEX* images of two observations each of two of the host galaxies of our initial ULUV sample using the *GALEX* source catalogue, NGC 5907 (*top*) and NGC 7549 (*bottom*). The NUV band is in yellow, and the FUV band in blue. NUV source extraction regions are marked in magenta and the FUV regions in cyan. The position of the ULUV candidate is marked with a 5 arcsecond red circle – although it is clear from the corresponding source extraction regions that the flux does not come from a point source but rather a large region of the host galaxy, and that the shape of the region changes between observations.

5.2.2 Matching using UVOT

After finding the *GALEX* catalogue unsuitable for our purposes, we required a UV imaging mission with an analysis pipeline that can reliably identify point sources in other galaxies. We found that the *Swift* Ultraviolet/Optical Telescope (UVOT) and *XMM-Newton* Optical/UV Monitor (OM) missions are both able to achieve this to a better degree

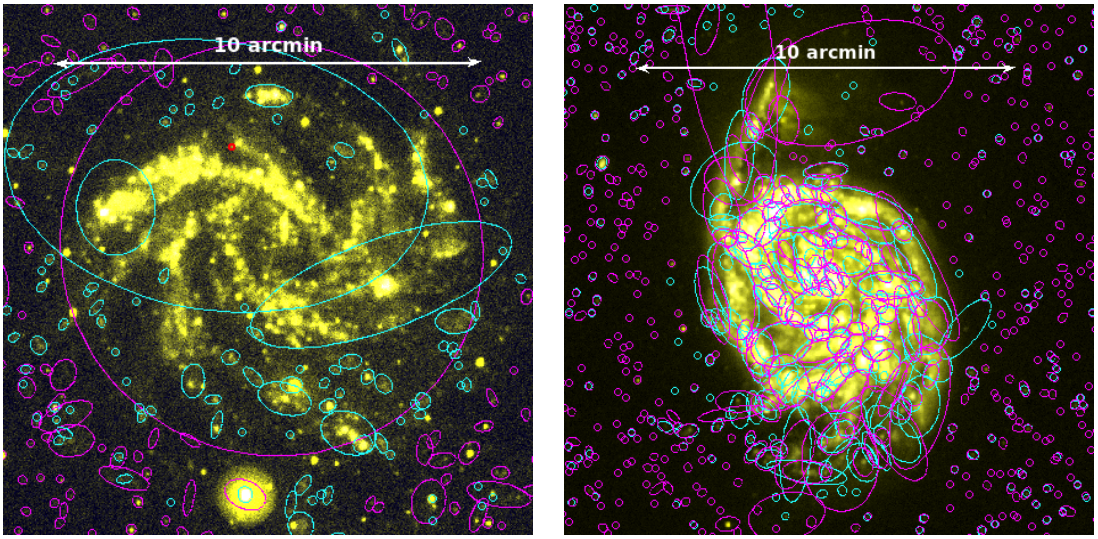

Figure 5.2: *GALEX* images of NGC 6946 (*left*, with the position of NGC 6946 ULUV marked with a 5 arcsecond red circle) and M51 (*right*). Band colours and source extraction regions are as in Fig. 5.1.

than *GALEX*, successfully identifying sources within other galaxies at the angular scale of their PSF.

The two telescopes, while complementary optical/UV instruments to X-ray missions, are good survey instruments in their own right. Their pipelines and their data structures are almost identical, with a field of view of 17×17 arcminutes, angular resolution of 2.5 arcseconds and six different photometry bands, including three UV band filters: UVW1 (2600Å), UVM2 (2246Å), and UVW2 (1928Å) (Page et al., 2012, 2014). Which of the two we focus on depends on how the telescopes are used: *Swift* is often used for short, repeated observations to monitor the flux of a source over time. While observations with *Swift* therefore tend to be shorter and thus shallower than those with *XMM-Newton*, UVOT has a far higher sky coverage than OM (~ 300 degrees^2, or 0.7% of the sky, compared to 30–80 degrees^2 for OM), and is likely to revisit sources more often, making it easier to identify varying sources. Therefore we decided that the UVOT Serendipitous Source Catalogue was the most suitable for constructing a sample of ULUVs.

The UVOT Serendipitous Source Catalogue is made up of data taken between 2005 and 2010, containing 13,860,569 detections of 6,200,016 sources (Page et al., 2014). We selected detections from the UVOT catalogue with a detection significance greater than 3.5σ in at least one band, and that were not flagged as extended in any band. We matched

Table 5.1: The sample of ULUV candidates selected from the *Swift* UVOT Serendipitous Source Catalogue.

Name	Host Galaxy	D^a	n^b	$\bar{L}^c$ ($\times 10^{38}$ erg s^{-1})		
		(Mpc)		UVW1	UVM2	UVW2
UVOTSSC1 J023436.6-084707	NGC 985	172.5	4	4.83	8.81	5.59
UVOTSSC1 J023437.3-084655	NGC 985	172.5	4	4.47	5.22	6.45
UVOTSSC1 J051203.5-154150	NGC 1832	27.1	4	...	4.87	2.90
UVOTSSC1 J095603.8+103003	IC 577	119.9	5	6.94	14.4	15.2
UVOTSSC1 J122201.6+042846a	M61	26.7	5	4.07	2.70	3.24
UVOTSSC1 J142931.9-294112*	ESO 447-G 007	231.7	3	39.5	...	23.6
UVOTSSC1 J223555.6+335743	NGC 7318A	86.4	2	3.54	5.01	8.13
UVOTSSC1 J234147.8-034008**	ARP 295A	88.7	7	12.6	...	...

[a]Host galaxy distance in Mpc.
[b]The number of observations made of this source.
[c]The average absorption-corrected luminosity across all observations in the respective band (note that not all observations may have used every band).
*This source is coincident with a foreground star.
**This source is confirmed to be a supernova (Schwehr & Li, 2006).

these detections with the RC3 and CNG galaxy catalogues and filtered out likely AGNs as before. Correcting fluxes for absorption was made more complicated by the UVOT catalogue not containing an $E(B-V)$ for each detection, therefore we instead used the Galactic extinction coefficient for the host galaxy recorded in RC3/CNG as a first order approximation to the Galactic extinction for the source. We calculated the absolute extinction for each band using the extinction laws in Cardelli et al. (1989). We calculated the intrinsic flux and luminosity in the same way as for *GALEX*, and similarly defined ULUV candidates as sources with a luminosity greater than 5×10^{38} erg s^{-1} in at least one of the UV bands, and a factor 1.5 flux variability.

Our final sample of ULUV candidates using the UVOT catalogue contains eight sources, with 34 detections between them. One source coincides with the location of a foreground star, and another is confirmed to be a supernova. The other six are located within spiral arms or otherwise bright regions of their host galaxies. We present the sample in Table 5.1.

The UVOT-selected sample still experiences some of the same pitfalls as the *GALEX* sample, especially for the sources in the most distant galaxies, in that it is clear that even with point source apertures of 5 arcsecond radius, there is a lot of contamination of the flux from the spiral arms and/or bright star forming regions that the sources are located in

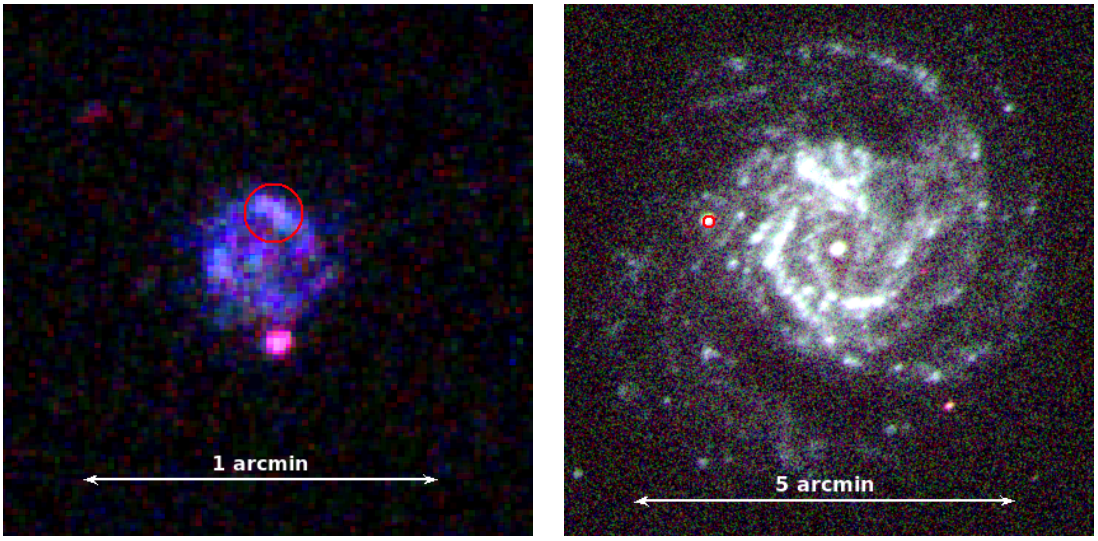

Figure 5.3: *Swift* UVOT images of two of the host galaxies of our ULUV sample using the UVOT source catalogue, IC 577 (*left*) and M61 (*right*). The UVW1 band is in red, the UVM2 band in green, and the UVW2 band in blue. The position of the ULUV candidate is marked with a 5 arcsecond red circle.

(see Fig. 5.3, left) – in the case of the most distant objects, the aperture radius extends over multiple kiloparsecs of space. Even in the case of the source in nearby M61, it appears to be associated with a bright star forming region of radius ~ 5 arcseconds (see Fig. 5.3, right) or ~ 1 kpc across. These sources are still of interest due to their variability, which implies the possible presence of an accreting compact object, and while their flux may be significantly contaminated by the surrounding star formation, we can still be confident that they are very luminous, since to achieve variability of a factor 1.5, the source must be contributing at least one third of the total flux of the region when at its brightest.

The UVOT pipeline was also unable to detect NGC 6946 ULUV as a point source, as the observations were not deep enough to distinguish the region from noise (see Fig. 5.4). It may also be affected by the detection of a larger, extended region to the northwest. Therefore it is likely that this method does not pick up many valid ULUV candidates due to *Swift* observations not being deep enough. This is one example where using *XMM-Newton* OM data to complement the *Swift* UVOT sample may offer an improvement on the list of sources, by detecting those with a lower flux.

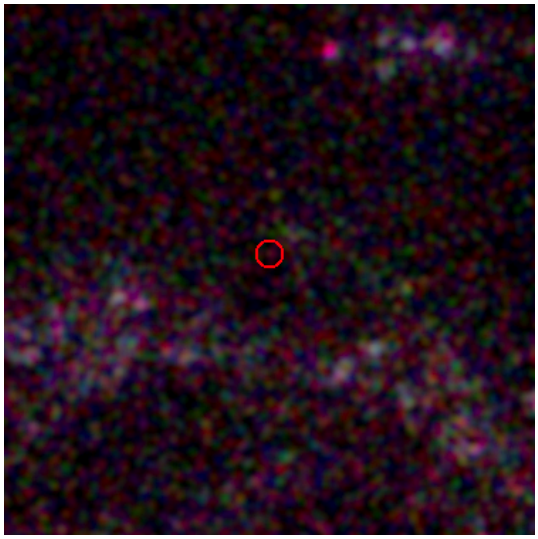

Figure 5.4: *Swift* UVOT close-up of the northern spiral arm of NGC 6946. The position of NGC 6946 ULUV is marked with a 5 arcsecond red circle. Bands are as in Fig. 5.3, with 5 arcsecond Gaussian smoothing applied to each band.

5.3 The case for HST follow-up

While the UVOT catalogue is a better resource for searching for ULUV candidates in other galaxies than *GALEX*, the likely contamination of the UV emission of the variable sources by surrounding star formation means that the UVOT data alone is not sufficient to attempt to characterise a down-scattering wind from a super-Eddington accreting source. However, since we are confident of the presence of a variable source within these regions, these are ideal candidates for follow-up with higher-resolution UV imaging, using the Hubble Space Telescope (*HST*).

None of the six viable ULUV candidates have yet been observed using the UV bands of *HST*, either with the WFC3/UVIS instrument or the ACS/SBC. However, there are *HST* observations of the source in NGC 7318 which demonstrate the resolving capability of *HST* and its potential use for identifying a UV point source. On examination of the optical image for the region in which the source is located (Fig. 5.5), we see two very bright point sources (both of which are slightly blended with another, dimmer source, but are significantly brighter than the extended emission surrounding them) as well as a handful of dimmer point sources and some background objects. Detailed photometry using *HST* data across multiple observations in the UV bands may be able to isolate

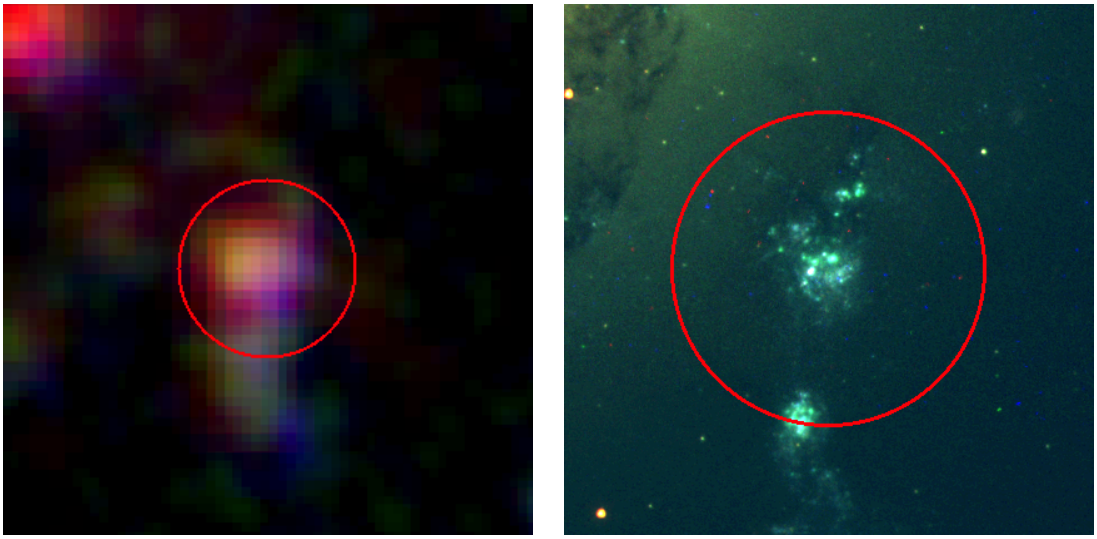

Figure 5.5: The star-forming region in which the NGC 7318 ULUV candidate is located, observed by *Swift* UVOT (*left*, with bands as in Fig. 5.3) and *HST* (*right*, with the F814W band in red, the F606W band in green and the F438W band in blue). The source position is marked with a 5 arcsecond red circle in each case.

which of these sources drives the overall variability of the UVOT source, and therefore is the ULUV candidate.

Once a source is identified using *HST*, SED fitting could then be used to attempt to characterise the optical and UV emission, although this approach is limited if observations are not contemporaneous. UVOT and *GALEX* photometry could also be used to establish upper limits in the fitting – or if the candidate ULUV happens to be an isolated bright source in the midst of extended emission, the *HST* data could be used to model the expected contribution to the UVOT or *GALEX* emission from star formation. As with NGC 6946 ULUV, obtaining an optical spectrum and modelling the emission lines to place limits on the energetics of the system would also go a long way towards constraining the models used to fit the optical/UV SED.

While blind UV searches have not yielded a large number of candidate ULUVs, it is worth noting that NGC 6946 ULUV is bright enough in the X-rays to manifest as a ULX in its own right. Therefore the softest ULXs, as well as soft sources at the Eddington Threshold, may also be good candidates for follow-up UV observations with UVOT and *HST*.

5.4 Conclusion

We use two different UV source catalogues, the *GALEX* source catalogue and the *Swift* UVOT Serendipitous Source Catalogue, to try to make a sample of ULUV sources in order to find and investigate the most extremely downscattered super-Eddington sources. We use a similar method to that described in Chapter 2, and define ULUVs as sources with monochromatic luminosity in any UV band $L > 5 \times 10^{38}\,\mathrm{erg\,s^{-1}}$, and varying by a factor of at least 1.5, in order to rule out star forming regions that do not contain a source of interest.

We find the *GALEX* catalogue to be unsuitable for this purpose because the pipeline prefers to fit large, extended sources to emission in other galaxies, rather than point sources, although its data could potentially be used to follow up on candidates found by other methods.

The *Swift* UVOT catalogue, on the other hand, is far better at identifying extragalactic point sources, however its depth and sky coverage is far more limited than *GALEX*'s. None-the-less, we found six viable ULUV candidates that contain a bright, varying UV source other than the AGN of the host galaxy. However, the UVOT point source aperture is 5 arcseconds, which is large enough for the source to be significantly contaminated by surrounding star formation. Therefore, we propose that this sample could act as a basis for *HST* observations in UV bands, which will be able to identify and resolve the varying source and allow SED fitting of the optical and UV emission.

The small number of viable ULUVs we are able to discover with current UV source catalogues may at first appear to rule out a large population of ULUVs, which could have implications for the predicted wind depth in models of super-Eddington accreting sources. However, since neither the *GALEX* nor the *Swift* UVOT source detection pipelines are able to detect NGC 6946 ULUV, we cannot be confident that all existing ULUVs have been detected. Performing searches using *HST* data directly may be a better way to quantify the number of ULUVs in nearby galaxies in the future.

CHAPTER 6

Conclusions and future work

The aim of this thesis is to create a large and clean catalogue of extragalactic X-ray sources – both ULXs and non-nuclear sources in lower luminosity regimes such as the Eddington Threshold – and to use the catalogue to explore the collective properties of ULXs, as well as to locate sources of particular interest that will help to advance our understanding of extreme accretion onto compact objects. In this section we summarise the findings of this investigation and suggest routes for further study in the future.

In Chapter 2 we described the creation of the catalogue using the *XMM-Newton* 3XMM-DR4 source catalogue as a basis and matching it with nearby galaxies. After the removal of AGNs and other contaminants, the catalogue contains 1,464 sources, 372 of which are ULXs. There are a few main differences between this catalogue and the Walton et al. (2011) catalogue on which the method was based. The more recent data set 3XMM-DR4 is $\sim 50\%$ larger than the previous iteration of the *XMM-Newton* Serendipitous Source Catalogue, providing a higher quantity of data to work with. *XMM-Newton* quality flags were used to filter out potential contamination from camera artefacts and sources with badly constrained fluxes, which introduces a radial bias to the sample but makes it on the whole cleaner than previous catalogues. There is also the effect of the differences in the data reduction pipeline between the 2XMM and 3XMM data releases of *XMM-Newton*, which causes some sources previously classified as ULXs to fall just below the luminosity cut-off or vice versa, which reduces the exact source overlap between the Walton et al. (2011) catalogue and this one. The final ULX count is less than that given in Walton et al. (2011) but they are overall more likely to be reliable candidates. The catalogue also contains a large number of lower-luminosity sources, including 666 objects at the Eddington Threshold, defined as those sources having $10^{38} < L_{\rm X} < 3 \times 10^{39}\,{\rm erg\,s^{-1}}$. This large sample of sources is a valuable resource that opens up investigation into the

boundaries between sub-Eddington and super-Eddington accretion.

When plotted in X-ray hardness ratio (i.e. colour) space, ULXs occupy a region very similar to lower luminosity X-ray sources and distinct from AGNs. For the most part, ULXs in spiral and elliptical host galaxies have the same distribution, but a subset of ULXs in spiral galaxies have harder colours. Upon examination of their host galaxies, many of the sources are in edge-on spirals or in regions of high Galactic obscuration, meaning that it is likely that there is no intrinsic difference in their spectra from the elliptical ULX population but rather that they are simply heavily absorbed.

The catalogue also contains six highly variable ULXs, one of which has a hard spectrum and was closely studied in Chapter 3. Furthermore, there are eight new IMBH candidates from the highest-luminosity objects in the sample, which are good targets for follow-up investigations to measure their distances to test whether they truly lie within their apparent host galaxy or are background sources. Also among the ULXs are 33 sources with over an order of magnitude long-term variability in the flux – making them objects of especial interest since transience is a feature of the three NS ULXs detected to date and may be an indicator of the presence of such a source. Finally, the catalogue contains 666 Eddington Threshold sources, four of which are studied further in Chapter 4.

With the refinement of the catalogue creation method and our improved understanding of the effects of *XMM-Newton* quality flags, we can apply this method to the latest data release of the 3XMM Serendipitous Source Catalogue, 3XMM-DR7 (Rosen et al., 2016), released in June 2017. Its sky coverage has increased to $\sim 2.5\%$, a 30% increase on the sky coverage of 3XMM-DR4, and it contains 34% more sources, as well as having undergone improvements to astrometry, photometry and data quality. This would allow the production of a larger and even more reliable catalogue of extragalactic X-ray binaries.

In the meantime, this catalogue offers the opportunity for multi-wavelength matching, to discover counterparts that will further inform our understanding of the workings of extreme accreting sources across the electromagnetic energy range. For example, selecting ULXs with hard colours can provide a sample suitable to be observed with *NuSTAR* to characterise the high-energy emission of a larger number of ULXs accreting in the hard ultraluminous regime, in order to gain a broader understanding of the high-energy component and thus the workings of the innermost part of super-Eddington accreting systems.

Observations of the softer ULXs and Eddington Threshold sources in the UV regime from *GALEX*, *Swift* UVOT and *HST* may uncover more ULUV candidates and allow further investigation of the extent of down-scattering in super-Eddington winds, especially with the difficulty of finding ULUV candidates serendipitously with current UV missions (see Chapter 5). Searching for counterparts in the near-infrared could indicate the presence of a red supergiant companion star, which would be expected to be dominant in near-infrared emission, and thus good targets for spectroscopy in order to calculate the relative motion in the system and thus derive a mass function. A search for near-infrared counterparts has already been performed with an early version of this catalogue (López et al., 2017) using the William Herschel Telescope, providing a number of potential candidates for spectroscopic follow-up.

There are a number of upcoming missions that will open up further opportunities for multi-wavelength follow-up. One such mission is the *Large Synoptic Survey Telescope* (*LSST*), an 8.4 m optical telescope with first light due in 2019, which will survey the entire available sky every few days with an angular resolution of ~ 0.7 arcseconds at median expected seeing (Ivezic et al., 2008). While it will not be sufficient to resolve optical counterparts in crowded stellar fields, it will be useful in assisting the discovery of optical counterparts for more isolated and optically-faint objects, with the co-adding of multiple visits enabling a survey depth of $r \sim 27.5$. Additionally, with hundreds of visits per object, the optical variability of counterparts can be monitored, facilitating the investigation of links between optical and X-ray variability for extragalactic X-ray sources.

Follow-up of extragalactic X-ray sources in the radio band is important for detecting the presence of radio jets, which may indicate a source accreting in the hard sub-Eddington state or transitioning between states. The brightness of the core of a radio jet at the location of the X-ray source may then be used to constrain the mass of the object using the X-ray/radio fundamental plane. A current spin-off project from this catalogue involved using the *VLA* FIRST survey to find radio counterparts to the ULX sample, then following up a possible counterpart with a *Chandra* observation and a joint *European VLBI Network* (*EVN*) and *e-MERLIN* observation performed quasi-simultaneously. The combination of *EVN* and *e-MERLIN* allows for a very high resolution (~ 1 milliarcsecond) radio image from the very long baseline interferometry, combined with the detection of

extended emission such as that from radio jets from the short baselines of the *MERLIN* network[1]. Crucially, the detection of a radio core at the location of the ULX will confirm it as the source of radio emission and allow an estimation of its mass using the simultaneous radio and X-ray data.

Searching for radio counterparts for extragalactic X-ray sources will be made easier by the advent of future radio telescope projects such as the *Square Kilometre Array* (*SKA*). Expected to begin observations in 2020, the initial capabilities of *SKA* include an angular resolution of 0.25 arcseconds for the *SKA*-mid array and a high sensitivity of $0.75\,\mu\mathrm{Jy\,hr}^{-1/2}$ – incrementally higher than the *Arecibo* and *FAST* radio telescopes, and an order of magnitude more sensitive than the *MERLIN* array – over a continuous frequency range of 0.35–1.4 GHz (Dewdney et al., 2015). The high sensitivity of *SKA* will allow us to probe further into the low end of the IMBH mass range on the fundamental plane, as well as providing the data quality to study IMBH radio jets in detail.

The discovery of a number of transient ULXs provides a sample of ideal targets for further X-ray follow-up to determine whether pulsations can be detected and thus whether any of the transients are NS ULXs. Given their transient nature, a good approach would be to monitor their flux using *Swift* and trigger a deep observation with another telescope when they enter a high-flux state, to allow the collection of sufficient data for analysis, since their low-flux state may be orders of magnitude fainter. The current data on these objects, as well as any new data obtained, can then be searched for pulsations using an accelerated epoch folding search (see below).

Much of the remainder of the thesis contains examples of investigations that emerged from the opportunities presented by the catalogue. We performed a follow-up investigation into a hard, variable ULX discovered during the catalogue study, M51 ULX-7, in Chapter 3. After accounting for contamination of the source X-ray spectrum due to the presence of soft diffuse emission, the spectrum is found to be a consistently hard PL shape with $\Gamma \approx 1.5$ for the majority of observations, despite ULX-7's flux varying over well over an order of magnitude. ULX-7 also has high short-term variability, with fractional rms of 30–40% for all observations and evidence of band-limited noise in the

[1] http://www.evlbi.org/user_guide/user_guide.html

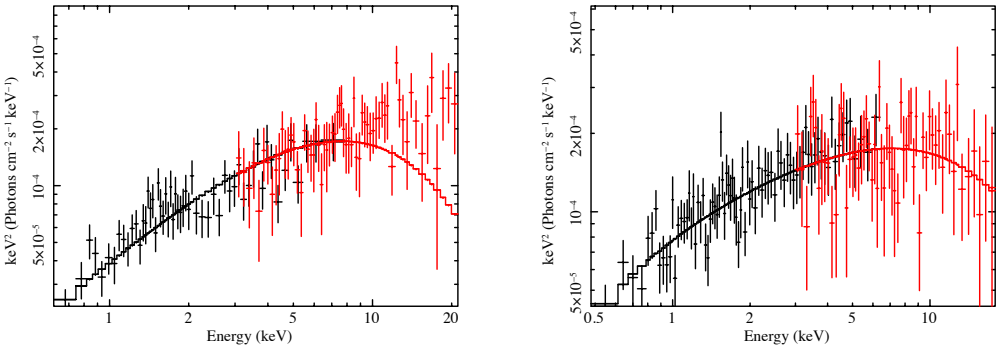

Figure 6.1: Simulated *Chandra* and *NuSTAR* data for ULX-7, for 40 ks and 200 ks respectively. *Left*, simulation with an underlying PL spectrum, plotted with a cut-off PL model with cut-off energy E_c = 6 keV, which can be ruled out at 3σ. *Right*, simulation with an underlying cut-off PL spectrum, with cut-off energy E_c = 18 keV. A cut-off PL model is a significant improvement to the fit over a simple PL model (although this is not the case for the *Chandra* data alone).

power spectrum from its low-frequency break. This high variability puts ULX-7 at odds with the hard ultraluminous regime, which is not expected to be highly variable. The high X-ray/optical flux ratio of the possible optical counterparts to ULX-7 and high variability on short timescales makes it unlikely that the source is a background AGN. Instead, ULX-7 could be an IMBH accreting in a persistent hard state. Assuming this is the case, the lack of a radio detection and high-frequency break in the power spectrum as well as the X-ray flux can be used to place limits on the BH mass, placing it well within the IMBH regime at $\sim 1,000\,M_\odot$. However, a potential break in the energy spectrum above 10 keV may rule out a typical hard accretion state – if this is the case, it is possible that ULX-7 is a NS ULX instead, which would be consistent with its large variation in flux and a high energy turnover similar to that seen in a typical ultraluminous state spectrum.

Better constraints on the high-energy spectrum of ULX-7 would enable the presence (or not) of a high-energy turnover to be confirmed, which would enable us to tell these two possibilities apart. A proposal to observe M51 for 40 ks with *Chandra* and 100 ks with *NuSTAR* simultaneously (PI: Brightman) was recently accepted (and increased to 200 ks on *NuSTAR*) which will provide sufficient data to make this distinction. Fig. 6.1 shows simulations of the expected spectra of ULX-7 at the flux it was last observed at with *NuSTAR*. At this flux, a ULX-like spectrum with a turnover at 6 keV can be rejected at

3σ significance if the underlying spectrum is a PL. Conversely, should the spectrum turn over at 18 keV, this can be recovered from the data, with a cut-off PL fitting significantly better than a simple PL spectrum.

While a simple search for a periodic signal did not reveal any evidence for ULX-7 being a ULX pulsar, the other NS ULXs discovered so far have had period derivatives which indicate pulsar spin-up taking place (Bachetti et al., 2014; Fürst et al., 2016; Israel et al., 2017a). This means that an accelerated epoch folding search is required to strongly detect the pulsation signal for these sources, therefore another good follow-up to the ULX-7 investigation would be to do this for the various *XMM-Newton* observations that exist already, as well as any future ones, to detect or to rule out the existence of accelerating pulsations in this source.

The second follow-up investigation based on the catalogue in Chapter 2 was into the population of Eddington Threshold sources, which we described in Chapter 4. The lower luminosities and thus generally lower fluxes of these objects make them a more challenging population to study compared with ULXs, so we looked for Eddington Threshold sources with the best available data quality, with at least four observations with *XMM-Newton* and at least two of them having over 1,000 counts, as well as having variability of at least a factor of two. Four sources in the catalogue met these criteria, all of them very soft (a consequence of the selection conditions): NGC 300 X-1, M51 ULS, NGC 4395 ULX-1 and NGC 6946 ULX-1.

Even in this small sample, the Eddington Threshold is found to be a heterogeneous population of sources. NGC 300 X-1 is a bright, persistent example of the steep PL state, and a well-studied source. M51 ULS is a classic example of a ULS, with a soft thermal spectrum and little to no hard emission at all. Along with other ULSs, it is consistent with being a super-Eddington accreting source viewed at very high inclinations and/or at a very high accretion rate, causing all hard central emission along the line of sight to be obscured and down-scattered. NGC 4395 ULX-1 and NGC 6946 ULX-1 are similarly very soft, but have very steep PL tails ($\Gamma > 3$) rather than the curvature expected for a black body. These are harder to explain, but this investigation finds them likely to be intermediate sources between the soft ultraluminous and ULS regimes, in which a only very small amount of hard emission reaches the observer. M51 ULS and NGC 6946 ULX-1 both

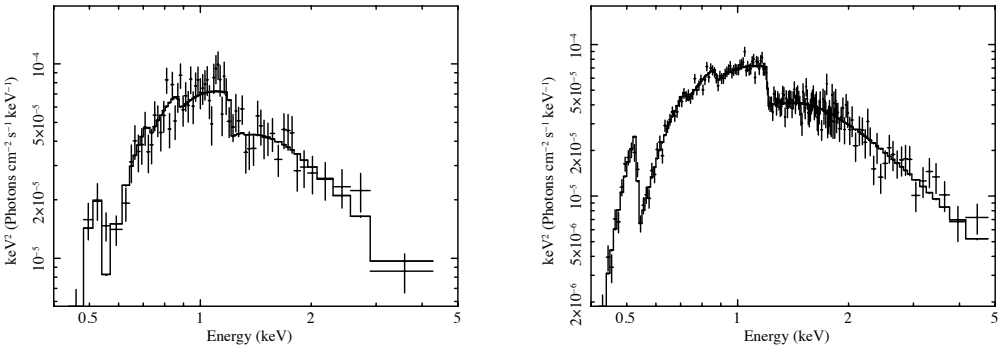

Figure 6.2: *Left*, the *Chandra* spectrum of NGC 6946 ULX-1 from observation C1 (see Chapter 4), with the best-fitting absorbed PL and absorption edge model, with $N_{\rm H} = (5.4 \pm 0.7) \times 10^{21}\,{\rm cm}^{-2}$, $\Gamma = 4.6 \pm 0.3$, $E_{\rm edge} = 1.21^{+0.09}_{-0.05}\,{\rm keV}$ and $\tau = 0.5 \pm 0.2$. The spectrum has $\sim 1,900$ counts, collected over 59 ks. *Right*, the simulated *Athena* spectrum of NGC 6946 ULX-1 for a 20 ks observation, using the same model parameters as the best-fitting model to the *Chandra* data. It is plotted with the best-fitting absorbed PL and absorption edge model, with $N_{\rm H} = (5.6 \pm 0.2) \times 10^{21}\,{\rm cm}^{-2}$, $\Gamma = 4.55 \pm 0.09$, $E_{\rm edge} = 1.20 \pm 0.01\,{\rm keV}$ and $\tau = 0.60 \pm 0.07$, and goodness-of-fit $\chi^2 = 164.2/169$. The spectrum has $\sim 15,000$ counts.

show evidence of a strong absorption edge which, if it can be identified as a blue-shifted absorption feature, will provide further evidence towards their spectra being dominated by a fast outflowing wind.

While the Eddington Threshold pushes the capabilities of current instrumentation to their limits, the far higher effective area of future missions such as *Athena* will allow this population to be studied in far more detail. An example of a simulated 20 ks *Athena* WFI observation of NGC 6946 ULX-1 is shown alongside the longest *Chandra* observation – despite being a third of the duration, the *Athena* spectrum has almost eight times as many counts (and nearly twice as many counts as the longest *XMM-Newton* observation at 110 ks and $\sim 8,300$ counts) and the spectral model can be far better constrained. An example of a simulated 20 ks *Athena* X-IFU observation of NGC 4395 ULX-1 is shown in Fig. 6.3 alongside the best *XMM-Newton* observation. It has around 10,000 more counts than the *XMM-Newton* spectrum despite being a fifth of the duration, and the individual spectral lines from the `mekal` components can be resolved, allowing these spectral features to be far more precisely characterised. This illustrates how high-quality data for the Eddington Threshold population will be far easier and less time-intensive to achieve using

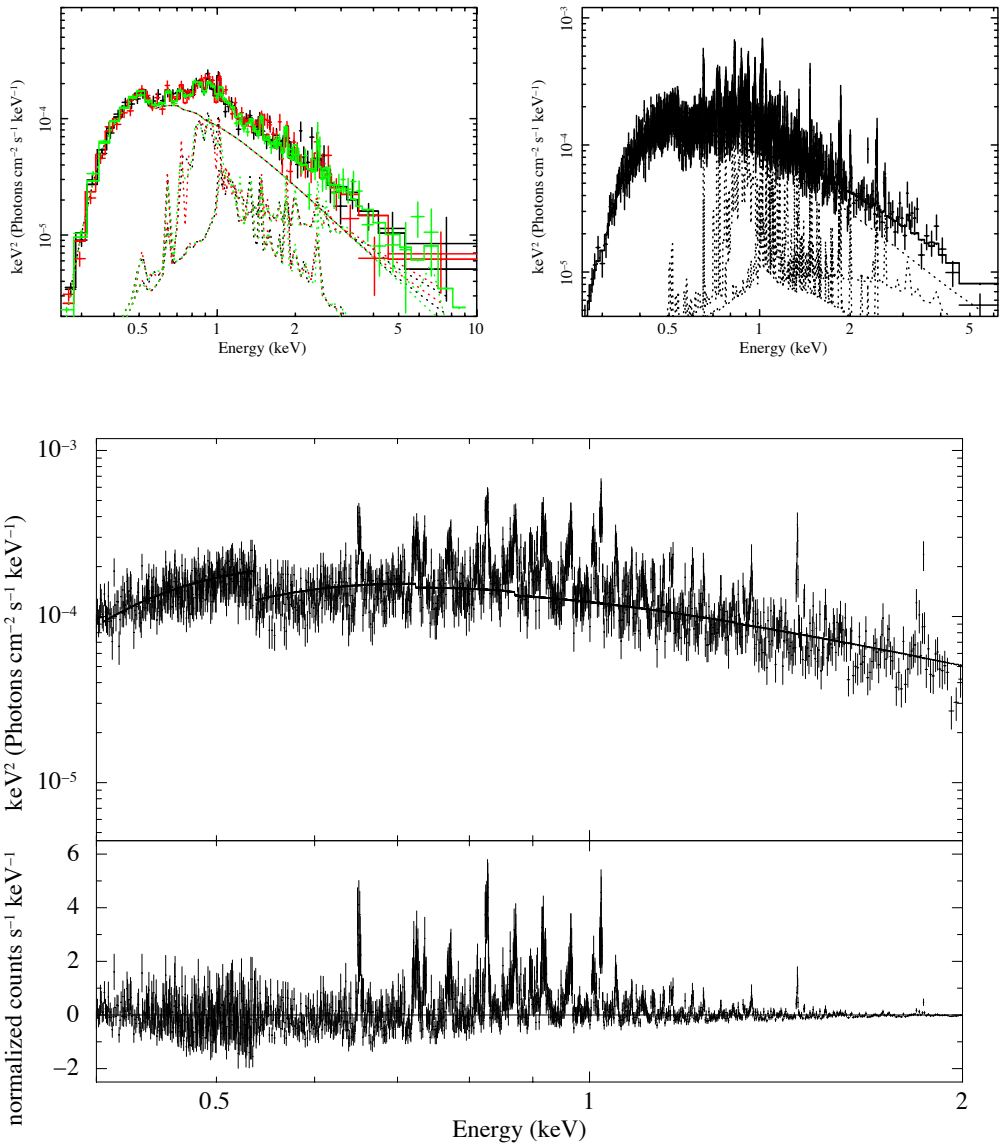

Figure 6.3: *Top left*, the *XMM-Newton* spectrum of NGC 6946 ULX-1 from observation X3 (see Chapter 4), with the best-fitting absorbed PL and two-`mekal`-component model, with $N_{\rm H} = (1.3^{+0.2}_{0.1}) \times 10^{21}$ cm^{-2}, $\Gamma = 3.8^{+0.2}_{-0.1}$, $kT_1 = 0.68 \pm 0.03$ keV and $kT_2 = 1.5^{+0.3}_{-0.2}$. The spectrum has $\sim 32,000$ counts, collected over 104 ks. *Top right*, the simulated *Athena* X-IFU spectrum of NGC 6946 ULX-1 for a 20 ks observation, using the same model parameters as the best-fitting model to the *XMM-Newton* data. It is plotted with the best-fitting absorbed PL and two-mekal-component model, with $N_{\rm H} = (1.38 \pm 0.05) \times 10^{21}$ cm^{-2}, $\Gamma = 3.86 \pm 0.07$, $kT_1 = 0.677 \pm 0.008$ keV and $kT_2 = 1.7 \pm 0.1$ keV, and goodness- of-fit $\chi^2 = 1563.3/1549$. The spectrum has $\sim 42,000$ counts. *Bottom*, The same simulated X-IFU spectrum plotted over the energies 0.4–2 keV with the best-fitting absorbed PL and shown along with the residuals. Individual emission lines in the `mekal` components are resolved and can clearly be seen in the spectrum residuals.

the next generation of space telescopes.

Expanding upon the idea that ULSs are super-Eddington accreting systems viewed at a very high inclinations and/or accretion rates, we went on to investigate a further prediction of this model in Chapter 5 by looking for ultraluminous UV sources (ULUVs) – the expected manifestation of the most extremely obscured or down-scattered super-Eddington accretors (Poutanen et al., 2007). For this investigation, ULUVs are defined as having luminosity in a UV band of $L > 5 \times 10^{38}\,\mathrm{erg\,s^{-1}}$ and at least a factor 1.5 variability to rule out bright star-forming regions. We attempted to make samples of ULUVs using both the *GALEX* and *Swift* UVOT telescopes, finding the *GALEX* source extraction pipeline unsuitable for the study of point sources in other galaxies. Six potential ULUV candidates were identified using UVOT, although the 5 arcsecond PSF still allows for a great deal of contamination from surrounding star-forming regions.

In order to more fully characterise the accreting sources, *HST* follow-up in UV bands will allow individual counterparts to be identified due to its high spatial resolution. Observations in multiple bands – both those where the UV counterpart can be isolated and those from missions such as *GALEX* and *Swift* UVOT which will be able to at least place upper limits on the emission in higher-frequency UV bands – will allow the creation of SEDs that can be fitted with models of the combination of a disc and a companion star. UV follow-up of soft ULXs may also result in the discovery of further ULUVs.

This work presents only the beginning of the potential research avenues opened up by the resource of a large, clean catalogue of extragalactic X-ray sources. It is our hope that this sample will provide the opportunity to perform further valuable science in this fascinating field.

Bibliography

Abazajian, K., Adelman-McCarthy, J. K., Agüeros, M. A., et al. 2004, AJ, 128, 502

Abbott, B. P., Abbott, R., Abbott, T. D., et al. 2016, Physical Review Letters, 116, 061102

Abolmasov, P., Fabrika, S., Sholukhova, O., & Afanasiev, V. 2007, Astrophysical Bulletin, 62, 36

Abolmasov, P., Fabrika, S., Sholukhova, O., & Kotani, T. 2008, ArXiv e-prints

Abramowicz, M. A., Czerny, B., Lasota, J. P., & Szuszkiewicz, E. 1988, ApJ, 332, 646

Arnaud, K. A. 1996, in Astronomical Society of the Pacific Conference Series, Vol. 101, Astronomical Data Analysis Software and Systems V, ed. G. H. Jacoby & J. Barnes, 17

Awaki, H., Kunieda, H., Ishida, M., et al. 2016, in Proc. SPIE, Vol. 9905, Space Telescopes and Instrumentation 2016: Ultraviolet to Gamma Ray, 990512

Bachetti, M., Harrison, F. A., Walton, D. J., et al. 2014, Nature, 514, 202

Bachetti, M., Rana, V., Walton, D. J., et al. 2013, ApJ, 778, 163

Barnard, R., Clark, J. S., & Kolb, U. C. 2008, A&A, 488, 697

Barnard, R., Primini, F., Garcia, M. R., Kolb, U. C., & Murray, S. S. 2015, ApJ, 802, 85

Barret, D., Nandra, K., Barcons, X., et al. 2013, in SF2A-2013: Proceedings of the Annual meeting of the French Society of Astronomy and Astrophysics, ed. L. Cambresy, F. Martins, E. Nuss, & A. Palacios, 447–453

Barret, D., Lam Trong, T., den Herder, J.-W., et al. 2016, in , 9905 – 9905 – 41

Bartlett, M. S. 1948, Nature, 161, 686

Begelman, M. C., King, A. R., & Pringle, J. E. 2006, MNRAS, 370, 399

Belczynski, K., Bulik, T., Fryer, C. L., et al. 2010, ApJ, 714, 1217

Berghea, C. T., & Dudik, R. P. 2012, ApJ, 751, 104

Bianchi, L., Conti, A., & Shiao, B. 2014, Advances in Space Research, 53, 900

Binder, B., Gross, J., Williams, B. F., & Simons, D. 2015, MNRAS, 451, 4471

Binder, B., Williams, B. F., Eracleous, M., et al. 2011, ApJ, 742, 128

Blair, W. P., Fesen, R. A., & Schlegel, E. M. 2001, AJ, 121, 1497

Bolton, C. T. 1972, Nature Physical Science, 240, 124

Bradt, H. V. D., Ohashi, T., & Pounds, K. A. 1992, ARAA, 30, 391

Briel, U. G., Aschenbach, B., Balasini, M., et al. 2000, in Proc. SPIE, Vol. 4012, X-Ray Optics, Instruments, and Missions III, ed. J. E. Truemper & B. Aschenbach, 154–164

Brightman, M., Harrison, F., Walton, D. J., et al. 2015, ArXiv e-prints

Buccheri, R., Bennett, K., Bignami, G. F., et al. 1983, A&A, 128, 245

Cardelli, J. A., Clayton, G. C., & Mathis, J. S. 1989, ApJ, 345, 245

Carpano, S., Pollock, A. M. T., Wilms, J., Ehle, M., & Schirmer, M. 2007, A&A, 461, L9

Charles, P. A., & Coe, M. J. 2003, ArXiv Astrophysics e-prints

Chaty, S. 2011, in Astronomical Society of the Pacific Conference Series, Vol. 447, Evolution of Compact Binaries, ed. L. Schmidtobreick, M. R. Schreiber, & C. Tappert, 29

Colbert, E. J. M., & Mushotzky, R. F. 1999, ApJ, 519, 89

Colbert, E. J. M., & Ptak, A. F. 2002, APJS, 143, 25

Crowther, P. A., Barnard, R., Carpano, S., et al. 2010, MNRAS, 403, L41

Cseh, D., Webb, N. A., Godet, O., et al. 2015, MNRAS, 446, 3268

Dadina, M., Masetti, N., Cappi, M., et al. 2013, A&A, 559, A86

Dall'Osso, S., Perna, R., & Stella, L. 2015, MNRAS, 449, 2144

Davidson, K., & Ostriker, J. P. 1973, ApJ, 179, 585

Davis, D. S., & Mushotzky, R. F. 2004, ApJ, 604, 653

Davis, J. E. 2001, ApJ, 562, 575

de Jager, O. C., Raubenheimer, B. C., & Swanepoel, J. W. H. 1989, A&A, 221, 180

de Vaucouleurs, G. 1994, in Quantifying Galaxy Morphology at High Redshift

de Vaucouleurs, G., de Vaucouleurs, A., Corwin, Jr., H. G., et al. 1991, Third Reference Catalogue of Bright Galaxies. Volume I: Explanations and references. Volume II: Data for galaxies between 0^h and 12^h. Volume III: Data for galaxies between 12^h and 24^h.

den Herder, J. W., Brinkman, A. C., Kahn, S. M., et al. 2001, A&A, 365, L7

Devi, A. S., Misra, R., Shanthi, K., & Singh, K. Y. 2008, ApJ, 682, 218

Dewangan, G. C., Griffiths, R. E., Choudhury, M., Miyaji, T., & Schurch, N. J. 2005, ApJ, 635, 198

Dewdney, P., Turner, W., Braun, R., et al. 2015, SKA1 SYSTEM BASELINEV2 DESCRIPTION

Di Stefano, R., & Kong, A. K. H. 2004, ApJ, 609, 710

Done, C. 2010, ArXiv e-prints

Done, C., & Gierliński, M. 2005, MNRAS, 364, 208

Done, C., Gierliński, M., & Kubota, A. 2007, A&AR, 15, 1

Doroshenko, V., Santangelo, A., & Ducci, L. 2015, A&A, 579, A22

Dunn, R. J. H., Fender, R. P., Körding, E. G., Belloni, T., & Cabanac, C. 2010, MNRAS, 403, 61

Earnshaw, H. M., & Roberts, T. P. 2017, ArXiv e-prints

Earnshaw, H. M., Roberts, T. P., Heil, L. M., et al. 2016, MNRAS, 456, 3840

Edlén, B., & Swings, P. 1942, ApJ, 95, 532

Einstein, A. 1915, Sitzungsberichte der Königlich Preußischen Akademie der Wissenschaften (Berlin), Seite 778-786.

Fabbiano, G. 1988, ApJ, 325, 544

—. 1989, ARAA, 27, 87

Fabrika, S., Ueda, Y., Vinokurov, A., Sholukhova, O., & Shidatsu, M. 2015, Nature Physics, 11, 551

Farrell, S. A., Webb, N. A., Barret, D., Godet, O., & Rodrigues, J. M. 2009, Nature, 460, 73

Farrell, S. A., Servillat, M., Pforr, J., et al. 2012, ApJL, 747, L13

Fender, R., & Belloni, T. 2012, Science, 337, 540

Feng, H., & Kaaret, P. 2005, ApJ, 633, 1052

—. 2007, ApJL, 660, L113

Feng, H., & Soria, R. 2011, NewAR, 55, 166

Feng, H., Tao, L., Kaaret, P., & Grisé, F. 2016, ApJ, 831, 117

Forster, K., Harrison, F. A., Dodd, S. R., et al. 2014, in Proc. SPIE, Vol. 9149, Observatory Operations: Strategies, Processes, and Systems V, 91490R

Frank, J., King, A., & Raine, D. J. 2002, Accretion Power in Astrophysics: Third Edition, 398

Friedman, H., Lichtman, S. W., & Byram, E. T. 1951, PhysRev, 83, 1025

Fürst, F., Walton, D. J., Harrison, F. A., et al. 2016, ApJL, 831, L14

Gao, Y., Wang, Q. D., Appleton, P. N., & Lucas, R. A. 2003, ApJL, 596, L171

Garmire, G. P., Bautz, M. W., Ford, P. G., Nousek, J. A., & Ricker, Jr., G. R. 2003, in Proc. SPIE, Vol. 4851, X-Ray and Gamma-Ray Telescopes and Instruments for Astronomy., ed. J. E. Truemper & H. D. Tananbaum, 28–44

Geller, M. J., Hwang, H. S., Fabricant, D. G., et al. 2014, APJS, 213, 35

Ghosh, H., Mathur, S., Fiore, F., & Ferrarese, L. 2008, ApJ, 687, 216

Giacconi, R. 2003, Rev. Mod. Phys., 75, 995

Giacconi, R., Gursky, H., Kellogg, E., Schreier, E., & Tananbaum, H. 1971a, ApJL, 167, L67

Giacconi, R., Gursky, H., Paolini, F. R., & Rossi, B. B. 1962, Phys. Rev. Lett., 9, 439

Giacconi, R., Kellogg, E., Gorenstein, P., Gursky, H., & Tananbaum, H. 1971b, ApJL, 165, L27

Giacconi, R., Branduardi, G., Briel, U., et al. 1979, ApJ, 230, 540

Gil de Paz, A., Boissier, S., Madore, B. F., et al. 2007, APJS, 173, 185

Gilfanov, M. 2010, in Lecture Notes in Physics, Berlin Springer Verlag, Vol. 794, Lecture Notes in Physics, Berlin Springer Verlag, ed. T. Belloni, 17

Gladstone, J. C., Copperwheat, C., Heinke, C. O., et al. 2013, APJS, 206, 14

Gladstone, J. C., Roberts, T. P., & Done, C. 2009, MNRAS, 397, 1836

Godet, O., Barret, D., Webb, N. A., Farrell, S. A., & Gehrels, N. 2009, ApJL, 705, L109

Gold, T. 1968, Nature, 218, 731

González-Martín, O., & Vaughan, S. 2012, A&A, 544, A80

Grimm, H.-J., Gilfanov, M., & Sunyaev, R. 2002, A&A, 391, 923

—. 2003, Chinese Journal of Astronomy and Astrophysics Supplement, 3, 257

Grinberg, V., Pottschmidt, K., Böck, M., et al. 2014, A&A, 565, A1

Grotrian, W. 1939, Naturwissenschaften, 27, 214

Gültekin, K., Cackett, E. M., King, A. L., Miller, J. M., & Pinkney, J. 2014, ApJL, 788, L22

Gültekin, K., Cackett, E. M., Miller, J. M., et al. 2009, ApJ, 706, 404

Harrison, F. A., Boggs, S., Christensen, F., et al. 2010, in Space Telescopes and Instrumentation 2010: Ultraviolet to Gamma Ray, Vol. 7732, 77320S

Harrison, F. A., Craig, W. W., Christensen, F. E., et al. 2013, ApJ, 770, 103

Hasinger, G., & van der Klis, M. 1989, A&A, 225, 79

Hayashi, T., Sato, T., Kikuchi, N., et al. 2016, in Proc. SPIE, Vol. 9905, Space Telescopes and Instrumentation 2016: Ultraviolet to Gamma Ray, 99055D

Heger, A., Fryer, C. L., Woosley, S. E., Langer, N., & Hartmann, D. H. 2003, ApJ, 591, 288

Heida, M., Jonker, P. G., Torres, M. A. P., et al. 2016, MNRAS, 459, 771

—. 2014, MNRAS, 442, 1054

Heil, L. M., Vaughan, S., & Roberts, T. P. 2009, MNRAS, 397, 1061

Heil, L. M., Vaughan, S., & Uttley, P. 2012, MNRAS, 422, 2620

Hernández-García, L., Vaughan, S., Roberts, T. P., & Middleton, M. 2015, MNRAS, 453, 2877

Hewish, A., Bell, S. J., Pilkington, J. D. H., Scott, P. F., & Collins, R. A. 1968, Nature, 217, 709

Høg, E., Fabricius, C., Makarov, V. V., et al. 2000, A&A, 355, L27

Hornschemeier, A. E., Brandt, W. N., Garmire, G. P., et al. 2001, ApJ, 554, 742

Israel, G. L., Belfiore, A., Stella, L., et al. 2017a, Science, 355, 817

Israel, G. L., Papitto, A., Esposito, P., et al. 2017b, MNRAS, 466, L48

Ivanova, N. 2013, MmSAI, 84, 123

Ivezic, Z., Tyson, J. A., Abel, B., et al. 2008, ArXiv e-prints

Jerius, D., Donnelly, R. H., Tibbetts, M. S., et al. 2000, in Proc. SPIE, Vol. 4012, X-Ray Optics, Instruments, and Missions III, ed. J. E. Truemper & B. Aschenbach, 17–27

Kaaret, P., & Feng, H. 2009, ApJ, 702, 1679

Kaaret, P., Feng, H., & Roberts, T. P. 2017, ARAA, 55, 303

Kaaret, P., Feng, H., Wong, D. S., & Tao, L. 2010, ApJL, 714, L167

Kaaret, P., Ward, M. J., & Zezas, A. 2004, MNRAS, 351, L83

Kajava, J. J. E., & Poutanen, J. 2009, MNRAS, 398, 1450

Kalberla, P. M. W., Burton, W. B., Hartmann, D., et al. 2005, A&A, 440, 775

Kaplan, D. L., Frail, D. A., Gaensler, B. M., et al. 2004, APJS, 153, 269

Karachentsev, I. D., Karachentseva, V. E., Huchtmeier, W. K., & Makarov, D. I. 2004, AJ, 127, 2031

Kerr, R. P. 1963, Phys. Rev. Lett., 11, 237

Kilgard, R. E., Cowan, J. J., Garcia, M. R., et al. 2005, APJS, 159, 214

King, A. R. 2004, MNRAS, 347, L18

King, A. R., Davies, M. B., Ward, M. J., Fabbiano, G., & Elvis, M. 2001, ApJL, 552, L109

Kitaguchi, T., Bhalerao, V., Cook, W. R., et al. 2014, in Proc. SPIE, Vol. 9144, Space Telescopes and Instrumentation 2014: Ultraviolet to Gamma Ray, 91441R

Koljonen, K. I. I., Hannikainen, D. C., McCollough, M. L., Pooley, G. G., & Trushkin, S. A. 2010, MNRAS, 406, 307

Körding, E., Falcke, H., & Markoff, S. 2002, A&A, 382, L13

Körding, E. G., Fender, R. P., & Migliari, S. 2006, MNRAS, 369, 1451

Körding, E. G., Migliari, S., Fender, R., et al. 2007, MNRAS, 380, 301

Krautter, J., Zickgraf, F.-J., Appenzeller, I., et al. 1999, A&A, 350, 743

Kubota, A., & Done, C. 2016, MNRAS, 458, 4238

Leutenegger, M. A., Audard, M., Boyce, K. R., et al. 2016, in Proc. SPIE, Vol. 9905, Space Telescopes and Instrumentation 2016: Ultraviolet to Gamma Ray, 99053U

Li, X.-D. 2015, NewAR, 64, 1

Liu, J.-F., & Bregman, J. N. 2005, APJS, 157, 59

Liu, J.-F., Bregman, J. N., Irwin, J., & Seitzer, P. 2002, ApJL, 581, L93

Liu, Q. Z., & Mirabel, I. F. 2005, A&A, 429, 1125

López, K. M., Heida, M., Jonker, P. G., et al. 2017, ArXiv e-prints

Lorimer, D. R., & Kramer, M. 2004, Handbook of Pulsar Astronomy

Luangtip, W., Roberts, T. P., & Done, C. 2016, MNRAS, 460, 4417

Lumb, D. H., Schartel, N., & Jansen, F. A. 2012, Optical Engineering, 51, 011009

Lutovinov, A., Revnivtsev, M., Gilfanov, M., et al. 2005, A&A, 444, 821

Maccarone, T. J. 2003, A&A, 409, 697

Madau, P., & Rees, M. J. 2001, ApJL, 551, L27

Maddox, L. A., Cowan, J. J., Kilgard, R. E., Schinnerer, E., & Stockdale, C. J. 2007, AJ, 133, 2559

Madhusudhan, N., Rappaport, S., Podsiadlowski, P., & Nelson, L. 2008, ApJ, 688, 1235

Madsen, K. K., Harrison, F. A., An, H., et al. 2014, in Proc. SPIE, Vol. 9144, Space Telescopes and Instrumentation 2014: Ultraviolet to Gamma Ray, 91441P

Mapelli, M., Zampieri, L., & Mayer, L. 2012, MNRAS, 423, 1309

Martin, C., Barlow, T., Barnhart, W., et al. 2003, in Proc. SPIE, Vol. 4854, Future EUV/UV and Visible Space Astrophysics Missions and Instrumentation., ed. J. C. Blades & O. H. W. Siegmund, 336–350

Martin, D. C., Fanson, J., Schiminovich, D., et al. 2005, ApJL, 619, L1

Mason, K. O., Breeveld, A., Much, R., et al. 2001, A&A, 365, L36

Mateos, S., Carrera, F. J., Page, M. J., et al. 2010, A&A, 510, A35

McClintock, J. E., & Remillard, R. A. 2006, Black hole binaries, 157–213

McHardy, I. M., Arévalo, P., Uttley, P., et al. 2007, MNRAS, 382, 985

McHardy, I. M., Koerding, E., Knigge, C., Uttley, P., & Fender, R. P. 2006, Nature, 444, 730

Meidinger, N., Eder, J., Eraerds, T., et al. 2016, in , 9905 – 9905 – 12

Mezcua, M., Roberts, T. P., Lobanov, A. P., & Sutton, A. D. 2015, MNRAS, 448, 1893

Mezcua, M., Roberts, T. P., Sutton, A. D., & Lobanov, A. P. 2013, MNRAS, 436, 3128

Middleton, M. J., Heil, L., Pintore, F., Walton, D. J., & Roberts, T. P. 2015a, MNRAS, 447, 3243

Middleton, M. J., Sutton, A. D., & Roberts, T. P. 2011, MNRAS, 417, 464

Middleton, M. J., Walton, D. J., Fabian, A., et al. 2015b, MNRAS, 454, 3134

Migliazzo, J. M., Gaensler, B. M., Backer, D. C., et al. 2002, ApJL, 567, L141

Miller, J. M., Fabian, A. C., & Miller, M. C. 2004, ApJL, 614, L117

Miller, J. M., Homan, J., Steeghs, D., et al. 2006, ApJ, 653, 525

Miller, M. C., & Hamilton, D. P. 2002, MNRAS, 330, 232

Mineo, S., Gilfanov, M., & Sunyaev, R. 2012, MNRAS, 419, 2095

Mirabel, F. 2017, NewAR, 78, 1

Misner, C. W., Thorne, K. S., & Wheeler, J. A. 1973, Gravitation

Mitsuda, K., Inoue, H., Koyama, K., et al. 1984, PASJ, 36, 741

Miyawaki, R., Makishima, K., Yamada, S., et al. 2009, PASJ, 61, 263

Moretti, A., Campana, S., Lazzati, D., & Tagliaferri, G. 2003, ApJ, 588, 696

Morrissey, P., Conrow, T., Barlow, T. A., et al. 2007, APJS, 173, 682

Motch, C., Pakull, M. W., Grisé, F., & Soria, R. 2011, Astronomische Nachrichten, 332, 367

Motta, S., Muñoz-Darias, T., Casella, P., Belloni, T., & Homan, J. 2011, MNRAS, 418, 2292

Motta, S. E. 2016, Astronomische Nachrichten, 337, 398

Muñoz-Darias, T., Motta, S., & Belloni, T. M. 2011, MNRAS, 410, 679

Mukherjee, E. S., Walton, D. J., Bachetti, M., et al. 2015, ApJ, 808, 64

Mushtukov, A. A., Suleimanov, V. F., Tsygankov, S. S., & Poutanen, J. 2015, MNRAS, 454, 2539

Nandra, K., Barret, D., Barcons, X., et al. 2013, ArXiv e-prints

Okada, K., Dotani, T., Makishima, K., Mitsuda, K., & Mihara, T. 1998, PASJ, 50, 25

Ostriker, J. P., & Gunn, J. E. 1969, ApJ, 157, 1395

Owen, R. A., & Warwick, R. S. 2009, MNRAS, 394, 1741

Page, M. J., Brindle, C., Talavera, A., et al. 2012, MNRAS, 426, 903

Page, M. J., Yershov, V., Breeveld, A., et al. 2014, 37

Piconcelli, E., Cappi, M., Bassani, L., Di Cocco, G., & Dadina, M. 2003, A&A, 412, 689

Pinto, C., Middleton, M. J., & Fabian, A. C. 2016, Nature, 533, 64

Pintore, F., Zampieri, L., Wolter, A., & Belloni, T. 2014, MNRAS, 439, 3461

Poutanen, J., Lipunova, G., Fabrika, S., Butkevich, A. G., & Abolmasov, P. 2007, MNRAS, 377, 1187

Prestwich, A. H., Irwin, J. A., Kilgard, R. E., et al. 2003, ApJ, 595, 719

Pringle, J. E. 1981, ARAA, 19, 137

Rampadarath, H., Morgan, J. S., Soria, R., et al. 2015, MNRAS, 452, 32

Rau, A., Meidinger, N., Nandra, K., et al. 2013, ArXiv e-prints

Read, A. M., Rosen, S. R., Saxton, R. D., & Ramirez, J. 2011, A&A, 534, A34

Reeves, J. N., & Turner, M. J. L. 2000, MNRAS, 316, 234

Remillard, R. A., & McClintock, J. E. 2006, ARAA, 44, 49

Roberts, T. P. 2007, APSS, 311, 203

Roberts, T. P., Levan, A. J., & Goad, M. R. 2008, MNRAS, 387, 73

Roberts, T. P., & Warwick, R. S. 2000, MNRAS, 315, 98

Rosen, S., Watson, M., Pye, J., et al. 2015, in Astronomical Society of the Pacific Conference Series, Vol. 495, Astronomical Society of the Pacific Conference Series, ed. A. R. Taylor & E. Rosolowsky, 319

Rosen, S. R., Webb, N. A., Watson, M. G., et al. 2016, A&A, 590, A1

Rybicki, G. B., & Lightman, A. P. 1979, Radiative processes in astrophysics

Salvesen, G., Miller, J. M., Reis, R. C., & Begelman, M. C. 2013, MNRAS, 431, 3510

Schlafly, E. F., & Finkbeiner, D. P. 2011, ApJ, 737, 103

Schwarzschild, K. 1916, Sitzungsberichte der Königlich Preußischen Akademie der Wissenschaften (Berlin), 1916, Seite 189-196

Schwehr, J., & Li, W. 2006, IAUC, 8728

Servillat, M., Farrell, S. A., Lin, D., et al. 2011, ApJ, 743, 6

Shakura, N. I., & Sunyaev, R. A. 1973, A&A, 24, 337

Shapiro, S. L., & Teukolsky, S. A. 1983, Black holes, white dwarfs, and neutron stars: The physics of compact objects

Shidatsu, M., Done, C., & Ueda, Y. 2016, ApJ, 823, 159

Shore, S. N. 1992, in Astronomical Society of the Pacific Conference Series, Vol. 22, Nonisotropic and Variable Outflows from Stars, ed. L. Drissen, C. Leitherer, & A. Nota, 342

Shtykovskiy, P., & Gilfanov, M. 2005, MNRAS, 362, 879

Sirianni, M., Jee, M. J., Benítez, N., et al. 2005, PASP, 117, 1049

Smartt, S. J. 2009, ARAA, 47, 63

Smith, J. F., & Courtier, G. M. 1976, RSPSA, 350, 421

Soria, R. 2007, APSS, 311, 213

Soria, R., & Kong, A. 2016, MNRAS, 456, 1837

Steiner, J. F., Narayan, R., McClintock, J. E., & Ebisawa, K. 2009, PASP, 121, 1279

Stella, L., White, N. E., & Rosner, R. 1986, ApJ, 308, 669

Stetson, P. B. 1987, PASP, 99, 191

Stobbart, A.-M., Roberts, T. P., & Wilms, J. 2006, MNRAS, 368, 397

Strohmayer, T. E., Mushotzky, R. F., Winter, L., et al. 2007, ApJ, 660, 580

Strüder, L., Briel, U., Dennerl, K., et al. 2001, A&A, 365, L18

Sutton, A. D., Roberts, T. P., Gladstone, J. C., et al. 2013a, MNRAS, 434, 1702

Sutton, A. D., Roberts, T. P., Gladstone, J. C., & Walton, D. J. 2015, MNRAS, 450, 787

Sutton, A. D., Roberts, T. P., & Middleton, M. J. 2013b, MNRAS, 435, 1758

Sutton, A. D., Roberts, T. P., Walton, D. J., Gladstone, J. C., & Scott, A. E. 2012, MNRAS, 423, 1154

Swartz, D. A., Ghosh, K. K., Tennant, A. F., & Wu, K. 2004, APJS, 154, 519

Swartz, D. A., Soria, R., Tennant, A. F., & Yukita, M. 2011, ApJ, 741, 49

Taam, R. E., & Ricker, P. M. 2010, NewAR, 54, 65

Takahashi, T., Kokubun, M., Mitsuda, K., et al. 2016, in Proc. SPIE, Vol. 9905, Space Telescopes and Instrumentation 2016: Ultraviolet to Gamma Ray, 99050U

Tao, L., Feng, H., Grisé, F., & Kaaret, P. 2011, ApJ, 737, 81

Tauris, T. M., & van den Heuvel, E. P. J. 2006, Formation and evolution of compact stellar X-ray sources, ed. W. H. G. Lewin & M. van der Klis, 623–665

Terashima, Y., Inoue, H., & Wilson, A. S. 2006, ApJ, 645, 264

Terashima, Y., & Wilson, A. S. 2004, ApJ, 601, 735

Tsunemi, H., Hayashida, K., Tsuru, T. G., et al. 2016, in Proc. SPIE, Vol. 9905, Space Telescopes and Instrumentation 2016: Ultraviolet to Gamma Ray, 990510

Tsygankov, S. S., Mushtukov, A. A., Suleimanov, V. F., & Poutanen, J. 2016, MNRAS, 457, 1101

Tully, R. B., & Fisher, J. R. 1988, Catalog of Nearby Galaxies, 224

Turner, M. J. L., Abbey, A., Arnaud, M., et al. 2001, A&A, 365, L27

Urquhart, R., & Soria, R. 2016a, MNRAS, 456, 1859

—. 2016b, ApJ, 831, 56

Urry, C. M., & Shafer, R. A. 1984, ApJ, 280, 569

Uttley, P., & Klein-Wolt, M. 2015, MNRAS, 451, 475

van der Klis, M. 1989, in NATO Advanced Science Institutes (ASI) Series C, Vol. 262, NATO Advanced Science Institutes (ASI) Series C, ed. H. Ögelman & E. P. J. van den Heuvel, 27

van Genderen, A. M. 2001, A&A, 366, 508

van Paradijs, J., & McClintock, J. E. 1995, X-ray Binaries, 58

Vaughan, S., Edelson, R., Warwick, R. S., & Uttley, P. 2003, MNRAS, 345, 1271

Verbunt, F. 1993, ARAA, 31, 93

Véron-Cetty, M.-P., & Véron, P. 2010, A&A, 518, A10

Vesperini, E., McMillan, S. L. W., D'Ercole, A., & D'Antona, F. 2010, ApJL, 713, L41

Vinokurov, A., Fabrika, S., & Atapin, K. 2016, ArXiv e-prints

Visser, M. 2007, ArXiv e-prints

Walton, D. J., Roberts, T. P., Mateos, S., & Heard, V. 2011, MNRAS, 416, 1844

Walton, D. J., Harrison, F. A., Grefenstette, B. W., et al. 2014, ApJ, 793, 21

Walton, D. J., Harrison, F. A., Bachetti, M., et al. 2015a, ApJ, 799, 122

Walton, D. J., Middleton, M. J., Rana, V., et al. 2015b, ApJ, 806, 65

Walton, D. J., Fuerst, F., Harrison, F. A., et al. 2016, ArXiv e-prints

Watson, M. G., Auguères, J.-L., Ballet, J., et al. 2001, A&A, 365, L51

Webb, N., Cseh, D., Lenc, E., et al. 2012, Science, 337, 554

Webster, B. L., & Murdin, P. 1972, Nature, 235, 37

Wegner, W. 2006, MNRAS, 371, 185

Weisskopf, M. C. 2012, Optical Engineering, 51, 011013

Weisskopf, M. C., Brinkman, B., Canizares, C., et al. 2002, PASP, 114, 1

Wilms, J., Allen, A., & McCray, R. 2000, ApJ, 542, 914

Winter, L. M., Mushotzky, R. F., & Reynolds, C. S. 2007, ApJ, 655, 163

Yoshida, T., Ebisawa, K., Matsushita, K., Tsujimoto, M., & Kawaguchi, T. 2010, ApJ, 722, 760

Yuan, H. B., Liu, X. W., & Xiang, M. S. 2013, MNRAS, 430, 2188

Zdziarski, A. A., & Gierliński, M. 2004, Progress of Theoretical Physics Supplement, 155, 99

Zhang, S.-N. 2013, Frontiers of Physics, 8, 630

Zhang, W. M., Soria, R., Zhang, S. N., Swartz, D. A., & Liu, J. F. 2009, ApJ, 699, 281

Zolotukhin, I., Webb, N. A., Godet, O., Bachetti, M., & Barret, D. 2016, ApJ, 817, 88